Title
The Impact of External Forcing and Disturbance on the Regional and Global Climate

Author
Huang, Huilin

Publication Date
2021

Peer reviewed|Thesis/dissertation

UNIVERSITY OF CALIFORNIA

Los Angeles

The Impact of External Forcing and Disturbance on the Regional and Global Climate

A dissertation submitted in partial satisfaction of the requirements for the degree Doctor of Philosophy in Geography

by

Huilin Huang

2021

ABSTRACT OF THE DISSERTATION

The Impact of External Forcing and Disturbance

on the Regional and Global Climate

by

Huilin Huang

Doctor of Philosophy in Geography

University of California, Los Angeles, 2021

Professor Yongkang Xue, Chair

The earth system has been modified by human activities over the past few centuries, mainly through the greenhouse gases (GHGs) and aerosol emissions, land use and land cover changes (LULCCs), and fire regime changes induced by human. This PhD study seeks to understand and quantify the impact of different forcings and disturbance on regional and global climate, especially through land-atmosphere interactions, using climate model simulations. Chapter 2 examines the aerosol indirect effects on ice cloud particle size and consequent impacts on monsoon climate. Simulations show a negative radiative forcing (0.5–1.0 W m^{-2}) at the top of the atmosphere, caused by both particle size decreases and cloud cover change. This radiative forcing is influenced directly by cloud microphysics and indirectly by large-scale circulation, which contributes to large uncertainties in aerosol modeling studies.

In Chapter 3, the large-scale LULCC impact on global temperature and precipitation is investigated by implementing a yearly-updated vegetation map into a climate model. LULCCs influence the local climate by modifying surface biophysical properties (albedo and roughness). Chapter 3 shows that LULCC-induced non-radiative cooling can lead to an asymmetric atmospheric cooling and an anomalous heat transport across the equator, accomplished by changes in Hadley circulation and ITCZ. This, for the first time, connects the local and global effects of LULCC from the perspective of energy budget and energy transport within the climate system.

Wildfire is one of the primary disturbances to the world's ecosystem yet the modeling study of fire effects is still in an early stage. A fire-coupled vegetation model is developed to investigate fire effects on terrestrial ecosystem and surface energy in Chapters 4 and 5. In the long term, fire reduced tree fraction by 30-50% in tropical savanna, decreasing leaf area index and vegetation height by 0.52 m^2 m^{-2} (12.5%) and 5.76 m (49.1%). While current fire models mainly work on the fire effect at annual and longer time scales, Chapter 5, for the first time, quantifies monthly to annual fire impact using a fire-vegetation model. The characteristics of simulated fire effects at intra-seasonal to seasonal scales are analyzed and are compared with observations.

This dissertation of Huilin Huang is approved.

Thomas Welch Gillespie

Dennis P. Lettenmaier

Kuo-Nan Liou

Gregory Stewart Okin

Yongkang Xue, Committee Chair

University of California, Los Angeles

2021

This dissertation is dedicated to my parents and my grandparents.

Table of Contents

Chapter 1 Introduction **1**

1.1 Land-atmosphere interactions in a changing environment **1**

1.2 Anthropogenic aerosol emissions and aerosol-cloud interactions **2**

1.3 Land use and land cover change effect on surface energy and climate system **3**

1.4 The role of fire in the terrestrial ecosystem and surface energy **5**

Chapter 2 Assessing aerosol indirect effect on clouds and regional climate **16**

2.1 Introduction **18**

2.2 Description of cloud parameterization **22**

2.2.1 Parameterization of aerosol effect on ice clouds 22

2.2.2 Parameterization of aerosol effect on liquid clouds 23

2.3. Model, datasets and experiment design **23**

2.3.1 Model Description and Datasets 23

2.3.2 Experiment design 25

2.4. Aerosol effect on ice clouds **27**

2.5 Comparison between aerosol effects on liquid clouds and ice clouds **33**

2.6 Conclusion **36**

Tables and Figures **39**

Reference **53**

Chapter 3 Assessing global and regional effects of reconstructed land use and land cover change on climate since 1950 using a coupled land-atmosphere-ocean model 62

3.1 Introduction 64

3.2. Model, methodology, and experiment design 69

3.2.1 Model, LULCC map, and experiment design 69

3.2.2 Decomposition metric 72

3.2.3 The energy flux framework 74

3.2.4 Statistical Methods 75

3.3 Results 76

3.3.1 Global and regional changes of temperature, precipitation, and Hadley circulation due to large-scale LULCC 76

3.3.2 LST response and its contribution from radiation and turbulent fluxes 78

3.3.3 The effect of LULCC on precipitation and large-scale circulation from the perspective of meridional energy transport 81

3.4 Discussion 85

3.4.1 LST response in observational studies 85

3.4.2 The regional and global effects of LULCC 85

3.4.3 Uncertainties in LULCC simulation 87

3.5 Conclusions 88

Tables and Figures 90

Reference 104

Chapter 4 Modeling long-term fire impact on ecosystem characteristics and surface energy using a process-based vegetation-fire model SSiB4/TRIFFID-Fire v1.0 116

4.1 Introduction 118

4.2 Method 121

4.2.1 Land and vegetation model 121

4.2.2 Fire model and modifications 122

4.2.3 Implementing fire model in SSiB4/TRIFFID 127

4.3 Experimental setup and data 128

4.3.1 Experimental design 128

4.3.2 Model input and validation data 129

4.4 Results 130

4.4.1 Burned Area 131

4.4.2 Fire emissions 135

4.4.3 PFT distribution and GPP 136

4.4.4 Fire effects on ecosystem characteristics and surface properties 138

4.5 Conclusions and discussions 141

Tables and Figures 144

Reference 159

Chapter 5 Improving SSiB4/TRIFFID-Fire and modeling the short-term fire effects on vegetation dynamics and surface energy in Southern Hemisphere Africa 172

5.1 Introduction 174

5.2 Method 177

5.2.1 The SSiB4/TRIFFID-Fire vegetation-fire model 177

5.2.2 Model Improvement 178

5.2.3 Experiment design 180

5.2.4 Validation data 181

5.3 Modeling fire effects in SHAF 182

5.3.1 Model validation 182

5.3.2 Fire effects on vegetation 186

5.3.3 Fire effects on surface energy 188

5.4 Discussion and conclusion 190

5.4.1 Surface darkening effects due to fire 190

5.4.2 Uncertainty and limitation 191

5.4.3 Conclusions 193

Tables and Figures 195

Appendix A 216

Appendix B 228

LIST OF FIGURES

Error! Reference source not found.

Error! Reference source not found.

Error! Reference source not found.

Error! Reference source not found.

Error! Reference source not found.

Error! Reference source not found.

Error! Reference source not found.

Error! Reference source not found.

Figure 2.8 JJA latitude-height cross-section of (a) streamline (v; -w*-100) in CTL1 and (b) differences between ICE and CTL1 averaged over 15°W-10°E (ICE-CTL1

Figure 2.9 JJA differences of a) moisture flux (m s-1) at 850 hPa and vertically integrated moisture flux divergence (mm day-1) and b) 500 hPa vertical velocity (mb day-1) in West Africa between ICE and CTL1 (ICE-CTL1)

Figure 2.10 Differences of Rel (μm) in JJA between LIQ and CTL2 (LIQ-CTL2)

Figure 2.11 Differences of in a) TOA upward shortwave radiation (W m-2), b) column cloud cover (%), c) surface temperature (K), and d) precipitation (mm day-1) in JJA between LIQ and CTL2 (LIQ-CTL2)

Figure 2.12 Aerosol indirect effects on a) TOA radiation (W m-2), b) surface radiation (W m-2), c) surface temperature (K), and d) precipitation (mm day-1) on the Global scale, Northern Hemisphere, East Asia, West Africa, and South Asia

Figure 3.1 LULCC fraction difference between (a) 1950 and 1948 (The boxes show ten degraded regions, whose coordinates and name are summarized in Table 1), (b) 1970 and 1948, (c)

1990 and 1948, and (d) 2015 and 1948. The red color indicates an increase in anthropogenic land use while the blue color indicates a decrease in anthropogenic land use compared to 1948.

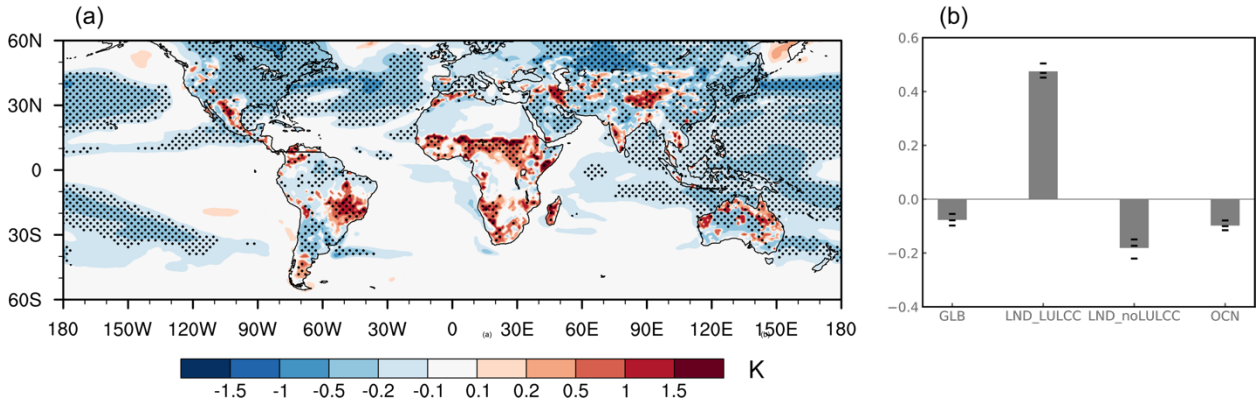

Figure 3.2 (a) Annual surface temperature difference (K) due to LULCC effects during 1950-2015 (LULCC – CTL). Stippling indicates that the response is statistically significant at the 95% confidence level. (b) Temperature difference (K) over the globe (GLB), land areas with LULCC (LND_LULCC), land areas without LULCC (LND_noLULCC), and ocean (OCN) in 60 °S-60 °N. The black lines indicate the response in three ensemble members.

Figure 3.3 (a) Annual difference of precipitation (mm day-1) due to LULCC during 1950-2015 (LULCC – CTL; Black line: zero contour of the 700-hPa annual-mean vertical velocity during 1950–2015 over oceans). Stippling indicates statistical significance at the 90% confidence level. (b) Annual difference of zonal-mean stream function (kg s-1) between LULCC and CTL during 1950-2015. Changes of stream function in color shadings and the climatological value in CTL in white contours.

Figure 3.4 Decomposition of annual LST change (K) due to LULCC effects during 1950-2015 (LULCC-CTL). (a) Difference in LST between LULCC and CTL. (b) - (g) decomposed

LST changes due to changes in surface albedo (ABD: $\frac{-SW_{in}\Delta\alpha_s}{4\sigma LST^3}$ in Eq. 2), incoming shortwave radiation (SW_in: $(1-\alpha_s)\,\Delta SWin4\sigma LST3$), incoming longwave radiation (LW_in: $\Delta LWin4\sigma LST3$), latent heat flux (LH: $-\Delta LH4\sigma LST3$), sensible heat flux (SH: $-\Delta SH4\sigma LST3$), and ground heat flux (G: $-\Delta G4\sigma LST3$), respectively. (h) Sum of surface temperature contribution from (b) – (g). (i) The difference between (a) *and (h)*

Figure 3.5 Differences of annual (a) specific humidity (g kg-1) and (b) temperature (K) between LULCC and CTL during 1950-2015 (LULCC-CTL). The contours represent the climatological mean from CTL and the shaded colors represent LULCC-CTL. Stippling indicates that the response is statistically significant at the 95% confidence level.

Figure 3.6 Annual LST changes (K) due to LULCC and its contribution from albedo (ABD), incoming shortwave (SW_in), incoming longwave radiation (LW_in), latent heat (LH), sensible heat (SH), and ground heat (G) in (a) LULCC regions in low and mid latitudes and (b) non-LULCC regions during the 1950-2015 period. The black lines indicate the response in three ensemble members.

Figure 3.7 Decomposition of annual SH changes (W m-2) due to LULCC effects during 1950-2015 (LULCC-CTL). (a) Difference in SH between LULCC and CTL. (b) - (d) Decomposed SH changes due to changes in surface temperature (TS: $\frac{\rho C_p}{r_a}\Delta LST$ in Eq 4.1), air temperature (TA: $-\frac{\rho C_p}{r_a}\Delta T_a$), and aerodynamic resistance (RA: $-\frac{(LST-T_a)\rho C_p}{r_a^2}\Delta r_a$). (e) Sum of SH changes from (b)-(d). (f) The difference between (a) and (e).Figure 3.8 Decomposition of annual LH changes (W m-2) due to LULCC effects during 1950-2015 (LULCC-CTL). (a) Difference in LH between LULCC and CTL (b) - (d) Decomposed LH changes due to changes in surface vapor pressure (ES: $\frac{\rho C_p}{\lambda(r_a+r_c)}\Delta e_s$), atmosphere vapor

pressure (EA: $-\frac{\rho C_p}{\lambda(r_a+r_c)}\Delta e_a$), and surface resistance (RA+RC: $-\frac{(e_s-e_a)\rho C_p}{\lambda(r_a+r_c)^2}\Delta(r_a+r_c)$). (e) Sum of LH changes from (b)-(d). (f) The difference between (a) and (e).

Figure 3.9 Annual LH changes (W m-2) due to LULCC and its contribution from surface vapor pressure (ES: $\frac{\rho C_p}{\lambda(r_a+r_c)}\Delta e_s$), atmosphere vapor pressure (EA: $-\frac{\rho C_p}{\lambda(r_a+r_c)}\Delta e_a$), surface resistance (RA+RC: $-\frac{(e_s-e_a)\rho C_p}{\lambda(r_a+r_c)^2}\Delta(r_a+r_c)$), and others in degraded regions in low and mid latitudes during 1950-2015. The black lines indicate the response in three ensemble members.

Figure 3.10 (a) The annual difference of 1950-2015 zonal-mean precipitation (PRE; black; in mm day-1), evaporation (EVP; red; in mm day-1), and moisture flux convergence (MFC; blue; in mm day-1) between LULCC and CTL (LULCC-CTL) over land. (b) Same as Fig. 10a but over the ocean. (c) Atmospheric column MFC (shaded; mm day-1) and moisture flux at 850 hPa (vector; g kg-1 m s-1) between LULCC and CTL (LULCC-CTL)

Figure 3.11 The 1950-2015 annual zonal mean (a) atmospheric heating in CTL (dash) and its difference between LULCC and CTL (solid). (b) The 1950-2015 atmospheric energy transport in CTL (dash; blue) and LULCC (dash; red) and its difference between LULCC and CTL (solid). The bottom right of Fig. 11b shows the enlarged box of atmosphere energy transport in CTL and LULCC near the equator. (c) The 1950-2015 annual difference of zonal annual atmospheric heating (R_{ATM}; black) and its components: R_{TOA} (red), $-R_{SFC}$ (orange), LH (blue), and SH (green) between LULCC and *CTL*

Figure 3.12 The 1950-2015 annual-mean difference of zonal wind (m s-1) between LULCC and CTL (color shadings) and climatological zonal wind in CTL (black contours). Stippling indicates statistical significance at 95% confidence level.

Figure 4.1 Schematic diagram of fire model coupling in SSiB4/TRIFFID-Fire (Tair: air temperature; Pres: surface pressure; Dp: population density; fcrop: crop fraction; Tc: canopy temperature; Res: autotrophic respiration; SM: soil moisture; LST: land surface temperature; RH: relative humidity; VHT: vegetation height)

Figure 4.2 Experiment design for FIRE-ON and FIRE-OFF experiments

Figure 4.3 Spatial distribution of annual burned fraction (%) averaged over 2000–2014 for (a) GFED4s and (c) SSiB4/TRIFFID-Fire. The right panel shows the zonal mean burned area (Mha) for (b) GFED4s and (d) SSiB4/TRIFFID-Fire

Figure 4.4 (a) Map of 14 regions used in this study, after Giglio et al. (2006, 2010) and van der Werf et al. (2006, 2010) (b) Annual burned area (Mha) averaged over 2000-2014 for GFED4s and SSiB4/TRIFFID-Fire in 14 regions (c) Annual burned area (Mha) for 2000–2014 for GFED4s and SSiB4/TRIFFID-Fire in 14 GFED regions. The "*" and the red color indicate the positive correlation is significant at $p < 0.05$.

Figure 4.5 Temporal correlation of monthly burned area averaged over 2000-2014 between SSiB4/TRIFFID-Fire and GFED4s (grids with annual burned fraction < 0.001 % are masked)Figure 5. Temporal correlation of monthly burned area averaged over 2000-2014 between SSiB

Figure 4.6 The contribution of monthly burned area to annual burned area (%) over the (a) GLOB, (b) SHAF, (c) SHSA, (d) NHSA, (e) SEAS, (f) EQAS, (g) BOAS, and (h) AUST averaged over 2000-2014 for SSiB4/TRIFFID-Fire and GFED4s

Figure 4.7 (a) Spatial distribution of annual carbon emission (g C yr-1) averaged over 2000–2014 for GFED4s and (b) the latitudinal distribution of carbon emission (Tg C yr-1); (c), (d)

Same as (a), (b) but for SSiB4/TRIFFID-Fire (g C yr-1); (e) Annual carbon emission (Pg C yr-1) for GFED4s for 2000-2014 and for SSiB4/TRIFFID-Fire for 1948-2014

Figure 4.8 (a) Annual carbon emission averaged over 2000-2014 for GFED4s and SSiB4/TRIFFID-Fire in 14 GFED regions; (b)-(d) annual carbon emission in (b) SHAF, (c) NHAF, and (d) SHSA for 2000–2014 for GFED4s and SSiB4/TRIFFID-Fire. The "*" and red color indicate the correlation is significant at $p < 0.05$.

Figure 4.9 Monthly CO emission in Africa averaged in 2000-2014 from (a) Zheng et al. (2019) and (b) SSiB4/TRIFFID-Fire

Figure 4.10 The fractional coverage of trees in (a) GLC2000, (c) FIRE-ON, and (e) FIRE-OFF and the fractional coverage of grasses in (b) GLC2000, (d) FIRE-ON, and (f) FIRE-OFF in 2000

Figure 4.11 Differences in (a) tree cover (BET, NET, and BDT; %) (b) grass cover (C3 and C4; %), (c) LAI (m2 m-2), and (d) Vegetation height (m) in SSiB4/TRIFFID-Fire averaged over 2000-2014 between FIRE-ON and FIRE-OFF

Figure 4.12 Differences in net shortwave (a, b; W m-2), sensible heat (c, d; W m-2), latent heat (e,f; W m-2), and surface temperature (g, h; K) in DJF (a, c, e, and g), and JJA (b, d, f, and h) averaged over 2000-2014 between FIRE-ON and FIRE-OFF.

Figure 5.1 $f(\theta)$ calibration for (a) C4 grasses and (b) C3 grasses

Figure 5.2 Experiment Design for fire effects in SHAF (0ºN-37ºN; 0ºW-50ºW

Figure 5.3 (a)-(d) Climate of SHAF from Sheffield et al. (2006) averaged in 2000-2014 (a) annual mean air temperature (Tair), (b) annual total precipitation (PRE), (c) monthly Tair (d) Monthly Pre, and (e) dominant PFTs for each grid simulated in SSiB4/TRIFFID-Fire

Figure 5.4 (a) Annual burned fraction (BF) averaged over 2000–2014 in GFED4s, (b) same as (a) but in SSiB4/TRIFFID-Fire, (c) Annual carbon emission (EM) averaged over 2000–2014 in SSiB4/TRIFFID-Fire, and (d) Contribution of monthly burned fraction to annual burned fraction in model and observation (BA: total burned area in SHAF; SCC: spatial correlation coefficient; COR: temporal correlation coefficient).

Figure 5.4 (a) Annual burned fraction (BF) averaged over 2000–2014 in GFED4s, (b) same as (a) but in SSiB4/TRIFFID-Fire, (c) Annual carbon emission (EM) averaged over 2000–2014 in SSiB4/TRIFFID-Fire, and (d) Contribution of monthly burned fraction to annual burned fraction in model and observation (BA: total burned area in SHAF; SCC: spatial correlation coefficient; COR: temporal correlation coefficient).

Figure 5.5 Annual GPP averaged over 2000–2011 in (a) FLUXNET-MTE, (b) SSiB4/TRIFFID-Fire, (c) Point-by-point climatology monthly correlation between FLUXNET-MTE and SSiB4/TRIFFID-Fire , and (d) Monthly GPP in model and observation

Figure 5.6 Annual LH averaged over 2000–2014 in (a) FLUXCOM-METEO, (b) s SSiB4/TRIFFID-Fire, Annual SH averaged over 2000–2014 in (c) FLUXCOM-METEO, (d) SSiB4/TRIFFID-Fire, Monthly (e) LH and (f) SH in model, FLUXCOM-METEO, and FLUXCOM-RS. The dots in (e) and (f) denote the regional mean values while the bars denote the LH/SH values within one standard deviation of the mean of all grid points

Figure 5.7 (a)-(b) 2000–2014 annual (a) tree fraction and (b) C4/C3 grass fraction in FIREOFF, (c)-(d) 2000–2014 annual fire effects on (c) tree fraction and (b) grass fraction (e) Monthly fire effects on the fractional coverage of trees and C4/C3 grasses with burned area overlaid (The areal-average is calculated using grids with an annual burned fraction of more than 10%). The y-axis of burned fraction in (e) is reversed.

Figure 5.8 2000–2014 annual fire effects on (a) LAI and (b) GPP, and (c) Monthly fire effects on the LAI/GPP with burned area overlaid (The areal-average is calculated using grids with an annual burned fraction of more than 10%). The y-axis of burned fraction in (c) is reversed.

Figure 5.9 2000–2014 annual fire effects on (a) NSW, (b) SH, (c) LH, and (d) annual fire effects on NSW, SH, LH, and TMP for each grid with an annual burned fraction greater than 10%. The dots denote the areal-average fire effects in SHAF

Figure 5.10 2000–2014 monthly fire effects on (a) NSW, (b) SH, (c) LH, (d) TMP, (e) canopy transpiration, and (f) soil evaporation with burned fraction overlaid. The y-axis of burned fraction in (a-c) and (e) are reversed.

Figure 5.11 2000-2014 monthly fire effects on (a) θ_1, (b) θ_2, and (c) θ_3 with burned fraction overlaid. The y-axis of burned fraction in (a) is reversed.**Figure 5.11** 2000-2014 monthly fire effects on (a) θ_1, (b) θ_2, and (c) θ_3 with burned fraction overlaid

LIST OF TABLES

(Figure 2.3b)

Error! Reference source not found.

Error! Reference source not found.

Table 3.2 Experiment design

Table 4.1 The upper (θ_{up}) and lower (θ_{low}) thresholds of root zone soil moisture for PFTs in SSiB4/TRIFFID-Fire

Table 4.2 The disturbance rate implicitly including fire disturbance (γ_v) and excluding fire disturbance (γ_v').

Table 4.3 Datasets used to drive SSIB4/TRIFFID-Fire and evaluate simulations

Table 5.1 Datasets used to drive SSiB4/TRIFFID-Fire and evaluate simulations

ACKNOWLEDGEMENTS

Earning a Ph.D. is very hard and not an individual achievement. I would like to appreciate my advisor Prof. Yongkang Xue for his guidance, support, and encouragement throughout my graduate studies at UCLA. I have learned much from his insightful and invaluable instructions. I would also like to thank Dr. Dennis Lettenmaier, Dr. Gregory Okin, Dr. Thomas Gillespie, and Dr. Kuo-nan Liou for their helpful comments on my dissertation and collaborations on other projects which broaden the scope of my Ph.D. study. For my dissertation, I received help as well from Dr. Yu Gu and Dr. Gang Chen at UCLA Atmospheric and Oceanic Sciences Department, Dr. Bin Zhao at Pacific Northwest National Laboratory, Dr. Nagaraju Chilukoti at National Institute of Technology, Dr. Jiwoo Lee at Livermore Berkeley National Laboratory, Dr. Fang Li at the Institute of Atmospheric Physics Chinese Academy of Sciences, Dr. Fernando De Sales at San Diego State University, and Dr. Weidong Guo at Nanjing University.

I am also grateful to the postdoctoral researchers, graduate students, and visiting scholars in my group, including Qian Li, Ye Liu, Ismaila Diallo, Jiping Quan, Xiaobo He, Khalil Ganem, and Zhanmei Yang. I also thank my friends Junzhe Zhang, Jessica Fayne, Zhaoxin Ban, Lu Su, Jiwoo Han, Chelsea Robinson, Dian Tri Irawaty, Mu Xiao, Qian Cao, Ting Yuan, Shengan Zhan, Mike Fischella, and Solomon Vimal from Geography Department, and friends from Civil Engineering Department including Yufei Liu and Dongyue Li. Thank you for lending me your ears and eyes to help discuss my work and have taught me through discussing your own research. I also thank our department staff for their help, especially Kasi McMurray, Jenee Misraje, and Brian Won.

Last but not least, I would like to give my greatest thanks to my family, particularly my parents and grandparents, for their endless love, wholehearted support, and all the sacrifice they

had made for me. Without their continuous encouragement and unconditional support, I probably would not have been able to achieve my Ph.D.

VITA

Education

2018-present	C.Phil. in Geography, University of California, Los Angeles, USA
2015-2017	M.A. in Geography, University of California, Los Angeles, USA
2011-2015	B.S. in Atmospheric Sciences, Nanjing University, Nanjing, China

Professional Experience

2021	Teaching Associate, University of California, Los Angeles, USA
2015-2020	Graduate Student Researcher, University of California, Los Angeles, USA
2020	Teaching Assistant, University of California, Los Angeles, USA
2017	Teaching Assistant, University of California, Los Angeles, USA

Publications

Huang, H., Xue, Y., Li, F., and Liu, Y.: Modeling long-term fire impact on ecosystem characteristics and surface energy using a process-based vegetation–fire model SSiB4/TRIFFID-Fire v1.0, Geoscientific Model Development, 13, 6029-6050, 10.5194/gmd-13-6029-2020, 2020.

Huang, H., Xue, Y., Chilukoti, N., Liu, Y., Chen, G., and Diallo, I.: Assessing global and regional effects of reconstructed land use and land cover change since 1950 on climate using a coupled land-atmosphere-ocean model, *Journal of Climate*, 33(20), 8997-9013, 10.1175/JCLI-D-20-0108.1, 2020

Huang, H., Gu, Y., Xue, Y., Jiang, J., and Zhao, B.: Assessing aerosol indirect effect on clouds and regional climate of East/South Asia and West Africa using NCEP GFS, *Climate Dynamics*, 52(9-10), 5759-5774, 2019

Wanders, N., Bachas, A., He, X. G., **Huang, H.**, Koppa, A., Mekonnen, Z. T., Pagan, B. R. et al.: Forecasting the Hydroclimatic Signature of the 2015/16 El Nino Event on the Western United States, *Journal of Hydrometeorology*, 18, 177-186, 10.1175/Jhm-D-16-0230.1, 2017

Xue, Y., Yao, T., Boone, A. A., Diallo, I., Liu, Y., Zeng, X., Lau, W. K.-M. et al.: Impact of Initialized Land Surface Temperature and Snowpack on Subseasonal to Seasonal Prediction Project, Phase I (LS4P-I): Organization and Experimental design, Geosci. Model Dev. Discuss., https://doi.org/10.5194/gmd-2020-329, (*in review)*.

Liu, Y., Guo, W., **Huang, H.**, Ge, J., Qiu, B.: Estimating global aerodynamic parameters in 1982-2017 using remote-sensing data and a turbulent transfer model, (*in review*).

Huang, H., Fischella, M., Liu, Y., Ban, Z., Fayne, J., Li, D., Cavanaugh, K., and Lettenmaier,

D.: Limited changes in mechanisms or intensity of Western U.S. floods over the last half century, (*in review*).

Huang, H., Y., Xue, Y., Liu, F., Li, G., Okin, 2021: Improving SSiB4/TRIFFID-Fire vegetation-fire model and modeling the short-term fire effects on vegetation dynamics and surface energy in Southern Hemisphere Africa, (*in prep*)

Selected Presentation

Oral Presentation

Huang, H.*, Xue, Y., Li, F., and Liu, Y: Modeling fire impact on vegetation dynamics at seasonal and interannual scales using SSiB4/TRIFFID-Fire. 2020 Fire Model Intercomparison (FireMIP) Project Workshop, Beijing, Oct 2020

Huang, H.*, Xue, Y., Chilukoti, N., Liu, Y., and Chen, G.: Assessing global and regional effects of reconstructed land use and land cover change since 1950 on climate using a coupled land-atmosphere-ocean model. Oral presentation, AMS Annual Meeting, Boston, Jan 2020

Huang, **H.***, Xue, Y., Chilukoti, N., Liu, Y., and Chen, G.: Assessing global and regional effects of reconstructed land use and land cover change since 1950 on climate using a coupled land-atmosphere-ocean model. Oral presentation, AGU Annual Meeting, San Francisco, Dec 2019

Huang, **H.***, Oaida, C., and Xue, Y.: Modeling aerosols in snow in SSiB. Oral presentation, Second International GEWEX/GASS/LS4P and TPEMIP Workshop, Nanjing, July, 2019

Huang, **H.***, Gu, Y., Xue, Y., Jiang, J. H., and Zhao, B.: Assessing aerosol indirect effects on clouds and regional climate of East/South Asia and West Africa using NCEP GFS. Oral presentation, AGU Annual Meeting, Washington, D.C., Dec 2018

Poster Presentation

Huang, **H.**, Xue, Y., Liu, Y., and Li, F.: Assessing aerosol indirect effects on clouds and regional climate of East/South Asia and West Africa using NCEP GFS. Poster presentation, AGU Annual Meeting, San Francisco, Dec 2020

Fischella, M., **Huang**, **H.**, Liu, Y., Ban, Z., Fayne, J. V., Li, D., and Lettenmaier, D. P., 2019: Dynamics and changes in Western U.S. floods. Poster presentation, AGU Annual Meeting, San Francisco, Dec 2019

Huang, **H.***, Gu, Y., Xue, Y., Lu, C., and Jiang, J. H.: Assessing aerosol indirect effects on clouds and regional climate of East/South Asia and West Africa using NCEP GFS. Poster presentation, AGU Annual Meeting, New Orleans, Dec 2017

Huang, **H.***, Gu, Y., Xue, Y., and Lu, C.: Assessing the aerosol direct and first indirect effects using ACM/GCM simulation results. Poster presentation, AGU Annual Meeting, San Francisco, Dec 2016

Chapter 1 Introduction

1.1 Land-atmosphere interactions in a changing environment

Land provides the lower boundary for the atmosphere, with which they exchange energy, water, and biogeochemical tracers such as anthropogenic greenhouse gases (GHGs) and aerosols. Land absorbs shortwave and longwave radiation and warms up the atmosphere through the emission of longwave radiation and the transfer of sensible heat and latent heat to the atmosphere. It plays an important role in the water cycle mainly through terrestrial precipitation, evapotranspiration within the ecosystem, and sublimation from solid ice and snow. Land acts as both a source and a sink of GHGs and modulates atmospheric composition through emissions and removals trace gases and aerosols.

Over the past few centuries, humans have significantly transformed land surface to derive valuable natural resources and ecosystem services, such as food, fiber, shelter, and freshwater (Ramankutty and Foley, 1999). These human activities affect the climate system through changes in forcing and multiple biophysical and biogeochemical feedbacks (Jia et al., 2019). The GHG and aerosol emissions, agriculture activities, and deforestation/afforestation directly affects the atmospheric composition, hydrological cycle, and climate system across different spatial and temporal scales. In return, changes in the climate system (e.g., temperature, precipitation, and atmospheric composition) also influence the terrestrial ecosystem through CO_2 fertilization, nitrogen deposition, and changes in fire regimes. This study is inspired to understand the interactions between land and atmosphere in a changing world. Specifically, we look at 1) aerosol indirect effects on ice clouds and the consequent impact on monsoon climate; 2) the effects of land use and land cover changes (LULCC) on regional and global climate; and 3) the long-term and short-term effects of fire on terrestrial ecosystem and surface energy.

1.2 Anthropogenic aerosol emissions and aerosol-cloud interactions

Aerosols come from both natural and anthropogenic sources and contribute large uncertainties to estimates of the earth's changing energy budget. Dust is the most common natural aerosol produced primarily from deserts, yet its atmospheric concentration has been doubled during the twentieth century due to human land-use practices and climate change-induced drought (Mahowald et al., 2010). Anthropogenic aerosols include sulfate, nitrate, organic carbon (OC), and black carbon (BC), resulting from intensive human activities such as fossil fuel burning (Penner et al., 2001). The concentration of anthropogenic aerosols is dramatically increased since the mid-nineteenth century, coincident with the industrial revolution (McConnell et al., 2007). Aloft in the atmosphere, aerosols influence the atmosphere radiation by scattering and absorbing solar radiation, known as aerosol direct effects. Aerosols also act as cloud condensation nuclei and ice forming nuclei, influencing cloud droplets number, effective radius, and cloud water content, referred to as aerosol indirect effects (Lohmann and Feichter, 2005). The aerosol indirect effects are usually split into two effects: the first indirect effect, whereby an increase in aerosol concentration causes an increase in droplet number and usually a decrease in droplet size (Twomey, 1974), and the second indirect effect, whereby reduced droplet size affects the precipitation efficiency, tending to increase the liquid water content, the cloud lifetime, and the cloud thickness (Albrecht, 1989; Pincus and Baker, 1994).

This multifaceted influence makes the aerosol one of the least predictable elements in weather and climate modeling (IPCC, 2013). It is thus of immense importance to evaluate aerosol direct and indirect effects by combining the latest knowledge from observations and climate models. While aerosol direct effects and indirect effects on liquid clouds have been widely studied

(Lohmann and Feichter, 2005; Lau et al., 2006; Li et al., 2016; Huang, 2017), fewer observational and modeling studies were conducted on aerosol indirect effects on ice clouds, mainly due to a lack of observations and parameterization (Jiang et al., 2013). Chapter 2 of this dissertation mainly focuses on the aerosol indirect effect on ice clouds and its consequent impact on monsoon climate. By applying the latest observational-based parameterization linking ice cloud nuclei size to aerosol loading and convection strength in a GCM simulation, we aim to evaluate the radiative forcing of aerosol indirect effects and the subsequent impact on monsoon climate.

1.3 Land use and land cover change effect on surface energy and climate system

Land use and land cover change (LULCC) is one of the most important forcings affecting climate in the past century. It consists of a wide range of land surface conversions, including deforestation to crops and pasturelands, desertification, reforestation, and urbanization (Mahmood et al., 2014). The local and regional impacts of LULCC have been extensively investigated in observational and modeling studies. Most studies find that deforestation and desertification have caused an increase in surface albedo (Gash and Nobre, 1997; Steyaert and Knox, 2008; Loarie et al., 2011) especially when snow is present (Betts, 2001). The reduction in net radiation tends to reduce the local land surface temperature (LST) via the radiation budget (Davin et al., 2007). Meanwhile, changes in leaf area, surface roughness, and aerodynamic and canopy resistance influence the momentum and energy flux exchanges between land and atmosphere (Lee et al., 2011; Guo et al., 2016; Liu et al., 2016). Through the alternation of land-atmosphere energy and water exchange, LULCC can influence boundary layer evolution, atmospheric convection, cloud formation, and local and regional climate, especially the Sahel droughts and East Asian drought (Xue and Shukla, 1993; Xue, 1996; Lyons, 2002; Nair et al., 2011; Boone et al., 2016).

However, there remains a lack of a comprehensive understanding of how LULCC influences remote and global climate due to the inconsistent simulated effects in different climate models (Pielke et al., 2007; Pitman et al., 2009; Pielke et al., 2011; Swann et al., 2012; Devaraju et al., 2015; Lejeune et al., 2017). The uncertainties lie in several modeling aspects, including different land surface schemes (Koster et al., 2006), different LULCC implementations (Boone et al., 2016), and also whether prescribed SSTs with interannual and seasonal variations, slab ocean models or coupled ocean models were employed (Pitman et al. 2009; Pielke et al. 2011). Although some early GCMs reported the continental LULCC might affect ITCZ and tropical rainfall, the mechanisms have not been explicitly investigated (Chase and Pielke, 1995; Zhao et al., 2001; Snyder, 2010; Schneck and Mosbrugger, 2011).

Chapter 3 provides an assessment of large-scale LULCC effects on global temperature and precipitation since 1950 by implementing a yearly-updated vegetation map into a GCM. The main result in this Chapter has been published in Huang et al. (2020a). We applied multiple methodologies to identify the key processes that produce the global impact of LULCC. Using the decomposed temperature metric (DTM), we attribute the local and remote temperature change to surface radiation and energy changes induced by LULCC. The application of the energy flux framework enables us to review the remote LULCC impact on Hadley circulation and ITCZ from the perspective of energy budget and meridional energy transport. This study, for the first time, connects the local and global effects of LULCC from the perspective of energy budget and energy transport within the climate system.

1.4 The role of fire in the terrestrial ecosystem and surface energy

Wildfire is a primary disturbance to vegetation structure and plays a major role in the global carbon cycles and biogeochemical processes (Sousa, 1984). In the past few decades, fire regimes (burned area, intensity, and duration) have been altered by direct (land management) and indirect (climate change) human impact. Every year in the dry seasons, fires throughout the world leave behind numerous scars in the landscape. Through prevalent disturbance on surface albedo and vegetation characteristics, fire exerts radiative forcing on the earth's surface and modifies the energy partitioning between latent heat and sensible heat, referred to as the biogeophysical effects of fire (Chambers and Chapin, 2002; Bond-Lamberty et al., 2009). Changes in the boundary layer may cause feedback on monsoon and impact on precipitation through biosphere-atmosphere interactions (Wendt et al., 2007; De Sales et al., 2016; Saha et al., 2016). Fires are also important sources of global carbon emission, aerosols, and trace gases, contributing to both an increase in the greenhouse gases and the global cloud condensation nuclei through biogeochemistry processes (Scholes et al., 1996).

Since the early 2000s, fire models have been developed within Dynamic Global Vegetation Models (DGVMs) to describe the burned area, fire emissions, and fire disturbance on terrestrial ecosystems (Thonicke et al., 2001; Venevsky et al., 2002; Arora and Boer, 2005; Thonicke et al., 2010; Li et al., 2012). The models have been extensively used to reconstruct fire history (Yang et al., 2015; van Marle et al., 2017; Li et al., 2019) and to attribute historical variability of the burned area to various climate and anthropogenic driving factors (Kloster et al., 2012; Andela et al., 2017; Forkel et al., 2019; Teckentrup et al., 2019). Some models have been used to assess fire impact on the terrestrial carbon cycle and surface energy, yet they mostly did not describe vegetation fraction

changes caused by fire (Li et al., 2014; Poulter et al., 2015; Yang et al., 2015; Yue et al., 2015; Seo and Kim, 2019; Zou et al., 2020).

The final two chapters of this dissertation are motivated to enhance the understanding of long-term and short-term fire effects on the ecosystem and surface energy. In Chapter 4, we develop a fire-coupled DGVM that updates fire-induced carbon loss and vegetation distribution change every 10 days. The model is then used to assess the role of fire in the terrestrial ecosystem and surface energy by comparing a reference simulation with fire and a sensitivity simulation representing "a world without fire." The main result in this Chapter has been published in Huang et al. (2020b). In Chapter 5, I further improve the model performance in simulating fires in Southern Hemisphere Africa and apply it to study the evolvement of fire effect in the fire season and the following recovery season.

Reference

Albrecht, B. A.: Aerosols, Cloud Microphysics, and Fractional Cloudiness, Science, 245, 1227-1230, DOI 10.1126/science.245.4923.1227, 1989.

Andela, N., Morton, D. C., Giglio, L., Chen, Y., van der Werf, G. R., Kasibhatla, P. S., DeFries, R. S., Collatz, G. J., Hantson, S., Kloster, S., Bachelet, D., Forrest, M., Lasslop, G., Li, F., Mangeon, S., Melton, J. R., Yue, C., and Randerson, J. T.: A human-driven decline in global burned area, Science, 356, 1356-1361, 10.1126/science.aal4108, 2017.

Arora, V. K., and Boer, G. J.: Fire as an interactive component of dynamic vegetation models, J Geophys Res-Biogeo, 110, 10.1029/2005jg000042, 2005.

Betts, R. A.: Biogeophysical impacts of land use on present-day climate: near-surface temperature change and radiative forcing, Atmos Sci Lett, 2, 39-51, 10.1006/asle.2001.0023, 2001.

Bond-Lamberty, B., Peckham, S. D., Gower, S. T., and Ewers, B. E.: Effects of fire on regional evapotranspiration in the central Canadian boreal forest, Global Change Biol, 15, 1242-1254, 10.1111/j.1365-2486.2008.01776.x, 2009.

Boone, A. A., Xue, Y. K., De Sales, F., Comer, R. E., Hagos, S., Mahanama, S., Schiro, K., Song, G. Q., Wang, G. L., Li, S., and Mechoso, C. R.: The regional impact of Land-Use Land-cover Change (LULCC) over West Africa from an ensemble of global climate models under the auspices of the WAMME2 project, Climate Dynamics, 47, 3547-3573, 10.1007/s00382-016-3252-y, 2016.

Chambers, S. D., and Chapin, F. S.: Fire effects on surface-atmosphere energy exchange in Alaskan black spruce ecosystems: Implications for feedbacks to regional climate, J Geophys Res-Atmos, 108, 10.1029/2001jd000530, 2002.

Chase, T. N., and Pielke, R. A.: The sensitivity of a General Circulation Model to large scale vegetation changes, Atmospheric science paper; no. 581, 1995.

Davin, E. L., de Noblet-Ducoudre, N., and Friedlingstein, P.: Impact of land cover change on surface climate: Relevance of the radiative forcing concept, Geophys Res Lett, 34, 10.1029/2007gl029678, 2007.

De Sales, F., Xue, Y. K., and Okin, G. S.: Impact of burned areas on the northern African seasonal climate from the perspective of regional modeling, Climate Dynamics, 47, 3393-3413, 10.1007/s00382-015-2522-4, 2016.

Devaraju, N., Bala, G., and Modak, A.: Effects of large-scale deforestation on precipitation in the monsoon regions: Remote versus local effects, P Natl Acad Sci USA, 112, 3257-3262, 10.1073/pnas.1423439112, 2015.

Forkel, M., Andela, N., Harrison, S. P., Lasslop, G., van Marle, M., Chuvieco, E., Dorigo, W., Forrest, M., Hantson, S., Heil, A., Li, F., Melton, J., Sitch, S., Yue, C., and Arneth, A.: Emergent relationships with respect to burned area in global satellite observations and fire-enabled vegetation models, Biogeosciences, 16, 57-76, 10.5194/bg-16-57-2019, 2019.

Gash, J. H. C., and Nobre, C. A.: Climatic effects of Amazonian deforestation: Some results from ABRACOS, B Am Meteorol Soc, 78, 823-830, Doi 10.1175/1520-0477(1997)078<0823:Ceoads>2.0.Co;2, 1997.

Guo, W. D., Wang, X. Q., Sun, J. N., Ding, A. J., and Zou, J.: Comparison of land-atmosphere interaction at different surface types in the mid- to lower reaches of the Yangtze River valley, Atmos Chem Phys, 16, 9875-9890, 10.5194/acp-16-9875-2016, 2016.

Huang, H.: Assessing the Aerosol Direct, Semi-Direct and Indirect Effects using Global Circulation Model Simulation Results, UCLA, 2017.

Huang, H., Xue, Y., Chilukoti, N., Liu, Y., Chen, G., and Diallo, I.: Assessing Global and Regional Effects of Reconstructed Land-Use and Land-Cover Change on Climate since 1950 Using a Coupled Land–Atmosphere–Ocean Model, J Climate, 33, 8997-9013, 2020a.

Huang, H., Xue, Y., Li, F., and Liu, Y.: Modeling long-term fire impact on ecosystem characteristics and surface energy using a process-based vegetation–fire model SSiB4/TRIFFID-Fire v1.0, Geosci. Model Dev., 13, 6029-6050, 10.5194/gmd-13-6029-2020, 2020b.

IPCC: Climate Change 2013: The Physical Science Basis. Contribution of Working Group I to the Fifth Assessment Report of the Intergovernmental Panel on Climate Change, Cambridge University Press, Cambridge, United Kingdom and New York, NY, USA, 1535 pp., 2013.

Jia, G., Shevliakova, E., Artaxo, P., De-Docoudré, N., Houghton, R., House, J., Kitajima, K., Lennard, C., Popp, A., and Sirin, A.: Land–climate interactions, 2019.

Jiang, Y. Q., Liu, X. H., Yang, X. Q., and Wang, M. H.: A numerical study of the effect of different aerosol types on East Asian summer clouds and precipitation, Atmos Environ, 70, 51-63, 10.1016/j.atmosenv.2012.12.039, 2013.

Kloster, S., Mahowald, N. M., Randerson, J. T., and Lawrence, P. J.: The impacts of climate, land use, and demography on fires during the 21st century simulated by CLM-CN, Biogeosciences, 9, 509-525, 2012.

Koster, R. D., Guo, Z. C., Dirmeyer, P. A., Bonan, G., Chan, E., Cox, P., Davies, H., Gordon, C. T., Kanae, S., Kowalczyk, E., Lawrence, D., Liu, P., Lu, C. H., Malyshev, S., McAvaney, B., Mitchell, K., Mocko, D., Oki, T., Oleson, K. W., Pitman, A., Sud, Y. C., Taylor, C. M., Verseghy, D., Vasic, R., Xue, Y. K., and Yamada, T.: GLACE: The Global Land-Atmosphere Coupling Experiment. Part I: Overview, J Hydrometeorol, 7, 590-610, Doi 10.1175/Jhm510.1, 2006.

Lau, K. M., Kim, M. K., and Kim, K. M.: Asian summer monsoon anomalies induced by aerosol direct forcing: the role of the Tibetan Plateau, Climate Dynamics, 26, 855-864, 10.1007/s00382-006-0114-z, 2006.

Lee, X., Goulden, M. L., Hollinger, D. Y., Barr, A., Black, T. A., Bohrer, G., Bracho, R., Drake, B., Goldstein, A., Gu, L. H., Katul, G., Kolb, T., Law, B. E., Margolis, H., Meyers, T., Monson, R., Munger, W., Oren, R., Kyaw, T. P. U., Richardson, A. D., Schmid, H. P., Staebler, R., Wofsy, S.,

and Zhao, L.: Observed increase in local cooling effect of deforestation at higher latitudes, Nature, 479, 384-387, 10.1038/nature10588, 2011.

Lejeune, Q., Seneviratne, S. I., and Davin, E. L.: Historical Land-Cover Change Impacts on Climate: Comparative Assessment of LUCID and CMIP5 Multimodel Experiments, J Climate, 30, 1439-1459, 2017.

Li, F., Zeng, X. D., and Levis, S.: A process-based fire parameterization of intermediate complexity in a Dynamic Global Vegetation Model, Biogeosciences, 9, 2761-2780, 10.5194/bg-9-2761-2012, 2012.

Li, F., Bond-Lamberty, B., and Levis, S.: Quantifying the role of fire in the Earth system - Part 2: Impact on the net carbon balance of global terrestrial ecosystems for the 20th century, Biogeosciences, 11, 1345-1360, 10.5194/bg-11-1345-2014, 2014.

Li, F., Martin, M. V., Andreae, M. O., Arneth, A., Hantson, S., Kaiser, J. W., Lasslop, G., Yue, C., Bachelet, D., Forrest, M., Kluzek, E., Liu, X. H., Mangeon, S., Melton, J. R., Ward, D. S., Darmenov, A., Hickler, T., Ichoku, C., Magi, B. I., Sitch, S., van der Werf, G. R., Wiedinmyer, C., and Rabin, S. S.: Historical (1700-2012) global multi-model estimates of the fire emissions from the Fire Modeling Intercomparison Project (FireMIP), Atmos Chem Phys, 19, 12545-12567, 10.5194/acp-19-12545-2019, 2019.

Li, Z. Q., Lau, W. K. M., Ramanathan, V., Wu, G., Ding, Y., Manoj, M. G., Liu, J., Qian, Y., Li, J., Zhou, T., Fan, J., Rosenfeld, D., Ming, Y., Wang, Y., Huang, J., Wang, B., Xu, X., Lee, S. S., Cribb, M., Zhang, F., Yang, X., Zhao, C., Takemura, T., Wang, K., Xia, X., Yin, Y., Zhang, H., Guo, J., Zhai, P. M., Sugimoto, N., Babu, S. S., and Brasseur, G. P.: Aerosol and monsoon climate interactions over Asia, Reviews of Geophysics, 54, 866-929, 10.1002/2015rg000500, 2016.

Liu, Y., Guo, W. D., and Song, Y. M.: Estimation of key surface parameters in semi-arid region and their impacts on improvement of surface fluxes simulation, Sci China Earth Sci, 59, 307-319, 10.1007/s11430-015-5140-4, 2016.

Loarie, S. R., Lobell, D. B., Asner, G. P., and Field, C. B.: Land-Cover and Surface Water Change Drive Large Albedo Increases in South America, Earth Interact, 15, Artn 7 10.1175/2010ei342.1, 2011.

Lohmann, U., and Feichter, J.: Global indirect aerosol effects: a review, Atmos Chem Phys, 5, 715-737, 2005.

Lyons, T. J.: Clouds prefer native vegetation, Meteorol Atmos Phys, 80, 131-140, DOI 10.1007/s007030200020, 2002.

Mahmood, R., Pielke, R. A., Hubbard, K. G., Niyogi, D., Dirmeyer, P. A., McAlpine, C., Carleton, A. M., Hale, R., Gameda, S., Beltrán-Przekurat, A., Baker, B., McNider, R., Legates, D. R., Shepherd, M., Du, J., Blanken, P. D., Frauenfeld, O. W., Nair, U. S., and Fall, S.: Land cover changes and their biogeophysical effects on climate, Int J Climatol, 34, 929-953, doi:10.1002/joc.3736, 2014.

Mahowald, N. M., Kloster, S., Engelstaedter, S., Moore, J. K., Mukhopadhyay, S., McConnell, J. R., Albani, S., Doney, S. C., Bhattacharya, A., Curran, M. A. J., Flanner, M. G., Hoffman, F. M., Lawrence, D. M., Lindsay, K., Mayewski, P. A., Neff, J., Rothenberg, D., Thomas, E., Thornton, P. E., and Zender, C. S.: Observed 20th century desert dust variability: impact on climate and biogeochemistry, Atmos Chem Phys, 10, 10875-10893, 10.5194/acp-10-10875-2010, 2010.

McConnell, J. R., Edwards, R., Kok, G. L., Flanner, M. G., Zender, C. S., Saltzman, E. S., Banta, J. R., Pasteris, D. R., Carter, M. M., and Kahl, J. D. W.: 20th-century industrial black carbon emissions altered arctic climate forcing, Science, 317, 1381-1384, 10.1126/science.1144856, 2007.

Nair, U. S., Wu, Y., Kala, J., Lyons, T. J., Pielke, R. A., and Hacker, J. M.: The role of land use change on the development and evolution of the west coast trough, convective clouds, and precipitation in southwest Australia, J Geophys Res-Atmos, 116, 10.1029/2010jd014950, 2011.

Penner, J. E., Andreae, M., Annegarn, H., Barrie, L., Feichter, J., Hegg, D., Jayaraman, A., Leaitch, R., Murphy, D., and Nganga, J.: Aerosols, their direct and indirect effects, in: Climate Change 2001:

The Scientific Basis. Contribution of Working Group I to the Third Assessment Report of the Intergovernmental Panel on Climate Change, Cambridge University Press, 289-348, 2001.

Pielke, R. A., Adegoke, J., Beltran-Przekurat, A., Hiemstra, C. A., Lin, J., Nair, U. S., Niyogi, D., and Nobis, T. E.: An overview of regional land-use and land-cover impacts on rainfall, Tellus B, 59, 587-601, 10.1111/j.1600-0889.2007.00251.x, 2007.

Pielke, R. A., Pitman, A., Niyogi, D., Mahmood, R., McAlpine, C., Hossain, F., Goldewijk, K. K., Nair, U., Betts, R., Fall, S., Reichstein, M., Kabat, P., and de Noblet, N.: Land use/land cover changes and climate: modeling analysis and observational evidence, Wires Clim Change, 2, 828-850, 10.1002/wcc.144, 2011.

Pincus, R., and Baker, M. B.: Effect of Precipitation on the Albedo Susceptibility of Clouds in the Marine Boundary-Layer, Nature, 372, 250-252, 1994.

Pitman, A. J., de Noblet-Ducoudre, N., Cruz, F. T., Davin, E. L., Bonan, G. B., Brovkin, V., Claussen, M., Delire, C., Ganzeveld, L., Gayler, V., van den Hurk, B. J. J. M., Lawrence, P. J., van der Molen, M. K., Muller, C., Reick, C. H., Seneviratne, S. I., Strengers, B. J., and Voldoire, A.: Uncertainties in climate responses to past land cover change: First results from the LUCID intercomparison study, Geophys Res Lett, 36, 2009.

Poulter, B., Cadule, P., Cheiney, A., Ciais, P., Hodson, E., Peylin, P., Plummer, S., Spessa, A., Saatchi, S., Yue, C., and Zimmermann, N. E.: Sensitivity of global terrestrial carbon cycle dynamics to variability in satellite-observed burned area, Global Biogeochem Cy, 29, 207-222, 2015.

Ramankutty, N., and Foley, J. A.: Estimating historical changes in global land cover: Croplands from 1700 to 1992, Global Biogeochem Cy, 13, 997-1027, Doi 10.1029/1999gb900046, 1999.

Saha, M. V., Scanlon, T. M., and D'Odorico, P.: Suppression of rainfall by fires in African drylands, Geophys Res Lett, 43, 8527-8533, 10.1002/2016gl069855, 2016.

Schneck, R., and Mosbrugger, V.: Simulated climate effects of Southeast Asian deforestation: Regional processes and teleconnection mechanisms, J Geophys Res-Atmos, 116, 10.1029/2010jd015450, 2011.

Scholes, R. J., Ward, D. E., and Justice, C. O.: Emissions of trace gases and aerosol particles due to vegetation burning in southern hemisphere Africa, J Geophys Res-Atmos, 101, 23677-23682, Doi 10.1029/95jd02049, 1996.

Seo, H., and Kim, Y.: Interactive impacts of fire and vegetation dynamics on global carbon and water budget using Community Land Model version 4.5, Geosci Model Dev, 12, 457-472, 10.5194/gmd-12-457-2019, 2019.

Snyder, P. K.: The Influence of Tropical Deforestation on the Northern Hemisphere Climate by Atmospheric Teleconnections, Earth Interact, 14, 2010.

Sousa, W. P.: The Role of Disturbance in Natural Communities, Annu Rev Ecol Syst, 15, 353-391, DOI 10.1146/annurev.es.15.110184.002033, 1984.

Steyaert, L. T., and Knox, R. G.: Reconstructed historical land cover and biophysical parameters for studies of land-atmosphere interactions within the eastern United States, Journal of Geophysical Research: Atmospheres, 113, 2008.

Swann, A. L. S., Fung, I. Y., and Chiang, J. C. H.: Mid-latitude afforestation shifts general circulation and tropical precipitation, P Natl Acad Sci USA, 109, 712-716, 10.1073/pnas.1116706108, 2012.

Teckentrup, L., Harrison, S. P., Hantson, S., Heil, A., Melton, J. R., Forrest, M., Li, F., Yue, C., Arneth, A., Hickler, T., Sitch, S., and Lasslop, G.: Response of simulated burned area to historical changes in environmental and anthropogenic factors: a comparison of seven fire models, Biogeosciences, 16, 3883-3910, 2019.

Thonicke, K., Venevsky, S., Sitch, S., and Cramer, W.: The role of fire disturbance for global vegetation dynamics: coupling fire into a Dynamic Global Vegetation Model, Global Ecol Biogeogr, 10, 661-677, DOI 10.1046/j.1466-822x.2001.00175.x, 2001.

Thonicke, K., Spessa, A., Prentice, I. C., Harrison, S. P., Dong, L., and Carmona-Moreno, C.: The influence of vegetation, fire spread and fire behaviour on biomass burning and trace gas emissions: results from a process-based model (vol 7, pg 1991, 2010), Biogeosciences, 7, 2191-2191, 10.5194/bg-7-2191-2010, 2010.

Twomey, S.: Pollution and Planetary Albedo, Atmos Environ, 8, 1251-1256, 1974.

van Marle, M. J. E., Kloster, S., Magi, B. I., Marlon, J. R., Daniau, A. L., Field, R. D., Arneth, A., Forrest, M., Hantson, S., Kehrwald, N. M., Knorr, W., Lasslop, G., Li, F., Mangeon, S., Yue, C., Kaiser, J. W., and van der Werf, G. R.: Historic global biomass burning emissions for CMIP6 (BB4CMIP) based on merging satellite observations with proxies and fire models (1750-2015), Geosci Model Dev, 10, 3329-3357, 10.5194/gmd-10-3329-2017, 2017.

Venevsky, S., Thonicke, K., Sitch, S., and Cramer, W.: Simulating fire regimes in human-dominated ecosystems: Iberian Peninsula case study, Global Change Biol, 8, 984-998, DOI 10.1046/j.1365-2486.2002.00528.x, 2002.

Wendt, C. K., Beringer, J., Tapper, N. J., and Hutley, L. B.: Local boundary-layer development over burnt and unburnt tropical savanna: an observational study, Bound-Lay Meteorol, 124, 291-304, 2007.

Xue, Y., and Shukla, J.: The Influence of Land Surface Properties on Sahel Climate. Part 1: Desertification, J Climate, 6, 2232-2245, 10.1175/1520-0442(1993)006<2232:tiolsp>2.0.co;2, 1993.

Xue, Y. K.: The impact of desertification in the Mongolian and the Inner Mongolian grassland on the regional climate, J Climate, 9, 2173-2189, Doi 10.1175/1520-0442(1996)009<2173:Tiodit>2.0.Co;2, 1996.

Yang, J., Tian, H. Q., Tao, B., Ren, W., Pan, S. F., Liu, Y. Q., and Wang, Y. H.: A growing importance of large fires in conterminous United States during 1984-2012, J Geophys Res-Biogeo, 120, 2625-2640, 10.1002/2015jg002965, 2015.

Yue, C., Ciais, P., Cadule, P., Thonicke, K., and van Leeuwen, T. T.: Modelling the role of fires in the terrestrial carbon balance by incorporating SPITFIRE into the global vegetation model

ORCHIDEE - Part 2: Carbon emissions and the role of fires in the global carbon balance, Geosci Model Dev, 8, 1321-1338, 10.5194/gmd-8-1321-2015, 2015.

Zhao, M., Pitman, A. J., and Chase, T.: The impact of land cover change on the atmospheric circulation, Climate Dynamics, 17, 467-477, Doi 10.1007/Pl00013740, 2001.

Zou, Y. F., Wang, Y. H., Qian, Y., Tian, H. Q., Yang, J., and Alvarado, E.: Using CESM-RESFire to understand climate-fire-ecosystem interactions and the implications for decadal climate variability, Atmos Chem Phys, 20, 995-1020, 10.5194/acp-20-995-2020, 2020.

Chapter 2 Assessing aerosol indirect effect on clouds and regional climate

[**Huang, H.**, Gu, Y., Xue, Y., Jiang, J., and Zhao, B.: Assessing aerosol indirect effect on clouds and regional climate of East/South Asia and West Africa using NCEP GFS, Climate Dynamics, 10.1007/s00382-018-4476-9, 2018.]

Abstract

Aerosols can act as cloud condensation nuclei and ice nuclei, resulting in changes in cloud droplet/particle number/size, and hence altering the radiation budget. This study investigates the interactions between aerosols and ice clouds by incorporating the latest ice clouds parameterization in an atmospheric general circulation model (AGCM). The simulation shows a decrease in effective ice cloud crystal size corresponding to aerosol increase, referred to as the aerosol first indirect effect, which has not been comprehensively studied. Ice clouds with smaller particles reflect more shortwave radiation and absorb more infrared radiation, resulting in radiation change by 0.5 - 1.0 W m^{-2} at the top of the atmosphere (TOA). The TOA radiation field is also influenced by cloud cover change due to aerosol-induced circulation change. Such aerosol effects on precipitation highly depend on the existence of a deep convection system: interactions between

aerosols and ice clouds create dipole precipitation anomalies in the Asian monsoon regions; while in West Africa, enhanced convections are constrained by anticyclone effects at high levels and little precipitation increase is found. We also conduct an experiment to assess interactions between aerosols and liquid clouds and compare the climatic effects with that due to ice clouds. Radiation and temperature changes generated by liquid clouds are normally 1-2 times larger than those generated by ice clouds. The radiation change has a closer relationship to liquid cloud droplet size than liquid cloud cover, in contrast with what we find for ice clouds.

2.1 Introduction

Aerosols play an important role in the earth energy balance, cloud-radiation interactions, and global and regional weather and climate system (Haywood and Boucher, 2000; Lohmann and Feichter, 2005; Tao et al., 2012; Li et al., 2016b). Despite in progress in recent aerosol and cloud researches, assessing the aerosols and cloud effect remain as the largest uncertainty in interpretations of Earth's changing energy budget and predictions of future climate changes (IPCC, 2013).

Aerosols are found to affect cloud droplet/particle number, effective radius (Re), and cloud water content, referred to as the aerosol indirect effect. The aerosol indirect effect is usually divided into two components: the first indirect effect, whereby an increase in aerosol concentration causes an increase in droplet/particle concentration, and the second indirect effect, whereby the reduction in cloud droplet/particle size results in changes in precipitation efficiency (Penner et al., 2001). The first and second indirect effects are also termed as the "cloud albedo" and "cloud lifetime" effects, respectively.

Error! Reference source not found. is a schematic diagram that illustrates the aerosol indirect radiative effects on both ice and liquid clouds, in which aerosols are released primarily from the land surface and further affect surface radiation budget and precipitation. Aerosol effects on liquid clouds are relatively simple because only the liquid phase is involved. Since the 1970s, several microphysical, thermodynamic, and dynamic processes have been proposed and tested (Twomey, 1974; Albrecht, 1989; Kaufman and Fraser, 1997). Current aerosol research generally agrees that the presence of aerosols provides more cloud condensation nuclei, which increases the cloud droplet number concentration (CDNC) that decreases Re under fixed liquid water path (LWP) conditions, called the aerosol first indirect effect (Feingold et al., 2003; Kim et al., 2008). This is

usually accompanied by an increase in cloud albedo, an enhanced reflection, and a cooling effect (Twomey, 1974). Smaller Re also means that it takes longer to reach sizes large enough for precipitation, named as the aerosol second indirect effect. Drizzle suppression has been consistently observed and simulated in polluted air, which is attributed to this effect (Albrecht, 1989). Moreover, the aerosol second indirect effect may enhance cloud lifetime and cloud cover, imposing an additional surface cooling.

A number of studies have been carried out to explain the aerosol – liquid clouds interactions (ACI) in recent years. Intensified deep convection in polluted conditions due to aerosol processes is reported in several studies (Tao et al., 2007; Rosenfeld et al., 2008; Lebo and Seinfeld, 2011; Li et al., 2011; Lebo, 2014; Lebo and Morrison, 2014). Some studies suggested that the delayed precipitation due to aerosol-cloud interactions leads to an invigoration of upward wind and more persistent updrafts above the freezing (Rosenfeld et al., 2008; Li et al., 2011). Other studies related the convective invigoration to stronger low-level convergence caused by the interactions between the aerosol-induced cold pool and the lower-level wind shear (Tao et al., 2007; Lebo and Seinfeld, 2011; Lebo, 2014; Lebo and Morrison, 2014). Moreover, coupled with atmospheric dynamics, ACI may produce a chain of complex interactions with monsoon climate and weather events (Li et al., 2016a).

There were fewer observations of ice and mixed-phase clouds and related analyses compared to liquid clouds. Some early studies revealed complex interactions between radiative heating and ice microphysics and indicated the need for sophisticated models to properly simulate the cirrus cloud life cycle (Ackerman et al., 1988; Sassen and Cho, 1992). Previous laboratory experiment on homogeneous nucleation and various heterogeneous nucleation modes suggested the formation of ice clouds was more complex than liquid clouds (Diehl and Mitra, 1998). In recent

years, more remote sensing data are available from the NASA's A-Train (Aqua, Aura, CloudSat and CALIPSO satellites) and other lidar-based ground cloud observations such as the NASA Micro-Pulse Lidar Network (MPLNET) (Welton et al., 2001; Campbell et al., 2002; L'Ecuyer and Jiang, 2010; Zhao et al., 2018). Based on the CloudSat radar and CALIPSO lidar, Berry and Mace (2014) investigated the distribution, microphysical properties, and radiative properties of tropical ice clouds in Southeast Asia. They found the warming effect of the cirrus clouds had been almost fully compromised by the surface cooling effect there. Recent studies by Campbell et al. (2016) and Lolli et al. (2017) showed the contributions of cirrus cloud to global radiation budgets. However, it is hard to reduce the uncertainty in the estimation of ice cloud radiative forcing.

After evaluating both cloud and water vapor simulations in CMIP5 climate models, Jiang et al. (2013) showed that although many models added some treatments for aerosol - liquid clouds interactions, the number of GCMs including aerosol effects on ice cloud is somewhat lacking, mainly because of the large uncertainties in ice cloud nucleation modes and limited computational resources (Gu et al., 2012). Most GCMs have used prescribed ice particle sizes for the sake of computational cost while others have built the parameterization by relating ice crystal size to ice water content (IWC) and temperature (Gu et al., 2012). In early GCM studies considering aerosol indirect effect on ice clouds, most only focused on certain heterogeneous nucleation microphysics processes which subsequently affect cloud properties (Storelvmo et al., 2008; Yun and Penner, 2012), and only limited aerosol types were included, such as sulfate, soot, and dust (Penner et al., 2009; Liu et al., 2012). In this study, we employ the ice cloud parameterization developed by Jiang et al. (2011), which expands from the traditional Re–IWC relationship to the Re-IWC-AOD (aerosol optical depth) relationship, with the NCEP Global Forecast System (GFS). This parameterization makes use of data from A-Train satellites coupled with recent developments in

aerosol research to provide insight towards including the aerosol indirect effect on ice clouds in GCMs (L'Ecuyer and Jiang, 2010). This parameterization does not distinguish between different microphysics processes which are not fully understood and may induce large uncertainties. Moreover, it applies total AOD to represent aerosol loading and is not restricted to certain types of aerosols. The relatively simple mathematical expression makes this formulation easy to incorporate in GCMs to study aerosol indirect effects.

This parameterization has been adopted by Gu et al. (2012) to investigate dust aerosol impact on the North African climate, by prescribing AOD = 0.5 for North Africa and AOD = 0.1 for elsewhere. They found that reduced ice crystal size resulted in less outgoing longwave radiation (OLR) and more upward shortwave radiation (USW) at TOA in cloudy regions due to the aerosol first indirect effect. Precipitation was found to increase corresponding to enhanced convection. Our experiment adopts more reasonable AOD estimation of the aerosol mixing ratio from the GOCART (Goddard Chemistry Aerosol Radiation and Transport) data (Chin et al., 2002). In this work, we extend the investigation to the aerosol indirect radiative effect and large-scale circulation in major monsoon regions, i.e., East/South Asia, and West Africa. Here aerosol indirect radiative effect has been used to present the instantaneous radiative impact of atmosphere particles on TOA and surface energy balance due to the interactions between aerosol and clouds (including climate feedbacks). We also include a set of experiments assessing aerosol effects due to liquid clouds, which is used to compare with those due to ice clouds to make a preliminary evaluation on the relative effects of different aerosol-cloud interactions. The following chapters of this paper are organized as follows: in Section 2, we provide a brief introduction to the cloud parameterizations used for aerosols, followed by a description of the GFS, aerosol dataset, and experiment design in

Section 3; the model simulation results are presented in Sections 4 and 5, including effects on ice clouds and liquid clouds; and conclusions are given in Section 6.

2.2 Description of cloud parameterization

2.2.1 Parameterization of aerosol effect on ice clouds

We followed the approach presented by Jiang et al. (2011), in which ice crystal size was related to both AOD and IWC. This formulation used cloud top ice cloud effective radius (called Rei afterward) and AOD from Aqua satellite's Moderate-resolution Imaging Spectroradiometer (MODIS) MYD08-D3 and MYD04-L2 datasets. The IWC was from Aura satellite's Microwave Limb Sounder (MLS) Version 2.2 Level 2 data (Wu et al., 2008). The MODIS and MLS measurements were collocated by averaging the MODIS data onto the MLS footprints (Jiang et al., 2009). Four years satellite data from August 2004 to July 2008 has been employed in the parameterization, and the relationships were derived using 215hPa IWC, at which level IWC is a good indicator of convective intensity (Gu et al., 2012). Using least-squares fitting, Jiang et al. (2011) derived an empirical formula to describe the variations with convection and AOD:

$$Rei = \varepsilon \cdot AOD^{\eta} \cdot \left[1 - exp\left(-\frac{CONV_i}{\alpha}\right)\right] \cdot exp(-\beta \cdot CONV_i). \quad (2.1)$$

The equation has three different terms, and each represents different processes. The first term, $Rei = \varepsilon \cdot AOD^{\eta}$ represents the modulation of AOD on Rei where η is a parameter determining how strong the aerosol effect is, and ε is a scaling constant. The second term, $[1 - exp(-CONV_i/\alpha)]$, represents the growth of Rei with respect to convection. The convective index $CONV_i$ is defined as $CONV_i = IWC_i/\overline{IWC}$, where IWC_i represents an individual measurement of 215 hPa. $\overline{IWC}$ is the mean of all 215-hPa measurements. The third term, $1/exp(\beta \cdot CONV_i)$, is formulated to model the decrease of Rei with $CONV_i$, especially at large $CONV_i$ valuces. ε, α, β,

and η are parameters determined by performing a two-dimensional least-squares fitting to NASA's A-Train observational data.

The ice cloud parameterization developed by Jiang et al. (2011) represented one of the first attempts to captures aerosol indirect effects on Rei. The simple mathematical expression can be easily applied in the climate models to estimate the first indirect effects on ice cloud. In the parameterization, the dependence of Rei on convection and AOD is assumed to be decoupled, i.e., $Rei = r_{AOD} \cdot r_{CONV}$, in order to obtain a simple mathematical expression for the observed Rei-CONV-AOD relation.

2.2.2 Parameterization of aerosol effect on liquid clouds

We employed the empirically derived liquid cloud parametrization developed by Boucher and Lohmann (1995), which was an early attempt to relate CDNC to the sulfate aerosol mixing ratio. This parameterization has been widely adopted by different GCMs and has generated many consistent results, despite the difference in estimated radiative effect on the global scale (Lohmann and Roeckner, 1996; Rotstayn, 1999; Ming et al., 2005). Considering the different cloud amount, cloud water, and auto-conversion schemes in those GCMs, it seems that Boucher's parameterization captures some core processes of aerosol-cloud interactions. Since aerosol effects on liquid clouds in this study are only used to compare with those on ice clouds, we adopt this early parameterization considering its rather stable performance.

2.3. Model, datasets and experiment design

2.3.1 Model Description and Datasets

In this paper, we adopt the GFS in the second version of the NCEP Climate Forecast (CFS) coupled with SSiB2 (CFSv2/SSiB2). The horizontal resolution of the model is set at T126, which represents grid points spaced equally over 384 longitudes and 190 latitudes, approximately 1° × 1°

at the equator (Saha et al., 2014). Sixty-four vertical levels are used, most of which are in the troposphere. Parameterization of convective gravity wave drag is based on the theory of Chun and Baik (1998). Shortwave and longwave radiation are parameterized using the Rapid Radiative Transfer Models (RRTMG) RRTMG_SW (v3.8) and RRTMG_LW (v4.82) from Atmospheric and Environmental Research (AER) (Mlawer et al., 1997; Pincus et al., 2003; Clough et al., 2005). The cloud microphysical processes except auto-conversion are parameterized following Zhao and Carr (1997). This prognostic cloud parameterization scheme includes both cloud water and cloud ice, as well as some microphysical processes for both the convective and grid-scale precipitation production. The auto-conversion parameterization in GFS is based on Sundqvist et al. (1989). The simplified Arakawa -Schubert (SAS) has been used as the convection scheme in the GFS model, and the mass-flux shallow convection scheme is parameterized based on the SAS with a few key modifications (Arakawa and Schubert, 1974; Pan and Wu, 1994). The parameterization developed by Hong and Pan (1996) was incorporated to describe the planetary boundary layer diffusion. The NCEP GFS is coupled with the second generation of the Simplified Simple Biosphere Model (SSiB2) as the land surface model (Xue et al., 1991; Zhan et al., 2003; Xue et al., 2004).

The NCEP GFS has been modified to simulate the role of aerosols in affecting radiation field and cloud properties by applying the simulated global aerosol dataset from the GOCART model. The GOCART data has been widely used in many aerosol studies in the research community and produced reasonable results (Kaufman et al., 2002; Gu et al., 2015).. The monthly 1998-2010 climatology aerosol mixing ratio in GOCART has been generated using assimilated meteorology fields from the Data Assimilation System (GEOS DAS) (Chin et al., 2000; Chin et al., 2002). The GOCART simulates major tropospheric aerosol components, including sulfate, dust, black carbon (BC), organic carbon (OC), and sea-salt aerosols (accumulation mode and coarse

mode), among which dust is divided into 5 bin sizes (0.1–1, 1–1.8, 1.8–3.0, 3.0–6.0, and 6.0–10 μm). Three-dimensional monthly averages of the aerosol mixing ratio are available with a horizontal resolution of 1° latitude × 1.25° longitude degrees and 72 vertical layers. The GOCART data also provide the optical properties (i.e., extinction, scattering and absorption coefficient, single-scattering albedo, asymmetry factor, and phase function) of all types of aerosols under 36 relative humidity conditions. The modified GFS model transforms climatological aerosol GOCART data set onto model grids and computes aerosol optical properties, single scattering albedo, and asymmetry parameter for each model vertical layer. It computes mean aerosols optical properties over each shortwave and longwave radiation spectral band for all aerosol components using the Mie scattering to incorporate aerosol direct effect. The 550 nm AOD has been used in the Jiang's parameterization to study aerosol indirect effect on ice clouds.

2.3.2 Experiment design

In this work, we conducted model simulations from January 1st, 2006, for six years, using a prescribed climatology SST from WAMME II (Xue et al., 2016) to exclude feedback from the ocean. Aerosol direct effect was included in all experiments by incorporating monthly climatology of aerosol mixing ratio from GOCART. Our experiment design is summerized **Error! Reference source not found.**.

Case 1 (ICE-CTL1) was used to analyze the climatic effect of aerosols due to the indirect effect on ice clouds. In the control simulation, CTL1, AOD calculated from GOCART aerosol mixing ratio was employed for the aerosol direct effect scheme in the model. Whereas AOD = 0.01 was used in the aerosols - ice clouds interactions scheme, i.e., the aerosol indirect effect scheme. In the GOCART data set, AOD in JJA is generally smaller than 0.1 over most parts of the

ocean (tropical and mid-latitude Pacific, mid-latitude Atlantic Ocean, and tropical Indian Ocean). Over the tropical Pacific Ocean, it is even smaller than 0.05. As such, 0.01 has been selected in this study to represent a clean condition in the atmosphere for the CTL1. In the ICE experiment, AOD calculated from GOCART aerosol mixing ratio was still applied for the aerosol direct effect scheme. The ice cloud interaction scheme (Jiang et al., 2011) used the GOCART data to represent a current aerosol scenario. There was no aerosol liquid cloud interaction scheme in the original GFS. Therefore, in Case 1 aerosol indirect effects on liquid clouds were not included (**Error! Reference source not found.**).

We used Case 2 (LIQ-CTL2) to assess the aerosol indirect effect on liquid clouds (**Error! Reference source not found.**). In Case 2, the aerosol direct effect was included in both CTL2 and LIQ by using the AOD calculated from GOCART aerosol mixing ratio. A pre-industrial sulfate mixing ratio averaged from 256 model runs from AMIP CAM5 (Qian et al., 2015) was employed in the liquid cloud parameterization in CTL2. GOCART sulfate concentration was used in the liquid cloud parameterization in LIQ to be representative of current aerosol distribution. There are no interactions between aerosol and ice clouds in Case 2.

The model is set to output at 6-hourly intervals (e.g., at 06:00, 12:00, 18:00, 24:00 UTC) and averaged to get monthly results. The first year has been used for spin-up and the last five years have been averaged for analyses, and we focus on results for June–July–August (JJA) during which there are strong interactions between aerosols, clouds, and the monsoon. It should be noted that the aerosol direct effect is included in all experiments by employing GOCART data in radiative processes. Moreover, SST response to aerosol effects and the feedbacks to the climate system through the air-sea coupling has been excluded to better focus on the mechanisms of aerosol

indirect effects. This methodology has been widely used in previous aerosol-climate interaction studies (Menon et al., 2002; Lau and Kim, 2006; Jiang et al., 2013).

2.4. Aerosol effect on ice clouds

This study continues the work of Gu et al. (2015), who investigated the direct radiative effect of dust aerosols on the regional climate of North Africa and South/East Asia. The extensive evaluations of the GFS/SSiB2 in the climate simulation have been presented in previous studies (Xue et al., 2004; Xue et al., 2010; Gu et al., 2017). In this study, we have also compared the GFS/SSiB2's simulation with the Climatic Research Unit (CRU) time-series (TS) Version 3.22 temperature and the Version-2 Global Precipitation Climatology Project (GPCP) precipitation (Adler et al., 2003; Harris et al., 2014). The results show that GFSv2/SSiB2 captures the main features of global temperature pattern although a warm bias exists over the Northern Hemisphere high latitudes. As for precipitation, the GFS/SSiB2 captures the tropical rain belt and three major summer monsoons in West Africa, South Asia, and East Asia compared to the GPCP dataset but with a dry bias in West African and South Asian monsoon precipitation, generally consistent with previous studies. The precipitation deficit may arise from the underestimation of the intense rainfall events caused by neglecting aerosol-cloud interactions (Jiang et al., 2017) and the poor performance in simulating atmospheric mesoscale systems in GCM (Goswami and Goswami, 2017).

We first evaluate the aerosol indirect effect on ice clouds using the 5-year simulation results in Case 1. **Error! Reference source not found.** illustrates the difference of AOD used in Jiang's parameterization between ICE (AOD calculated from GOCART mixing ratio) and CTL1 (AOD = 0.01) in June–July–August (JJA). Total AOD has the largest magnitude over North Africa and West Asia, among which dust aerosol is dominant. Other regions with large aerosols include South

Africa, South Asia, and East Asia, where sulfate aerosol plays a comparable role as dust aerosol. The BC distribution is similar to that of sulfate with a smaller magnitude, except for tropical forest regions where biomass burnings release a large portion of soot (not shown). In this study, we focus on the aerosol effects in selected regions (latitude: 5 °S - 40 °N; longitude 40 °W - 130 °E) including West Africa, South Asia, and East Asia, which have both large AOD and high cloud cover and are supposed to have large aerosol-cloud interactions.

Figure 2.3a shows the difference in Rei between ICE and CTL. With increased aerosol loading, Rei has decreased globally, especially in West Africa, East/South Asia, and in the North Indian Ocean due to interactions between aerosol and ice clouds (**Error! Reference source not found.**). According to Twomey (1974), aerosols provide more cloud condensation nuclei, which increases the cloud droplet number concentration and decreases Rei. In a recent study of aerosol indirect effect on ice crystal size, Zhao et al. (2018) showed that Rei decreased with increased aerosol loading in moist conditions, consistent with the "Twomey effect" for liquid clouds. Our simulation result is consistent with previous studies showing that Rei decreases with increasing aerosol concentration (Jiang et al., 2008). The maximum change occurs in the North Indian Ocean where the magnitude is about -5 μm. Over most regions, ice clouds with smaller particles have higher albedo, thus reflecting more shortwave radiation at TOA (Figure 2.3b). The changes in shortwave radiation are closely correlated with changes in Rei in most regions, except in part of the Sahel region and the equatorial Indian Ocean. Meanwhile, the OLR decreases in South/East Asia because smaller particles trap more infrared radiation, while in North Africa and the equatorial Indian Ocean, OLR increases can be found (Figure 2.3c). The change of radiation on TOA in North Africa and the Indian Ocean will be discussed in the next paragraph. It is harder to draw a conclusion as to whether aerosols exert a positive or negative net radiative effect on TOA

because it depends on the relative contribution of shortwave and longwave radiation change. In this experiment, TOA radiation is decreased by 0.62 W m^{-2} on a global scale corresponding to increased aerosol loading.

We further investigate why the response of USW and OLR in North Africa and the Equatorial Indian Ocean is different from that in East and South Asia. The previous discussion suggests TOA USW/OLR negatively/positively correlated to the Rei change, respectively. In addition, TOA radiation is also influenced by cloud cover change. Figure 2.3e shows high cloud cover change, which is mostly related to ice clouds. Total cloud cover change in the entire atmospheric column is similar to that of high cloud cover with a larger magnitude. Changes in cloud cover are positively/negatively correlated to the TOA USW/OLR, i.e., greater cloud cover reflects more solar radiation and absorbs more infrared radiation, thus increases the upward shortwave radiation and decreases the OLR. In South/East Asia, both enhanced high cloud cover and reduced Rei increases TOA USW and decreases TOA OLR. In West Africa and Equatorial Indian Ocean, the reduction in cloud cover leads to decrease/increase in TOA USW/OLR, opposite to the radiative effect of reduced Rei. The model results suggest the TOA USW and OLR are dominated by the cloud cover change compared to Rei change in West Africa and Equatorial Indian Ocean (Figure 2.3e). The change in cloud cover depends on convection, precipitation efficiency, and cloud lifetime and is closely related to local microphysical conditions. Figure 2.3f shows that change in IWC at 200 hPa, which is approximately the level of convective detrainment (Folkins and Martin, 2005). The 200 hPa IWC is normally assumed as a good indicator of convective intensity. A reduction in convection may help explain the cloud cover change in North and West Africa (Figure 2.3f).

To better investigate the relationship between changes in the radiation field and changes in

Rei/cloud cover, we further check the correlation between ΔUSW and ΔRei, ΔULW and ΔRei, ΔUSW and ΔCC, and ΔULW and ΔCC in the selected region (Figure 2.4). The region selected here is the same one shown in Figure 2.3. Here ΔUSW, ΔULW, ΔRei, and ΔCC are used to denote the difference of USW, ULW, Rei, and in cloud cover between ICE and CTL1 (ICE - CTL1). Each point in Figure 2.4 stands for one grid point in the selected region. We then calculate the cross-correlation between ΔUSW and ΔRei, ΔULW and ΔRei, ΔUSW and ΔCC, and ΔULW and ΔCC in the selected region. T-test ($t = \sqrt{n-2}\frac{r}{\sqrt{1-r^2}}$) has been applied to examine if the correlation is significant and each plot shows a highly significant correlation (p=0.000). Compared to ΔRei, ΔCC has a closer correlation to both ΔUSW and ΔULW, and the correlation between ΔCC and ΔULW can be as high as -0.91(Figure 2.4d). Moreover, ΔULW (Figure 2.4b and Figure 2.4d) has a higher correlation to both ΔRei and ΔCC, compared to that of ΔUSW (Figure 2.4a and Figure 2.4c), indicating that spatial pattern of ΔULW is similar to that of ΔCC and ΔRei. Figure 2.4 suggests that aerosols may perturb the radiative budget on TOA through both their effects on Rei and the secondary effects on cloud cover. The radiation perturbation due to cloud cover change is likely to be as important as that due to particle size change.

Figure 2.5a and Figure 2.5b show aerosol effects on surface net radiation and surface latent heat flux. Surface radiation decreases by 1.13 W m^{-2} globally (Figure 2.5a). A similar pattern is observed in latent heat change, with a smaller magnitude (Figure 2.5b). The energy budget over the ocean is not analyzed due to fixed SST. The precipitation change (Figure 2.5c) generally corresponds to the changes in IWC (Figure 2.3f) and cloud cover (Figure 2.3e) in the monsoon regions. It should be noted that in the cloud parameterization of GFS, precipitation is diagnostically calculated directly from the cloud mixing ratio (Zhao and Carr, 1997) and the influence of particle size on precipitation efficiency is not considered (Kessler, 1995). Therefore, the effect of aerosol

on the auto-conversion rate and precipitation is not included and aerosol second indirect effect is neglected in this study. Precipitation change in Figure 2.5c shows quite different patterns in the Asian and West African monsoon regions. Over East and South Asia, several dipole anomalies are found, indicating that aerosols affect precipitation regions through modulation of microphysical processes affecting large-scale dynamic conditions; whereas in West Africa, only the decrease in precipitation is found. The different mechanisms of aerosol effect on precipitation over different monsoon regions will be further discussed later. Simulations show a general decrease in surface temperature (Figure 2.5d) in response to a reduction in surface radiation (Figure 2.5a). In West Africa, the increase in temperature is caused by decreased latent heat corresponding to weakened precipitation.

Error! Reference source not found. shows the latitude-height cross section of the streamline in CTL1 and the differences between ICE and CTL1 in East Asia (upper panel) and South Asia (bottom panel). Three major convection zones are depicted in **Error! Reference source not found.**a and **Error! Reference source not found.**b. The first one occurs around 10°N in tropical regions. Another deep convection is found over Southeast China from 20°N to 32°N associated with the ITCZ, accompanied by the East Asian monsoon. The last one exists north of 40°N, where the monsoon inflow is elevated by topography and forms a cyclone in the south. Similar deep convections are found in South Asian monsoon regions from 10°N to 15°N (**Error! Reference source not found.**c, **Error! Reference source not found.**b). The prevalence of deep convection systems is the major difference between the Asian and West African monsoon systems and influences the aerosol indirect effect on precipitation.

Error! Reference source not found.b and **Error! Reference source not found.**d show the differences of a latitude-height cross section of the streamline between ICE and CTL1.

Descending anomalies are produced by strong radiative cooling over the East Asia monsoon region between 35°N-45°N and the South Asia region between 0°N-15°N, which can be inferred from a decrease in cloud cover and IWC (Figure 2.3e, Figure 2.3f). The suppressed convection in East Asia causes a southward wind anomaly in low levels, hampers the monsoon flow from moving inland (**Error! Reference source not found.**), and causes low precipitation there (Figure 2.5c). It converges with the low-level southward wind anomaly and is enhanced by upper-level heating, producing a deep convection anomaly between 25°N-30°N (**Error! Reference source not found.**b and **Error! Reference source not found.**). These circulation changes result in moisture convergence and precipitation increase over Southeast China and divergence and precipitation decrease around 35 °N (**Error! Reference source not found.**a). A similar precipitation dipole occurs in Southeast Asia (Figure 2.5c), also caused by the large-scale circulation anomaly (**Error! Reference source not found.**d). A cooling in the south and a heating in the North in the high troposphere can be inferred from the dipole anomalies in cloud cover and IWC (Figure 2.3e, Figure 2.3f). The heating anomaly favors a southward flow at the TOA, causing a descending in the south and rising in the north (**Error! Reference source not found.**b). The convection change finally leads to a dipole in precipitation anomaly over South Asia and the North Indian Ocean.

Error! Reference source not found. shows the latitude-height cross-section of wind streamlines in CTL1 and the differences between ICE and CTL1 and their changes in West Africa (15°W-10°E). The meridional monsoon inflow from 5°N to 17°N in CTL1 brings abundant moisture inland (**Error! Reference source not found.**a). A deep moist convection exists around 10°N and a shallower dry convection is present north of 15°N, associated with the thermal low. The dry convection is capped below 500 hPa by anticyclonic circulation of the Saharan high. Two major southward flows are present in mid to high levels: one existing over the Guinea Coast is

caused by deep convection and is accompanied by a subsidence around the Gulf of Guinea; another occurs at 600 hPa and is the outflow of the Saharan high (**Error! Reference source not found.**a).

Similar to the scenario in the Asian monsoon, a strong descending anomaly from TOA to land surface is present in the deep convection regime in West Africa (**Error! Reference source not found.**b), caused by longwave cooling due to less cloud cover (Figure 2.3e). The descendence is found in all levels in the deep convection zone from 10°N to 15°N (**Error! Reference source not found.**b). **Error! Reference source not found.**a displays the anomaly of 850-hPa moisture flux and vertically integrated moisture flux divergence in West Africa, which shows moisture flux divergence at low levels, corresponding to decreased convection. This moisture divergence directly leads to precipitation decrease over the Sahel region (Figure 2.5c). The weakened convection also causes surface temperature increase by 0.5 K from 5°N to 20°N (Figure 2.5d). For other regions outside the deep convection zone, although strengthened convection can be found around 15°N, it is confined below 600 hPa by the Saharan High (**Error! Reference source not found.**b). Consequently, it does not result in apparent IWC increase (Figure 2.3f) and precipitation increase (Figure 2.5c) in the north. **Error! Reference source not found.**b shows the 500-hPa vertical velocity over West Africa. Only a few regions show convection increase and they are rather weak compared with the strong convection decrease in the south. Because the enhanced convection is constrained at low levels by the Saharan high, it does not result in apparent precipitation increase in the Northern part of West Africa. Consequently, no apparent precipitation dipole anomaly is found in the African monsoon region.

2.5 Comparison between aerosol effects on liquid clouds and ice clouds

A set of experiments was designed to compare the relative magnitude of climate impact due to aerosol effect on liquid clouds with that on ice clouds. Similar to the ice cloud experiments, the liquid cloud experiments are designed to show the difference between a current scenario and a clean scenario. In CTL2, pre-industrial sulfate concentration, which mainly comes from natural sources such as forest fires or oxidation of dimethyl sulfide (DMS) is specified. In the LIQ experiment (**Error! Reference source not found.**), GOCART sulfate aerosol is specified. Industrial sulfate aerosols are produced by oxidation of SO_2 and emitted from anthropogenic activities such as coal burning (Chin et al., 2002). The relatively short lifetime of sulfate makes its spatial distribution more homogeneous. The source regions (East Asia, South Asia, Europe, and East America) normally have larger aerosol concentrations.

Error! Reference source not found. shows liquid cloud effective radius (called Rel hereafter) in LIQ and CTL2 in each hemisphere and compares them with satellite retrieval from the International Satellite Cloud Climatology Project (ISCCP) in Han et al. (1994) . The simulated Rel is systematically smaller than satellite observation by about 2 μm, comparable with the estimated bias of the satellite retrieval, 1-2 μm. Moreover, according to Han et al. (1994), the estimated contrast between land and sea is 3.3 μm, and the contrast between the Northern and Southern Hemispheres is 0.7 μm. Our model reasonably reproduces the land-sea contrast and the hemispheric contrast obtained from the satellite data.

Figure 2.10 shows the JJA difference of Rel between LIQ and CTL2. Decreased Rel is found in three major monsoon regions and varies with sulfate loading. Liquid clouds with smaller droplets size have larger albedo and reflect more solar radiation, thus increasing global upward shortwave radiation on TOA (**Error! Reference source not found.**a), especially over North

Hemisphere continents where most Rel changes occur (Figure 2.10). Global shortwave radiation is reduced by 2.86 W m^{-2} at TOA, which is about the same magnitude as the aerosol direct effects, consistent with the previous estimation with some uncertainty (Kiehl and Briegleb, 1993). The longwave radiative effect is neglected here because liquid clouds are thick enough to act as black bodies (Boucher and Lohmann, 1995). Major cloud cover decrease is found in tropical regions (**Error! Reference source not found.**b), which could be due to aerosol-induced changes in dynamic conditions, such as regional convection and large-scale circulation. TOA shortwave radiation (**Error! Reference source not found.**a) is dominated by the changes in liquid cloud droplet effective radius (Figure 2.10). The cloud cover change plays a secondary effect, different from the aerosol indirect effects on ice clouds, where radiation field is affected by both changes in crystal size and cloud cover. **Error! Reference source not found.**c shows decreased temperature over most regions especially over the extra-tropics, corresponding to decreased surface radiation. The temperature increase in West Africa and Southeast Asia (**Error! Reference source not found.**c) is related to a reduction in latent heat caused by weakened precipitation (**Error! Reference source not found.**d).

We compare the relative importance of aerosol indirect effects on ice clouds and liquid clouds at both global and regional scales. **Error! Reference source not found.**a and **Error! Reference source not found.**b show the TOA and surface aerosol indirect radiative effects. We find the magnitude of change in liquid clouds is 1-2 times larger than that due to ice clouds. The relatively smaller radiation feedback due to ice clouds is caused by the longwave absorption effect, which partly offsets the shortwave reflecting effect. In contrast, the longwave feedback due to the response of liquid clouds is negligible as discussed before.

Error! Reference source not found.c and **Error! Reference source not found.**d summarize the aerosol indirect effects on regional surface temperature and precipitation. Most regions show decreased surface temperature resulted from aerosol indirect effects, and the global mean temperature change is 1-2 times larger in liquid clouds than in ice clouds. At the regional scale, temperature response caused by the aerosol indirect effect on ice clouds can be comparable to that caused by liquid clouds. The aerosol indirect effect on globally averaged precipitation is close to zero because precipitation changes are heterogeneous and even with opposite signs in different regions. In general, continental precipitation decreases due to aerosol effects on liquid clouds, whereas precipitation changes due to aerosol effects on ice clouds are less conclusive. Nevertheless, aerosols modify the precipitation distribution pattern in regions where the deep convection system exists as discussed earlier. Whether it will cause precipitation increase or decrease in East/South Asia is highly dependent on the specific region we focus on; whereas in West Africa, the enhanced convection anomaly is confined in the lower level, which does not finally result in precipitation increase. It should be noted that most GCMs, including the GFS, do not consider the impact of cloud droplets/particles size change on precipitation efficiency (Gu et al., 2012). Therefore, the differences in precipitation are directly reflected by IWC change (Figure 2.3e), which is associated with the interactions and feedback among aerosols, radiation, clouds, and dynamic field. The microphysical properties are modulated by the first indirect aerosol radiative effect and, in turn, affect the simulated climate.

2.6 Conclusion

This study carries out a series of simulations to investigate the aerosol indirect effect on clouds. The ice cloud parameterization developed by Jiang et al. (2011) and the liquid cloud

parameterization by Boucher and Lohmann (1995) have been incorporated separately to test aerosol indirect effects on ice clouds and liquid clouds. In the ice cloud experiments (Case 1), the experiments use AOD = 0.01 to represent a clean atmospheric condition and AOD from GOCART for the current scenario. In the liquid cloud experiments (Case 2), the pre-industrial sulfate aerosol concentration is used to represent a clean scenario, and the GOCART sulfate concentration from GOCART is used to represent a current scenario. For each experiment, 6-year numerical simulations have been conducted using WAMME II climatology SST.

It is shown that aerosols act as ice clouds nuclei, which enhances cloud scattering and absorption effects. Overall, the aerosols first indirect effect results in negative radiative effects at TOA. In addition, the TOA radiation budget is also perturbed by cloud cover changes induced by effects of cloud microphysics and associated convection, with a similar magnitude as the Rei effect. Aerosols mainly change the precipitation distribution pattern and create anomaly dipoles in the South/East Asian regions but not West Africa, where convection is constrained by the Saharan High. Therefore, enhanced convection is confined in the low level, thus resulting in precipitation decrease only. We also test the sensitivity for different AODs in the clean scenario by using AOD = 0.1 in the control experiment. The conclusions are consistent and comparable in all radiation and climate variables. Therefore, we suppose the aerosol influence on regional climate is not very sensitive to the AOD values used for clean conditions as long as the values can properly represent a clean atmosphere.

We also include experiments assessing aerosol indirect effects on liquid clouds and compare with those on ice clouds. Previous studies mostly investigated aerosol indirect effect on either liquid or ice clouds separately. This study includes both effects and provides a preliminary comparison of the relative magnitude of these two effects. Both ice cloud experiments and liquid

cloud experiments are designed to show the difference between a current scenario and a clean scenario. Different from ice clouds, the longwave radiative changes of liquid clouds are negligible because most of them are thick enough to act as black bodies (Boucher and Lohmann, 1995). Radiation and temperature changes generated by aerosol effects on liquid clouds are normally 1-2 times larger than those generated by aerosol effects on ice clouds. Moreover, radiation change is directly related to liquid cloud droplets size change in most regions, different from the aerosol effect on ice clouds.

IPCC (2013) has pointed out that "Clouds and aerosols continue to contribute the largest uncertainty to estimates and interpretations of the Earth's changing energy budget." Our simulation results confirm that inherent complexity of aerosol-cloud interactions is the main reason inhibiting a better understanding and description of the aerosol indirect effect. Aerosol interactions with ice clouds are different from those with liquid clouds in reference to OLR, radiative heating, and their further effects on convection strength and precipitation. Even the aerosol indirect effect on ice clouds varies from region to region depending on different climate dynamic conditions. These features make the aerosol climate effect more dependent on GCM dynamics, microphysical parameterization, and aerosol optical properties provided by aerosol data. Moreover, the parameterizations themselves would induce some bias. The ice cloud parameterization of Jiang et al. (2011) does not include the interactions between microphysical and dynamical processes because they are very complicated and are not yet well understood--this is supposed to cause some bias although we do not know how large it could be. The parameterization represents one of the first attempts to use satellite data to quantify the first indirect effect of aerosols on ice clouds for use in climate models. Recent aerosol and clouds measurements from CALIPSO and CloudSat offer vertically-resolved aerosol and clouds distribution, which could be applied to provide a

height-resolved ice cloud parameterization. However, different from GOCART, CALIPSO assigned only one aerosol type to each atmospheric layer, rather than a mixture of aerosol compositions (Omar et al., 2009), which is difficult to be directly introduced to the GFS. Given the huge uncertainties estimating aerosol climate effect, we propose that the optimization of aerosol simulation should include the improvement of GCMs, a better description of aerosol optical properties in the aerosol data sets, and the development of parameterization for aerosol-cloud interactions.

Tables and Figures

Table 2.1 Table of experiment

Case		Aero Direct effect scheme	Aero - Ice Cloud Interaction scheme	Aero - Liq Cloud Interactions scheme	Note
Case 1	CTL1	AOD (GOCART mixing ratio)	Jiang (AOD=0.01)	--	ICE minus CTL1 shows aerosol – ice clouds interaction
	ICE		Jiang (GOCART mixing ratio)	--	
Case 2	CTL2	AOD (GOCART mixing ratio)	--	Boucher (pre-industrial sulfate mixing ratio)	LIQ minus CTL2 shows aerosol – liquid clouds interaction
	LIQ		--	Boucher (GOCART sulfate mixing ratio)	

Table 2.2 Annual averaged liquid clouds effective radius (μm) in LIQ and CTL2 averaged over Northern Hemisphere (0-60°N), Northern Hemisphere land, Northern Hemisphere ocean, Southern Hemisphere (50°S-0), Southern Hemisphere land, Southern Hemisphere ocean, and their differences between LIQ and CTL2

Region	**CTL2**	**LIQ**	**LIQ - CTL2**
NH	6.92	5.68	-1.24
NH_land	6.94	5.52	-1.42
NH_ocean	9.07	7.94	-1.13
SH	9.62	8.59	-1.03
SH_land	6.85	6.06	-0.79
SH_ocean	10.09	9.14	-0.95

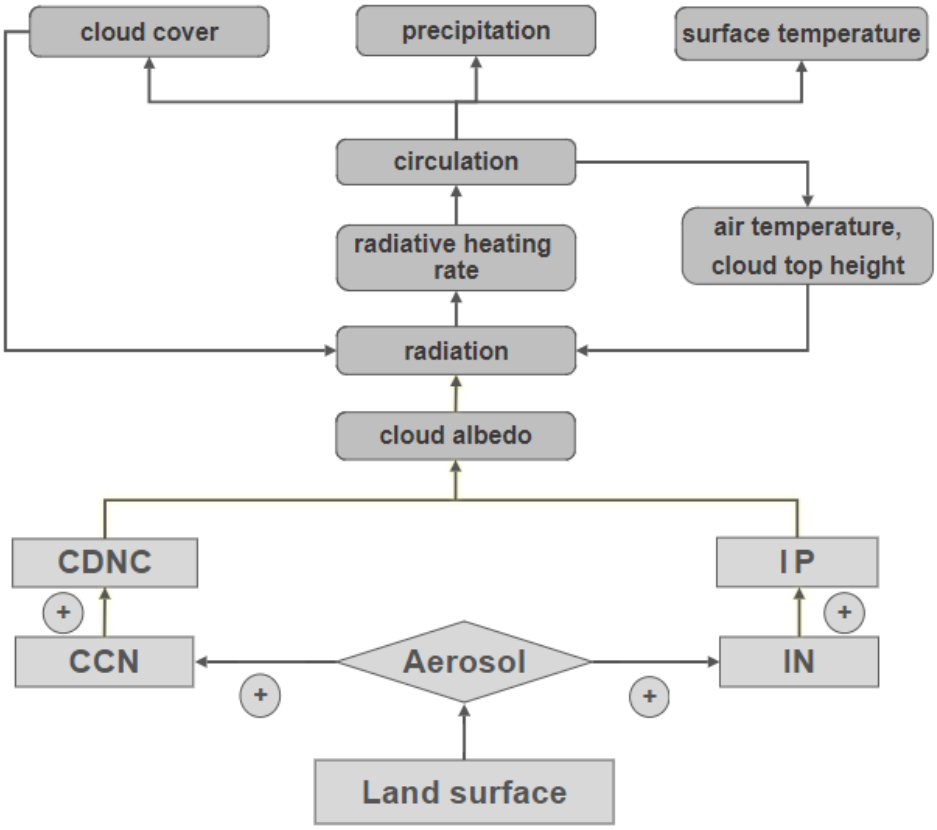

Figure 2.1 Schematic diagram of aerosol indirect radiative effect on ice clouds and liquid clouds (adapted from Lohmann and Feichter (2005)). CCN denotes cloud condensation nuclei and IN represents ice forming nuclei. CDNC denotes the cloud droplet number concentration, and IP represents the number concentration of ice particles

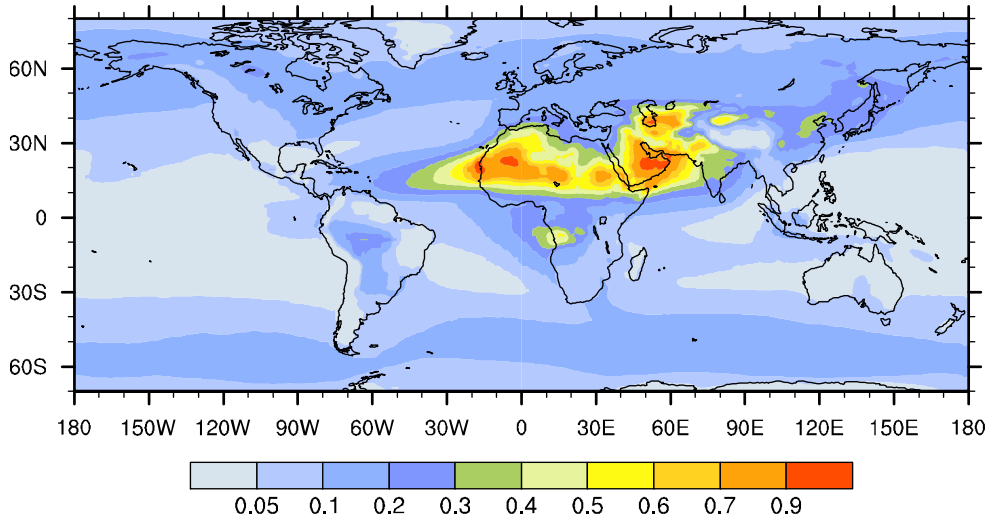

Figure 2.2 Differences of AOD used in Jiang's parameterization between ICE (AOD from GOCART data) and CTL1 (AOD = 0.01) in June–July–August (JJA).

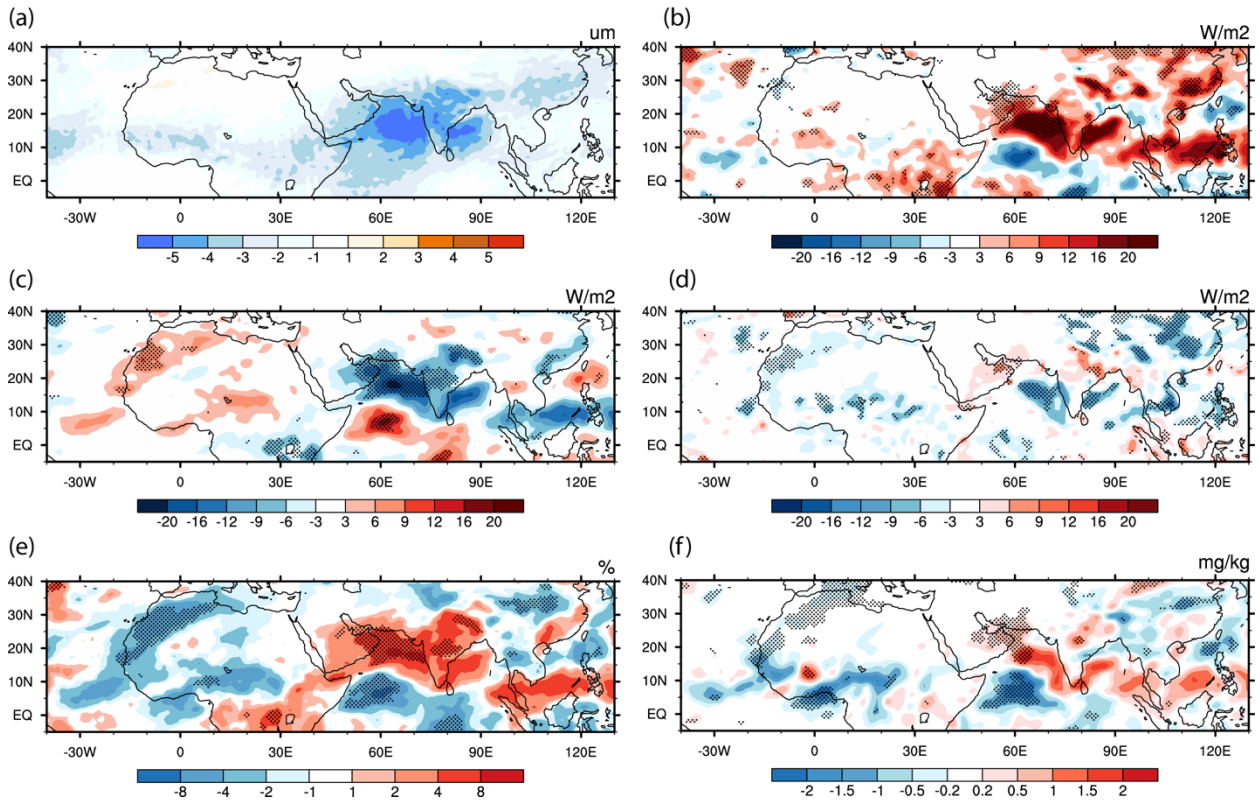

Figure 2.3 Differences of a) Rei at 215 hPa (μm), b) TOA USW (W m^{-2}), c) TOA OLR (W m^{-2}), d) TOA net radiation (W m^{-2}), e) high cloud cover (%), and f) IWC at 200 hPa (mg kg^{-1}) in JJA between ICE and CTL1 (ICE-CTL1)

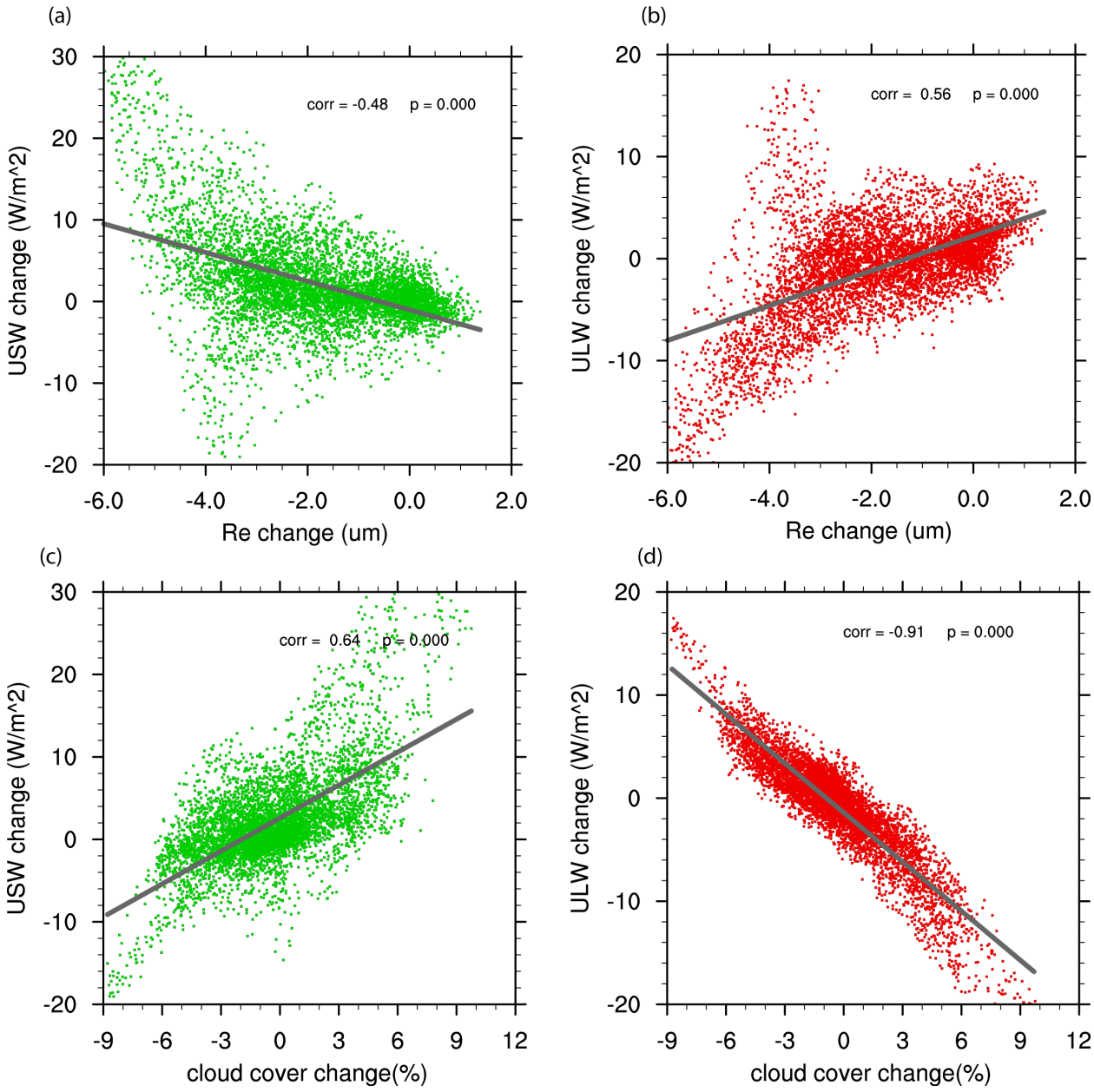

Figure 2.4 Differences of TOA USW (a, c) and ULW (b, d) as a function of Rei change (top panel) and high cloud cover (bottom panel) in JJA between ICE and CTL1 (ICE-CTL1). Each point stands for one grid point in the selected region

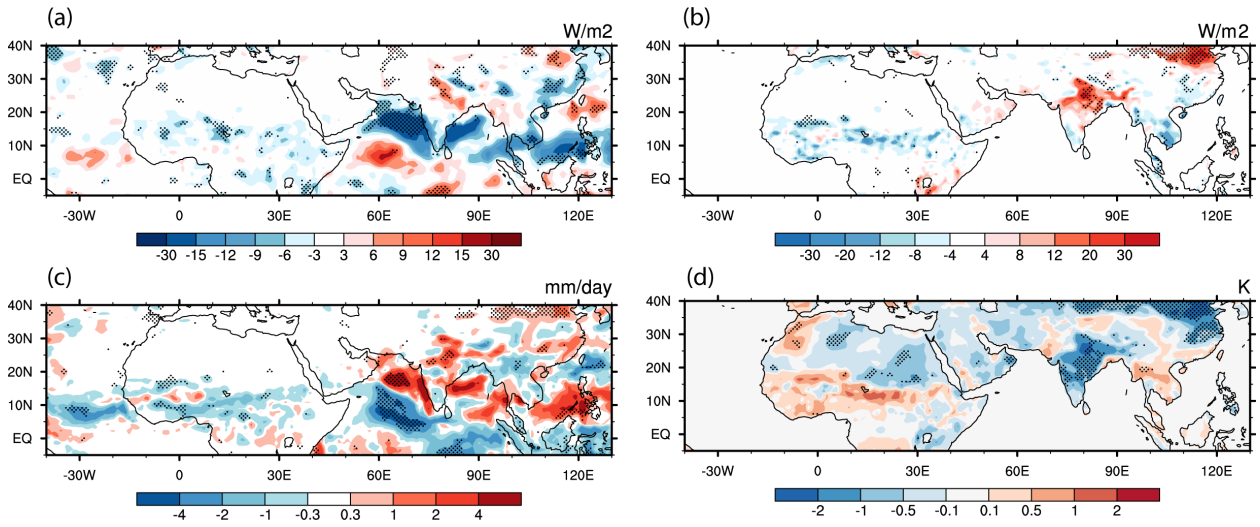

Figure 2.5 JJA differences of a) surface net radiation (W m^{-2}), b) latent heat (W m^{-2}), c) precipitation (mm day^{-1}), and d) surface temperature (K) between ICE and CTL1 (ICE-CTL1)

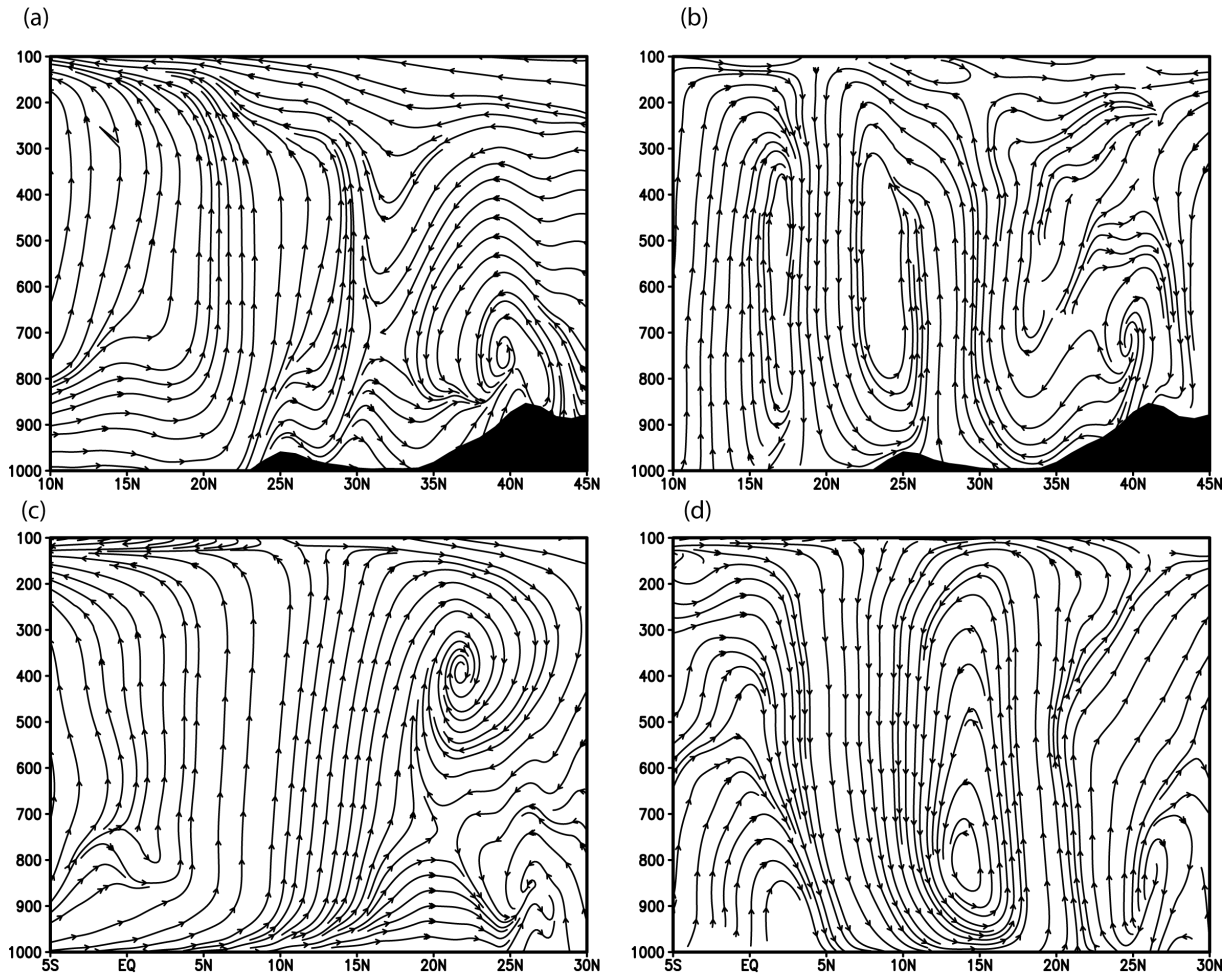

Figure 2.6 JJA latitude-height cross section of (a, c) streamline (v; -w*-100) in CTL1 and (b, d) differences between ICE and CTL1 (ICE-CTL1) averaged over 105°E - 130°E (upper panel) and over 60°E -70 °E (bottom panel)

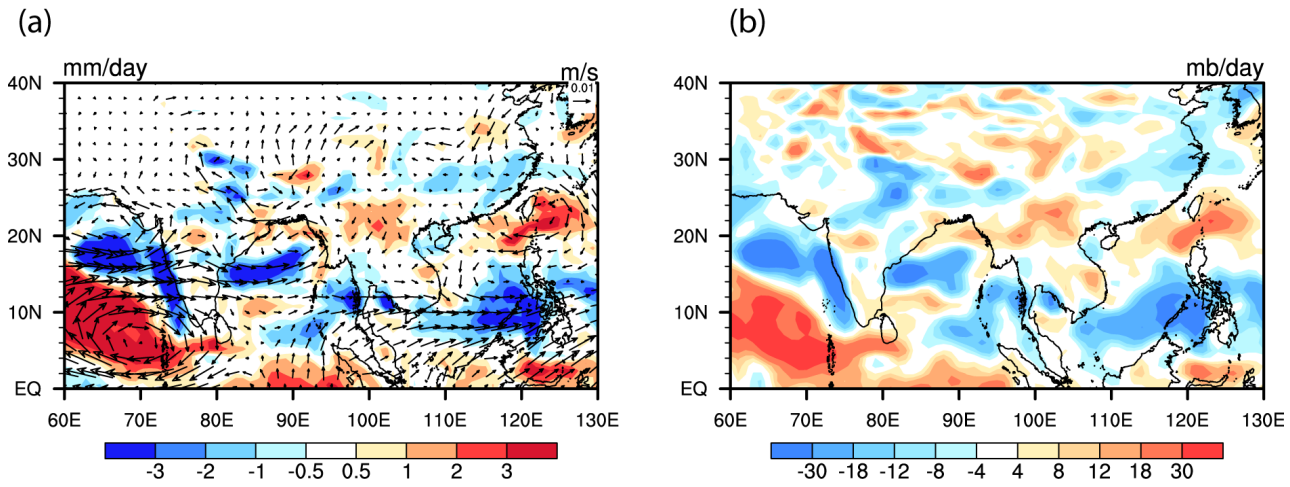

Figure 2.7 JJA differences of a) moisture flux (m s^{-1}) at 850 hPa and vertically integrated moisture flux divergence (mm day^{-1}) and b) 500 hPa vertical velocity (mb day^{-1}) in East and Southeast Asia between ICE and CTL1 (ICE-CTL1)

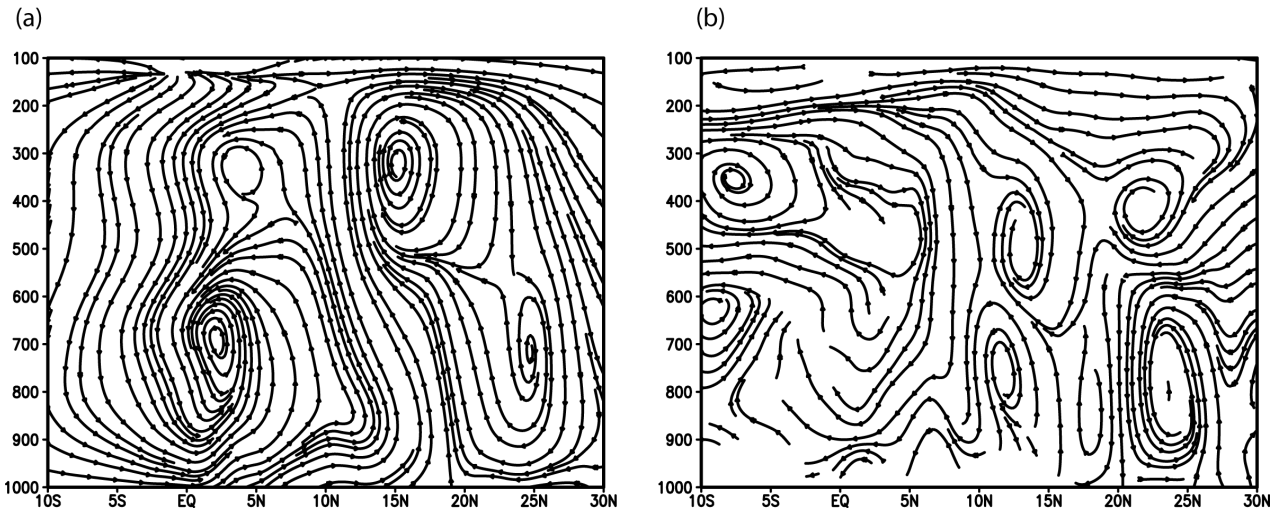

Figure 2.8 JJA latitude-height cross-section of (a) streamline (v; -w*-100) in CTL1 and (b) differences between ICE and CTL1 averaged over 15°W-10°E (ICE-CTL1

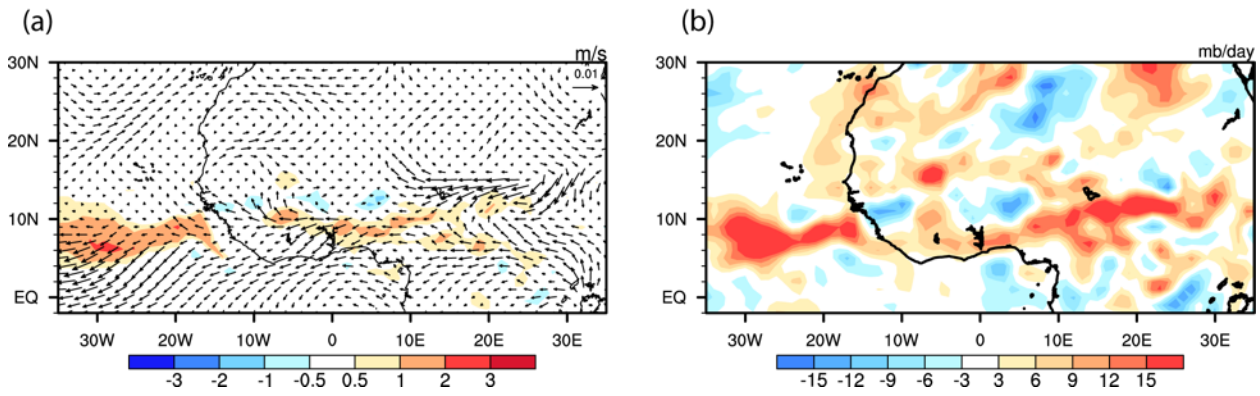

Figure 2.9 JJA differences of a) moisture flux (m s^{-1}) at 850 hPa and vertically integrated moisture flux divergence (mm day^{-1}) and b) 500 hPa vertical velocity (mb day^{-1}) in West Africa between ICE and CTL1 (ICE-CTL1)

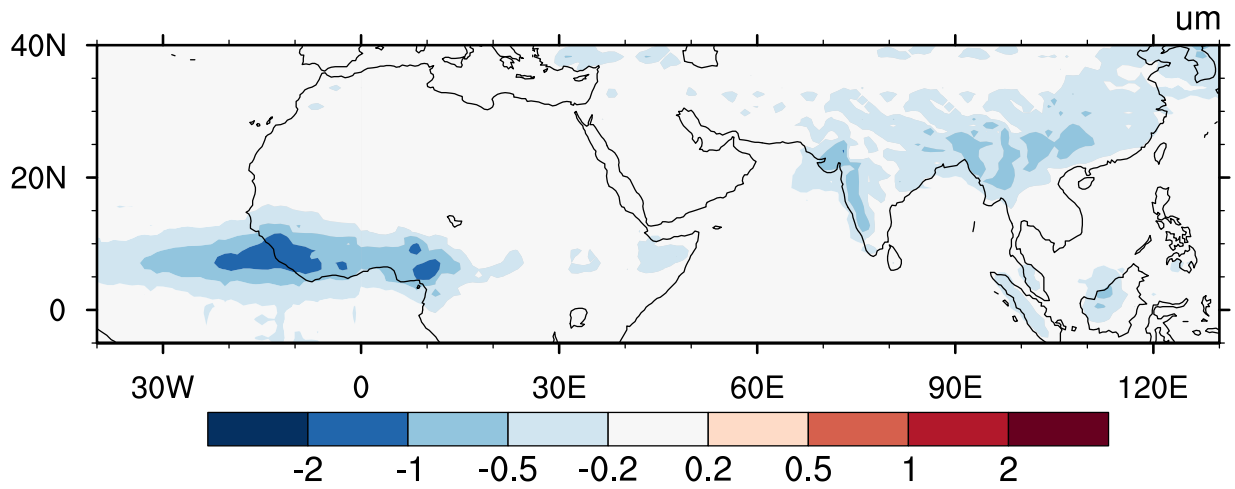

Figure 2.10 Differences of Rel (μm) in JJA between LIQ and CTL2 (LIQ-CTL2)

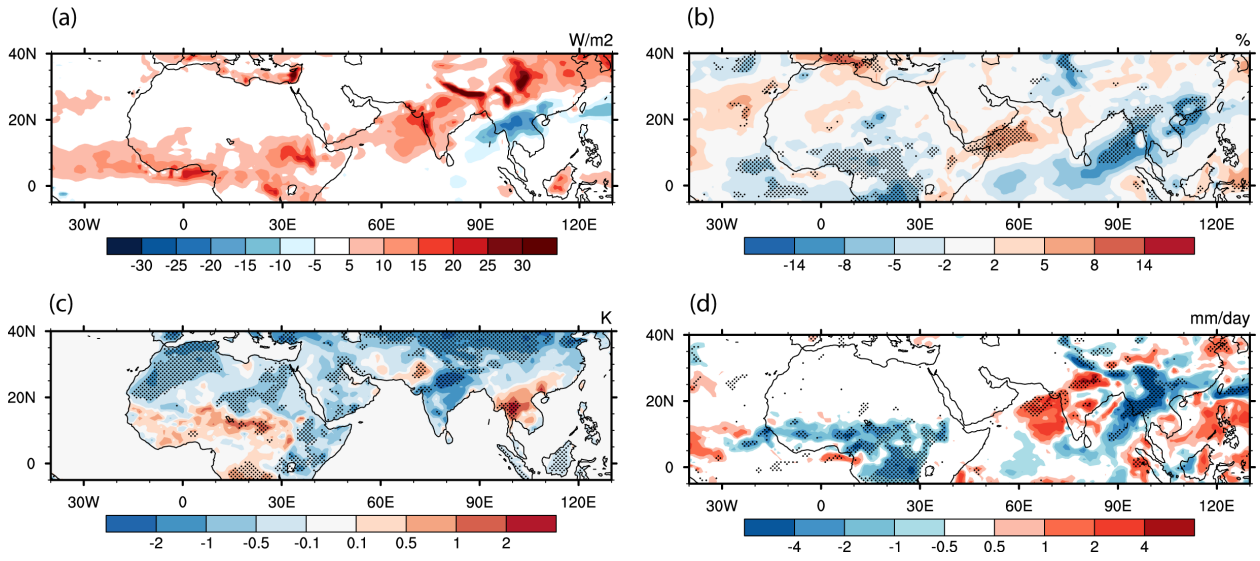

Figure 2.11 Differences of in a) TOA upward shortwave radiation (W m^{-2}), b) column cloud cover (%), c) surface temperature (K), and d) precipitation (mm day^{-1}) in JJA between LIQ and CTL2 (LIQ-CTL2)

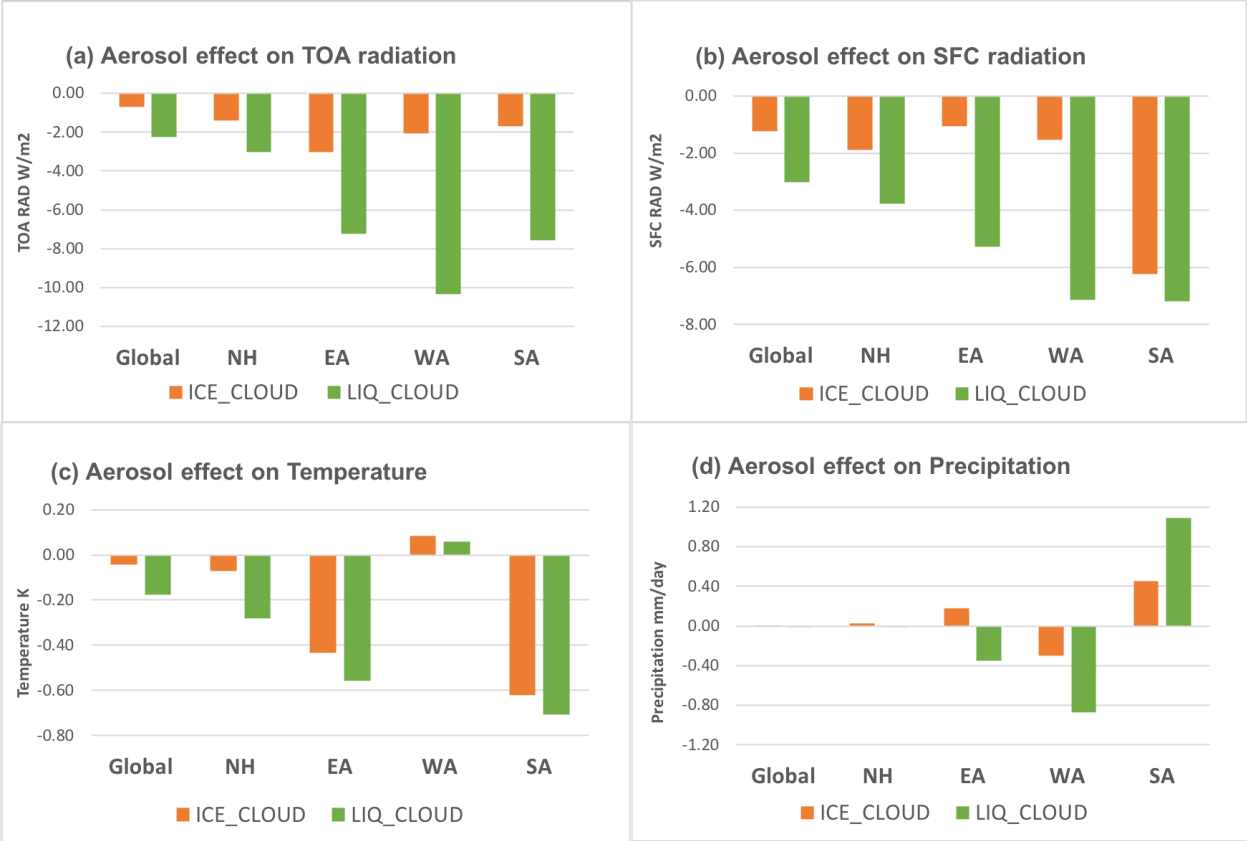

Figure 2.12 Aerosol indirect effects on a) TOA radiation (W m^{-2}), b) surface radiation (W m^{-2}), c) surface temperature (K), and d) precipitation (mm day^{-1}) on the Global scale, Northern Hemisphere, East Asia, West Africa, and South Asia

Reference

Ackerman, T. P., Liou, K. N., Valero, F. P. J., and Pfister, L.: Heating Rates in Tropical Anvils, J Atmos Sci, 45, 1606-1623, Doi 10.1175/1520-0469(1988)045<1606:Hrita>2.0.Co;2, 1988.

Adler, R. F., Huffman, G. J., Chang, A., Ferraro, R., Xie, P. P., Janowiak, J., Rudolf, B., Schneider, U., Curtis, S., Bolvin, D., Gruber, A., Susskind, J., Arkin, P., and Nelkin, E.: The version-2 global precipitation climatology project (GPCP) monthly precipitation analysis (1979-present), J Hydrometeorol, 4, 1147-1167, Doi 10.1175/1525-7541(2003)004<1147:Tvgpcp>2.0.Co;2, 2003.

Albrecht, B. A.: Aerosols, Cloud Microphysics, and Fractional Cloudiness, Science, 245, 1227-1230, DOI 10.1126/science.245.4923.1227, 1989.

Arakawa, A., and Schubert, W. H.: Interaction of a Cumulus Cloud Ensemble with the Large-Scale Environment, Part I, J Atmos Sci, 31, 674-701, 10.1175/1520-0469(1974)031<0674:ioacce>2.0.co;2, 1974.

Berry, E., and Mace, G. G.: Cloud properties and radiative effects of the Asian summer monsoon derived from A-Train data, J Geophys Res-Atmos, 119, 9492-9508, 10.1002/2014jd021458, 2014.

Boucher, O., and Lohmann, U.: The Sulfate-Ccn-Cloud Albedo Effect - a Sensitivity Study with 2 General-Circulation Models, Tellus B, 47, 281-300, DOI 10.1034/j.1600-0889.47.issue3.1.x, 1995.

Campbell, J. R., Hlavka, D. L., Welton, E. J., Flynn, C. J., Turner, D. D., Spinhirne, J. D., III, V. S. S., and Hwang, I. H.: Full-Time, Eye-Safe Cloud and Aerosol Lidar Observation at Atmospheric Radiation Measurement Program Sites: Instruments and Data Processing, Journal of Atmospheric and Oceanic Technology, 19, 431-442, 10.1175/1520-0426(2002)019<0431:ftesca>2.0.co;2, 2002.

Campbell, J. R., Lolli, S., Lewis, J. R., Gu, Y., and Welton, E. J.: Daytime Cirrus Cloud Top-of-the-Atmosphere Radiative Forcing Properties at a Midlatitude Site and Their Global Consequences, J Appl Meteorol Clim, 55, 1667-1679, 10.1175/Jamc-D-15-0217.1, 2016.

Chin, M., Rood, R. B., Lin, S. J., Muller, J. F., and Thompson, A. M.: Atmospheric sulfur cycle simulated in the global model GOCART: Model description and global properties, J Geophys Res-Atmos, 105, 24671-24687, Doi 10.1029/2000jd900384, 2000.

Chin, M., Ginoux, P., Kinne, S., Torres, O., Holben, B. N., Duncan, B. N., Martin, R. V., Logan, J. A., Higurashi, A., and Nakajima, T.: Tropospheric aerosol optical thickness from the GOCART model and comparisons with satellite and Sun photometer measurements, J Atmos Sci, 59, 461-483, Doi 10.1175/1520-0469(2002)059<0461:Taotft>2.0.Co;2, 2002.

Chun, H. Y., and Baik, J. J.: Momentum flux by thermally induced internal gravity waves and its approximation for large-scale models, J Atmos Sci, 55, 3299-3310, Doi 10.1175/1520-0469(1998)055<3299:Mfbtii>2.0.Co;2, 1998.

Clough, S. A., Shephard, M. W., Mlawer, E., Delamere, J. S., Iacono, M., Cady-Pereira, K., Boukabara, S., and Brown, P. D.: Atmospheric radiative transfer modeling: a summary of the AER codes, J Quant Spectrosc Ra, 91, 233-244, 10.1016/j.jqsrt.2004.05.058, 2005.

Diehl, K., and Mitra, S. K.: A laboratory study of the effects of a kerosene-burner exhaust on ice nucleation and the evaporation rate of ice crystals, Atmos Environ, 32, 3145-3151, 1998.

Feingold, G., Eberhard, W. L., Veron, D. E., and Previdi, M.: First measurements of the Twomey indirect effect using ground-based remote sensors, Geophys Res Lett, 30, 10.1029/2002gl016633, 2003.

Folkins, I., and Martin, R. V.: The vertical structure of tropical convection and its impact on the budgets of water vapor and ozone, J Atmos Sci, 62, 1560-1573, Doi 10.1175/Jas3407.1, 2005.

Goswami, B. B., and Goswami, B. N.: A road map for improving dry-bias in simulating the South Asian monsoon precipitation by climate models, Climate Dynamics, 49, 2025-2034, 10.1007/s00382-016-3439-2, 2017.

Gu, Y., Liou, K. N., Jiang, J. H., Su, H., and Liu, X.: Dust aerosol impact on North Africa climate: a GCM investigation of aerosol-cloud-radiation interactions using A-Train satellite data, Atmos Chem Phys, 12, 1667-1679, 10.5194/acp-12-1667-2012, 2012.

Gu, Y., Xue, Y., De Sales, F., and Liou, K. N.: A GCM investigation of dust aerosol impact on the regional climate of North Africa and South/East Asia, Climate Dynamics, 46, 2353-2370, 10.1007/s00382-015-2706-y, 2015.

Gu, Y., Liou, K. N., Jiang, J. H., Fu, R., Lu, S., and Xue, Y.: A GCM investigation of impact of aerosols on the precipitation in Amazon during the dry to wet transition, Climate Dynamics, 48, 2393-2404, 10.1007/s00382-016-3211-7, 2017.

Han, Q. Y., Rossow, W. B., and Lacis, A. A.: Near-Global Survey of Effective Droplet Radii in Liquid Water Clouds Using Isccp Data, J Climate, 7, 465-497, Doi 10.1175/1520-0442(1994)007<0465:Ngsoed>2.0.Co;2, 1994.

Harris, I., Jones, P. D., Osborn, T. J., and Lister, D. H.: Updated high-resolution grids of monthly climatic observations - the CRU TS3.10 Dataset, Int J Climatol, 34, 623-642, 10.1002/joc.3711, 2014.

Haywood, J., and Boucher, O.: Estimates of the direct and indirect radiative forcing due to tropospheric aerosols: A review, Reviews of Geophysics, 38, 513-543, Doi 10.1029/1999rg000078, 2000.

Hong, S. Y., and Pan, H. L.: Nonlocal boundary layer vertical diffusion in a Medium-Range Forecast Model, Mon Weather Rev, 124, 2322-2339, Doi 10.1175/1520-0493(1996)124<2322:Nblvdi>2.0.Co;2, 1996.

IPCC: Climate Change 2013: The Physical Science Basis. Contribution of Working Group I to the Fifth Assessment Report of the Intergovernmental Panel on Climate Change, Cambridge University Press, Cambridge, United Kingdom and New York, NY, USA, 1535 pp., 2013.

Jiang, J. H., Su, H., Schoeberl, M. R., Massie, S. T., Colarco, P., Platnick, S., and Livesey, N. J.: Clean and polluted clouds: Relationships among pollution, ice clouds, and precipitation in South America, Geophys Res Lett, 35, 10.1029/2008gl034631, 2008.

Jiang, J. H., Su, H., Massie, S. T., Colarco, P. R., Schoeberl, M. R., and Platnick, S.: Aerosol-CO relationship and aerosol effect on ice cloud particle size: Analyses from Aura Microwave Limb Sounder and Aqua Moderate Resolution Imaging Spectroradiometer observations, J Geophys Res-Atmos, 114, 10.1029/2009jd012421, 2009.

Jiang, J. H., Su, H., Zhai, C., Massie, S. T., Schoeberl, M. R., Colarco, P. R., Platnick, S., Gu, Y., and Liou, K. N.: Influence of convection and aerosol pollution on ice cloud particle effective radius, Atmos Chem Phys, 11, 457-463, 10.5194/acp-11-457-2011, 2011.

Jiang, M., Feng, J., Li, Z., Sun, R., Hou, Y.-T., Zhu, Y., Wan, B., Guo, J., and Cribb, M.: Potential influences of neglecting aerosol effects on the NCEP GFS precipitation forecast, Atmos Chem Phys, 17, 13967-13982, 2017.

Jiang, Y. Q., Liu, X. H., Yang, X. Q., and Wang, M. H.: A numerical study of the effect of different aerosol types on East Asian summer clouds and precipitation, Atmos Environ, 70, 51-63, 10.1016/j.atmosenv.2012.12.039, 2013.

Kaufman, Y. J., and Fraser, R. S.: The effect of smoke particles on clouds and climate forcing, Science, 277, 1636-1639, DOI 10.1126/science.277.5332.1636, 1997.

Kaufman, Y. J., Tanre, D., and Boucher, O.: A satellite view of aerosols in the climate system, Nature, 419, 215-223, 10.1038/nature01091, 2002.

Kessler, E.: On the Continuity and Distribution of Water Substance in Atmospheric Circulations, Atmos Res, 38, 109-145, Doi 10.1016/0169-8095(94)00090-Z, 1995.

Kiehl, J. T., and Briegleb, B. P.: The Relative Roles of Sulfate Aerosols and Greenhouse Gases in Climate Forcing, Science, 260, 311-314, DOI 10.1126/science.260.5106.311, 1993.

Kim, B. G., Miller, M. A., Schwartz, S. E., Liu, Y. G., and Min, Q. L.: The role of adiabaticity in the aerosol first indirect effect, J Geophys Res-Atmos, 113, 10.1029/2007jd008961, 2008.

L'Ecuyer, T. S., and Jiang, J. H.: Touring the atmosphere aboard the A-Train, Phys Today, 63, 36-41, 2010.

Lau, K. M., and Kim, K. M.: Observational relationships between aerosol and Asian monsoon rainfall, and circulation, Geophys Res Lett, 33, 10.1029/2006gl027546, 2006.

Lebo, Z. J., and Seinfeld, J. H.: Theoretical basis for convective invigoration due to increased aerosol concentration, Atmos Chem Phys, 11, 5407-5429, 10.5194/acp-11-5407-2011, 2011.

Lebo, Z. J.: The Sensitivity of a Numerically Simulated Idealized Squall Line to the Vertical Distribution of Aerosols, J Atmos Sci, 71, 187-202, 10.1175/Jas-D-14-0068.1, 2014.

Lebo, Z. J., and Morrison, H.: Dynamical Effects of Aerosol Perturbations on Simulated Idealized Squall Lines, Mon Weather Rev, 142, 991-1009, 10.1175/Mwr-D-13-00156.1, 2014.

Li, S., Wang, T., Solmon, F., Zhuang, B., Wu, H., Xie, M., Han, Y., and Wang, X.: Impact of aerosols on regional climate in southern and northern China during strong/weak East Asian summer monsoon years, Journal of Geophysical Research: Atmospheres, 121, 4069-4081, 10.1002/2015JD023892, 2016a.

Li, Z., Niu, F., Fan, J., Liu, Y., Rosenfeld, D., and Ding, Y.: Long-term impacts of aerosols on the vertical development of clouds and precipitation, Nature Geosci, 4, 888-894, 2011.

Li, Z. Q., Lau, W. K. M., Ramanathan, V., Wu, G., Ding, Y., Manoj, M. G., Liu, J., Qian, Y., Li, J., Zhou, T., Fan, J., Rosenfeld, D., Ming, Y., Wang, Y., Huang, J., Wang, B., Xu, X., Lee, S. S., Cribb, M., Zhang, F., Yang, X., Zhao, C., Takemura, T., Wang, K., Xia, X., Yin, Y., Zhang, H., Guo, J., Zhai, P. M., Sugimoto, N., Babu, S. S., and Brasseur, G. P.: Aerosol and monsoon climate interactions over Asia, Reviews of Geophysics, 54, 866-929, 10.1002/2015rg000500, 2016b.

Liu, X., Shi, X., Zhang, K., Jensen, E. J., Gettelman, A., Barahona, D., Nenes, A., and Lawson, P.: Sensitivity studies of dust ice nuclei effect on cirrus clouds with the Community Atmosphere Model CAM5, Atmos. Chem. Phys., 12, 12061-12079, 10.5194/acp-12-12061-2012, 2012.

Lohmann, U., and Roeckner, E.: Design and performance of a new cloud microphysics scheme developed for the ECHAM general circulation model, Climate Dynamics, 12, 557-572, DOI 10.1007/s003820050128, 1996.

Lohmann, U., and Feichter, J.: Global indirect aerosol effects: a review, Atmos Chem Phys, 5, 715-737, 2005.

Lolli, S., Campbell, J. R., Lewis, J. R., Gu, Y., Marquis, J. W., Chew, B. N., Liew, S. C., Salinas, S. V., and Welton, E. J.: Daytime Top-of-the-Atmosphere Cirrus Cloud Radiative Forcing Properties at Singapore, J Appl Meteorol Clim, 56, 1249-1257, 10.1175/Jamc-D-16-0262.1, 2017.

Menon, S., Hansen, J., Nazarenko, L., and Luo, Y.: Climate effects of black carbon aerosols in China and India, Science, 297, 2250-2253, 10.1126/science.1075159, 2002.

Ming, Y., Ramaswamy, V., Ginoux, P. A., Horowitz, L. W., and Russell, L. M.: Geophysical Fluid Dynamics Laboratory general circulation model investigation of the indirect radiative effects of anthropogenic sulfate aerosol, J Geophys Res-Atmos, 110, 10.1029/2005jd006161, 2005.

Mlawer, E. J., Taubman, S. J., Brown, P. D., Iacono, M. J., and Clough, S. A.: Radiative transfer for inhomogeneous atmospheres: RRTM, a validated correlated-k model for the longwave, J Geophys Res-Atmos, 102, 16663-16682, Doi 10.1029/97jd00237, 1997.

Omar, A. H., Winker, D. M., Vaughan, M. A., Hu, Y., Trepte, C. R., Ferrare, R. A., Lee, K.-P., Hostetler, C. A., Kittaka, C., Rogers, R. R., Kuehn, R. E., and Liu, Z.: The CALIPSO Automated Aerosol Classification and Lidar Ratio Selection Algorithm, Journal of Atmospheric and Oceanic Technology, 26, 1994-2014, 10.1175/2009jtecha1231.1, 2009.

Pan, H. L., and Wu, W. S.: Implementing a mass flux convective parameterization package for the NMC medium-range forecast model, Numerical Weather Prediction 10th Conference (Nwp), 96-98, 1994.

Penner, J. E., Andreae, M., Annegarn, H., Barrie, L., Feichter, J., Hegg, D., Jayaraman, A., Leaitch, R., Murphy, D., and Nganga, J.: Aerosols, their direct and indirect effects, in: Climate Change 2001: The Scientific Basis. Contribution of Working Group I to the Third Assessment Report of the Intergovernmental Panel on Climate Change, Cambridge University Press, 289-348, 2001.

Penner, J. E., Chen, Y., Wang, M., and Liu, X.: Possible influence of anthropogenic aerosols on cirrus clouds and anthropogenic forcing, Atmos. Chem. Phys., 9, 879-896, 10.5194/acp-9-879-2009, 2009.

Pincus, R., Barker, H. W., and Morcrette, J.-J.: A fast, flexible, approximate technique for computing radiative transfer in inhomogeneous cloud fields, Journal of Geophysical Research: Atmospheres, 108, n/a-n/a, 10.1029/2002jd003322, 2003.

Qian, Y., Yan, H. P., Hou, Z. S., Johannesson, G., Klein, S., Lucas, D., Neale, R., Rasch, P., Swiler, L., Tannahill, J., Wang, H. L., Wang, M. H., and Zhao, C.: Parametric sensitivity analysis of precipitation at global and local scales in the Community Atmosphere Model CAM5, Journal of Advances in Modeling Earth Systems, 7, 382-411, 10.1002/2014ms000354, 2015.

Rosenfeld, D., Lohmann, U., Raga, G. B., O'Dowd, C. D., Kulmala, M., Fuzzi, S., Reissell, A., and Andreae, M. O.: Flood or drought: How do aerosols affect precipitation?, Science, 321, 1309-1313, 10.1126/science.1160606, 2008.

Rotstayn, L. D.: Indirect forcing by anthropogenic aerosols: A global climate model calculation of the effective-radius and cloud-lifetime effects, J Geophys Res-Atmos, 104, 9369-9380, Doi 10.1029/1998jd900009, 1999.

Saha, S., Moorthi, S., Wu, X. R., Wang, J., Nadiga, S., Tripp, P., Behringer, D., Hou, Y. T., Chuang, H. Y., Iredell, M., Ek, M., Meng, J., Yang, R. Q., Mendez, M. P., Van Den Dool, H., Zhang, Q., Wang, W. Q., Chen, M. Y., and Becker, E.: The NCEP Climate Forecast System Version 2, J Climate, 27, 2185-2208, 10.1175/Jcli-D-12-00823.1, 2014.

Sassen, K., and Cho, B. S.: Subvisual Thin Cirrus Lidar Dataset for Satellite Verification and Climatological Research, J Appl Meteorol, 31, 1275-1285, Doi 10.1175/1520-0450(1992)031<1275:Stcldf>2.0.Co;2, 1992.

Storelvmo, T., Kristjansson, J. E., and Lohmann, U.: Aerosol influence on mixed-phase clouds in CAM-Oslo, J Atmos Sci, 65, 3214-3230, 10.1175/2008jas2430.1, 2008.

Sundqvist, H., Berge, E., and Kristjansson, J. E.: Condensation and Cloud Parameterization Studies with a Mesoscale Numerical Weather Prediction Model, Mon Weather Rev, 117, 1641-1657, Doi 10.1175/1520-0493(1989)117<1641:Cacpsw>2.0.Co;2, 1989.

Tao, W. K., Li, X. W., Khain, A., Matsui, T., Lang, S., and Simpson, J.: Role of atmospheric aerosol concentration on deep convective precipitation: Cloud-resolving model simulations, J Geophys Res-Atmos, 112, 10.1029/2007jd008728, 2007.

Tao, W. K., Chen, J. P., Li, Z. Q., Wang, C., and Zhang, C. D.: Impact of Aerosols on Convective Clouds and Precipitation, Reviews of Geophysics, 50, 10.1029/2011rg000369, 2012.

Twomey, S.: Pollution and Planetary Albedo, Atmos Environ, 8, 1251-1256, 1974.

Welton, E. J., Campbell, J. R., Spinhirne, J. D., and Scott, V. S.: Global monitoring of clouds and aerosols using a network of micro-pulse lidar systems, P Soc Photo-Opt Ins, 4153, 151-158, Doi 10.1117/12.417040, 2001.

Wu, D. L., Jiang, J. H., Read, W. G., Austin, R. T., Davis, C. P., Lambert, A., Stephens, G. L., Vane, D. G., and Waters, J. W.: Validation of the Aura MLS cloud ice water content measurements, J Geophys Res-Atmos, 113, 10.1029/2007jd008931, 2008.

Xue, Y., Sellers, P. J., Kinter, J. L., and Shukla, J.: A Simplified Biosphere Model for Global Climate Studies, J Climate, 4, 345-364, 10.1175/1520-0442(1991)004<0345:asbmfg>2.0.co;2, 1991.

Xue, Y., Juang, H. M. H., Li, W. P., Prince, S., DeFries, R., Jiao, Y., and Vasic, R.: Role of land surface processes in monsoon development: East Asia and West Africa, Journal of Geophysical Research: Atmospheres, 109, n/a-n/a, 10.1029/2003jd003556, 2004.

Xue, Y., De Sales, F., Lau, W. K. M., Boone, A., Kim, K.-M., Mechoso, C. R., Wang, G., Kucharski, F., Schiro, K., Hosaka, M., Li, S., Druyan, L. M., Sanda, I. S., Thiaw, W., Zeng, N., Comer, R. E., Lim, Y.-K., Mahanama, S., Song, G., Gu, Y., Hagos, S. M., Chin, M., Schubert, S., Dirmeyer, P., Ruby Leung, L., Kalnay, E., Kitoh, A., Lu, C.-H., Mahowald, N. M., and Zhang, Z.: West African monsoon decadal variability and surface-related forcings: second West African Monsoon Modeling and Evaluation Project Experiment (WAMME II), Climate Dynamics, 47, 3517-3545, 10.1007/s00382-016-3224-2, 2016.

Xue, Y. K., De Sales, F., Lau, W. K. M., Boone, A., Feng, J. M., Dirmeyer, P., Guo, Z. C., Kim, K. M., Kitoh, A., Kumar, V., Poccard-Leclercq, I., Mahowald, N., Moufouma-Okia, W., Pegion, P., Rowell, D. P., Schemm, J., Schubert, S. D., Sealy, A., Thiaw, W. M., Vintzileos, A., Williams, S. F., and Wu, M. L. C.: Intercomparison and analyses of the climatology of the West African Monsoon in the West African Monsoon Modeling and Evaluation project (WAMME) first model intercomparison experiment, Climate Dynamics, 35, 3-27, 10.1007/s00382-010-0778-2, 2010.

Yun, Y., and Penner, J. E.: Global model comparison of heterogeneous ice nucleation parameterizations in mixed phase clouds, Journal of Geophysical Research: Atmospheres, 117, n/a-n/a, 10.1029/2011JD016506, 2012.

Zhan, X. W., Xue, Y. K., and Collatz, G. J.: An analytical approach for estimating CO2 and heat fluxes over the Amazonian region, Ecol Model, 162, 97-117, 2003.

Zhao, B., Liou, K. N., Gu, Y., Jiang, J. H., Li, Q. B., Fu, R., Huang, L., Liu, X. H., Shi, X. J., Su, H., and He, C. L.: Impact of aerosols on ice crystal size, Atmos Chem Phys, 18, 1065-1078, 10.5194/acp-18-1065-2018, 2018.

Zhao, Q. Y., and Carr, F. H.: A prognostic cloud scheme for operational NWP models, Mon Weather Rev, 125, 1931-1953, Doi 10.1175/1520-0493(1997)125<1931:Apcsfo>2.0.Co;2, 1997.

Chapter 3 Assessing global and regional effects of reconstructed land use and land cover change on climate since 1950 using a coupled land-atmosphere-ocean model

This chapter has been published in its current form in the Journal of Climate. © American Meteorological Society. Used with permission. The supplementary material for this chapter is provided in Appendix A.

[**Huang, H.**, Y. Xue, N. Chilukoti, Y. Liu, G. Chen, and I. Diallo: Assessing Global and Regional Effects of Reconstructed Land-Use and Land-Cover Change on Climate since 1950 Using a Coupled Land–Atmosphere–Ocean Model. J. Climate, 33, 8997–9013, https://doi.org/10.1175/JCLI-D-20-0108.1, 2020.]

Abstract

Land use and land cover change (LULCC) is one of the most important forcings affecting climate in the past century. This study evaluates the global and regional LULCC impacts in 1950-2015 by employing an annually updated LULCC map in a coupled land-atmosphere-ocean model. The difference between LULCC and control experiments shows an overall land surface temperature (LST) increase by 0.48 K in the LULCC regions and a widespread LST decrease by 0.18 K outside the LULCC regions. A decomposed temperature metric (DTM) is applied to quantify the relative contribution of surface processes to temperature changes. Furthermore, while

precipitation in the LULCC areas is reduced in agreement with declined evaporation, LULCC causes a southward displacement of the Intertropical Convergence Zone (ITCZ) with a narrowing by 0.5 degrees, leading to a tripole anomalous precipitation pattern over the warm pool. The DTM shows that the temperature response in LULCC regions results from the competing effect between increased albedo (cooling) and reduced evaporation (warming). The reduced evaporation indicates less atmospheric latent heat release in convective processes and thus a drier and cooler troposphere, resulting in a reduction in surface cooling outside the LULCC regions. The southward shift of the ITCZ implies a northward cross-equatorial energy transport anomaly in response to reduced latent/sensible heat of the atmosphere in the Northern Hemisphere, where LULCC is more intensive. Tropospheric cooling results in the equatorward shift of the upper-tropospheric westerly jet in both hemispheres, which, in turn, leads to an equatorward narrowing of the Hadley circulation and ITCZ.

3.1 Introduction

Land use and land cover change (LULCC) consists of a wide range of land surface conversions including the conversion from forests to crops and pasturelands, reforestation of formerly agricultural areas, afforestation, and all kinds of urbanization (Mahmood et al., 2014). From the years 1700 to 2000, 42% to 68% of the global land surface has been transformed from natural vegetation into agriculture, rangeland, and woodland (Hurtt et al., 2006). By the end of the 20th century, most LULCC had taken place over the temperate regions of the Northern Hemisphere (NH), such as East Asia, South Asia, Europe, and North America (Ramankutty and Foley, 1999). After a rapid increase in the rate of deforestation during the 1980s and 1990s, recent satellite observations indicate a slowdown of LULCC in the past decade (FAO, 2007). Reforestation and afforestation are observed in Western Europe, North America, and China as a result of land abandonment and afforestation efforts (Nagendra and Southworth, 2009), while deforestations are still concentrated in the tropics.

Previous observation studies agree that LULCC modifies the surface properties through changing soil and vegetation characteristics, including albedo, leaf area index (LAI), and roughness length (Gash and Nobre, 1997; Dias et al., 2002; Lyons, 2002; Chagnon et al., 2004; Davin and de Noblet-Ducoudre, 2010; Nair et al., 2011; Guo et al., 2016; Liu et al., 2016). When LULCC takes place, conversions from forests to crops/grasslands normally cause a higher albedo because the multiple reflections within the canopy are diminished in low vegetations. A reconstructed land cover and biophysical parameter map by Steyaert and Knox (2008) showed that the albedo of the Eastern United States increased by ~5% from 1650 to 1992, caused by the extensive LULCC which replaced deciduous forests and native grasslands with agricultural crops and pastures. Albedo contrast due to LULCC is especially amplified when snow is present: open

land is normally entirely snow-covered, meaning the albedo can be as high as 0.9, whereas tree crowns will remain exposed above the snow in the forest (Betts, 2001). The increase in albedo reflects more incident radiation and leads to a change in radiative forcing by -0.15 ± 0.10 W m^{-2} globally, according to the Intergovernmental Panel on Climate Change Fifth Assessment Report (IPCC AR5) (Myhre et al., 2013). The reduction in net radiation tends to reduce the local land surface temperature (LST) via the radiation budget, referred to as the albedo effect (Davin et al., 2007).

Meanwhile, changes in LAI, vegetation cover, and surface roughness decrease the evapotranspiration on the leaf surface (Forster and Ramaswamy, 2007; Strack et al., 2008; Peng et al., 2014; Bright et al., 2017; Liu et al., 2019). A conversion from forest with deeper root depth to grassland/crop with shallower root depth results in a depressed latent heat (LH) within the planetary boundary layer (PBL) and potentially modifies atmospheric humidity and canopy air temperature. The change in aerodynamic roughness alters the surface wind speed and thus changes the momentum and water vapor exchange between land and atmosphere (Lee et al., 2011). Therefore, a higher Bowen ratio (the ratio of sensible heat to latent heat fluxes) and a modification in water cycles is found due to LULCC. The reduced latent and sensible heat (SH) fluxes tend to increase the LST by modifying the surface energy balance, referred to as the evaporation effect.

The LST response to LULCC is highly heterogeneous and can be warming or cooling, depending on its location and magnitude associated with the relative magnitude of albedo effect and evaporation effect (Betts, 2000; Davin and de Noblet-Ducoudre, 2010; Arora and Montenegro, 2011; Li et al., 2015). Various methods have been proposed to evaluate the relative contributions of radiation and biophysical properties such as LH, SH, and aerodynamic resistance to the temperature response (Lee et al., 2011; Luyssaert et al., 2014; Chen and Dirmeyer, 2016; Rigden

and Li, 2017). One of the widely used methods is the intrinsic biophysical mechanism (IBM) which attributes changes in LST to changes in net radiation, aerodynamic resistance, and the Bowen ratio (Lee et al., 2011). This approach has been widely used to investigate changes of temperature and the contributing factors (Lee et al., 2011; Peng et al., 2014; Zhao et al., 2014; Bright et al., 2017) and has been further developed to include atmospheric feedbacks (Chen and Dirmeyer, 2016). However, it is reported that the IBM overestimates the contribution of aerodynamic resistance by assuming independence between the aerodynamic resistance and the Bowen ratio (Rigden and Li, 2017). As the Bowen ratio is directly influenced by albedo and aerodynamic resistance, the evaluation of its contributions to temperature changes also includes those from radiation and resistance.

Another decomposition metric decomposes changes in LST to changes in incoming radiation, surface albedo, ground heat, sensible heat, and latent heat fluxes, providing a detailed breakdown of all components in the surface energy budget (Juang et al., 2007; Luyssaert et al., 2014; Xu et al., 2015; Chen and Dirmeyer, 2016; Winckler et al., 2017; Hirsch et al., 2018). However, it does not link changes in turbulent fluxes with changes in biophysical properties such as surface roughness (Rigden and Li, 2017). Moreover, it does not include the effect of atmospheric temperature and moisture conditions on LST. This method is further developed in this study to link latent and sensible heat fluxes to surface conditions (temperature and vapor pressure), atmospheric feedbacks (temperature and vapor pressure), and surface roughness, thus providing a diagnostic framework for evaluating the relative contribution of each variable to LST changes in general circulation model (GCM) simulations.

The climate effect of LULCC on local and regional precipitation has been thoroughly observed and simulated in the past few years. Many studies agree that LULCC causes a decrease

in local precipitation due to local land-atmosphere interactions, such as a decrease in evapotranspiration, soil moisture, and clouds (Xue, 1996; Pitman et al., 2004; Xue et al., 2016; Quesada et al., 2017). Some studies point out that the effects of afforestation-deforestation on monsoon precipitation depend on the relative location of the perturbed area and large-scale circulation (Xue and Shukla, 1996; Boone et al., 2016). Meanwhile, there remains a lack of a comprehensive understanding of how LULCC influences remote and global climate because the LULCC effects on precipitation and temperature outside the LULCC areas are inconsistent among previous model simulations (Pielke et al., 2007; Pitman et al., 2009; Pielke et al., 2011; Swann et al., 2012; Devaraju et al., 2015; Lejeune et al., 2017). Some early GCM simulations report that drastic LULCC in the tropical regions can affect remote regions through atmospheric teleconnections, although their mechanisms need further investigation (Chase and Pielke, 1995; Zhao et al., 2001; Snyder, 2010; Schneck and Mosbrugger, 2011). The Land-Use and Climate, IDentification of robust impacts models (LUCID; Pitman et al. 2009) are atmosphere-only GCMs with fixed sea surface temperatures (SST), which show no remote impact of LULCC. Using the Climate Model Intercomparison Project Phase 5 (CMIP5) model results, recent studies show that LULCC induces warming in low latitudes and cooling in high latitudes (Winckler et al., 2019a; Winckler et al., 2019b). However, there is less agreement about the latitude at which deforestation starts to have a cooling effect.

A few early Atmospheric General Circulation Model (AGCM) studies report that LULCC could change the large-scale circulation by shifting the ITCZ in the North African continent (Xue and Shukla, 1993), displacing the African easterly jet (Li et al., 2007) and changing the strength and position of the Hadley and Walker circulation (Zhao et al. 2001; Snyder 2010). Recent literature shows that the global impact of LULCC by previous modeling studies can be reviewed

and explained from the perspective of global energy budget and energy transport (Swann et al. 2012; Devaraju et al. 2015; Lague and Swann 2016; Devaraju et al. 2018). The results consistently show that continental deforestation/afforestation can exert a significant impact on global-scale circulations, tropical precipitation, and cloud cover through atmospheric teleconnections. This energy transport approach has been widely used in different studies to explore the global impact of large-scale forcings, i.e., aerosol radiative effect (Ming and Ramaswamy 2009; Ming et al. 2011; Haywood et al. 2016) and Arctic sea-ice loss (Chiang and Bitz, 2005; Broccoli et al., 2006; Deser et al., 2016; Tomas et al., 2016; Cvijanovic et al., 2017). It seems reasonable that drastic LULCC may also exert a global impact as one of the most important forcings in the past century (Mahmood et al. 2014). However, current studies of the global impact of LULCC are based on idealized experiment designs: either they convert all forests to grasses (Devaraju et al., 2015) or they replace all C3 grasses/agricultures with deciduous trees (Swann et al., 2012; Lague and Swann, 2016). Moreover, these studies applied slab ocean models, which may overestimate the local thermodynamic impact of air-sea coupling and may even modify the spatial structure of the response compared to the full-depth ocean (Deser et al., 2016). Therefore, a fully coupled ocean model that includes both dynamical and thermodynamic processes is needed for a proper representation of oceanic feedbacks. In this study, the remote impact of LULCC will be identified, and the key processes controlling the remote impact will be analyzed by using a coupled land-atmosphere-ocean GCM. Our study mainly focuses on how LULCC would invoke a global impact on precipitation and large-scale circulation, especially on the ITCZ and Hadley circulation.

In this study, we aim to investigate the global biophysical impacts of LULCC and identify the processes that affect land-atmosphere-ocean interactions. A LULCC map with interannual variations has been developed based on historical and future land use data from Hurtt et al. (2006;

2011). By implementing the yearly-updated vegetation map into a GCM, we provide an assessment of large-scale LULCC on the global climate since 1950. In section 2, we provide a brief introduction to the annually updated LULCC map used in the simulation, a description of the CFSv2 GCM, experiment design, temperature decomposition metric, and the statistical method. The response of global and regional temperature and precipitation, along with the key mechanisms that control those responses are presented in section 3. Discussions and conclusions are given in section 4.

3.2. Model, methodology, and experiment design

3.2.1 Model, LULCC map, and experiment design

In this research, we adopt the second version of the National Centers for Environmental Prediction (NCEP) Climate Forecast System (CFSv2), a fully coupled atmosphere-ocean-land model (Saha et al., 2014). The atmospheric model is NCEP's Global Forecast System (GFS) with the horizontal resolution of the model set at T126, approximately 100-km grid resolution. Sixty-four vertical levels are used, most of which are in the troposphere. The ocean model is from Geophysical Fluid Dynamics Laboratory Modular Ocean Model version 4 (MOM4; Griffies et al., 2003). The NCEP CFS is coupled with the second generation of the Simplified Simple Biosphere Model (SSiB2) as the land surface model (Xue et al., 1991; Zhan et al., 2003; hereafter CFSv2/SSiB2). The CFSv2/SSiB2 has been extensively used to study different aspects of the climate, including the influence of atmosphere-ocean interactions (Lee et al. 2019), aerosol indirect effects (Huang et al., 2019), and the potential role of spring LST anomaly on seasonal prediction (Xue et al., 2018; Diallo et al., 2019). A detailed description of the parameterizations of this version of CFSv2/SSiB2 can be found in Huang et al. (2019).

The SSiB2 is a state-of-the-art vegetation biophysical model that includes climate-vegetation biophysical processes by explicitly considering the exchanges of energy and water between the land and the atmosphere (Xue et al., 1991; Sellers et al., 1996; Zhan et al., 2003). The vegetation map applied in CFSv2/SSiB2 includes 13 types (Fig. S1) as in Xue et al. (2004), and each grid cell has one vegetation type. Each vegetation type includes a set of parameters, including roughness length, LAI, displacement height, greenness, and vegetation fractional coverage with climatological seasonal variations. SSiB2 has been implemented for global and regional climate simulations and highlights the importance of land-atmosphere interaction studies (Kang et al., 2007; Li et al., 2007; Ma et al., 2013a; Ma et al., 2013b; Boone et al., 2016).

The LULCC map is generated based on the Land-Use Harmonization 2 (LUH2) datasets from Hurtt et al. (2006, 2011). The global gridded land-use data LUH2 includes 600 years of annual land-use transition mapping for the period of 1500–2100. It has been widely used as forcing data for global LULCC simulations including the CMIP5/CMIP6 (Findell et al., 2009; Brovkin et al., 2013; Lawrence et al., 2016). In this study, the crop and pasture fractions in LUH2 have been added to obtain an estimate of the total land cover change. The combined crop and pasture fraction changes are defined as the LULCC fraction. Figure 3.1 shows the snapshots of the LULCC fraction relative to 1948 in the years 1950, 1970, 1990, and 2015. Significant land conversions occur after 1970 and continue for several decades, except for over the southern United States and Western Europe where there is a clear decrease in the amount of land converted to crops or pastures (Figure 2.1b-d).

A methodology has been developed to convert the LULCC fraction map to the annually updated vegetation map. Once the LULCC fraction exceeds a threshold value (***a***) or the fraction change compared to 1948 exceeds a threshold value (***b***), the area is degraded annually based on

the default SSiB2 land cover classification map in Fig. S1. The forests are degraded to low vegetations (grassland and shrub), and low vegetations are degraded to bare soil regions. By degrading plant functional types (PFTs), the associated surface parameters (LAI, transmittance, greenness, fractional coverage, vegetation height, displacement height, roughness length, soil parameters) are changed to show the LULCC effects. In this study, we only consider the simplest land degradation from forests to low vegetations and from low vegetations to bare soil and neglect other types of LULCC such as reforestation, irrigation, and urbanization.

The methodology for developing the annually-updated vegetation map is used in Chilukoti and Xue (2020) to assess global impact of LULCC. After comparing with observed temperature and precipitation, Chilukoti and Xue (2020) concluded that LULCC simulations with the annually updated vegetation map had a smaller bias and a better interannual variability compared to control simulations with the potential vegetation map. The method in Chilukoti and Xue (2020) is further developed in this study by applying different criteria ***a*** and ***b*** in different time periods and ten degraded regions in Table 1. For each region, criteria ***a*** and ***b*** are chosen to make the fraction of land degradation grids in the SSiB2 vegetation map comparable to the LULCC fraction in LUH2 (Fig. S2). Intensive LULCC takes place before 1990 because of agricultural activity. There are a few regions (East China, Tibet, India, Mexico, and Australia) in which no further degradation is found after 1980 and some regions even show recovery. However, degradation continues in tropical regions, which may result in significant changes in the tropical climate. Compared with the potential vegetation map, about 20% of global land areas have land degradation in 2015 in the LULCC simulations.

GCM ensemble simulations are conducted to investigate the effect of LULCC on the global climate (Table 2). The sensitivity cases (LULCC) apply the vegetation map that is degraded

annually based on the LUH2 and are compared with the control cases (CTL) using the original SSiB2 vegetation map as in Xue et al. (2004). Both CTL and LULCC include three ensemble members whose initial conditions are obtained from years 8, 9, and 10 from the spin-up simulations. Previous LULCC studies have demonstrated that conducting ensemble simulations can effectively screen the model variability which would otherwise incorrectly hint a global teleconnection (Lorenz et al. 2016). The ensemble simulations start from 1949 and run with atmospheric CO_2 concentrations in 1949-2015 from the World Meteorological Organization (WMO) Global Atmospheric Watch.

Since the CFS reanalysis (CFSR; Saha et al., 2010) starts from the year 1979, spin-up runs are required to ensure a thermodynamically balanced initial condition for the simulations starting in 1949. This study applies the initial conditions from Lee et al. (2019) acquired by applying the 1949 ocean SST, CO_2, and solar constant and driving the CFS for ten years, referred to as spin-up simulations. After running the CFSv2/SSiB2 for several years, it is shown that the atmospheric conditions reach the 1949 conditions and the memory of the initial atmosphere is removed. Lee et al. (2019) have evaluated the multi-decadal simulation from the CTL and concluded that the CTL captures well the precipitation variability and its associated large scale features. A detailed description of the spin-up experiments and its validation against NCEP R1 reanalysis can be found in Lee et al. (2019).

3.2.2 Decomposition metric

We applied the decomposed temperature metric (DTM) developed by Juang et al. (2007) and Luyssaert et al. (2014) to quantify the relative dynamic contribution of albedo, incoming shortwave radiation, incoming longwave radiation, latent heat, sensible heat, and ground heat flux to temperature changes. The energy balance in the DTM can be arranged as follows:

$$\sigma LST^4 = (1 - \alpha_s)SW_{in} + LW_{in} - LH - SH - G, \quad (3.1)$$

where SW_{in} is incoming shortwave radiation, LW_{in} is incoming longwave radiation, LST is the surface temperature, σ is the Stephan–Boltzmann constant, LH is latent heat flux, SH is sensible heat flux, and G is ground heat flux. The changes in the energy fluxes and LST can be acquired by applying the first-order derivative of the left-hand side and right-hand side of Eq. (3.1) as in Luyssaert et al. (2014):

$$\Delta LST = \frac{1}{4\sigma LST^3}[-SW_{in}\Delta\alpha_s + (1 - \alpha_s)\Delta SW_{in} + \Delta LW_{in} - \Delta LH - \Delta SH - \Delta G + \Delta I]. \quad (3.2)$$

Δ indicates the LULCC minus CTL in our experiment. The residual term, ΔI, represents the residual due to the high order derivative, which includes the covariance between attributing variables which could not be quantified in the decomposition metric. As such, the contribution of energy budget changes to LST changes can be evaluated using Eq. (3.2).

The DTM is developed to further relate LH and SH with surface biophysical property and atmospheric condition changes induced by LULCC. Based on the bulk transfer equation (Verhoef et al., 1997), LH and SH over the vegetated surface are related to surface conditions, atmospheric variables, and aerodynamic resistance (Xue et al. 1991) as follows:

$$SH = \rho C_p \frac{LST - T_a}{r_a}, \quad (3.3.1)$$

$$LH = \frac{\rho C_p}{\lambda} \frac{e_s^* - e_a}{r_a + r_c}, \quad (3.3.2)$$

where ρ is the air density, C_p is the specific heat of air at constant pressure, T_a is the air temperature at the reference height, r_a is aerodynamic resistance, λ is the psychrometric constant (66.5 Pa/C), e_s^* is saturated vapor pressure at the surface, e_a is vapor pressure at the reference height, and r_c is bulk stomatal (canopy) resistance. We assume $r_a + r_c$ is the surface resistance for water vapor to distinguish it with aerodynamic resistance for heat (r_a).

The change of SH is decomposed to changes in LST, T_a, and r_a by implicit first-order derivative as in Eq. (3.2):

$$\Delta SH = \frac{\rho C_p}{r_a}\Delta LST - \frac{\rho C_p}{r_a}\Delta T_a - \frac{(T_s - T_a)\rho C_p}{r_a^2}\Delta r_a + \Delta I_1. \quad (3.4.1)$$

The terms on the right side of the equation indicate that the changes of SH is positively related to changes in LST and is negatively related to changes in atmospheric temperature and aerodynamic resistance. The LH response is decomposed in a similar way:

$$\Delta LH = \frac{\rho C_p}{\lambda(r_a + r_c)}\Delta e_s - \frac{\rho C_p}{\lambda(r_a + r_c)}\Delta e_a - \frac{(e_s - e_a)\rho C_p}{\lambda(r_a + r_c)^2}\Delta(r_a + r_c) + \Delta I_2. \quad (3.4.2)$$

It is assumed that the change of LH is positively related to change in surface moisture and is negatively related to changes in atmospheric moisture and resistance. Eqs. 3.4.1 and 3.4.2 will be employed in the analysis to evaluate the contribution of surface temperature/vapor pressure, atmospheric temperature/vapor pressure, and surface resistance to turbulent flux changes.

3.2.3 The energy flux framework

The energy flux framework developed by Kang et al. (2009) has been widely used to understand changes of Hadley circulation and ITCZ caused by atmospheric thermal forcing, such as aerosol radiative effects, Arctic sea-ice cover changes, asymmetric global warming, and idealized deforestation/afforestation, through changes of atmosphere meridional energy transport (Chiang and Bitz, 2005; Ming and Ramaswamy, 2009; Swann et al., 2012; Frierson et al., 2013; Devaraju et al., 2015; Haywood et al., 2016; Lague and Swann, 2016; Cvijanovic et al., 2017). Using this theoretical framework, we analyze changes of Hadley circulation and ITCZ in response to LULCC.

In the long-term average when the heat storage can be neglected, the energy transport across latitude θ, $F_a(\theta)$, can be calculated from the energy budget within the atmosphere (Hartmann 1994):

$$F_a(\theta) = \int_{-\frac{\pi}{2}}^{\theta} 2\pi a^2 cos\theta R_{ATM}\, d\theta, \quad (3.5)$$

where a is the earth radius. The atmospheric energy (R_{ATM}) is the thermal heating within the atmosphere calculated using top-of-atmosphere radiation (R_{TOA}), surface radiation (R_{SFC}), LH, and SH (Eq. S2 in supporting information).

When atmospheric thermal forcing occurs in one hemisphere (i.e., a cooling anomaly in the Northern Hemisphere), the energy imbalance between hemispheres necessitates a cross-equatorial energy transport towards the cooled (Northern) hemisphere. In the tropics, the anomalous energy transport across the equator is realized through anomalous mass transport towards the Northern Hemisphere by the upper branch of the Hadley circulation (Frierson, 2007), which would be accomplished by the southward shift of the rising branch of Hadley circulation and ITCZ (Kang et al. 2009). A detailed description of how the Hadley circulation and ITCZ position are related to the equatorial energy transport can be found in supporting information. Please note, we do not analyze the possible mechanisms that cause seasonal changes in ITCZ and Hadley circulation in this paper. This is because the energy flux framework we use to diagnose the shift of ITCZ is valid on the annual average when the rate of energy change in the atmosphere can be considered as negligible (i.e., $\frac{\partial E_a}{\partial t} = 0.$ in Eq. S1). For a specific season, the rate of energy change is not neglectable, which is beyond the scope of this study.

3.2.4 Statistical Methods

For the three-member ensembles, we calculate the ensemble mean first before the significance tests. Then the statistical significance of differences between LULCC and CTL is evaluated using the Student's t-test (Zwiers and Vonstorch, 1995). To account for the correlation in space, we perform a field significance test by estimating the false discovery rate (FDR; Wilks,

2006). The FDR not only tests field significance but also identifies the local grid points with p values small enough to reject the global null hypothesis (Lorenz et al., 2016).

3.3 Results

3.3.1 Global and regional changes of temperature, precipitation, and Hadley circulation due to large-scale LULCC

In this study, we focus on annual mean results averaged in 1950-2015 over all ensemble members in LULCC and CTL.

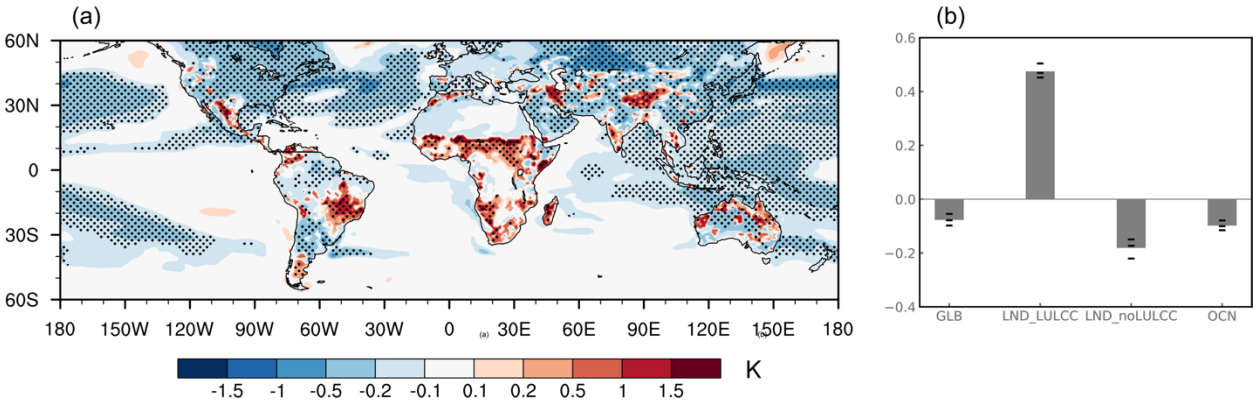

Figure ***3.2*** shows the difference of annual mean surface temperature between LULCC and CTL averaged over 1950-2015. We found a warming by 0.48 K averaged over the LULCC grids and a weak cooling (-0.18 K) averaged over the widespread non-LULCC land areas

(

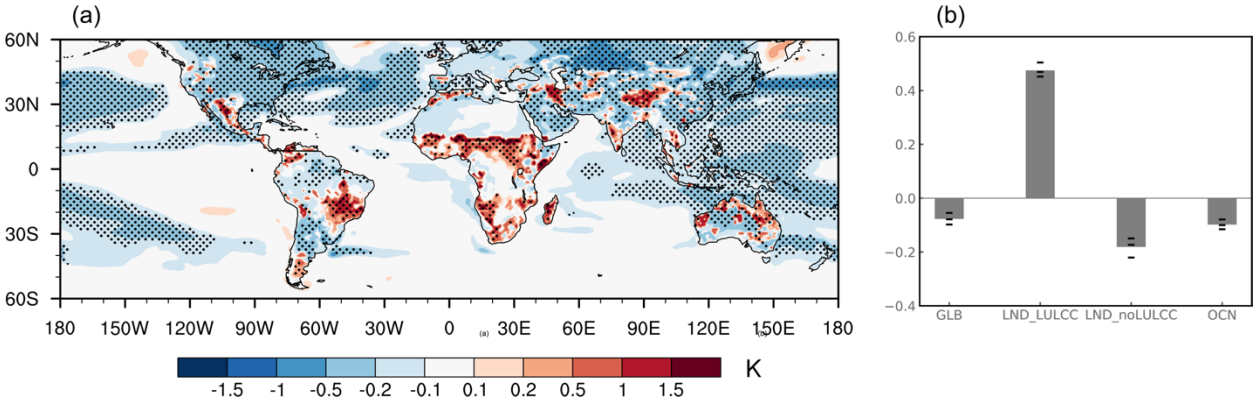

Figure ***3.2***b). Over the globe, a slight cooling is found by -0.08 K. The warming regions are concentrated in low-latitude degraded regions, such as West Africa, Southern Africa, South America (Brazil and south Argentina), and the Tibetan Plateau; while in the mid-latitude regions, such as central Asia, colder LST is found over the regions of land degradation (

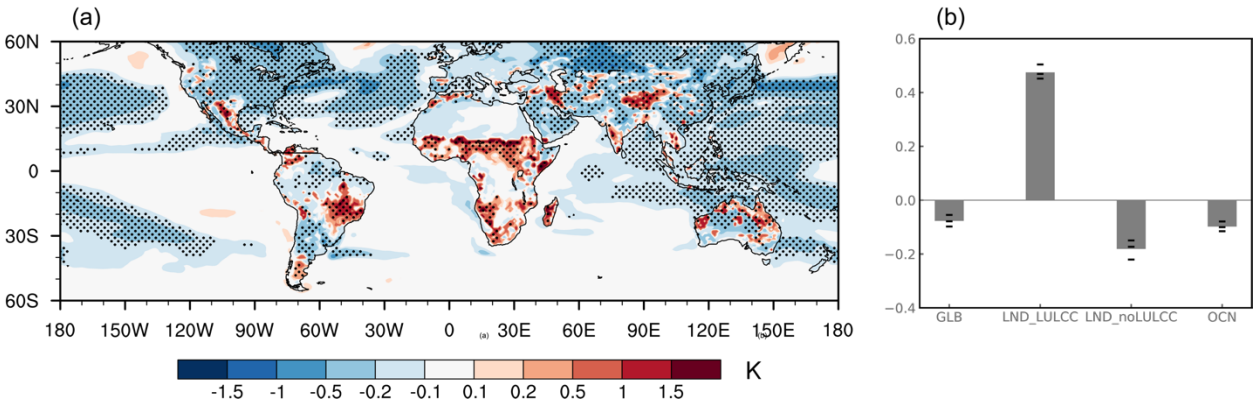

Figure ***3.2***a). Meanwhile, LULCC causes a widespread cooling by an average of 0.1 K over the ocean. The three ensemble members have similar temperature responses to LULCC in all regions in

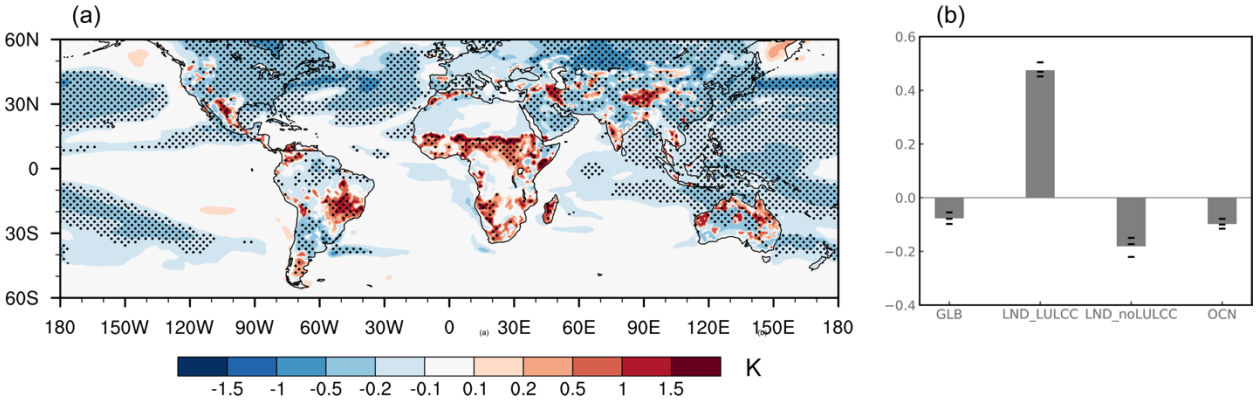

Figure ***3.2***b. As shown in previous studies, the response of LST is heterogeneous over different land regions and is influenced by the competing albedo (cooling) effect and evaporation (warming) effect (Chen and Dirmeyer 2016). In section 3.2, we will apply the decomposition method described in section 2.3 to quantify the contribution of each surface variable to temperature

changes and discuss the opposing LST responses in lower and mid latitudes and the cooling in the non-degraded regions.

For seasonal response, LULCC has caused temperature increases by 1.5 K in local warm seasons and by less than 0.5 K in local cold seasons (Fig. S3) at the low-latitude degraded regions (West Africa, Southern Africa, South America, and tropical Australia). In mid-latitude Central Asia, the surface temperature is cooled by about 1.5 K in winter and spring and warmed by 1 K in summer. Similar to the annual results, a widespread cooling is found in non-LULCC land regions and widespread ocean areas. Compared to the temperature change in LULCC regions, the temperature responses over non-LULCC regions are relatively small but consistent throughout the year.

LULCC also has substantial effects on precipitation. As shown in Figure 3.3a, annual precipitation reduction is found over degraded areas, including Northwest/Southern Africa, South America, East and South Asia, and Southern North America, as well as over the adjacent ocean regions. The precipitation response over the degraded region is strongest during the local monsoon seasons: the change peaks in DJF in Southern Hemisphere while it peaks in JJA in Northern Hemisphere (Fig. S4). Around the West tropical Pacific, a tripole anomaly pattern can be identified: precipitation increases along the equator along with significant decreases occurring to the south and the north of the equatorial region. The ITCZ boundary narrows by about 0.5 degrees following the definition in Byrne and Schneider (2016) (supporting information section 3). Moreover, the rising branch of the Hadley circulation is displaced southwards compared to its climatology location (Figure 3.3b), relocating the centroid of the convergence zone southward. In DJF and MAM (Figs. S4a and S4b), the contraction of the ITCZ is also shown in the tropical Pacific: the precipitations increase along the equator but decrease in the southern and northern boundaries of

ITCZ. The signal is weak in JJA and SON. The changes of ITCZ and large-scale circulation on annual scale will be analyzed in section 3.3 from the perspective of energy budget and meridional energy transport within the climate system.

3.3.2 LST response and its contribution from radiation and turbulent fluxes

Figure 3.4 shows the differences of LST between LULCC and CTL and decomposed LST change as a function of radiation, turbulent fluxes, and heat storage as introduced in Eq. (3.2). LULCC results in an increase in surface albedo because of the higher reflectivity of bare soil and low vegetation compared with tall vegetation. The changes in albedo contribute to a decrease of LST restricted to LULCC regions (Figure 3.4b). The widespread increase in SW_{in} tends to warm the surface (Figure 3.4c) and the extensive decrease in LW_{in} has a cooling effect on the surface (Figure 3.4d). The changes in SW_{in} and LW_{in} are related to climate feedback and will be explained later. Overall, both LH and SH decrease after land cover changes, indicating a general warming effect on the land surface (Figure 3.4e, f). Ground heat flux change plays a minor role in LULCC-induced LST change (Figure 3.4g). The minor differences between LULCC-induced LST change (Figure 3.4a) and the summed LST changes from each contributor (Figure 3.4h) show that the DTM can reasonably delineate the contribution of each process. The high order terms are larger over the semi-arid regions such as central Asia, Inland China, and the Sahel (Figure 3.4i).

The changes in SW_{in} and LW_{in} are related to atmospheric moisture/temperature conditions (Figure 3.5) and cloud feedback (Fig. S5). LULCC causes less evaporation to the PBL (Xue et al. 1997). The deficit in low-level specific humidity can extend to about 500 hPa and spread outside the LULCC regions (Figure 3.5a). The decrease in water vapor (Fig. S5a) is expected to reduce the latent heat release during convective processes and cool the tropospheric temperature, consistent with previous studies showing a reduction of convective heating due to LULCC (Ma et

al. 2013a, 2013b; Song 2013). The cooling signal is amplified with increasing elevation, with the maximum cooling anomalies occurring around 300 hPa (Figure 3.5b), which may be due to the larger moist adiabatic lapse rate in a drier atmosphere. The decrease in tropospheric temperature, in turn, is expected to emit less downward longwave radiation and reduce the longwave heating received by the surface (Figure 3.4d). Also, the reduction in latent heat release implies anomalous subsidence that results in decreased cloud cover in most LULCC regions (Fig. S5b). Therefore, the surface receives more solar radiation, which tends to increase the LST as shown in Figure 3.4c.

The DTM metric is applied in both degraded regions (Figure 3.6a) and non-degraded regions (Figure 3.6b) to quantify the contribution of each component to LST changes. The degraded area is further divided into lower latitudes (40°S-40°N) and mid latitudes (40°N-60°N; 40°S-60°S), as LST responds differently in these two areas. At lower latitudes, LULCC causes an increase in LST by 0.67 K; while at the mid latitudes a decrease in LST by 0.23 K is found (Figure 3.6a). The opposite LST responses between lower and middle latitudes are also reported in observational LULCC studies (Zhang et al., 2014; Li et al., 2015; Alkama and Cescatti, 2016; Bright et al., 2017; Duveiller et al., 2018). As shown in Figure 3.6a, the LST response is mainly determined by the relative magnitude between the albedo effect (ABD) and the evaporation effect (LH), among which LH contribution has the largest discrepancy at lower and mid latitudes. The difference in LH contribution to LST changes between low latitudes and mid latitudes can be as large as 0.58 K, the reason for which will be discussed later.

The application of DTM to LST decrease in non-degraded regions is shown in Figure 3.6b. The surface cooling (-0.18 K) is dominated by the reduction in LW_{in}, which is partly counterbalanced by the increased SW_{in}. As discussed before, land degradation reduces surface evapotranspiration and therefore atmospheric water vapor (Figure 3.5a), leading to cooler

tropospheric temperature and a reduction in cloud cover (Figure 3.5, Figure S5b). As a result, negative ΔLW_{in} and positive ΔSW_{in} are found over the non-LULCC regions.

We further investigate the response of SH and LH and link them to the changes in biophysical properties due to LULCC. The SH changes can be decomposed to three major components: surface temperature (ΔLST), atmospheric temperature (ΔT_a), and aerodynamic resistance (Δr_a). The contribution of surface and atmospheric temperature changes is generally spread over the globe (Figure 3.7b, c). As the sum of these two contributions produces a positive contribution to SH changes, an increase in the temperature gradient between surface and atmosphere is found, which tends to increase SH. The aerodynamic resistance increase due to lower surface roughness length and displacement height plays a dominant role in SH change and results in an overall SH decrease in degraded areas. The calculated SH changes from the decomposition components (Figure 3.7e) reproduce the simulated SH changes (Figure 3.7a) and the high order terms account for less than 5% in most LULCC regions (Figure 3.7f)

The decrease in LH is influenced by changes in LAI, soil moisture, aerodynamic resistance, and low-level moisture conditions (Nair et al. 2011; Wang et al. 2017). The change of LH is attributed to changes in surface vapor pressure (e_s), atmospheric vapor pressure (e_a), and surface resistance ($r_a + r_c$) as shown in Figure 3.8. The changes in surface vapor pressure caused by LULCC slightly increase LH in the tropical degraded region and decrease LH in other areas (Figure 3.8b). Meanwhile, atmospheric water vapor decreases globally ($\Delta e_a<0$), which contributes to an increase of LH ($-\frac{\rho C_p}{\lambda(r_a+r_c)}\Delta e_a > 0$; Figure 3.8c). The vapor pressure gradient between surface and atmosphere is thus enhanced and causes an overall increase in LH. In contrast, the increase in surface resistance contributes to significant LH decrease over degraded regions (Figure 3.8d). Since this process is dominant, LH decrease is found as a result of land degradation. The

surface resistance ($r_a + r_c$) for LH is closely related to soil moisture (Fig. S6) which controls the stomatal resistance. The changes in soil moisture are consistent with those in precipitation (Figure 3.3a). As in the SH analyses, the high order terms are very small for LH decomposition (Figure 3.8f).

The decomposition metric is applied to identify the important surface property that leads to different LH responses at lower and mid latitudes (Figure 3.6a). As shown in Figure 3.9, the change of LH is much larger at lower latitudes (-9.84 W m^{-2}) than at mid latitudes (-5.54 W m^{-2}). Our decomposition metric shows that the contribution from surface resistance to LH change is significantly different at lower latitudes (-14.78 W m^{-2}) and mid latitudes (-6.44 W m^{-2}). Surface resistance plays a dominant role in changing LH in the LULCC experiment, and the contributions from the surface and atmospheric vapor pressure are relatively small. It should be noted that the ensemble members have a similar result in the contribution of surface vapor pressure, atmosphere vapor pressure, and surface resistance to LH changes.

3.3.3 The effect of LULCC on precipitation and large-scale circulation from the perspective of meridional energy transport

LULCC causes changes in radiation, turbulent fluxes, moisture, and temperature in the PBL and also indirectly influences cloud cover, convection, and precipitation. Figure 3.10a and Figure 3.10b show the zonal-mean difference of precipitation, evapotranspiration, and moisture flux convergence (MFC) over land and ocean between LULCC and CTL in 1950-2015. The zonal-mean land precipitation changes are mostly consistent with evapotranspiration changes (Figure 3.10a), indicating that the local effect in the degraded areas is dominant. When LULCC occurs, land covers with more vegetation and larger LAI are degraded to those with less vegetation and smaller LAI, and therefore the moisture supply for precipitation from evapotranspiration is

decreased. As a result, precipitation is suppressed (Figure 3.3a) and cloud cover is decreased mainly in the degraded areas (Fig. S5b). Over the Pacific Ocean in the northern mid latitudes (Figure 3.10b), the precipitation change is affected by both evaporation and MFC changes. Ocean precipitation change around 40°N is associated with evaporation decrease in keeping with a cooling SST

(

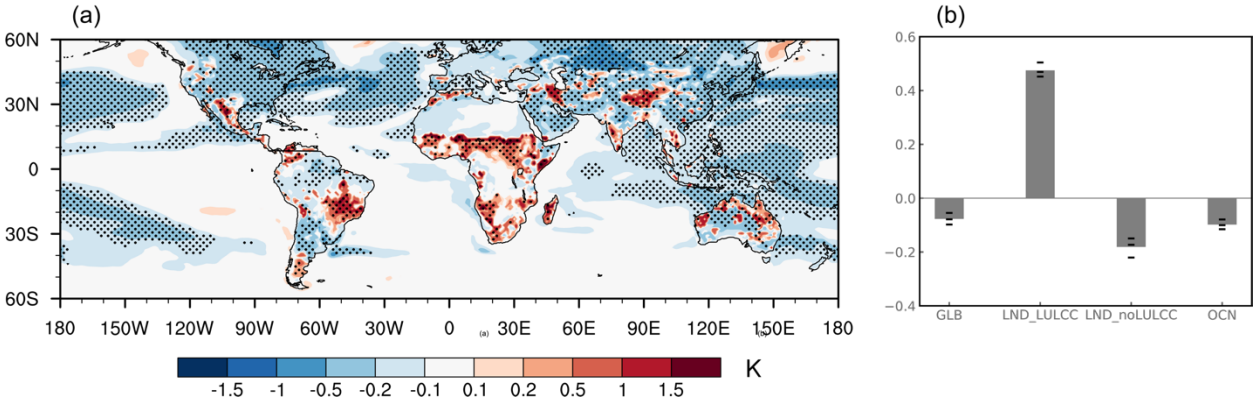

Figure ***3.2***a). In contrast, precipitation changes over the tropical oceans are mostly consistent with the MFC changes (Figure 3.10b). LULCC causes an increase in precipitation south of the equator but decreases at the southern and northern boundaries of the ITCZ (Figure 3.3, 3.10b), which is associated with anomalous moisture flux convergence around the equator and divergence on both sides (Figure 3.10c). The precipitation changes over tropical ocean indicate that the continental LULCC has a remote effect on tropical climate, mainly through changes in atmospheric moisture transport.

We investigate the LULCC impact on tropical precipitation using the energy flux framework in section 2.3. The atmosphere energy balance and energy transport in CTL is shown in Figure 3.11. The atmosphere has an energy surplus between about 35° N/S ($R_{ATM} > 0$ in Figure 3.11a), which is transported out of the tropics through energy flux divergence (positive slope in Figure 3.11b). Meanwhile, the atmospheric thermal cooling poleward of 35°N/S ($R_{ATM} < 0$ in

Figure 3.11a) necessitates a meridional energy flux convergence (negative slope in Figure 3.11b). The negative F_a (southward energy transport) at the equator in CTL indicates asymmetric atmospheric heating with respect to the two hemispheres in the climatology, associated with the shape of continents and atmosphere-ocean interactions (Xie, 2004).

The occurrence of LULCC results in intensive cooling anomalies, as indicated by the negative R_{ATM} difference in four latitude bands (Figure 3.11a). Three of the cooling bands are located in the Northern Hemisphere, with one in the tropical region and the others in the extra-tropics. One intensive LULCC region is located in the Southern Hemisphere tropical region. There is also an atmospheric energy surplus in regions without LULCC (Figure 3.11a), which is induced by climate feedbacks. The LULCC-induced R_{ATM} change is further attributed to changes in R_{TOA}, R_{SFC}, LH, and SH, as shown in Fig. 11c. The anomalous R_{TOA} and R_{SFC} offset each other, indicating that reflected shortwave radiation from the surface travels through the atmosphere with little absorption and produces a rather small radiative effect on the atmosphere. In contrast, the anomalous latent heat flux from the surface to the atmosphere is consistent with the change of atmospheric energy (ΔR_{ATM}) at almost all latitudes, and the sensible heat flux plays a similar, albeit secondary, role. Our results emphasize the importance of non-radiative cooling of the atmosphere by latent and sensible heat fluxes in the PBL for the atmospheric energy balance, which is confirmed by the evaporation effect of LULCC (Figs. 4e and 4f).

Due to the non-radiative cooling in LULCC bands, an anomalous energy flux convergence is found at the LULCC latitudes (Figure 3.11b), indicated by the negative slope of atmospheric energy flux. In regions without LULCC, the anomalous energy surplus (Figure 3.11a) induced by climate feedbacks corresponds to an energy flux divergence (Figure 3.11b). As the stronger atmospheric cooling occurs in the Northern Hemisphere, an anomalous northward energy transport

of 0.05 petawatts (PW) takes place across the equator (Figure 3.11b). According to the energy flux framework, the anomalous northward energy transport at the equator has been accomplished by the anomalous northward mass transport by the upper branch of Hadley circulation, necessitating a southward displacement of the rising branch of Hadley circulation (Figure 3.3b). The southward shift of the rising branch of Hadley circulation relocates the precipitation centroid of the ITCZ southward, and the intensified equatorial updraft causes an increase in moisture flux convergence around the equator, producing more precipitation there (Figure 3.3a, 3.10b).

A stronger descent is also found at the southern/northern boundaries of the Hadley circulation (Figure 3.3b), which gives rise to the narrowing of the ITCZ as shown in Figure 3.3a. The equatorward contraction is associated with the shift of the subtropical jets towards the equator as compared to the CTL (Figure 3.12). Previous studies have suggested that the increase in upper-tropospheric temperature gradient associated with tropospheric warming under greenhouse increases can lead to a stronger jet that moves poleward (e.g., Chen and Held, 2007; Chen et al., 2008), whereas the opposite is found for tropospheric cooling in response to more anthropogenic aerosols at the Northern Hemisphere mid latitudes (Ming and Ramaswamy, 2009; Ming et al., 2011). The change of subtropical jet can be viewed from the perspective of the thermal wind equation:

$$U = -\frac{R}{f}\ln\left(\frac{p_0}{p_1}\right)\left(\frac{\partial T}{\partial y}\right)_p, \tag{3.6}$$

where $\left(\frac{\partial T}{\partial y}\right)_p$ is the meridional temperature gradient in the layer between pressure levels p_0 and p_1, R is the gas constant for dry air, and f is the Coriolis force. In the LULCC experiment, the tropospheric cooling strengthens the meridional temperature gradient on the equatorward side of the jet while weakening it on the poleward side (Figure 3.5b). According to the thermal wind relationship (Eq. 3.6), the westerly jets are enhanced on the equatorward side and weakened on the

polar side in both hemispheres, which, in turn, causes an equatorial contraction of the Hadley circulation due to the interaction between the subtropical jet and the descending branch of the Hadley cell. It narrows the Hadley circulation, and the resulting anomalous moisture flux divergence (Figure 3.10c) causes a decrease in precipitation at the southern/northern boundary of the ITCZ (Figure 3.3a).

3.4 Discussion

3.4.1 LST response in observational studies

Our simulations show that LULCC can cause surface warming in low latitudes and cooling in high latitudes due to the competing effect between increased albedo and reduced evaporation. Observational studies provide independent information on the effects of deforestation on LST using satellite-retrieved products (Li et al. 2015; Alkama and Cescatti 2016; Duveiller et al. 2018), semiempirical-derived LST based on the FLUXNET observations (Bright et al. 2017). By comparing the LST differences between forests and grasses, observational studies confirm our conclusion that LULCC has caused a warming in lower latitudes and a cooling in boreal regions, although the latitudes with cooling vary among datasets (Li et al. 2015; Alkama and Cescatti 2016; Bright et al. 2017; Duveiller et al. 2018). However, since these observational-based LULCC studies exclude the nonlocal LULCC effects in their methodologies and do not consider the conversions from grass/shrub to bare ground that are included in our study, we are unable to make a quantitative comparison between simulated and observation-derived LST changes.

3.4.2 The regional and global effects of LULCC

In this study, we investigate both regional/local and global/nonlocal effects of LULCC during 1950-2015 using a coupled land-atmosphere-ocean earth system model. Over the degraded regions, the ensemble GCM simulations show that LULCC has caused a warming effect by 0.67

K in lower latitudes and a cooling effect by 0.23 K in mid-to-high latitudes. The DTM analysis shows that the temperature response is dominated by changes in the latent heat and sensible heat fluxes in the tropical regions and by albedo changes in mid-latitudes. We further conclude that the response of latent heat and sensible heat fluxes are dominated by surface roughness changes in a further developed DTM analysis. The precipitation is reduced due to the decrease in moisture supply from evapotranspiration associated with smaller LAI and vegetation fraction.

In the non-LULCC regions and oceans, we find a widespread cooling in surface temperature with a small seasonal variability throughout the year. Recent GCM studies on LULCC effects (Winckler et al., 2017; Devaraju et al., 2018; Winckler et al., 2019a; Winckler et al., 2019b) also reported that nonlocal effects dominated the global mean temperature change or temperature change in a few regions. Using the developed DTM analysis, we are able to attribute the temperature decrease in the non-LULCC regions to the reduction in surface longwave heating corresponding to the drier and cooler troposphere after LULCC.

A significant shrinking of ITCZ is simulated over tropical ocean associated with LULCC-induced tropospheric cooling and the resultant weakening and equatorward shift of the westerly jets. Meanwhile, a stronger non-radiative cooling in the Northern Hemisphere is caused by LULCC, which has been balanced by anomalous northward energy transport across the equator through the southward shift of Hadley cell. The responses of ITCZ have also been reported in a number of LULCC studies, which investigate the climate effects of idealized afforestation/deforestation in the Northern Hemisphere with slab ocean models (Swann et al. 2012; Devaraju et al. 2015; Lague and Swann 2016). However, slab ocean models were found to be insufficient to simulate the global/nonlocal impact with projected thermal forcing (Deser et al., 2016; Tomas et al., 2016), as they overestimate the local thermodynamic impact of air-sea coupling and modify the spatial

structure of the response compared to the fully coupled ocean model. Our study complements the previous LULCC studies by implementing annually-updated LULCC processes in both hemispheres and by using a fully coupled ocean model, in which the oceans are dynamically and thermodynamically coupled to the atmosphere.

3.4.3 Uncertainties in LULCC simulation

Previous studies (Lejeune et al. 2017; Pitman et al. 2009) have shown that simulated temperature and precipitation responses to LULCC have large discrepancies among GCMs. The uncertainties lie in several modeling aspects, such as different land surface schemes (Koster et al., 2006), different LULCC implementations (Boone et al., 2016), and also whether prescribed SSTs with interannual and seasonal variations, slab ocean models or coupled ocean models were employed (Pitman et al. 2009; Pielke et al. 2011). Pielke et al. (2011) pointed out that the coupling strength between land and atmosphere could be one of the reasons that cause large differences in LULCC simulations. Koster et al. (2006) compared the land-atmosphere coupling strength using twelve GCMs with various land schemes. Our model (NCEP GFS/SSiB2) has a medium coupling strength, close to the ensemble mean, indicating that the land surface influence on the atmosphere in SSiB2 is within the range of current land surface models.

The uncertainties in simulated LULCC effects in this study come from several aspects. First, we apply the most simple LULCC implementation by changing dominant vegetation type in one grid box in the LULCC map. Further implementation of vegetation tiling to improve the characterization of landscape complexity is needed. In addition, our simulations mainly consider deforestation and desertification while neglecting other types of LULCC such as irrigation, harvest, grazing, and urbanization. Furthermore, many countries adopted better land use management policies since the 21st century, such as reforestation and afforestation (Hua et al., 2016) to mitigate

climate changes, which have not been considered in our LULCC map. Although we have applied local and field significance tests, our conclusions are made based on a single model result. More analysis on LULCC effects, especially the nonlocal effects, should be carried out in the climate modeling community using land-atmosphere-ocean coupled models.

3.5 Conclusions

In this study, we investigated the global and regional effects of the LULCC in 1950-2015 on climate by conducting an ensemble of numerical simulations using the CFSv2/SSiB2. We incorporate the estimated land conversions by applying the LUH2 global land use reconstructions from Hurtt et al. (2006; 2011). The vegetation fraction in the designed LULCC areas is degraded annually to a lower fraction, and by 2015, about 20% of global land areas have land degradation compared with CTL simulation. The GCM ensemble simulations show that LULCC results in a warming effect at lower latitudes and a cooling effect at mid latitudes in degraded regions. Meanwhile, the LST decreases in non-LULCC regions due to reduced longwave heating of the surface by a drier and cooled troposphere. Extensive LULCC activities in 1950-2015 are found to reduce the regional rainfall over LULCC regions and adjacent oceans. LULCC also narrows the ITCZ by about 0.5 degrees and displaces it southward, forming a tripole precipitation anomaly around the warm pool. All ensemble members show a very similar magnitude of change, and both local and field significant tests are carried out to examine the statistical significance of the response.

The mechanism that causes a heterogeneous LST response in different latitudes is examined. The DTM analyses indicate that the temperature response is determined by the relative importance of increased albedo (cooling) and reduced evaporation (warming), and the magnitude of evaporation contribution decreases with latitude. We further decompose LH changes to those in surface vapor pressure, atmospheric vapor pressure, and surface resistance, and the results

identify the dominant role of surface resistance in LH changes. The contribution of surface resistance to LH changes is significantly larger in the lower latitudes than in higher latitudes.

The reduction in local precipitation after LULCC results from the decrease in moisture supply from evapotranspiration associated with smaller LAI and vegetation fraction. The reduced non-radiative heating (SH and LH) from the surface to the atmosphere after LULCC leads to an asymmetric atmospheric cooling and results in a northward heat transport across the equator, accomplished by a southward shift of the rising branch of Hadley cell. The narrowing of the ITCZ is consistent with the equatorward contraction of the Hadley circulation, which is expected from the tropospheric cooling and the resultant weakening and equatorward shift of the westerly jet.

This study has also demonstrated that to appropriately assess the local and remote responses to LULCC, it is critical to use multiple methodologies. By using the DTM metric, we conclude that evaporation effects and albedo effects are the lead factors that dominate the local LULCC effects on surface temperature in the low latitudes and mid latitudes, respectively. While the energy flux framework, which shows that LULCC has caused changes in atmospheric non-radiative heating due to the decrease of LH and SH from the surface, has been introduced to analyze the LULCC's remote effects on the ITCZ and Hadley circulation.

Tables and Figures

Table 3.1 The latitude and longitude of ten degraded regions used in the LULCC experiment

Region	lat_S	lat_N	lon_W	lon_E
South America	-56	12	-85	-32
Mexico	10	33	-120	-85
North America	30	55	-130	-107
Africa	-36	38	-18	60
Australia	-10	-45	112	155
East China	20	45	105	135
India	5	28	60	96
Central Asia	36	65	-18	155
Tibet	28	36	60	105
Southeast Asia	-10	20	95	155

Table 3.2 Experiment design

Case	Initial condition	LULCC map	Integration period
CTL_10th LULCC_10th	Jan. 1st 1949 based on 10 years of spin-up	Potential VEG map With annually updated LULCC conditions	1949-2015
CTL_9th LULCC_9th	Jan. 1st 1949 based on 9 years of spin-up	Potential VEG map With annually updated VEG LULCC conditions	1949-2015
CTL_8th LULCC_8th	Jan. 1st 1949 based on 8 years of spin-up	Potential VEG map With annually updated LULCC conditions	1949-2015

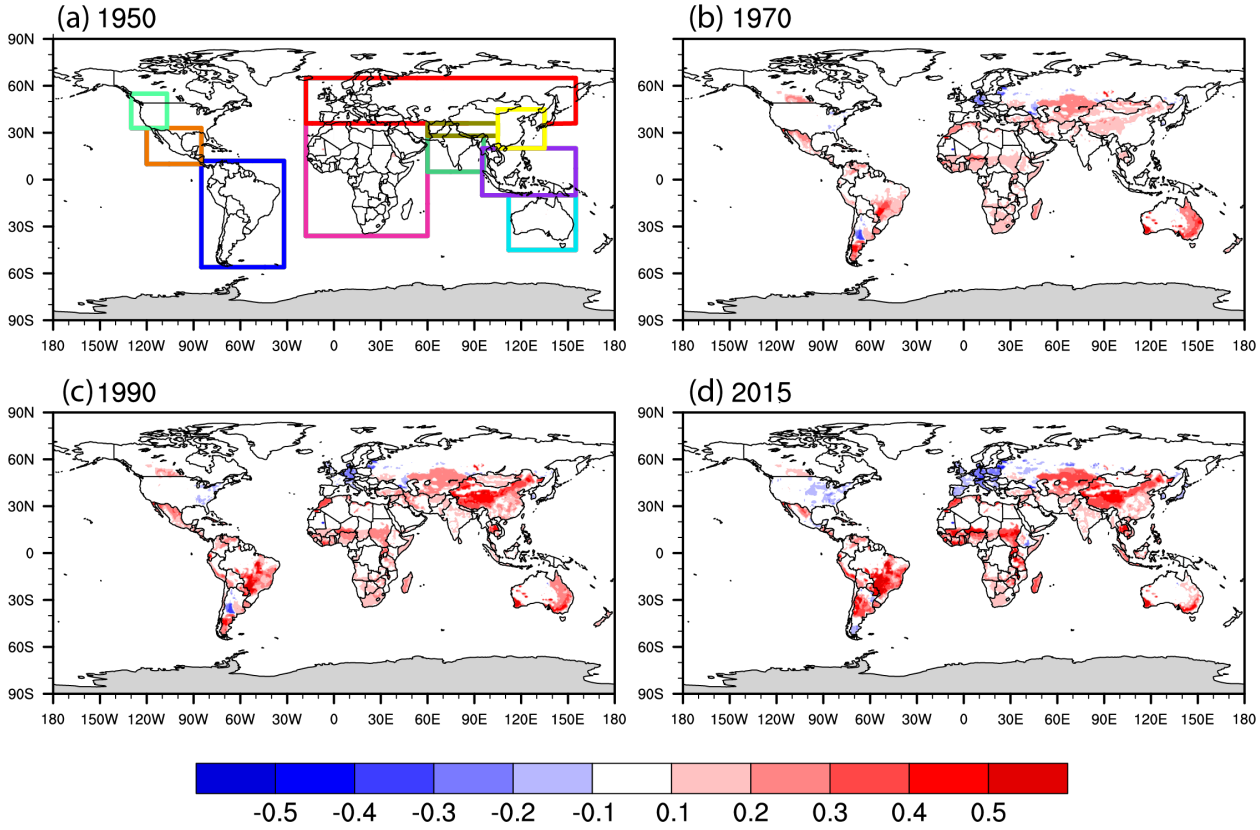

Figure 3.1 LULCC fraction difference between (a) 1950 and 1948 (The boxes show ten degraded regions, whose coordinates and name are summarized in Table 1), (b) 1970 and 1948, (c) 1990 and 1948, and (d) 2015 and 1948. The red color indicates an increase in anthropogenic land use while the blue color indicates a decrease in anthropogenic land use compared to 1948.

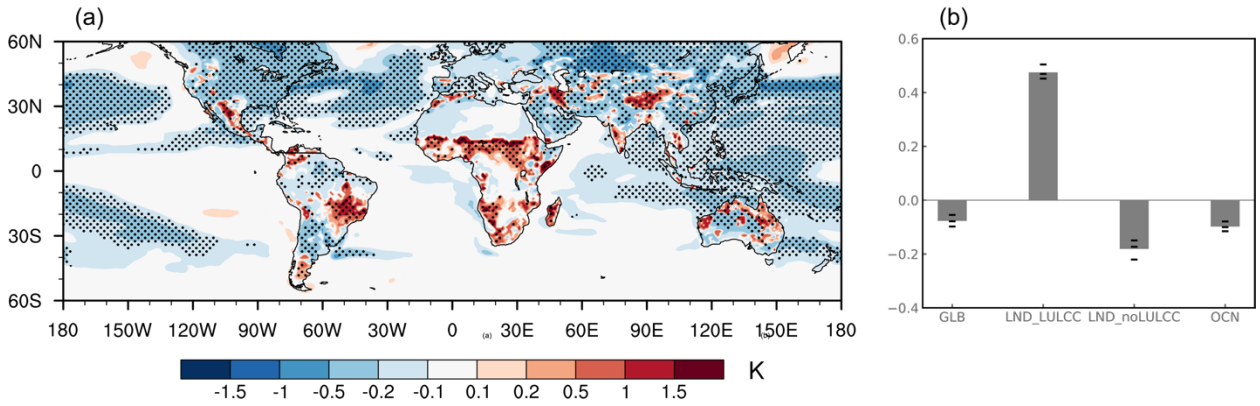

Figure 3.2 (a) Annual surface temperature difference (K) due to LULCC effects during 1950-2015 (LULCC – CTL). Stippling indicates that the response is statistically significant at the 95% confidence level. (b) Temperature difference (K) over the globe (GLB), land areas with LULCC (LND_LULCC), land areas without LULCC (LND_noLULCC), and ocean (OCN) in 60 °S-60 °N. The black lines indicate the response in three ensemble members.

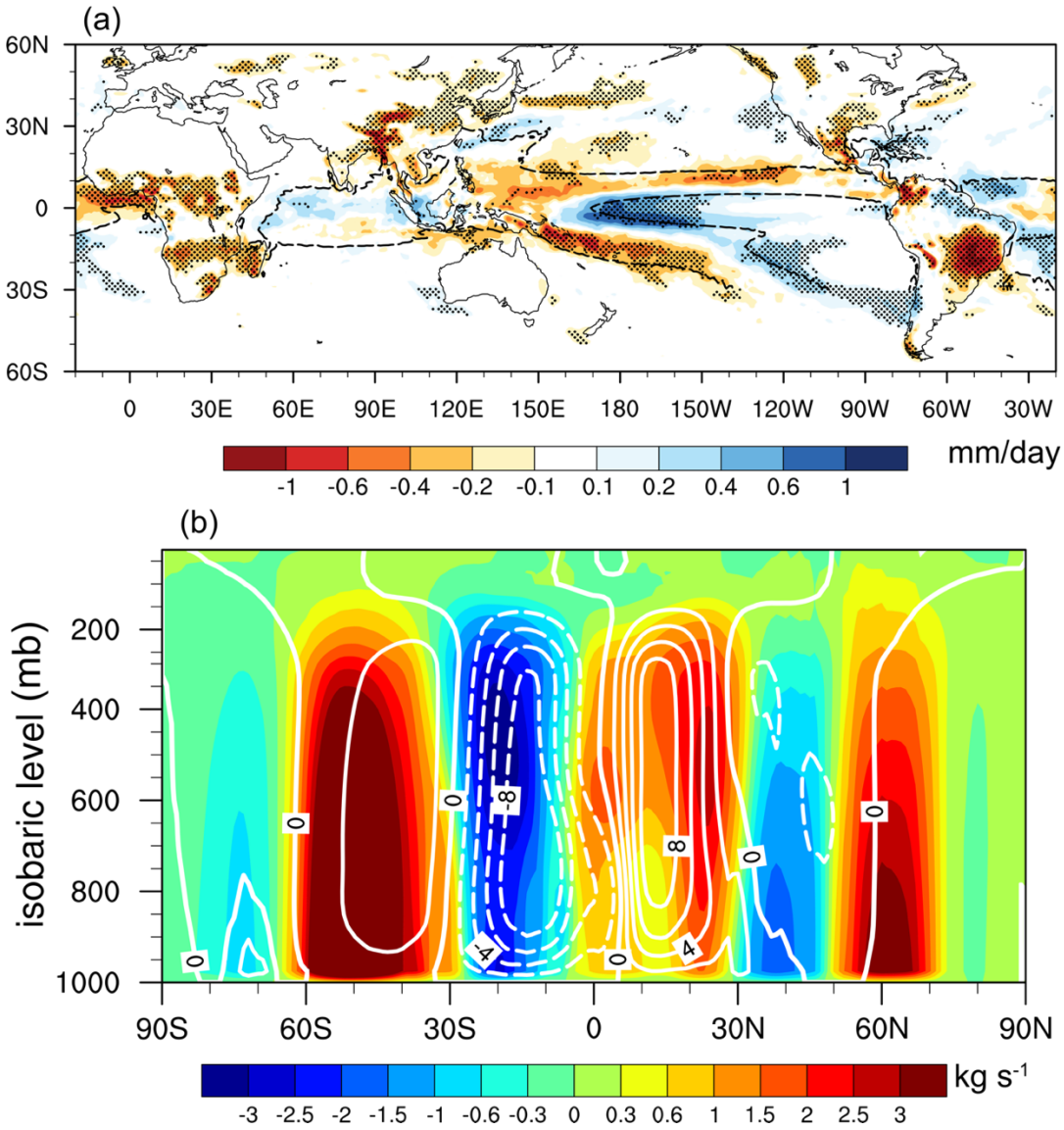

Figure 3.3 (a) Annual difference of precipitation (mm day^{-1}) due to LULCC during 1950-2015 (LULCC – CTL; Black line: zero contour of the 700-hPa annual-mean vertical velocity during 1950–2015 over oceans). Stippling indicates statistical significance at the 90% confidence level. (b) Annual difference of zonal-mean stream function (kg s^{-1}) between LULCC and CTL during 1950-2015. Changes of stream function in color shadings and the climatological value in CTL in white contours.

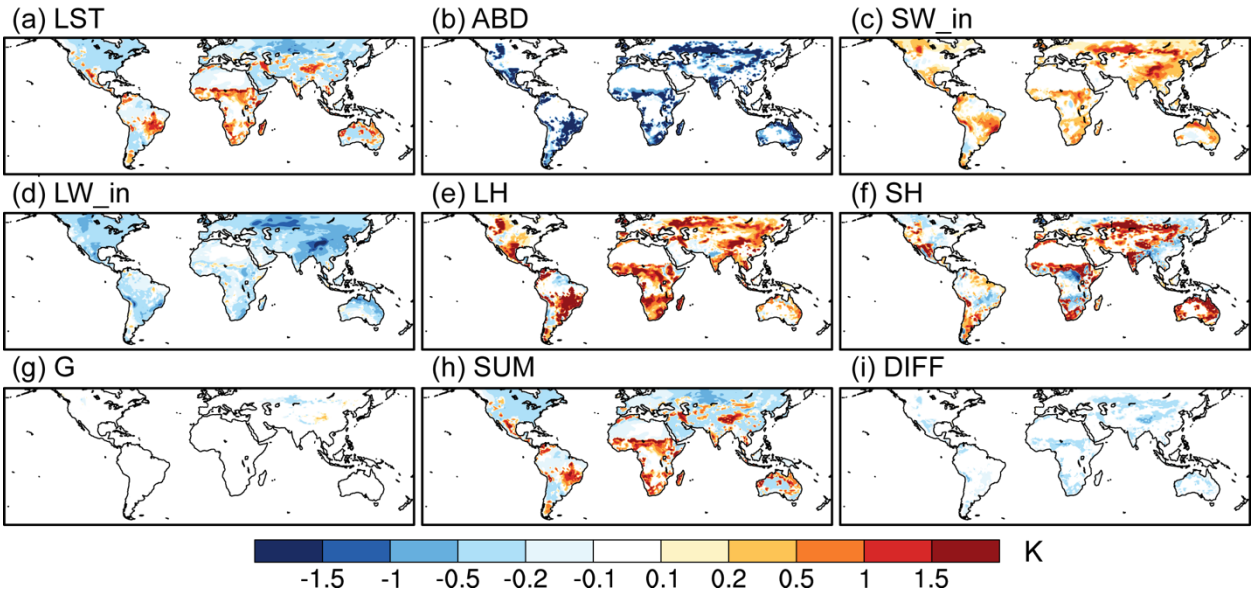

Figure 3.4 Decomposition of annual LST change (K) due to LULCC effects during 1950-2015 (LULCC-CTL). (a) Difference in LST between LULCC and CTL. (b) - (g) decomposed LST changes due to changes in surface albedo (ABD: $\frac{-SW_{in}\Delta\alpha_s}{4\sigma LST^3}$ in Eq. 2), incoming shortwave radiation (SW_in: $\frac{(1-\alpha_s)\Delta SW_{in}}{4\sigma LST^3}$), incoming longwave radiation (LW_in: $\frac{\Delta LW_{in}}{4\sigma LST^3}$), latent heat flux (LH: $\frac{-\Delta LH}{4\sigma LST^3}$), sensible heat flux (SH: $\frac{-\Delta SH}{4\sigma LST^3}$), and ground heat flux (G: $\frac{-\Delta G}{4\sigma LST^3}$), respectively. (h) Sum of surface temperature contribution from (b) – (g). (i) The difference between (a) and (h)

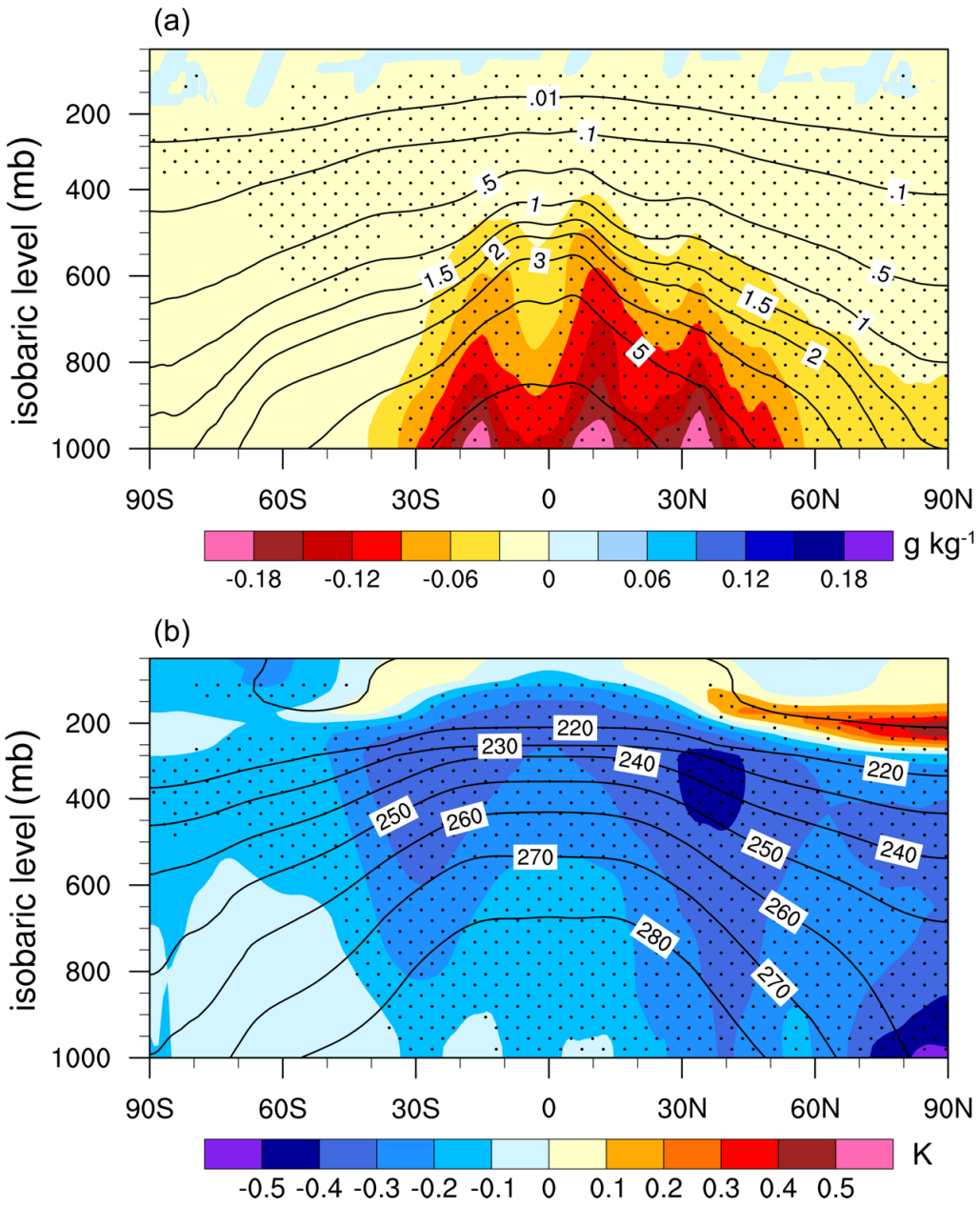

Figure 3.5 Differences of annual (a) specific humidity (g kg^{-1}) and (b) temperature (K) between LULCC and CTL during 1950-2015 (LULCC-CTL). The contours represent the climatological mean from CTL and the shaded colors represent LULCC-CTL. Stippling indicates that the response is statistically significant at the 95% confidence level.

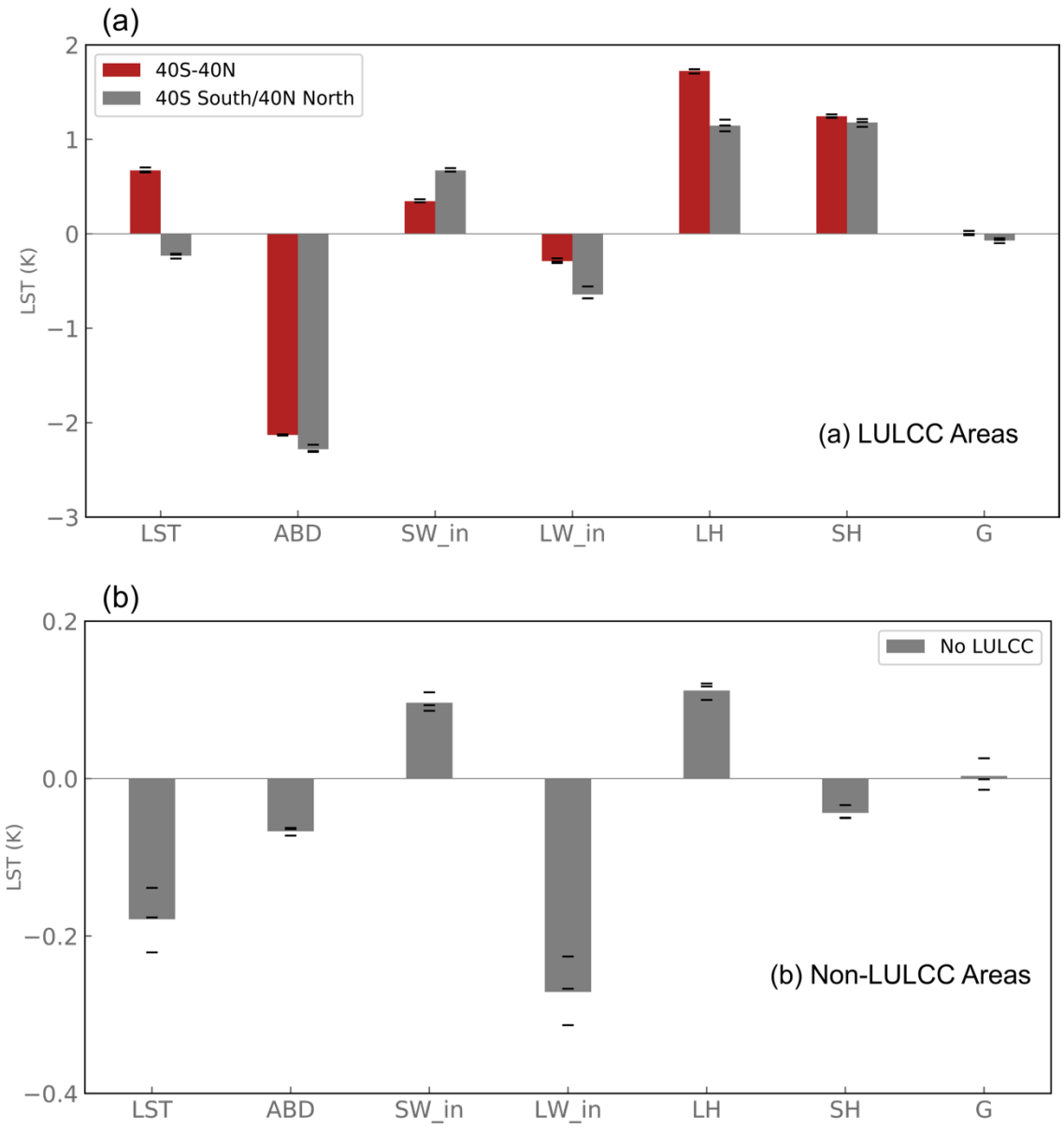

Figure 3.6 Annual LST changes (K) due to LULCC and its contribution from albedo (ABD), incoming shortwave (SW_in), incoming longwave radiation (LW_in), latent heat (LH), sensible heat (SH), and ground heat (G) in (a) LULCC regions in low and mid latitudes and (b) non-LULCC regions during the 1950-2015 period. The black lines indicate the response in three ensemble members.

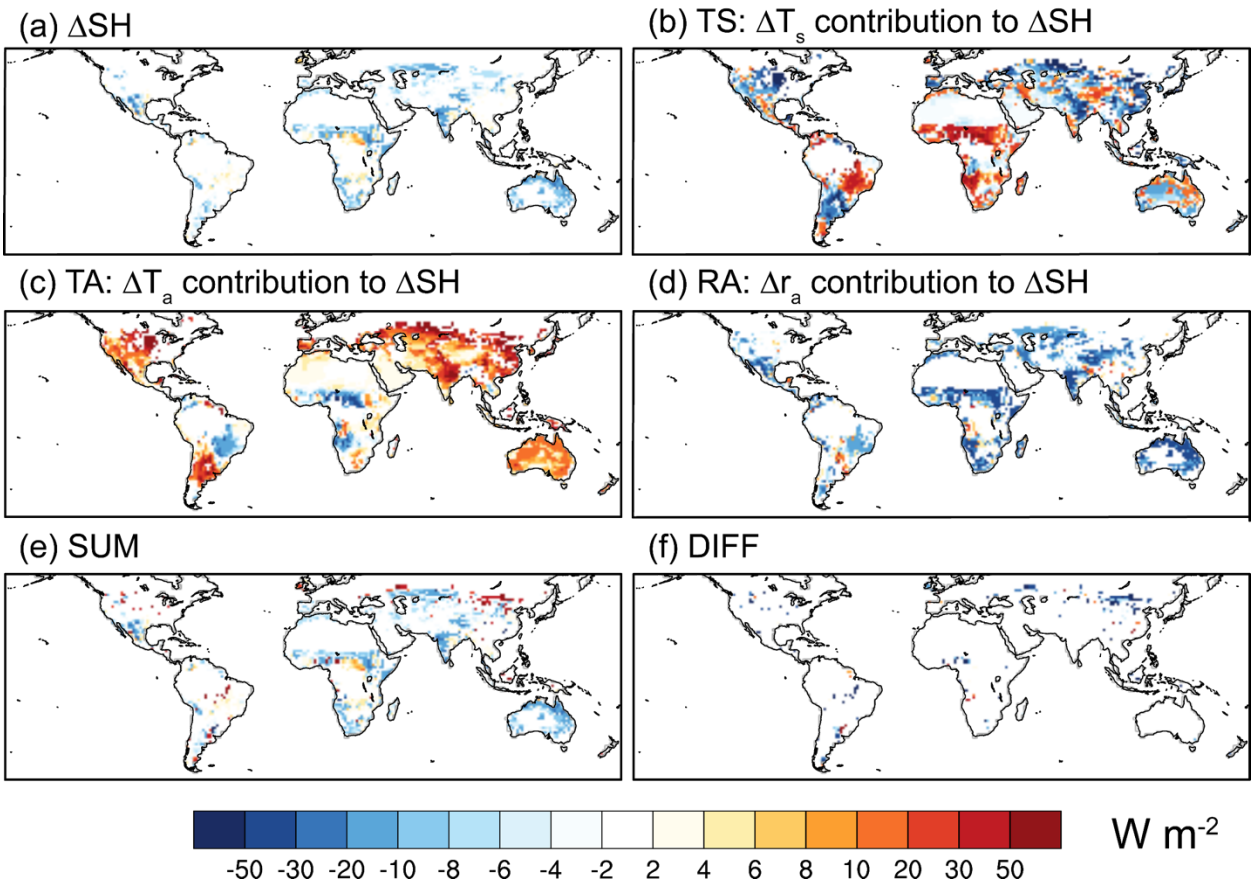

Figure 3.7 Decomposition of annual SH changes (W m^{-2}) due to LULCC effects during 1950-2015 (LULCC-CTL). (a) Difference in SH between LULCC and CTL. (b) - (d) Decomposed SH changes due to changes in surface temperature (TS: $\frac{\rho C_p}{r_a}\Delta LST$ in Eq 4.1), air temperature (TA: $-\frac{\rho C_p}{r_a}\Delta T_a$), and aerodynamic resistance (RA: $-\frac{(LST-T_a)\rho C_p}{r_a^2}\Delta r_a$). (e) Sum of SH changes from (b)-(d). (f) The difference between (a) and (e).

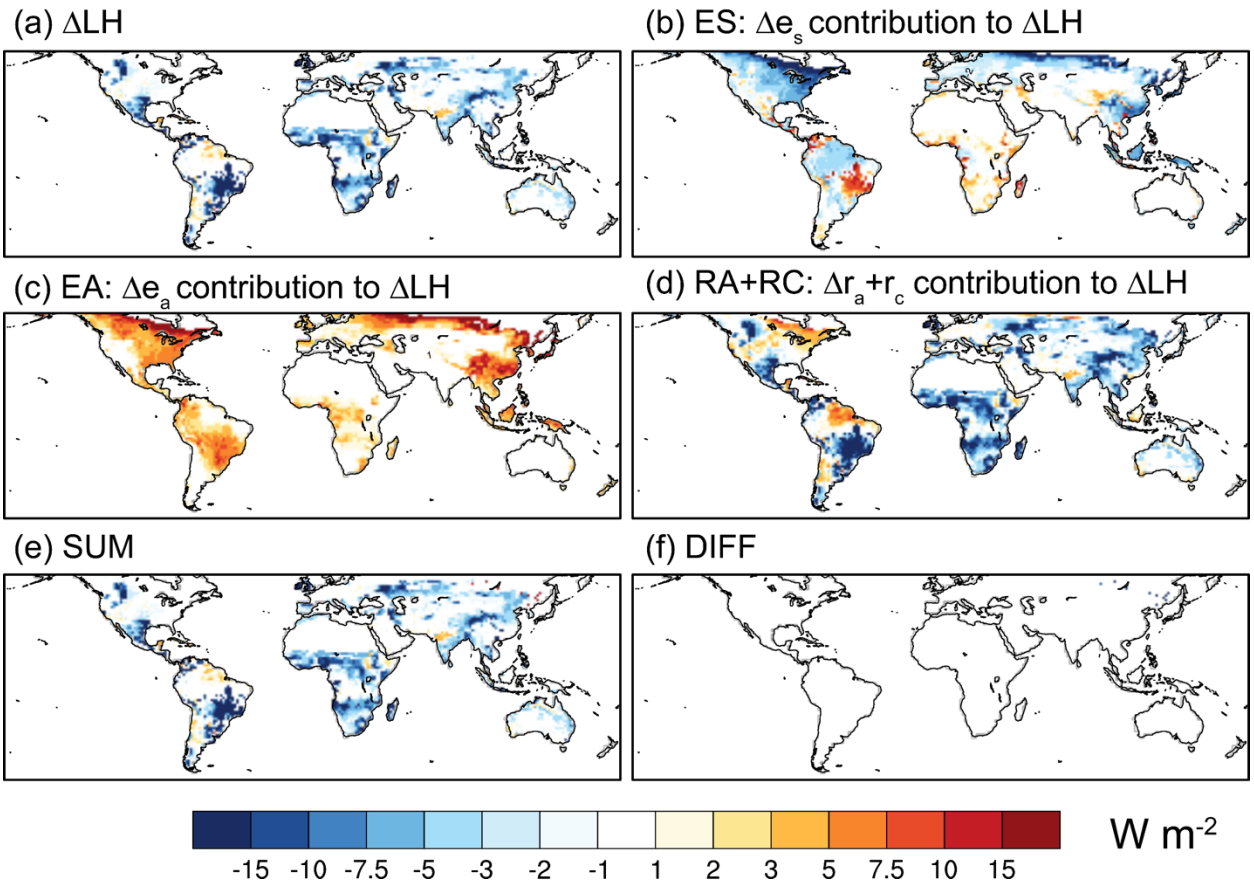

Figure 3.8 Decomposition of annual LH changes (W m^{-2}) due to LULCC effects during 1950-2015 (LULCC-CTL). (a) Difference in LH between LULCC and CTL (b) - (d) Decomposed LH changes due to changes in surface vapor pressure (ES: $\frac{\rho C_p}{\lambda(r_a+r_c)}\Delta e_s$), atmosphere vapor pressure (EA: $-\frac{\rho C_p}{\lambda(r_a+r_c)}\Delta e_a$), and surface resistance (RA+RC: $-\frac{(e_s-e_a)\rho C_p}{\lambda(r_a+r_c)^2}\Delta(r_a+r_c)$). (e) Sum of LH changes from (b)-(d). (f) The difference between (a) and (e).

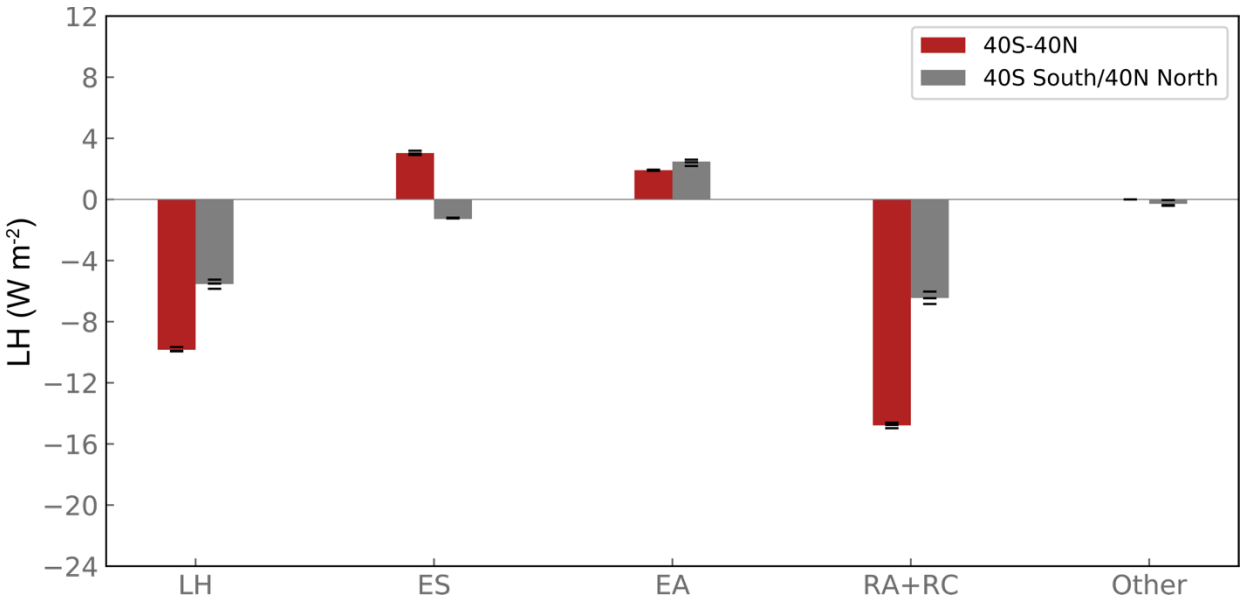

Figure 3.9 Annual LH changes (W m^{-2}) due to LULCC and its contribution from surface vapor pressure (ES: $\frac{\rho C_p}{\lambda(r_a+r_c)}\Delta e_s$), atmosphere vapor pressure (EA: $-\frac{\rho C_p}{\lambda(r_a+r_c)}\Delta e_a$), surface resistance (RA+RC: $-\frac{(e_s-e_a)\rho C_p}{\lambda(r_a+r_c)^2}\Delta(r_a+r_c)$), and others in degraded regions in low and mid latitudes during 1950-2015. The black lines indicate the response in three ensemble members.

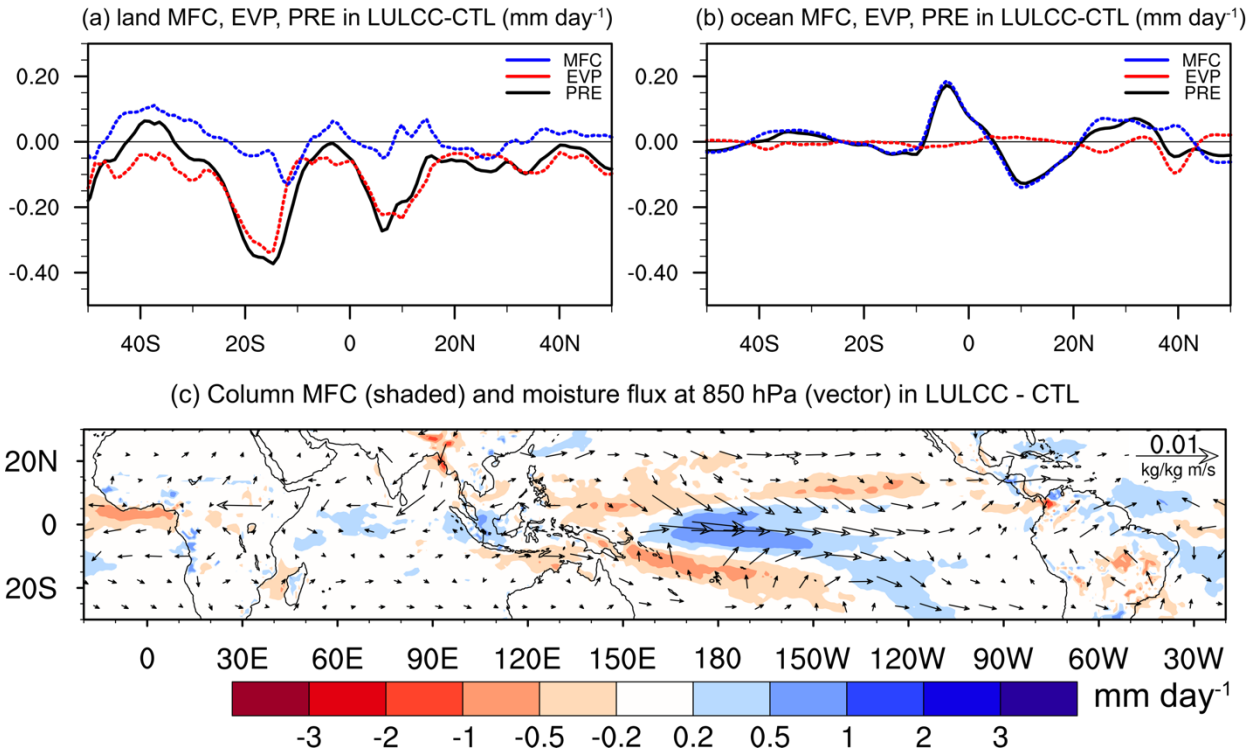

Figure 3.10 (a) The annual difference of 1950-2015 zonal-mean precipitation (PRE; black; in mm day^{-1}), evaporation (EVP; red; in mm day^{-1}), and moisture flux convergence (MFC; blue; in mm day^{-1}) between LULCC and CTL (LULCC-CTL) over land. (b) Same as Fig. 10a but over the ocean. (c) Atmospheric column MFC (shaded; mm day^{-1}) and moisture flux at 850 hPa (vector; g kg^{-1} m s^{-1}) between LULCC and CTL (LULCC-CTL)

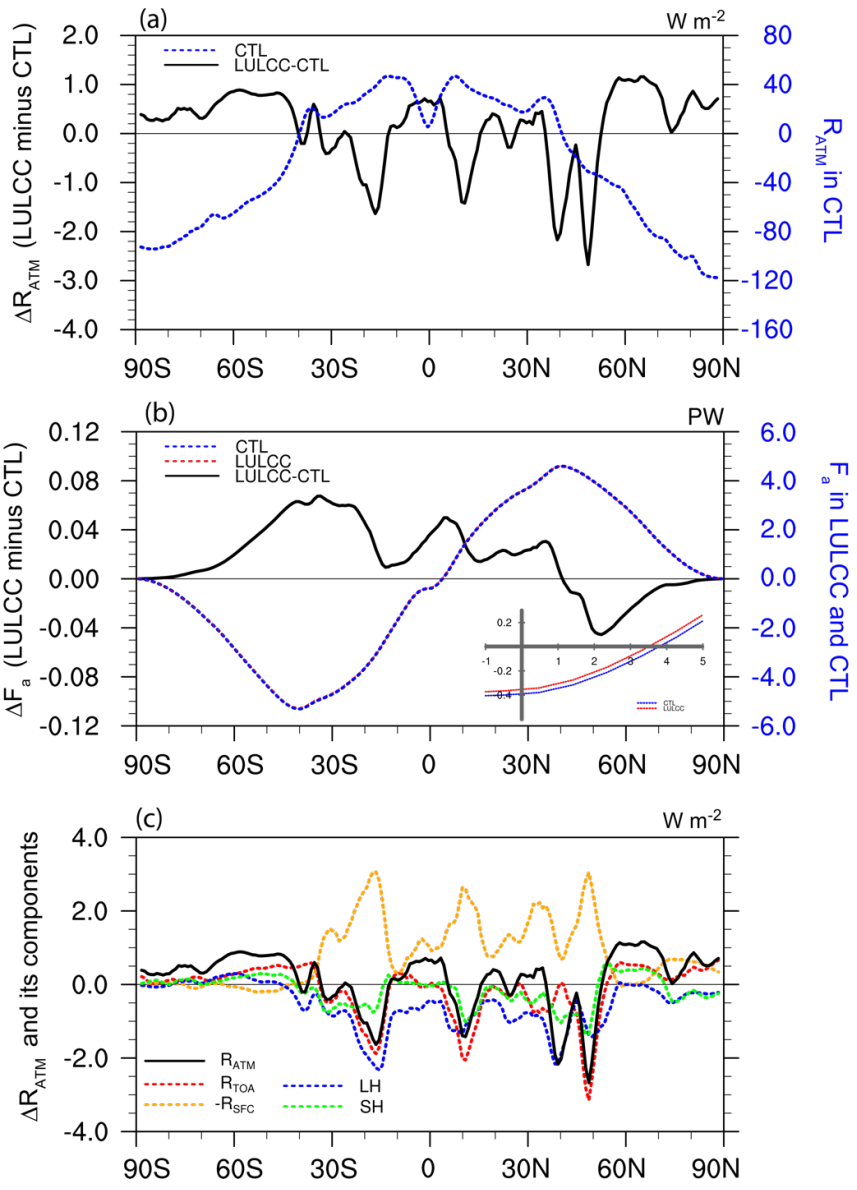

Figure 3.11 The 1950-2015 annual zonal mean (a) atmospheric heating in CTL (dash) and its difference between LULCC and CTL (solid). (b) The 1950-2015 atmospheric energy transport in CTL (dash; blue) and LULCC (dash; red) and its difference between LULCC and CTL (solid). The bottom right of Fig. 11b shows the enlarged box of atmosphere energy transport in CTL and LULCC near the equator. (c) The 1950-2015 annual difference of zonal annual atmospheric heating (R_{ATM}; black) and its components: R_{TOA} (red), $-R_{SFC}$ (orange), LH (blue), and SH (green) between LULCC and CTL

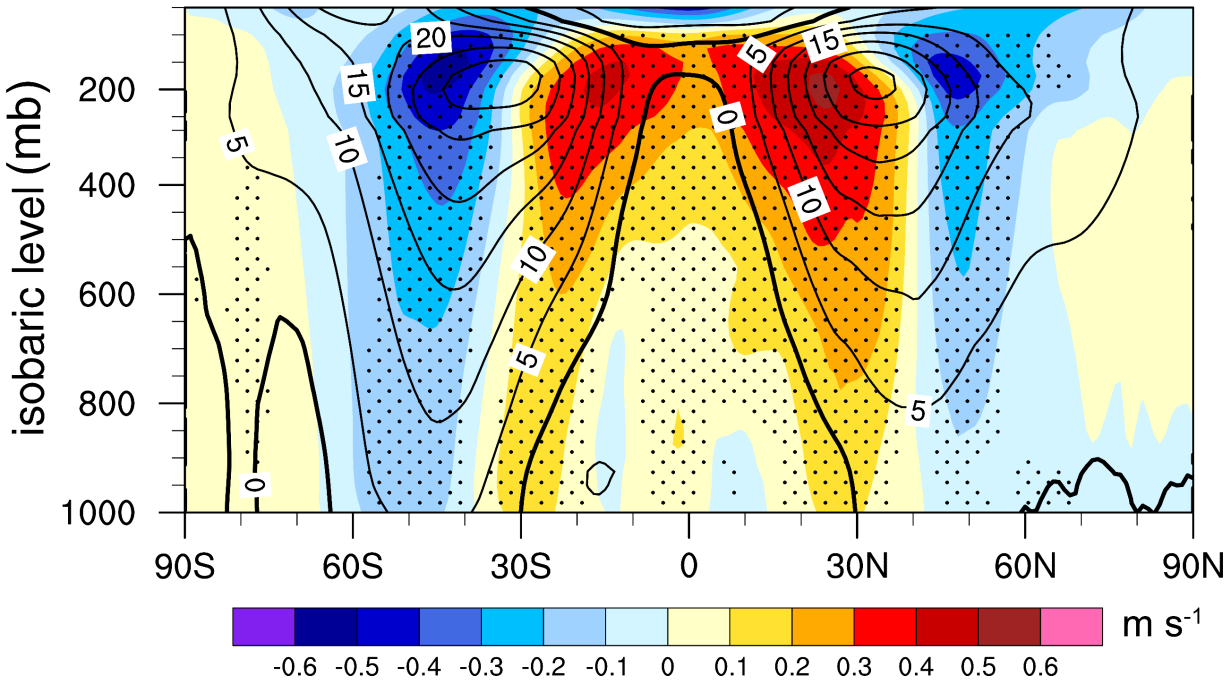

Figure 3.12 The 1950-2015 annual-mean difference of zonal wind (m s^{-1}) between LULCC and CTL (color shadings) and climatological zonal wind in CTL (black contours). Stippling indicates statistical significance at 95% confidence level.

Reference

Alkama, R., and Cescatti, A.: Biophysical climate impacts of recent changes in global forest cover, Science, 351, 600-604, 2016.

Arora, V. K., and Montenegro, A.: Small temperature benefits provided by realistic afforestation efforts, Nat Geosci, 4, 514-518, 10.1038/Ngeo1182, 2011.

Betts, R. A.: Offset of the potential carbon sink from boreal forestation by decreases in surface albedo, Nature, 408, 187-190, Doi 10.1038/35041545, 2000.

Betts, R. A.: Biogeophysical impacts of land use on present-day climate: near-surface temperature change and radiative forcing, Atmos Sci Lett, 2, 39-51, 10.1006/asle.2001.0023, 2001.

Boone, A. A., Xue, Y. K., De Sales, F., Comer, R. E., Hagos, S., Mahanama, S., Schiro, K., Song, G. Q., Wang, G. L., Li, S., and Mechoso, C. R.: The regional impact of Land-Use Land-cover Change (LULCC) over West Africa from an ensemble of global climate models under the auspices of the WAMME2 project, Climate Dynamics, 47, 3547-3573, 10.1007/s00382-016-3252-y, 2016.

Bright, R. M., Davin, E., O'Halloran, T., Pongratz, J., Zhao, K. G., and Cescatti, A.: Local temperature response to land cover and management change driven by non-radiative processes, Nat Clim Change, 7, 296-+, 10.1038/Nclimate3250, 2017.

Broccoli, A. J., Dahl, K. A., and Stouffer, R. J.: Response of the ITCZ to Northern Hemisphere cooling, Geophys Res Lett, 33, 10.1029/2005gl024546, 2006.

Brovkin, V., Boysen, L., Arora, V. K., Boisier, J. P., Cadule, P., Chini, L., Claussen, M., Friedlingstein, P., Gayler, V., van den Hurk, B. J. J. M., Hurtt, G. C., Jones, C. D., Kato, E., de Noblet-Ducoudre, N., Pacifico, F., Pongratz, J., and Weiss, M.: Effect of Anthropogenic Land-Use and Land-Cover Changes on Climate and Land Carbon Storage in CMIP5 Projections for the Twenty-First Century, J Climate, 26, 6859-6881, 10.1175/Jcli-D-12-00623.1, 2013.

Chagnon, F. J. F., Bras, R. L., and Wang, J.: Climatic shift in patterns of shallow clouds over the Amazon, Geophys Res Lett, 31, 10.1029/2004gl021188, 2004.

Chase, T. N., and Pielke, R. A.: The sensitivity of a General Circulation Model to large scale vegetation changes, Atmospheric science paper; no. 581, 1995.

Chen, G., and Held, I. M.: Phase speed spectra and the recent poleward shift of Southern Hemisphere surface westerlies, Geophys Res Lett, 34, 10.1029/2007gl031200, 2007.

Chen, G., Lu, J., and Frierson, D. M. W.: Phase Speed Spectra and the Latitude of Surface Westerlies: Interannual Variability and Global Warming Trend, J Climate, 21, 5942-5959, 10.1175/2008jcli2306.1, 2008.

Chen, L., and Dirmeyer, P. A.: Adapting observationally based metrics of biogeophysical feedbacks from land cover/land use change to climate modeling, Environ Res Lett, 11, 10.1088/1748-9326/11/3/034002, 2016.

Chiang, J. C. H., and Bitz, C. M.: Influence of high latitude ice cover on the marine Intertropical Convergence Zone, Climate Dynamics, 25, 477-496, 10.1007/s00382-005-0040-5, 2005.

Chilukoti, N., and Xue, Y.: An assessment of potential climate impact during 1948–2010 using historical land use land cover change maps, Int J Climatol, n/a, 10.1002/joc.6621, 2020.

Cvijanovic, I., Santer, B. D., Bonfils, C., Lucas, D. D., Chiang, J. C. H., and Zimmerman, S.: Future loss of Arctic sea-ice cover could drive a substantial decrease in California's rainfall, Nat Commun, 8, 10.1038/s41467-017-01907-4, 2017.

Davin, E. L., de Noblet-Ducoudre, N., and Friedlingstein, P.: Impact of land cover change on surface climate: Relevance of the radiative forcing concept, Geophys Res Lett, 34, 10.1029/2007gl029678, 2007.

Davin, E. L., and de Noblet-Ducoudre, N.: Climatic Impact of Global-Scale Deforestation: Radiative versus Nonradiative Processes, J Climate, 23, 97-112, 10.1175/2009jcli3102.1, 2010.

Deser, C., Sun, L. T., Tomas, R. A., and Screen, J.: Does ocean coupling matter for the northern extratropical response to projected Arctic sea ice loss?, Geophys Res Lett, 43, 2149-2157, 10.1002/2016gl067792, 2016.

Devaraju, N., Bala, G., and Modak, A.: Effects of large-scale deforestation on precipitation in the monsoon regions: Remote versus local effects, P Natl Acad Sci USA, 112, 3257-3262, 10.1073/pnas.1423439112, 2015.

Devaraju, N., Noblet-Ducoudré, N. d., Quesada, B., and Bala, G.: Quantifying the Relative Importance of Direct and Indirect Biophysical Effects of Deforestation on Surface Temperature and Teleconnections, J Climate, 31, 3811-3829, 10.1175/jcli-d-17-0563.1, 2018.

Diallo, I., Xue, Y. K., Li, Q., De Sales, F., and Li, W.: Dynamical downscaling the impact of spring Western US land surface temperature on the 2015 flood extremes at the Southern Great Plains: effect of domain choice, dynamic cores and land surface parameterization, Climate Dynamics, 53, 1039-1061, 10.1007/s00382-019-04630-6, 2019.

Dias, M. A. F. S., Rutledge, S., Kabat, P., Dias, P. L. S., Nobre, C., Fisch, G., Dolman, A. J., Zipser, E., Garstang, M., Manzi, A. O., Fuentes, J. D., Rocha, H. R., Marengo, J., Plana-Fattori, A., Sa, L. D. A., Alvala, R. C. S., Andreae, M. O., Artaxo, P., Gielow, R., and Gatti, L.: Cloud and rain processes in a biosphere-atmosphere interaction context in the Amazon Region, J Geophys Res-Atmos, 107, 10.1029/2001jd000335, 2002.

Duveiller, G., Hooker, J., and Cescatti, A.: The mark of vegetation change on Earth's surface energy balance, Nat Commun, 9, 2018.

FAO: State of the World's Forests, 2007.

Findell, K. L., Pitman, A. J., England, M. H., and Pegion, P. J.: Regional and Global Impacts of Land Cover Change and Sea Surface Temperature Anomalies, J Climate, 22, 3248-3269, 10.1175/2008jcli2580.1, 2009.

Forster, P., and Ramaswamy, V.: Changes in Atmospheric Constituents and in Radiative Forcing, Climate Change 2007: The Physical Science Basis, 129-234, 2007.

Frierson, D. M. W.: The dynamics of idealized convection schemes and their effect on the zonally averaged tropical circulation, J Atmos Sci, 64, 1959-1976, 10.1175/Jas3935.1, 2007.

Frierson, D. M. W., Hwang, Y. T., Fuckar, N. S., Seager, R., Kang, S. M., Donohoe, A., Maroon, E. A., Liu, X. J., and Battisti, D. S.: Contribution of ocean overturning circulation to tropical rainfall peak in the Northern Hemisphere, Nat Geosci, 6, 940-944, 10.1038/Ngeo1987, 2013.

Gash, J. H. C., and Nobre, C. A.: Climatic effects of Amazonian deforestation: Some results from ABRACOS, B Am Meteorol Soc, 78, 823-830, Doi 10.1175/1520-0477(1997)078<0823:Ceoads>2.0.Co;2, 1997.

Griffies, S., Harrison, M., Pacanowski, R., Rosati, A., Liang, Z., Schmidt, M., Simmons, H., and Slater, R.: A technical guide to MOM4. GFDL Ocean Group Tech. Rep. 5, NOAA, Geophysical Fluid Dynamics Laboratory, 2003.

Guo, W. D., Wang, X. Q., Sun, J. N., Ding, A. J., and Zou, J.: Comparison of land-atmosphere interaction at different surface types in the mid- to lower reaches of the Yangtze River valley, Atmos Chem Phys, 16, 9875-9890, 10.5194/acp-16-9875-2016, 2016.

Haywood, J. M., Jones, A., Dunstone, N., Milton, S., Vellinga, M., Bodas-Salcedo, A., Hawcroft, M., Kravitz, B., Cole, J., Watanabe, S., and Stephens, G.: The impact of equilibrating hemispheric albedos on tropical performance in the HadGEM2-ES coupled climate model, Geophys Res Lett, 43, 395-403, 10.1002/2015GL066903, 2016.

Hirsch, A. L., Guillod, B. P., Seneviratne, S. I., Beyerle, U., Boysen, L. R., Brovkin, V., Davin, E. L., Doelman, J. C., Kim, H., Mitchell, D. M., Nitta, T., Shiogama, H., Sparrow, S., Stehfest, E., van Vuuren, D. P., and Wilson, S.: Biogeophysical Impacts of Land-Use Change on Climate Extremes in Low-Emission Scenarios: Results From HAPPI-Land, Earth's Future, 6, 396-409, 10.1002/2017ef000744, 2018.

Hua, F. Y., Wang, X. Y., Zheng, X. L., Fisher, B., Wang, L., Zhu, J. G., Tang, Y., Yu, D. W., and Wilcove, D. S.: Opportunities for biodiversity gains under the world's largest reforestation programme, Nat Commun, 7, ARTN 12717

10.1038/ncomms12717, 2016.

Huang, H., Gu, Y., Xue, Y., Jiang, J., and Zhao, B.: Assessing aerosol indirect effect on clouds and regional climate of East/South Asia and West Africa using NCEP GFS, Climate Dynamics, 52, 5759-5774, 10.1007/s00382-018-4476-9, 2019.

Hurtt, G. C., Frolking, S., Fearon, M. G., Moore, B., Shevliakova, E., Malyshev, S., Pacala, S. W., and Houghton, R. A.: The underpinnings of land-use history: three centuries of global gridded land-use transitions, wood-harvest activity, and resulting secondary lands, Global Change Biol, 12, 1208-1229, 10.1111/j.1365-2486.2006.01150.x, 2006.

Juang, J. Y., Katul, G., Siqueira, M., Stoy, P., and Novick, K.: Separating the effects of albedo from eco-physiological changes on surface temperature along a successional chronosequence in the southeastern United States, Geophys Res Lett, 34, 10.1029/2007gl031296, 2007.

Kang, H. S., Xue, Y. K., and Collatz, G. J.: Impact assessment of satellite-derived leaf area index datasets using a general circulation model, J Climate, 20, 993-1015, 10.1175/Jcli4054.1, 2007.

Kang, S. M., Frierson, D. M. W., and Held, I. M.: The Tropical Response to Extratropical Thermal Forcing in an Idealized GCM: The Importance of Radiative Feedbacks and Convective Parameterization, J Atmos Sci, 66, 2812-2827, 10.1175/2009jas2924.1, 2009.

Koster, R. D., Guo, Z. C., Dirmeyer, P. A., Bonan, G., Chan, E., Cox, P., Davies, H., Gordon, C. T., Kanae, S., Kowalczyk, E., Lawrence, D., Liu, P., Lu, C. H., Malyshev, S., McAvaney, B., Mitchell, K., Mocko, D., Oki, T., Oleson, K. W., Pitman, A., Sud, Y. C., Taylor, C. M., Verseghy, D., Vasic, R., Xue, Y. K., and Yamada, T.: GLACE: The Global Land-Atmosphere Coupling Experiment. Part I: Overview, J Hydrometeorol, 7, 590-610, Doi 10.1175/Jhm510.1, 2006.

Lague, M. M., and Swann, A. L. S.: Progressive Midlatitude Afforestation: Impacts on Clouds, Global Energy Transport, and Precipitation, J Climate, 29, 5561-5573, 10.1175/Jcli-D-15-0748.1, 2016.

Lawrence, D. M., Hurtt, G. C., Arneth, A., Brovkin, V., Calvin, K. V., Jones, A. D., Jones, C. D., Lawrence, P. J., de Noblet-Ducoudre, N., Pongratz, J., Seneviratne, S. I., and Shevliakova, E.: The Land Use Model Intercomparison Project (LUMIP) contribution to CMIP6: rationale and experimental design, Geosci Model Dev, 9, 2973-2998, 2016.

Lee, J., Xue, Y., De Sales, F., Diallo, I., Marx, L., Ek, M., Sperber, K. R., and Gleckler, P. J.: Evaluation of multi-decadal UCLA-CFSv2 simulation and impact of interactive atmospheric-ocean feedback on global and regional variability, Climate Dynamics, 52, 3683-3707, 2019.

Lee, X., Goulden, M. L., Hollinger, D. Y., Barr, A., Black, T. A., Bohrer, G., Bracho, R., Drake, B., Goldstein, A., Gu, L. H., Katul, G., Kolb, T., Law, B. E., Margolis, H., Meyers, T., Monson, R., Munger, W., Oren, R., Kyaw, T. P. U., Richardson, A. D., Schmid, H. P., Staebler, R., Wofsy, S., and Zhao, L.: Observed increase in local cooling effect of deforestation at higher latitudes, Nature, 479, 384-387, 10.1038/nature10588, 2011.

Lejeune, Q., Seneviratne, S. I., and Davin, E. L.: Historical Land-Cover Change Impacts on Climate: Comparative Assessment of LUCID and CMIP5 Multimodel Experiments, J Climate, 30, 1439-1459, 2017.

Li, W. P., Xue, Y. K., and Poccard, I.: Numerical investigation of the impact of vegetation indices on the variability of West African summer monsoon, J Meteorol Soc Jpn, 85A, 363-383, Doi 10.2151/Jmsj.85a.363, 2007.

Li, Y., Zhao, M. S., Motesharrei, S., Mu, Q. Z., Kalnay, E., and Li, S. C.: Local cooling and warming effects of forests based on satellite observations, Nat Commun, 6, 10.1038/ncomms7603, 2015.

Liu, Y., Guo, W. D., and Song, Y. M.: Estimation of key surface parameters in semi-arid region and their impacts on improvement of surface fluxes simulation, Sci China Earth Sci, 59, 307-319, 10.1007/s11430-015-5140-4, 2016.

Liu, Y., Xue, Y. K., MacDonald, G., Cox, P., and Zhang, Z. Q.: Global vegetation variability and its response to elevated CO2, global warming, and climate variability - a study using the offline SSiB4/TRIFFID model and satellite data, Earth Syst Dynam, 10, 9-29, 2019.

Lorenz, R., Pitman, A. J., and Sisson, S. A.: Does Amazonian deforestation cause global effects; can we be sure?, J Geophys Res-Atmos, 121, 5567-5584, 10.1002/2015jd024357, 2016.

Luyssaert, S., Jammet, M., Stoy, P. C., Estel, S., Pongratz, J., Ceschia, E., Churkina, G., Don, A., Erb, K., Ferlicoq, M., Gielen, B., Grunwald, T., Houghton, R. A., Klumpp, K., Knohl, A., Kolb, T.,

Kuemmerle, T., Laurila, T., Lohila, A., Loustau, D., McGrath, M. J., Meyfroidt, P., Moors, E. J., Naudts, K., Novick, K., Otto, J., Pilegaard, K., Pio, C. A., Rambal, S., Rebmann, C., Ryder, J., Suyker, A. E., Varlagin, A., Wattenbach, M., and Dolman, A. J.: Land management and land-cover change have impacts of similar magnitude on surface temperature, Nat Clim Change, 4, 389-393, 10.1038/Nclimate2196, 2014.

Lyons, T. J.: Clouds prefer native vegetation, Meteorol Atmos Phys, 80, 131-140, DOI 10.1007/s007030200020, 2002.

Ma, H. Y., Mechoso, C. R., Xue, Y. K., Xiao, H., Neelin, J. D., and Ji, X.: On the Connection between Continental-Scale Land Surface Processes and the Tropical Climate in a Coupled Ocean-Atmosphere-Land System, J Climate, 26, 9006-9025, 2013a.

Ma, H. Y., Xiao, H., Mechoso, C. R., and Xue, Y. K.: Sensitivity of Global Tropical Climate to Land Surface Processes: Mean State and Interannual Variability, J Climate, 26, 1818-1837, 10.1175/Jcli-D-12-00142.1, 2013b.

Mahmood, R., Pielke, R. A., Hubbard, K. G., Niyogi, D., Dirmeyer, P. A., McAlpine, C., Carleton, A. M., Hale, R., Gameda, S., Beltrán-Przekurat, A., Baker, B., McNider, R., Legates, D. R., Shepherd, M., Du, J., Blanken, P. D., Frauenfeld, O. W., Nair, U. S., and Fall, S.: Land cover changes and their biogeophysical effects on climate, Int J Climatol, 34, 929-953, doi:10.1002/joc.3736, 2014.

Ming, Y., and Ramaswamy, V.: Nonlinear Climate and Hydrological Responses to Aerosol Effects, J Climate, 22, 1329-1339, 10.1175/2008jcli2362.1, 2009.

Ming, Y., Ramaswamy, V., and Chen, G.: A Model Investigation of Aerosol-Induced Changes in Boreal Winter Extratropical Circulation, J Climate, 24, 6077-6091, 10.1175/2011jcli4111.1, 2011.

Myhre, G., Shindell, D., Bréon, F.-M., Collins, W., Fuglestvedt, J., Huang, J., Koch, D., Lamarque, J.-F., Lee, D., Mendoza, B., Nakajima, T., Robock, A., Stephens, G., Takemura, T., and Zhang, H.: Anthropogenic and Natural Radiative Forcing, in: Climate Change 2013: The Physical Science Basis. Contribution of Working Group I to the Fifth Assessment Report of the Intergovernmental

Panel on Climate Change, edited by: Stocker, T. F., Qin, D., Plattner, G.-K., Tignor, M., Allen, S. K., Boschung, J., Nauels, A., Xia, Y., Bex, V., and Midgley, P. M., Cambridge University Press, Cambridge, United Kingdom and New York, NY, USA, 659–740, 2013.

Nagendra, H., and Southworth, J.: Reforesting landscapes: linking pattern and process, Springer Science & Business Media, 2009.

Nair, U. S., Wu, Y., Kala, J., Lyons, T. J., Pielke, R. A., and Hacker, J. M.: The role of land use change on the development and evolution of the west coast trough, convective clouds, and precipitation in southwest Australia, J Geophys Res-Atmos, 116, 10.1029/2010jd014950, 2011.

Peng, S. S., Piao, S. L., Zeng, Z. Z., Ciais, P., Zhou, L. M., Li, L. Z. X., Myneni, R. B., Yin, Y., and Zeng, H.: Afforestation in China cools local land surface temperature, P Natl Acad Sci USA, 111, 2915-2919, 10.1073/pnas.1315126111, 2014.

Pielke, R. A., Adegoke, J., Beltran-Przekurat, A., Hiemstra, C. A., Lin, J., Nair, U. S., Niyogi, D., and Nobis, T. E.: An overview of regional land-use and land-cover impacts on rainfall, Tellus B, 59, 587-601, 10.1111/j.1600-0889.2007.00251.x, 2007.

Pielke, R. A., Pitman, A., Niyogi, D., Mahmood, R., McAlpine, C., Hossain, F., Goldewijk, K. K., Nair, U., Betts, R., Fall, S., Reichstein, M., Kabat, P., and de Noblet, N.: Land use/land cover changes and climate: modeling analysis and observational evidence, Wires Clim Change, 2, 828-850, 10.1002/wcc.144, 2011.

Pitman, A. J., Narisma, G. T., Pielke, R. A., and Holbrook, N. J.: Impact of land cover change on the climate of southwest Western Australia, J Geophys Res-Atmos, 109, 10.1029/2003jd004347, 2004.

Pitman, A. J., de Noblet-Ducoudre, N., Cruz, F. T., Davin, E. L., Bonan, G. B., Brovkin, V., Claussen, M., Delire, C., Ganzeveld, L., Gayler, V., van den Hurk, B. J. J. M., Lawrence, P. J., van der Molen, M. K., Muller, C., Reick, C. H., Seneviratne, S. I., Strengers, B. J., and Voldoire, A.: Uncertainties in climate responses to past land cover change: First results from the LUCID intercomparison study, Geophys Res Lett, 36, 2009.

Quesada, B., Devaraju, N., de Noblet-Ducoudre, N., and Arneth, A.: Reduction of monsoon rainfall in response to past and future land use and land cover changes, Geophys Res Lett, 44, 1041-1050, 10.1002/2016gl070663, 2017.

Ramankutty, N., and Foley, J. A.: Estimating historical changes in global land cover: Croplands from 1700 to 1992, Global Biogeochem Cy, 13, 997-1027, Doi 10.1029/1999gb900046, 1999.

Rigden, A. J., and Li, D.: Attribution of surface temperature anomalies induced by land use and land cover changes, Geophys Res Lett, 44, 6814-6822, 10.1002/2017gl073811, 2017.

Saha, S., Moorthi, S., Pan, H. L., Wu, X. R., Wang, J. D., Nadiga, S., Tripp, P., Kistler, R., Woollen, J., Behringer, D., Liu, H. X., Stokes, D., Grumbine, R., Gayno, G., Wang, J., Hou, Y. T., Chuang, H. Y., Juang, H. M. H., Sela, J., Iredell, M., Treadon, R., Kleist, D., Van Delst, P., Keyser, D., Derber, J., Ek, M., Meng, J., Wei, H. L., Yang, R. Q., Lord, S., Van den Dool, H., Kumar, A., Wang, W. Q., Long, C., Chelliah, M., Xue, Y., Huang, B. Y., Schemm, J. K., Ebisuzaki, W., Lin, R., Xie, P. P., Chen, M. Y., Zhou, S. T., Higgins, W., Zou, C. Z., Liu, Q. H., Chen, Y., Han, Y., Cucurull, L., Reynolds, R. W., Rutledge, G., and Goldberg, M.: The Ncep Climate Forecast System Reanalysis, B Am Meteorol Soc, 91, 1015-1057, 10.1175/2010bams3001.1, 2010.

Saha, S., Moorthi, S., Wu, X. R., Wang, J., Nadiga, S., Tripp, P., Behringer, D., Hou, Y. T., Chuang, H. Y., Iredell, M., Ek, M., Meng, J., Yang, R. Q., Mendez, M. P., Van Den Dool, H., Zhang, Q., Wang, W. Q., Chen, M. Y., and Becker, E.: The NCEP Climate Forecast System Version 2, J Climate, 27, 2185-2208, 10.1175/Jcli-D-12-00823.1, 2014.

Schneck, R., and Mosbrugger, V.: Simulated climate effects of Southeast Asian deforestation: Regional processes and teleconnection mechanisms, J Geophys Res-Atmos, 116, 10.1029/2010jd015450, 2011.

Sellers, P. J., Randall, D. A., Collatz, G. J., Berry, J. A., Field, C. B., Dazlich, D. A., Zhang, C., Collelo, G. D., and Bounoua, L.: A Revised Land Surface Parameterization (SiB2) for Atmospheric GCMS. Part I: Model Formulation, J Climate, 9, 676-705, 10.1175/1520-0442(1996)009<0676:arlspf>2.0.co;2, 1996.

Snyder, P. K.: The Influence of Tropical Deforestation on the Northern Hemisphere Climate by Atmospheric Teleconnections, Earth Interact, 14, 2010.

Steyaert, L. T., and Knox, R. G.: Reconstructed historical land cover and biophysical parameters for studies of land-atmosphere interactions within the eastern United States, Journal of Geophysical Research: Atmospheres, 113, 2008.

Strack, J. E., Pielke, R. A., Steyaert, L. T., and Knox, R. G.: Sensitivity of June near-surface temperatures and precipitation in the eastern United States to historical land cover changes since European settlement, Water Resour Res, 44, 10.1029/2007wr006546, 2008.

Swann, A. L. S., Fung, I. Y., and Chiang, J. C. H.: Mid-latitude afforestation shifts general circulation and tropical precipitation, P Natl Acad Sci USA, 109, 712-716, 10.1073/pnas.1116706108, 2012.

Tomas, R. A., Deser, C., and Sun, L. T.: The Role of Ocean Heat Transport in the Global Climate Response to Projected Arctic Sea Ice Loss, J Climate, 29, 6841-6859, 10.1175/Jcli-D-15-0651.1, 2016.

Verhoef, A., DeBruin, H. A. R., and VandenHurk, B. J. J. M.: Some practical notes on the parameter kB(-1) for sparse vegetation, J Appl Meteorol, 36, 560-572, 1997.

Wilks, D. S.: On "field significance" and the false discovery rate, J Appl Meteorol Clim, 45, 1181-1189, Doi 10.1175/Jam2404.1, 2006.

Winckler, J., Reick, C. H., and Pongratz, J.: Robust Identification of Local Biogeophysical Effects of Land-Cover Change in a Global Climate Model, J Climate, 30, 1159-1176, 10.1175/Jcli-D-16-0067.1, 2017.

Winckler, J., Lejeune, Q., Reick, C. H., and Pongratz, J.: Nonlocal Effects Dominate the Global Mean Surface Temperature Response to the Biogeophysical Effects of Deforestation, Geophys Res Lett, 46, 745-755, 10.1029/2018gl080211, 2019a.

Winckler, J., Reick, C. H., Luyssaert, S., Cescatti, A., Stoy, P. C., Lejeune, Q., Raddatz, T., Chlond, A., Heidkamp, M., and Pongratz, J.: Different response of surface temperature and air temperature to deforestation in climate models, Earth Syst Dynam, 10, 473-484, 10.5194/esd-10-473-2019, 2019b.

Xie, S.-P.: The shape of continents, air-sea interaction, and the rising branch of the Hadley circulation, in: The Hadley Circulation: Present, Past and Future, Springer, 121-152, 2004.

Xu, Z. F., Mahmood, R., Yang, Z. L., Fu, C. B., and Su, H.: Investigating diurnal and seasonal climatic response to land use and land cover change over monsoon Asia with the Community Earth System Model, J Geophys Res-Atmos, 120, 1137-1152, 2015.

Xue, Y., Sellers, P. J., Kinter, J. L., and Shukla, J.: A Simplified Biosphere Model for Global Climate Studies, J Climate, 4, 345-364, 10.1175/1520-0442(1991)004<0345:asbmfg>2.0.co;2, 1991.

Xue, Y., and Shukla, J.: The Influence of Land Surface Properties on Sahel Climate. Part 1: Desertification, J Climate, 6, 2232-2245, 10.1175/1520-0442(1993)006<2232:tiolsp>2.0.co;2, 1993.

Xue, Y., and Shukla, J.: The Influence of Land Surface Properties on Sahel Climate. Part II. Afforestation, J Climate, 9, 3260-3275, 10.1175/1520-0442(1996)009<3260:tiolsp>2.0.co;2, 1996.

Xue, Y., Juang, H. M. H., Li, W. P., Prince, S., DeFries, R., Jiao, Y., and Vasic, R.: Role of land surface processes in monsoon development: East Asia and West Africa, Journal of Geophysical Research: Atmospheres, 109, n/a-n/a, 10.1029/2003jd003556, 2004.

Xue, Y., De Sales, F., Lau, W. K. M., Boone, A., Kim, K.-M., Mechoso, C. R., Wang, G., Kucharski, F., Schiro, K., Hosaka, M., Li, S., Druyan, L. M., Sanda, I. S., Thiaw, W., Zeng, N., Comer, R. E., Lim, Y.-K., Mahanama, S., Song, G., Gu, Y., Hagos, S. M., Chin, M., Schubert, S., Dirmeyer, P., Ruby Leung, L., Kalnay, E., Kitoh, A., Lu, C.-H., Mahowald, N. M., and Zhang, Z.: West African monsoon decadal variability and surface-related forcings: second West African Monsoon Modeling and Evaluation Project Experiment (WAMME II), Climate Dynamics, 47, 3517-3545, 10.1007/s00382-016-3224-2, 2016.

Xue, Y. K.: The impact of desertification in the Mongolian and the Inner Mongolian grassland on the regional climate, J Climate, 9, 2173-2189, Doi 10.1175/1520-0442(1996)009<2173:Tiodit>2.0.Co;2, 1996.

Xue, Y. K., Diallo, I., Li, W. K., Neelin, J. D., Chu, P. C., Vasic, R., Guo, W. D., Li, Q., Robinson, D. A., Zhu, Y. J., Fu, C. B., and Oaida, C. M.: Spring Land Surface and Subsurface Temperature

Anomalies and Subsequent Downstream Late Spring-Summer Droughts/Floods in North America and East Asia, J Geophys Res-Atmos, 123, 5001-5019, 2018.

Zhan, X. W., Xue, Y. K., and Collatz, G. J.: An analytical approach for estimating CO2 and heat fluxes over the Amazonian region, Ecol Model, 162, 97-117, 2003.

Zhang, M., Lee, X. H., Yu, G. R., Han, S. J., Wang, H. M., Yan, J. H., Zhang, Y. P., Li, Y. D., Ohta, T., Hirano, T., Kim, J., Yoshifuji, N., and Wang, W.: Response of surface air temperature to small-scale land clearing across latitudes, Environ Res Lett, 9, 10.1088/1748-9326/9/3/034002, 2014.

Zhao, L., Lee, X., Smith, R. B., and Oleson, K.: Strong contributions of local background climate to urban heat islands, Nature, 511, 216-219, 10.1038/nature13462, 2014.

Zhao, M., Pitman, A. J., and Chase, T.: The impact of land cover change on the atmospheric circulation, Climate Dynamics, 17, 467-477, Doi 10.1007/Pl00013740, 2001.

Zwiers, F. W., and Vonstorch, H.: Taking Serial-Correlation into Account in Tests of the Mean, J Climate, 8, 336-351, Doi 10.1175/1520-0442(1995)008<0336:Tsciai>2.0.Co;2, 1995.

Chapter 4 Modeling long-term fire impact on ecosystem characteristics and surface energy using a process-based vegetation-fire model SSiB4/TRIFFID-Fire v1.0

 The supplementary material for this chapter is provided in Appendix B.

[**Huang, H.**, Xue, Y., Li, F., and Liu, Y.: Modeling long-term fire impact on ecosystem characteristics and surface energy using a process-based vegetation-fire model SSiB4/TRIFFID-Fire v1. 0, Geoscientific Model Development, 1-41, 2020.]

Abstract

Fire is one of the primary disturbances to the distribution and ecological properties of the world's major biomes and can influence the surface fluxes and climate through vegetation-climate interactions. This study incorporates a fire model of intermediate complexity to a biophysical model with dynamic vegetation, SSiB4/TRIFFID (The Simplified Simple Biosphere Model coupled with the Top-down Representation of Interactive Foliage and Flora Including Dynamics Model). This new model, SSiB4/TRIFFID-Fire, updating fire impact on the terrestrial carbon cycle every 10 days, is then used to simulate the burned area during 1948-2014. The simulated global burned area in 2000-2014 is 471.9 Mha yr^{-1}, close to the estimate, 478.1 Mha yr^{-1}, in Global Fire Emission Database v4s (GFED4s) with a spatial correlation of 0.8. The SSiB4/TRIFFID-Fire

reproduces temporal variations of the burned area at monthly to interannual scales. Specifically, it captures the observed decline trend in northern African savanna fire and accurately simulates the fire seasonality in most major fire regions. The simulated fire carbon emission is 2.19 Pg yr^{-1}, slightly higher than the GFED4s (2.07 Pg yr^{-1}).

The SSiB4/TRIFFID-Fire is applied to assess the long-term fire impact on ecosystem characteristics and surface energy budget by comparing model runs with and without fire (FIRE-ON minus FIRE-OFF). The FIRE-ON simulation reduces tree cover over 4.5 % of the global land surface, accompanied by a decrease in leaf area index and vegetation height by 0.10 m^2 m^{-2} and 1.24 m, respectively. The surface albedo and sensible heat are reduced throughout the year, while latent heat flux decreases in the fire season but increases in the rainy season. Fire results in an increase in surface temperature over most fire regions.

4.1 Introduction

Wildfire, whether natural or human-made, is one of the primary ecosystem disturbances and it plays a major role in the terrestrial biogeochemical cycles and ecological succession across spatial and temporal scales (Sousa, 1984; Bowman et al., 2009). Every year in the dry season, wildfires burn about 400 Mha of land vegetated areas, leaving behind numerous scars in the landscape (Giglio et al., 2013; Chuvieco et al., 2016). Fires affect the climate through modification of water, energy, and momentum exchange between land and atmosphere (Chambers and Chapin, 2002; Bond-Lamberty et al., 2009) and can interact with monsoons by affecting atmospheric circulations (De Sales et al., 2016; Saha et al., 2016). Fires are also important sources of global carbon, aerosols, and trace gas emissions. Based on the latest satellite estimates, global fires emit 1.5 – 4.2 Pg C yr^{-1} carbon, 7 – 8.2 Pg C yr^{-1} CO_2, and 1.9 – 6.0 Tg C yr^{-1} black carbon to the atmosphere (Chuvieco et al., 2016; van der Werf et al., 2017; Li et al., 2019). Fire emissions contribute to increases in greenhouse gases and cloud condensation nuclei through geochemistry processes (Scholes et al., 1996), affecting radiative forcing, the hydrology cycle (Ward et al., 2012; Jiang et al., 2016; Hamilton et al., 2018), and air quality (van der Werf et al., 2010; Johnston et al., 2012)

Since the early 2000s, fire models have been developed within Dynamic Global Vegetation Models (DGVMs) to explicitly describe the burned area, fire emissions, and fire disturbance on terrestrial ecosystems (Thonicke et al., 2001; Venevsky et al., 2002; Arora and Boer, 2005; Thonicke et al., 2010; Li et al., 2012; Pfeiffer et al., 2013; Lasslop et al., 2014; Yue et al., 2014; Rabin et al., 2018; Burton et al., 2019; Venevsky et al., 2019). These fire models have various levels of complexity, from simple statistical models (SIMFIRE; Knorr et al., 2016) to complicated process-based ones such as SPITFIRE (Thonicke et al., 2010) and MC2 (Bachelet et al., 2015).

With increasing complexity, more fire processes and fire characteristics are considered in fire models. In general, current fire models broadly capture the global amounts and spatial distribution of burned area and carbon emissions, as compared to different observations. However, many empirically determined parameters are included in the complicated process-based models, which leads to large uncertainties. There is no model that outperforms other models across all fire variables (Hantson et al., 2020). Moreover, current fire models have deficiencies in simulating the peak fire month, fire season length, and interannual variability, as reported by the Fire Model Intercomparison Project (FireMIP; Li et al., 2019; Hantson et al., 2020). Most fire models show a 1-2 months shift in peak burned area and simulate a longer fire season compared to observations.

Fire models have been used to reconstruct fire history before the satellite era (Yang et al., 2015; van Marle et al., 2017; Li et al., 2019). In addition, they are widely used to attribute historical variability of burned area to various climate and anthropogenic driving factors (Kloster et al., 2012; Andela et al., 2017; Forkel et al., 2019; Teckentrup et al., 2019). Some fire models have been used to assess long-term fire impact on the terrestrial carbon cycle by comparing a reference simulation with fire and a sensitivity simulation representing "a world without fire." However, the simulated responses of vegetation and carbon cycle are divergent. Bond et al. (2005) reported that forest cover would double in a world without fire, while in the recent fire-coupled DGVMs, a much smaller tree cover reduction by 10% (ranges between 3 % and 25 %) is simulated when fire is taken into account (Lasslop et al., 2020). Earlier model-based studies reported that fire reduced terrestrial carbon uptake. However, the range of the quantified reduction was fairly broad (0.05–3.60 Pg C yr^{-1}), and most studies did not consider the fire effects on vegetation distribution and related mechanisms (Li et al., 2014; Poulter et al., 2015; Yang et al., 2015; Yue et al., 2015; Seo and Kim, 2019; Zou et al., 2020).

Thus far, only the fire model developed by Li et al. (2012; 2013) has been used to investigate the long-term fire effects on surface energy. By comparing the simulated climate with and without fire, Li et al. (2017) concluded that fire caused a significant decrease in surface radiation, latent heat, and a slight decrease in sensible heat fluxes through changes in biophysical properties such as albedo, Bowen ratio, and aerodynamic resistance. An increase in surface temperature was found over most fire regions. However, the long-term fire impact on vegetation distribution was not taken into account in Li et al. (2017), which has been widely observed on site-level studies (Higgins et al., 2007; Smit et al., 2010) and can cause substantial changes in aerodynamic resistance due to conversions of dominant PFT (Huang et al., 2020). Moreover, Li et al. (2017) focused on the annual fire impact on energy fluxes. Yet fire effects on energy budget can have large seasonal variations associated with the vegetation loss during the fire seasons and vegetation recovery during post-fire rainy seasons. The seasonal variations in fire effects have not been investigated in any fire studies.

In the original SSiB4/TRIFFID, the carbon disturbance caused by fire and insects was assumed to be a constant which depended solely on plant functional type (PFT) without spatial and temporal changes (Cox, 2001; Liu et al., 2019). However, the fire disturbance is highly varied with climate, vegetation productivity, and socio-economic conditions, which has a strong influence on vegetation dynamics, carbon cycling, and soil processes. In this study, we develop the fire modeling by incorporating the fire scheme of Li et al. (2012; 2013) to SSiB4/TRIFFID (hereafter SSiB4/TRIFFID-Fire). The SSiB4/TRIFFID-Fire model updates fire-induced carbon loss every 10 days, which has been rarely employed in current process-based fire models, and is used to provide a quantitative assessment of fire impact on ecosystem characteristics and surface energy at subseasonal, seasonal, interannual, and long-term scales. Specifically, our objectives are: (1) to

evaluate the climatology and interannual variability of burned area and carbon emissions simulated by offline SSiB4/TRIFFID-Fire; (2) to assess the ability of SSiB4/TRIFFID-Fire in capturing the fire seasonality in major fire regions; and (3) to assess the long-term fire impact on PFT distribution and vegetation properties and the resultant changes in seasonal surface energy budget and temperature. In Sect. 2, we provide a brief description of the DGVM, SSiB4/TRIFFID, and the fire model, Li et al. (2012; 2013), and the coupling procedures. The experimental design and data for model input and validation are introduced in Sect. 3. The fire model evaluation on the global scale and the application of long-term fire impact on the ecosystem characteristics and surface properties are presented in Sect. 4. Discussions and conclusions are given in Sect. 5.

4.2 Method

4.2.1 Land and vegetation model

The Simplified Simple Biosphere Model (SSiB; Xue et al., 1991; Zhan et al., 2003) is a biophysical model which simulates fluxes of surface radiation, momentum, sensible/latent heat, runoff, soil moisture, surface temperature, and vegetation gross/net primary productivity (GPP/NPP) based on energy and water balance. The SSiB was coupled with a dynamic vegetation model, the Top-down Representation of Interactive Foliage and Flora Including Dynamics Model (TRIFFID), to calculate leaf area index (LAI), canopy height, and PFT fractional coverage according to the carbon balance (Cox, 2001; Zhang et al., 2015; Harper et al., 2016; Liu et al., 2019). We have improved the PFT competition strategy and plant physiology processes to make the SSiB4/TRIFFID suitable for seasonal, interannual, and decadal studies (Zhang et al., 2015; Liu et al., 2019). SSiB4/TRIFFID includes seven PFTs: (1) broadleaf evergreen trees (BET), (2) needleleaf evergreen trees (NET), (3) broadleaf deciduous trees (BDT), (4) C3 grasses, (5) C4

plants, (6) shrubs, and (7) tundra. The coverage of a PFT is determined by net carbon availability, competition between species, and disturbance, which implicitly includes mortality due to fires, pests, and windthrow. A detailed description and validation of SSiB4/TRIFFID can be found in Zhang et al. (2015) and Liu et al. (2019).

4.2.2 Fire model and modifications

In this study, a process-based fire model of intermediate complexity has been implemented in the SSiB4/TRIFFID, called SSiB4/TRIFFID-Fire. The fire model developed by Li et al. (2012; 2013) was first built on the model platform of CLM-DGVM, and has been incorporated in IAP-DGVM (Zeng et al., 2014), CLM4.5 (Oleson et al., 2013), CLM5 (Lawrence et al., 2019), LM3 in Earth system model GFDL-ESM (Rabin et al., 2018; Ward et al., 2018), AVIM in Climate System Model BCC-CSM (W. P. Li, personal comm.), E3SM Land Model (ELM; Ricciuto et al., 2018), NASA GEOS catchment-CN4.5 model (Zeng et al., 2019), and DLEM (Yang et al., 2014), and partly used in GLASS-CTEM (Melton and Arora, 2016). The following briefly describes the fire schemes adapted from Li et al. (2012; 2013) and Li and Lawrence (2017) and our modifications.

The fire model comprises three parts: fire occurrence, fire spread, and fire impact. The basic equation is that the burned area in a grid cell (A_b, km^2 s^{-1}) is determined by the number of fires per time step (N_f, count s^{-1}) and the average spread area per fire (a, km^2 count^{-1}):

$$A_b = N_f a. \quad (1)$$

4.2.2.1 Fire occurrence

N_f is the product of the number of potential ignition counts due to both natural causes (I_n, count s^{-1} km^{-2}) and human ignitions (I_a, count s^{-1} km^{-2}), fuel availability (f_b), fuel combustibility (f_m), and human suppression factor (f_{eo}). In this paper, we only consider non-crop fire by excluding the cropland fraction (f_{crop}) from burning:

$$N_f = (I_n + I_a) f_b f_m f_{eo} (1 - f_{crop}) A_g, \quad (2)$$

where A_g is the land area of the grid cell (km^2). Fires in the croplands are excluded here due to their small extent within the major fire regions and their relatively low intensity (Bistinas et al., 2014). Cropland fire is still a major uncertainty in remote sensing datasets (Randerson et al., 2012), and more data and investigation are needed.

The number of natural ignitions is related to lightning flashes (I_l, count s^{-1}), cloud-to-ground lightning fraction, $\frac{1}{5.16+2.16\cos[3,min(60,\lambda)]}$, which depends on latitude λ (Prentice and Mackerras, 1977), and ignition efficiency (ψ = 0.22). The anthropogenic ignition, I_a, is parameterized using the number of potential anthropogenic ignitions by a person ($\alpha = 1.35 \times 10^{-9}$ count per person s^{-1}) and population density (D_p; person) (Venevsky et al., 2002):

$$I_n = \frac{\psi}{5.16+2.16\cos[3,min(60,\lambda)]} I_l, \quad (3)$$

$$I_a = \alpha D_p \times (6.8 D_p^{-0.6}). \quad (4)$$

The fuel availability f_b (fraction, range 0−1) is given as:

$$f_b = \begin{cases} 0 & B_{ag} \le B_{low} \\ \frac{B_{ag}-B_{low}}{B_{up}-B_{low}} & B_{low} < B_{ag} < B_{up}, \\ 1 & B_{ag} \ge B_{up} \end{cases} \quad (5)$$

where B_{ag} (g C m^{-2}) is the aboveground biomass (leaf and stem in SSiB4/TRIFFID-Fire) of all PFTs. Following Li et al. (2012), we use B_{low} = 155 g C m^{-2} as the lower fuel threshold, below which fire does not occur and B_{up} = 1050 g C m^{-2} as the upper fuel threshold, above which fuel load is not a constraint for fire occurrence.

Fuel combustibility f_m (fraction, 0−1) is given as:

$$f_m = f_{RH} f_\theta, \quad (6)$$

where f_{RH} and f_θ represent the dependence of fuel combustibility on relative humidity (RH; %)

and the root zone soil moisture (θ), respectively (Li and Lawrence, 2017). Following Li et al. (2013), we assume f_m= 0 when surface air temperature T is below -10 ℃. f_{RH} reflects the impact of real-time climate conditions on fuel combustibility while f_θ reflects the response of fuel combustibility to the preceding climate conditions (Shinoda and Yamaguchi, 2003):

$$f_{RH} = \begin{cases} 0 & RH \geq RH_{up} \\ \left(\frac{RH_{up}-RH}{RH_{up}-RH_{low}}\right)^{1.3} & RH_{low} < RH < RH_{up}, \\ 1 & RH \leq RH_{low} \end{cases} \quad (7)$$

$$f_\theta = \begin{cases} 0 & \theta \geq \theta_{up} \\ \left(\frac{\theta_{up}-\theta}{\theta_{up}-\theta_{low}}\right)^{0.7} & \theta_{low} < \theta < \theta_{up}. \\ 1 & \theta \leq \theta_{low} \end{cases} \quad (8)$$

Relative humidity suppresses fire occurrence when it is larger than RH_{up} = 70 %, and relative humidity does not constrain fire when it is smaller than RH_{low} = 30 %. The PFT-dependent θ_{up} and θ_{low} are used as the upper and lower thresholds of soil moisture in a similar way as the thresholds of relative humidity (Table 4.1). In Li fire scheme, this factor (f_θ) is parameterized using root-zone soil moisture potential factor β (0-1.0), a model-dependent variable used to calculate transpiration in CLM (Li and Lawrence 2017). β_{low}=0.85 and β_{up}=0.98 are used as the lower and upper thresholds for all PFTs, yet the narrow range of β in CLM5 has led to fire model too sensitive to drought. In SSiB4/TRIFFID-Fire, the root-zone soil moisture θ is found to be the best variable to describe the dependence of fuel combustibility on the preceding climate.

The human suppression factor (f_{eo}; 0-1) reflects the demographic (f_d) and economic (f_e) impact on fire occurrence in populated areas (population density $D_p > 0.1$ per person km^{-2}):

$$f_{seo} = f_d f_e. \quad (9)$$

The human suppression is assumed to be negligible (f_{seo}=1) when $D_p \leq$ 0.1 person km^{-2}. A detailed description of f_d and f_e parameterization can be found in Li et al. (2012; 2013).

4.2.2.2 Average spread area after fire ignition

The average spread area of a fire is assumed elliptical in shape with the ignition point located at one of the foci and the fastest spread occurring along the major axis. The average burned area of a fire a (km^2 per count) is represented as (Li et al., 2012):

$$a = \pi L_B (u_{max} g_0 F_m \tau / 1000)^2 F_{se}, \quad (10)$$

where L_B is the length-to-breadth ratio of the ellipse shape and is related to the wind speed, W (m s^{-1}):

$$L_B = 1.0 + 10.0[1 - \exp(-0.06W)]. \quad (11)$$

u_{max} is the PFT-dependent maximum fire spread rate (m s^{-1}; Table S4.1); $g_0 = 0.05$ is the dependence of fire spread rate perpendicular to the wind direction; F_m is the influence of fuel wetness on fire spread and is assumed to be related to f_m in the fire occurrence Eq. (6):

$$F_m = f_m^{0.5}. \quad (12)$$

τ (=3600*24 s) is the global average fire duration, which is simply taken to be one day as reported by Giglio et al. (2006). The human suppression factor, F_{se}, reflects the human impact on fire spread through fire-fighting activities and is parameterized following Li et al. (2013).

4.2.2.3 Carbon emissions, post-fire mortality, and emissions of aerosols and trace gases

In post-fire regions, the fire carbon emission, φ_j (g C s^{-1}), from the vegetation tissue (leaf, stem, root) of the *j*th PFT is calculated based on the burned area (A_b; km^2 s^{-1}):

$$\varphi_j = A_b \boldsymbol{C_j} \cdot \boldsymbol{CC_j}. \quad (13)$$

$\boldsymbol{C_j} = (C_{leaf}, C_{stem}, C_{root}, C_{litter})$ is carbon density vector (g C km^{-2}) for leaf, stem, root, and litter of the *j*th PFT calculated in TRIFFID. As the carbon cycle in current SSiB4/TRIFFID does not explicitly represent the litter carbon storage and decomposition, we assume the litter carbon and woody debris account for about 25% of aboveground biomass for global forest and about 30% for

savanna/grassland based on previous studies (Pan et al., 2011; de Oliveira et al., 2019). $\boldsymbol{CC_j}$ is the corresponding combustion completeness for leaf, stem, root, and litter of the *j*th PFT (Table S4.2). Meanwhile, fire-induced mortality transfers carbon from uncombusted leaf, stem, and root to litter:

$$\psi_j = A_b \boldsymbol{C}_j \cdot (1 - \boldsymbol{CC}_j) \cdot \boldsymbol{M}_j, \quad (14)$$

where $\boldsymbol{M}_j = (M_{leaf}, M_{stem}, M_{root})$ is the corresponding mortality factor (Table S4.2).

Finally, the emissions of trace gases and aerosols species x for the *j*th PFT ($EM_{x,j}$, g s^{-1}) can be calculated from carbon emissions (φ_j) using the PFT-dependent emission factor ($EF_{x,j}$, g species (kg dm)$^{-1}$):

$$EM_{x,j} = EF_{x,j} \frac{\varphi_j}{[C]}, \quad (15)$$

where $[C]$ (= 0.5 g C (kg dm)$^{-1}$) is a unit conversion factor from dry matter to carbon (Li et al., 2019). The emission factors, $EF_{x,j}$, of trace gases and aerosols in Table S4.3 are based on Andreae (2019). The emissions of trace gases and aerosols can be applied in the atmospheric chemistry model to calculate the production of secondary aerosols, transport of pollutants, and the resultant aerosol direct and indirect effects on climate.

4.2.2.4 Including the fire effect on the carbon pool

When Li et al. fire model is coupled with CLM, the vegetation distribution is prescribed using satellite-based land cover, and therefore the fire impact on vegetation cover is not simulated. In SSiB4/TRIFFID-Fire, the fire-related carbon loss due to combustion and post-fire mortality is transferred to changes of PFT fraction based on carbon balance.

In TRIFFID (Cox, 2001), the fractional change of the *j*th PFT ($\frac{df_j}{dt}$) is governed by the Lotka–Volterra equation:

$$\frac{df_j}{dt} = \frac{\lambda_j NPP_j f_j}{Cv_j}\left[1 - \sum_j c_{ij} f_j\right] - \gamma_j f_j, \quad (16)$$

where f_j is the fractional coverage of the *j*th PFT, $\lambda_j\ NPP_j$ is the carbon available for spreading, Cv_j is the carbon density (g C km^{-2}), c_{ij} is the competition coefficient between the *i*th and *j*th PFTs, and γ_j (s^{-1}) is the constant disturbance representing the loss of PFT fraction due to fires, pests, windthrow, and many other processes.

When fire model is coupled to SSiB4/TRIFFID, the loss of PFT fraction due to fires (β_j) can be explicitly derived from the fire-induced carbon loss:

$$\beta_j = \frac{(\varphi_j+\psi_j)\cdot f_j}{Cv_j}, \tag{17}$$

where φ_j and ψ_j are PFT-dependent carbon loss due to combustion and post-fire mortality, respectively. The fire-caused PFT fraction loss results in bare soil for vegetation spreading decided by the competition strategy in TRIFFID. As such, fire disturbance is explicitly represented which varies in space and time, and the original γ_j is adjusted to γ_j' to exclude fire disturbance (Table 4.2):

$$\frac{df_j}{dt} = \frac{\lambda_j \cdot NPP_j \cdot f_j}{c_j}\left[1 - \sum_j c_{ij} f_j\right] - \left(\gamma_j' + \beta_i\right) f_j.$$

4.2.3 Implementing fire model in SSiB4/TRIFFID

In SSiB4/TRIFFID, SSiB4 provides GPP, autotrophic respiration, and other physical variables such as canopy temperature and soil moisture every 3 hours for TRIFFID (Figure 4.1). TRIFFID accumulates the 3-hourly GPP and respiration and provides biotic carbon, PFT fractional coverage, vegetation height, and LAI every 10 days, which are used to update surface properties (albedo, canopy height, roughness length, and aerodynamic/canopy resistances) in SSiB4. When the fire model is included, it uses the meteorological forcings and physical variables provided by SSiB4 every 3 hours and the biophysical properties (PFT fraction and biotic carbon) provided by TRIFFID every 10 days. The fire model calculates the burned area, carbon combustion, post-fire

mortality, and emissions every 3 hours, and the fire-induced carbon loss is subtracted from fuel load. The carbon loss is accumulated within 10 days in the fire model and is transferred to TRIFFID on Day 10. TRIFFID updates the vegetation dynamics based on carbon balance on Day 10, using the net primary production, fire-induced carbon loss, and PFT competition strategy. The updated vegetation dynamics are transferred to SSiB4 to reflect fire effects on surface properties.

4.3 Experimental setup and data

4.3.1 Experimental design

Two sets of offline experiments have been conducted using SSiB4/TRIFFID-Fire, which consist of FIRE-ON (SSiB4/TRIFFID-Fire with fire model switched on) and FIRE-OFF (SSiB4/TRIFFID-Fire with fire model switched off). To obtain the initial conditions for these two experiments, similar to our previous SSiB4/TRIFFID experiments (Zhang et al., 2015; Liu et al., 2019), we conducted spin-up simulations ($SP_{FIRE\text{-}ON}$ and $SP_{FIRE\text{-}OFF}$) for 100 years to reach a quasi-equilibrium PFT distribution with and without fire disturbance. These spin-up simulations were initialized using the quasi-equilibrium state from Liu et al. (2019, SP_{INIT} in Figure 4.2) and were driven by climatology forcing averaged in 1948-1972 and atmospheric CO_2 concentration, population density, and GDP in 1948 (Figure 4.2). Following Liu et al. (2019), the quasi-equilibrium status is defined as the rate of relative change in fractional coverage of all PFTs is less than 2 % over the last 10 years of simulation.

Based on the quasi-equilibrium status with fire disturbance ($SP_{FIRE\text{-}ON}$), a transient run was performed (FIRE-ON) with the fire model turned on from 1948 to 2014 (Figure 4.2). The model was forced by 3-hourly meteorological forcings, yearly updated atmospheric CO_2 concentration, population density, and GDP data. FIRE-ON produced the fire regime, ecosystem, and surface

conditions during 1948-2014. A FIRE-OFF run, based on $SP_{FIRE\text{-}OFF}$, was carried out with the fire model switched off during 1948-2014. The vegetation distribution was allowed to respond to climate variations in both FIRE-ON and FIRE-OFF simulations and to fire disturbances only in the FIRE-ON.

4.3.2 Model input and validation data

The meteorological forcings used to drive SSiB4/TRIFFID-Fire for the period of 1948–2014 are from the Princeton global meteorological dataset for land surface modeling (Sheffield et al., 2006), including surface air temperature, surface pressure, specific humidity, wind speed, downward shortwave radiation flux, downward longwave radiation flux, and precipitation (Table 4.3). The dataset is constructed by combining global observation-based datasets with the NCEP/NCAR reanalysis. The spatial resolution is 1.0°×1.0°, and the temporal interval is 3 hours.

The required inputs for driving the fire model are listed in Table 4.3. The 2-hourly climatology lightning flashes data from NASA LIS/OTD v2.2 at 2.5°×2.5° resolution is used to calculate the number of natural ignitions. The population density data are provided by the Gridded Population of the World version 3 (GPWv3; Ciesin, 2014) for 1990-2005 and Database of the Global Environment version 3.1 (HYDEv3; Goldewijk et al., 2010) for 1850−1980. GDP per capita in 2000 is from van Vuuren et al. (2007). The population density and GDP data are used to calculate the human ignitions and suppression in the fire model. The agriculture fraction is obtained from the GLC2000, which represents the agriculture distribution for the year 2000 (Bartholome and Belward, 2005). All the datasets are resampled to 1.0°×1.0° spatial and 3-hourly temporal resolution.

The Global Fire Emission Database (GFED) is a fire dataset derived mainly from MODIS satellite observations (van der Werf et al., 2006; van der Werf et al., 2010; Giglio et al., 2013).

The GFED fire product provides the burned area and fire emissions on the global scale and has been widely used for fire model validation and calibration (van Marle et al., 2017; Li et al., 2019). The latest version of GFED, GFED4s, has included the contribution from small fires that are below the MODIS detection limit (van der Werf et al., 2017). The burned area and carbon emissions simulated by SSiB4/TRIFFID-Fire will be validated using gridded monthly GFED4s fire products in 2000–2014 at 0.25° spatial resolution.

We also evaluate the simulated vegetation distribution, CO emission from fire, and GPP with observations. We use the vegetation fraction from GLC2000 generated in Liu et al. (2019) by calculating the percentage of each land cover type in 1.0°×1.0° and converting to PFTs in SSiB4/TRIFFID-Fire. The CO emission from Zheng et al. (2019) is an inversion-based product that uses CO emission from multiple sources as prior, and performs inversion simulations constrained by atmosphere CO concentration retrieved from the satellite. It provides the latest CO emission estimate from fire in 2000-2017. FLUXNET Model Tree Ensemble (FLUXNET-MTE) GPP is upscaled from FLUXNET observations to the global scale using the machine learning technique MTE (Jung et al., 2011). The FLUXNET-MTE GPP at 0.5°×0.5° spatial resolution in 1982–2011 has been resampled to 1.0°×1.0° to be compared with SSiB4/TRIFFID-Fire.

4.4 Results

This section evaluates the model simulation of burned area, carbon emissions, PFT fraction, and GPP by comparing FIRE-ON results with GFED4s, GLC2000, and FLUXNET-MTE data. Specifically, we will focus on the model description of fire seasonality. After model validation, SSiB4/TRIFFID-Fire is applied to assess the long-term fire effect on the ecosystem and surface energy budget using the differences between the FIRE-ON and FIRE-OFF.

4.4.1 Burned Area

The simulations of burned area are evaluated using satellite-based product GFED4s for the period of 2000-2014. Figure 4.3 shows the 2000-2014 annual burned fraction in GFED4s and SSiB4/TRIFFID-Fire and their latitudinal distribution. The simulated global burned area is 471.9 Mha yr^{-1}, slightly higher than the estimate from MODIS Collection 6 in 2002-2016 (423 Mha yr^{-1}; (Giglio et al., 2018)) but very close to the value from GFED4s (478.1 Mha yr^{-1}). The spatial distribution of observed burned area is well captured in the SSiB4/TRIFFID-Fire simulation with a spatial correlation of 0.80. Both GFED4s and SSiB4/TRIFFID-FIRE show that the major burned area is concentrated in the tropical savannas (5-15º N; 5-20º S), including the Northern Hemisphere African (NHAF), Southern Hemisphere African (SHAF), Southern Hemisphere South American (SHSA), and northern Australia (Figure 4.3a and 3c). GFED4s shows that the Northern African savanna has a larger latitudinal burned area in a narrower fire band compared to the Southern African savanna (Figure 4.3b). SSiB4/TRIFFID-Fire captures the latitudinal band in burned Northern African savanna but underestimates its magnitude (Figure 4.3d). Another burned area peak occurs around 50º N in Boreal Asia (BOAS) and Boreal North America (BONA). The humid climate there suppresses fire ignition yet the high level of aboveground biomass and a lack of human suppression facilitate fire occurrence and spread, which results in an intermediate burned area in the boreal regions. The low burned fraction for deserts and tropical rainforests, which is caused respectively by low fuel availability and combustibility, are also well simulated (Figure 4.3a), leading to the minimum burned area around the equator and subtropical regions.

We also evaluate the 14 sub-regions following the definition in GFED according to the fire behavior similarity (van der Werf et al., 2006). The burned area in African savanna accounts for more than 60 % of the global burned area in both GFED4s and SSiB4/TRIFFID-Fire (Figure 4.4b).

The simulated burned areas in SHAF and NHAF are 168.3 Mha and 124.5 Mha, respectively, very close to GFED4s burned areas in SHAF (167.9 Mha) but slightly underestimated in NHAF (155.5 Mha). The negative bias in NHAF burned area is the main cause of the underestimation in the latitudinal fire distribution around 10° N (Figure 4.3d). SSiB4/TRIFFID-Fire also captures the burned fraction in other major fire regions such as Australia (AUST) and SHSA (Figure 4.4b), which are dominated by savanna fire. We notice that the burned area in western and central parts of temperate North America (TENA) is overestimated (Figure 4.3c and Figure 4.4b). Nevertheless, the burned area there is relatively small compared to that in major fire regions such as SHAF and NHAF. This shortcoming has been reported in a number of fire models (Pfeiffer et al., 2013; Lasslop et al., 2014; Yue et al., 2014; Venevsky et al., 2019). The reasons include an underestimate of anthropogenic suppression, inaccurate description of fuel pattern/grassland fraction, and landscape fragmentation from roads and other anthropogenic features. The burned area in the Middle East (MIDE) is also overestimated (Figure 4.4b) as a larger burned area is simulated at the northern boundary of the Sahara Desert and south of the Black Sea (Figure 4.3c). The simulated burned area is underestimated in BONA and BOAS where fire has a lower incidence but a longer duration compared to the global average (Ward et al., 2018; Venevsky et al., 2019). As we assume all fires persist for one day, the burned area in boreal regions is therefore underestimated. Further improvements, such as multi-day burning and a deliberate scheme for anthropogenic effect, are necessary in regional applications.

In 8 out of the 14 sub-regions, SSiB4/TRIFFID-Fire well reproduces the observed interannual variability (IAV) of burned area, with the correlation between simulations and observations significant at $p < 0.05$ (Figure 4.4c). The regions are NHAF, SHSA, AUST, TENA, Central America (CEAM), Europe (EURO), Southeast Asia (SEAS), and Equatorial Asia (EQAS).

In particular, a decline in NHAF burned area is found in both SSiB4/TRIFFID-Fire and GFED4s, which has been attributed to agricultural expansion and intensification in recent fire studies (Andela et al., 2017; Teckentrup et al., 2019). Although our model does not have an explicit description of agriculture fraction and intensification changes, the anthropogenic effect is implicitly included by relating fire suppression to population density and GDP (Li et al., 2013). Meanwhile, SSiB4/TRIFFID-Fire also captures the IAV in SEAS and EQAS, which is known to be driven by climate factors such as relative humidity and soil moisture.

The simulated IAV of SHAF burned area is not as good as other savanna fire regions (e.g., NHAF, SHSA, and AUST), although the IAV is small there (Figure 4.4c). Some studies have reported that humans have a substantial impact on SHAF fire, which limits the effect of climate-induced IAV (Archibald et al., 2010; Venevsky et al., 2019). In addition, the simulated IAV of burned areas is lower than observations in BONA and BOAS as the model fails to capture some extreme fire events (Fig. S4.1). The lower variability comes from the climatology lightning data (Pfeiffer et al., 2013). As lightning flash is the predominant ignition source in the Northern Hemisphere high latitudes, the application of climatology lightning has a greater impact in boreal regions than in other parts of the globe.

Figure 4.5 shows the pointwise temporal correlation of the multi-year monthly burned area between SSiB4/TRIFFID-Fire and GFED4s averaged in 2000-2014. SSiB4/TRIFFID-Fire captures the fire seasonality in most regions, including the Southern African savanna, South American savanna, the northeastern part of Boreal Asia, the eastern part of Boreal America, Southeast Asia, and Equatorial Asia. Specifically, we examine the simulation of peak fire month and fire season length in SSiB4/TRIFFID-Fire following the definition that fire seasons include months with more than 1/12 of the mean annual burned fraction (Venevsky et al., 2019). Over the

globe, August and December are the two peak fire months that have the largest contribution to the annual burned area (Figure 4.6a). SSiB4/TRIFFID-Fire generates two fire seasons in June-July-August and December-January-February, capturing the peak month in August but underestimating the burned area in December. In the tropical savannas (SHAF, SHSA, and NHAF), fire activities concentrate in the local dry season, and the burned area during the fire season accounts for more than 80 % of the annual burned area (Figure 4.6b-d). The burned area in Southern Hemisphere major fire regions, SHAF and SHSA, peaks in August and September in both observations and model. The simulated fire seasons in SHAF (June-October) and SHSA (July-October) match precisely with the observations. In other fire regions such as SEAS and EQAS, SSiB4/TRIFFID-Fire also reproduces the fire seasonality and peak fire months (Figure 4.6e-f). Compared with the latest results from other fire models (Hantson et al., 2020), our model produces more realistic burned area peak and fire season duration.

Figure 4.5 shows, however, that the fire seasonality in the Northern Hemisphere Africa, the western part of Boreal Asia, eastern China, western Australia, and the middle eastern US needs to be improved. The simulated fire season in West Africa is December-March (Figure 4.6d), slightly shifted from the fire season in GFED4s (November-February), which contributes to the lower fire peak in December in the global burned area. The recent FireMIP models also show a 2-months delay in peak fire month in Northern tropics (Hantson et al., 2020), which might be related to the representation of seasonality in vegetation production and fuel build up. In BOAS, the first fire season occurs in April and May. The observed fire season is not captured in SSiB4/TRIFFID-Fire as the model underestimates the burned area in western Siberia due to too wet moisture conditions that come from the high precipitation and specific humidity in the forcing data. A similar scenario is found in Western Australia (Figure 4.6h). Meanwhile, the absence of crop fire

in SSiB4/TRIFFID-Fire also contributes to the low temporal correlation with the observations in agricultural areas such as the middle eastern US and eastern China, where fires are used to clear the crop residues (Xia et al., 2013; van der Werf et al., 2017).

Overall, SSiB4/TRIFFID shows good consistency in the simulation of peak fire month and fire season duration in most regions, probably related to the better representation of vegetation-fire interactions in SSiB4/TRIFFID-Fire which updates fire effects on vegetation dynamics every 10 days. The inaccurate simulation of fire season in several fire regions could come from deficiency of the forcing data, the inaccuracy in dynamic vegetation processes, or some processes that control the fire but are not represented in the model. More comprehensive observational data are needed to improve the simulation in these areas.

4.4.2 Fire emissions

Biomass burning emissions are determined by burned area, fuel combustion rate per unit area, and emission factors per unit mass of fuel burned (van der Werf et al., 2017). The carbon emission in SSiB4/TRIFFID-Fire is 2.19 Pg yr^{-1}, higher than the estimate from GFED4s (2.07 Pg yr^{-1}) (Figure 4.7). SSiB4/TRIFFID-Fire captures the high carbon emissions in tropical savannas, the intermediate emissions in Northern Hemisphere boreal forests, and the low emissions in humid forests and deserts with a spatial correlation of 0.72, higher than the simulation in Li et al. (2013) (0.61 compared with the GFED3). In general, the spatial distribution of carbon emissions coincides with that of the burned area: SHAF, NHAF, and SHSA are the major fire emission regions and they contribute to 65.4% of the total emission in both GFED4s and SSiB4/TRIFFID-Fire (Figure 4.8a). The exception occurs in EQAS, BOAS, and BONA, where the fire emissions contribute to 11.6 % of the global emissions with only 2.5 % of the global burned area there. The regions have large areas of peatland, which contains a thick layer of soil carbon and emits several times more

trace gases per unit biomass combusted than fires in savannas (van der Werf et al., 2010). As our model does not include the peat soil type, fire emissions are underestimated in these regions.

The interannual variability (IAV) of fire emissions is captured in SSiB4/TRIFFID-Fire in 7 out of 14 fire regions with a significance level $p < 0.05$ (Fig. S2). Both model and observations have shown a decrease in carbon emissions in NHAF (Figure 4.8b), which contributes to the decrease in global fire emission in 2000-2014 (Figure 4.7e). SSiB4/TRFFID-Fire suggests that the decline of global fire emissions starts in the 1950s, which is also found in some of the FireMIP models (Li et al., 2019). Similar to our conclusions in the IAV of burned areas, the IAV of carbon emissions in SHSA is small and is not well represented in the model (Figure 4.8c).

The CO emission from fire is one of the key variables in fire modeling as CO plays a vital role in atmospheric chemistry. The simulated global CO emission is 433.7 Tg $year^{-1}$ in 2000-2014, very close to the observational estimates (434.0 Tg $year^{-1}$) from Zheng et al. (2019) with a spatial correlation of 0.74. The inversion-based and simulated monthly CO emissions in Africa are compared in Figure 4.9. We find the annual cycle of CO emission in SHAF is well captured in SSiB4/TRIFFID-Fire, which shows the largest CO emission occur in JJAS and the regions with high-emission (Figure 4.9b) are coincident with those in observations (Figure 4.9a). In NHAF, SSiB4/TRIFFID-Fire reproduces the large CO emission in DJF, although the model slightly underestimates CO emission in December and overestimates it in February. The seasonality of CO emission broadly follows that of burned area, which further demonstrates that our model has shown promising results in seasonal fire simulations.

4.4.3 PFT distribution and GPP

The simulation of vegetation coverage, which represents model description of biomass allocation and influences the fuel availability and flammability in fire modeling, is evaluated

against GLC2000 (Bartholome and Belward, 2005). As the dynamic vegetation model only includes natural PFTs, the simulated PFT fraction in one grid box is scaled using the non-agriculture fraction from GLC2000. Overall, the vegetated areas cover 80.6 % of global land areas, very close to the estimates from GLC2000 (80.8 %). The simulated tree cover is 34.1 %, higher than 29.8 % in GLC2000. Compared with the observations (Figure 4.10a), SSiB4/TRIFFID-Fire captures the fractional coverage of trees in the Amazon rainforest, tropical Africa, Equatorial Asia, Southeast Asia, Southeast North America, and Northern Hemisphere Boreal regions (Figure 4.10c). The BET is concentrated in tropics, and the NET is mostly found in the North America and Eurasia Boreal zones (Figs. S3a-c). The C3 and C4 grasses are found in the Northern Hemisphere Africa, Southern Africa, South America, Central US, Eurasian steppes, and east Australia (Figure 4.10b and 10d). The simulated C3 and C4 fractions are 11.1 % and 7.5%, respectively, similar to the estimates in GLC2000 (11.9 % for C3 and 7.9 % for C4; Liu et al. 2019). Shrubs are primarily located in the semi-arid regions and the pan-Arctic area and tundra is limited to the pan-Arctic area and Tibetan Plateau (Figs. S3f-g). SSiB4/TRIFFID-Fire is shown to capture some key processes of fire-vegetation interactions under the current climate, which is important to study fire effects on the ecosystem.

We also compare the simulated GPP averaged over 1982-2011 to FLUXNET-MTE GPP (Jung et al., 2011) to examine the modelled impact of fire on carbon. SSiB4/TRIFFID-Fire captures the distribution of global GPP with a spatial correlation of 0.93 ($p < 0.05$) (Fig. S4). The highest GPP occurs in the tropical evergreen forest and decreases with latitude in both observations and model. However, the simulated GPP has a negative bias in the Amazon tropical forest and a positive bias in tropical Africa and boreal regions. The simulated global GPP is 141 Pg C yr^{-1}, higher than the FLUXNET-MTE estimate (119 Pg C yr^{-1}; Jung et al., 2011), but is within the range

of simulated GPP in current DGVMs (111 - 151 Pg C yr^{-1}; (Piao et al., 2013)). In addition, the correlation of IAV of global GPP is 0.68 ($p < 0.05$) between SSiB4/TRIFFID-Fire and FLUXNET-MTE, indicating that the model has reasonably captured the terrestrial ecosystem variability during the historical period.

4.4.4 Fire effects on ecosystem characteristics and surface properties

In this section, we investigate long-term fire effects on ecosystem characteristics, surface properties, and surface energy budget using the differences between FIRE-ON and FIRE-OFF (FIRE-ON minus FIRE-OFF). In SSiB4/TRIFFID-Fire, fire is found to cause a strong decrease in tree fraction by 12.6 % (about 4.5 % of the land surface). Meanwhile, the fractional coverage of grass and bare land is increased on 3.4 % and 0.5 % of the land surface, respectively (Figure 4.11a-b). The tree cover reduction is concentrated in Southern Africa, Northern Africa, and South America, which are dominated by C4 savanna in FIRE-ON (Fig. S3), suggesting that fire is an important determinant of structure and functions of the savanna; otherwise it would be encroached by trees. The magnitude of change simulated is generally consistent with the results from long-term fire experiments in Kruger National Park, South Africa, which showed that fire reduced woody cover by 30-50% (Smit et al., 2010). The changes in the fractional coverage of trees and grass are associated with tree mortality after fire and the fast re-growth of grass PFTs with space and nutrient availability during the post-fire recovery season. Over the globe, fire is simulated to reduce LAI by 3.6% (0.10 m^2 m^{-2}) and shorten vegetation height by 12.7% (1.24 m).

In Africa, the simulated fire effects on vegetation structure (tree/grass cover, LAI, and vegetation height) peak in the tropical savanna surrounding the forests and gradually decrease towards the deserts (Figure 4.11). When fire model is turned off, the tree cover expands in the wetter savanna around the tropical African forest where the climate (mainly rainfall in the model)

allows for more trees to approach canopy closure such that grasses can be effectively excluded (Figure 4.10e). The grass cover shrinks to the southern/northern part of Southern/Northern African savanna (Figure 4.10f), where tree populations are constrained by environmental conditions.

Our results are consistent with the long-term fire experiments which reported that fire strongly affected vegetation structure, lowering the proportions of trees to fire-resistant grasses and reducing the vegetation height and aboveground biomass (Shackleton and Scholes, 2000; Higgins et al., 2007; van Wilgen et al., 2007; Furley et al., 2008; Smit et al., 2010; Devine et al., 2015), and that fire impact is more remarked in wetter savanna than in drier savanna (Moreira, 2000; Sankaran et al., 2005). However, the long-term fire experiments were only conducted in very limited regions and mostly focused on site-level fire impact (Furley et al., 2008). The assessment of continental and global fire impact on vegetation and carbon can only be achieved by fire-coupled DGVMs. After appropriate validation of fire effects on the local scale, SSiB4/TRIFFID-Fire can be used as an effective tool to describe the climate potential of the ecosystem without fire disturbance and to quantify fire impact on the global scale.

The changes in vegetation structure modify the albedo, aerodynamic resistance, and evapotranspiration processes, which further influences surface radiation and energy partitioning between latent heat and sensible heat fluxes. In this study, we investigate seasonal fire impact by distinguishing between fire season (DJF for NHAF, and JJA for SHAF and SHSA) and post-fire rainy season (JJA for NHAF, and DJF for SHAF and SHSA) for major fire regions. Because grass PFTs have a higher albedo than tree PFTs, the replacement of trees by grasses/savannas (Figure 4.11a-b) has caused an increase in grid-average albedo, which decreases the net radiation absorbed by surface (Figure 4.12a-b). The reduction in surface radiation is larger in fire season (DJF for NHAF, and JJA for SHAF and SHSA) as the exposure of bare land after fire further enhance the

albedo. The reduction in vegetation height between FIRE-ON and FIRE-OFF (Figure 4.11d) has significantly decreased the roughness length and increased the aerodynamic resistance (Liu et al., 2016), which causes a reduction of sensible heat flux by 4-8 W m^{-2} (Figure 4.12c-d). Our results are in agreement with the observational studies on different fire types (e.g., forest fire and savanna fire) showing that surface properties change after fire results in an increase in albedo (Gholz and Clark, 2002; Amiro et al., 2006b; Sun et al., 2010) and a decrease in sensible heat (Chambers and Chapin, 2002; Liu et al., 2005; Amiro et al., 2006a; Amiro et al., 2006b; Rogers et al., 2013).

The change of latent heat flux varies with seasons in tropical savanna. It is reduced in the fire season and enhanced in the rainy season for each fire region (Figure 4.12e-f). In SSiB4, the grid-average latent heat flux consists of canopy evapotranspiration, canopy interception, and soil evaporation, among which canopy interception normally plays a minor role. During the local fire season, the canopy transpiration is decreased (Fig S5a-b) due to fire-induced vegetation canopy loss. The soil evaporation does not change too much as there is not much surface water to evaporate (Fig S5c-d). Therefore, the grid average latent heat is decreased. During the post-fire rainy season, the canopy transpiration is still reduced as the vegetation has not recovered from the fire. However, the exposure of bare soil has produced more soil evaporation. Therefore, the latent heat can be increased due to enhanced soil evaporation. The significant increase in soil evaporation and latent heat during wet season has been widely observed after vegetation removal, especially when the soil is saturated (Langford, 1976; Dunin, 1987; Gholz and Clark, 2002; Santos et al., 2003; Amiro et al., 2006b). The increase is proposed to be caused by the exposure of moist soil surface, the increase in surface energy that can be used for evaporation, and the smaller surface resistance when dense plant canopy is removed by fire (Schulze et al., 1994). Despite the reduction in surface

radiation, the decreased surface fluxes associated with aerodynamic/surface resistance changes have resulted in an increase in surface temperature throughout the year (Figure 4.12g-h).

Our estimate of fire effects on radiation, surface fluxes, and temperature are qualitatively consistent with Li et al. (2017) but different in the partitioning between sensible heat and latent heat changes. The discrepancies might be attributed to the changes in vegetation distribution. As the vegetation distribution is prescribed in Li et al. (2017), trees and grass are growing taller and denser when the fire model is turned off. In contrast, fire has caused changes in vegetation distribution and conversions of dominant PFTs in SSiB4/TRIFFID-Fire. Tree PFTs are spreading in FIRE-OFF and encroaching the tropical savanna and grassland in Southern Africa, Northern Africa, and South America shown in FIRE-ON. Over the Africa and South American savanna, we find fire has reduced the area-averaged LAI and vegetation height by 0.52 m^2 m^{-2} (12.5 %) and 5.76 m (49.1%), respectively. The larger relative change in vegetation height is simulated as tree PFTs have a greater contrast with grass PFTs in vegetation height than in LAI. Compared with Li et al. (2017), SSiB4/TRIFFID-Fire simulates a greater change in vegetation height but a smaller change in LAI, which probably causes the larger sensible heat changes in our results. Other sources of uncertainties include the differences in the partitioning between latent heat and sensible heat fluxes in land surface models, the differences in the parameterization of the evaporation processes, and the changes due to atmospheric feedbacks, such as cloud cover and precipitation changes.

4.5 Conclusions and discussions

We have implemented a process-based fire model of intermediate complexity into a DGVM, SSiB4/TRIFFID, which is based on the surface water, carbon, and energy balances, as wells as the PFT competition. The high-frequency exchanges between fire model and SSiB4/TRIFFID allow vegetation dynamics and surface parameters, such as albedo and surface

roughness length, to be updated every 10 days based on surface carbon balance, which are rarely applied in other fire models. Moreover, the plant production and biomass allocation are reasonably reproduced in SSiB4/TRIFFID-Fire, which have been considered to contribute to the proper burned area simulation (Forkel et al., 2019; Hantson et al., 2020). The SSiB4/TRIFFID-Fire produces similar global burned area, major regional burned areas, and fire carbon emissions compared to GFED4s. The model captures the decreasing trend in burned area related to human suppression and land management and the interannual variability associated with moisture conditions. It reasonably reproduces the global GPP and PFT distribution, which is important to study fire effects on the ecosystem.

Future development of SSiB4/TRIFFID-Fire are in three aspects. First, SSiB4/TRIFFID-Fire does not explicitly represent the occurrence of peat fire, deforestation fire, and agriculture fire. The inclusion of peat fire and deforestation fire may reduce the negative bias in the burned area and carbon emission in EQAS, BOAS, and BONA, and the parameterization of agriculture fire may improve the fire seasonality simulation in the middle eastern US and eastern China. Second, the effect of agriculture expansion on fire suppression is not considered in current SSiB4/TRIFFID-Fire as we apply a constant agricultural fraction, which is expected to influence the spatial and temporal variations of burned area beyond GDP and population effects (Andela et al., 2017). Third, the carbon cycle in the current SSiB4/TRIFFID version does not explicitly represent the litter carbon storage and decomposition. Therefore, we assume aboveground litter to be 25% and 30% of aboveground biomass for global forest and savanna based on observations from Pan et al. (2011) and de Oliveira et al. (2019). The next generation of SSiB couples SSiB/TRIFFID with DayCent-SOM, which describes the full processes of litter accumulation and

decomposition constrained by nitrogen availability (Parton et al., 1994). An explicit scheme for litter combustion will be updated in the fire model in the new SSiB/TRIFFID.

The SSiB4/TRIFFID-Fire is then applied to study the long-term fire effects on ecosystem characteristics and surface energy. By comparing the simulations with and without fire, we show that fire has reduced global tree cover by 12.6 % (4.5 % of land surface). Meanwhile, the global LAI and vegetation height are decreased by 0.10 m^2 m^{-2} and 1.24 m, respectively. The surface radiation, sensible heat, and canopy evapotranspiration are decreased while the soil evaporation is increased especially during the post-fire rainy season. The change in surface fluxes has caused an increase in surface temperature over most fire regions. As Li et al. (2017) is the only modeling study investigating the long-term fire effects on land energy budget, our simulation provides another approach that quantifies fire effects using a different land surface model with different approaches in parameterizing some land surface processes and vegetation dynamics. More studies with more land surface models/fire models/vegetation dynamics are necessary to explore this issue further. A systematic comparison of long-term fire effects in different fire models such as the current FireMIP project, would allow evaluation of the robustness of model simulations and identification of key uncertainties of fire impacts.

Tables and Figures

Table 4.1 The upper (θ_{up}) and lower (θ_{low}) thresholds of root zone soil moisture for PFTs in SSiB4/TRIFFID-Fire

Vegetation Types	θ_{up}	θ_{low}
BET	0.80	0.30
NET	0.80	0.30
BDT	0.80	0.30
C3 grasses	0.75	0.30
C4 plants	0.75	0.30
Shrubs	0.60	0.30
Tundra	0.60	0.30

Table 4.2 The **disturbance** rate implicitly including fire disturbance (γ_v) and excluding fire disturbance (γ_v').

	BET	NET	BDT	C3 grasses	C4 plants	Shrubs	Tundra
γ_v	0.004 (0.04 with grasses)	0.004(0.04 with grasses)	0.004 (0.04 with grasses)	0.1	0.1	0.05	0.05
γ_v'	0.004	0.004	0.004	0.02	0.02	0.04	0.01

Table 4.3 Datasets used to drive SSIB4/TRIFFID-Fire and evaluate simulations

Variables	Sources	Resolution
Surface air temperature Surface pressure Specific humidity Wind speed Downward shortwave radiation Downward longwave radiation Precipitation	Sheffield et al. (2006)	1°, 3-hourly
Lightning frequency	NASA LIS/OTD v2.2	2.5°, 2-hourly
Population density	GPWv3 (CIESIN, 2005); HYDE v3.1 (Klein Goldewijk et al., 2010)	0.5°, 5 yearly 5', 10 yearly
Gross domestic product (GDP)	van Vuuren et al. (2006)	0.5°, in 2000
Agriculture fraction Vegetation distribution	GLC2000 (Bartholome et al., 2002)	1°, in 2000
Burned area Carbon emission	GFED4s (Randerson et al., 2012; van der Werf et al. 2017)	0.25°, monthly
CO emission	Zheng et al. (2019)	3.75° lon ×1.9° lat, monthly
GPP	FLUXNET-MTE (Jung et al. 2009)	0.5°, monthly

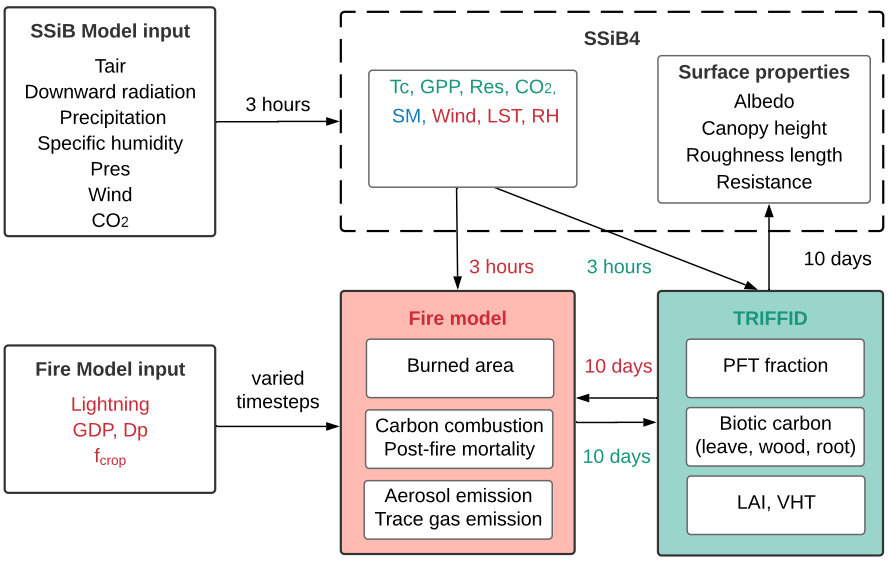

Figure 4.1 Schematic diagram of fire model coupling in SSiB4/TRIFFID-Fire (Tair: air temperature; Pres: surface pressure; Dp: population density; f_{crop}: crop fraction; Tc: canopy temperature; Res: autotrophic respiration; SM: soil moisture; LST: land surface temperature; RH: relative humidity; VHT: vegetation height)

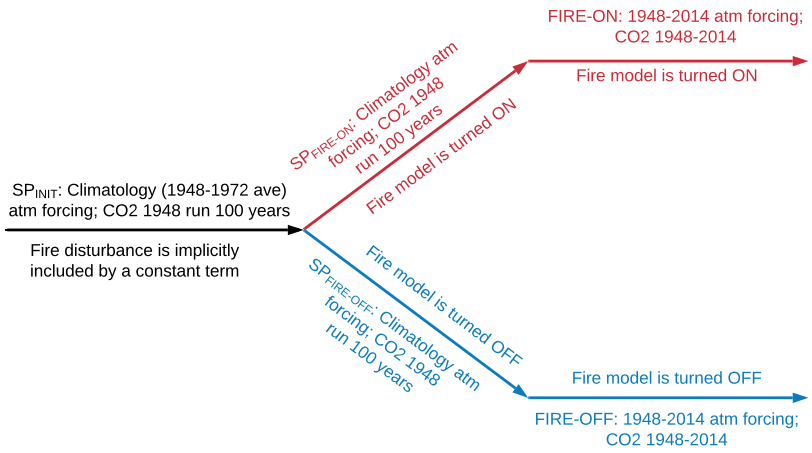

Figure 4.2 Experiment design for FIRE-ON and FIRE-OFF experiments

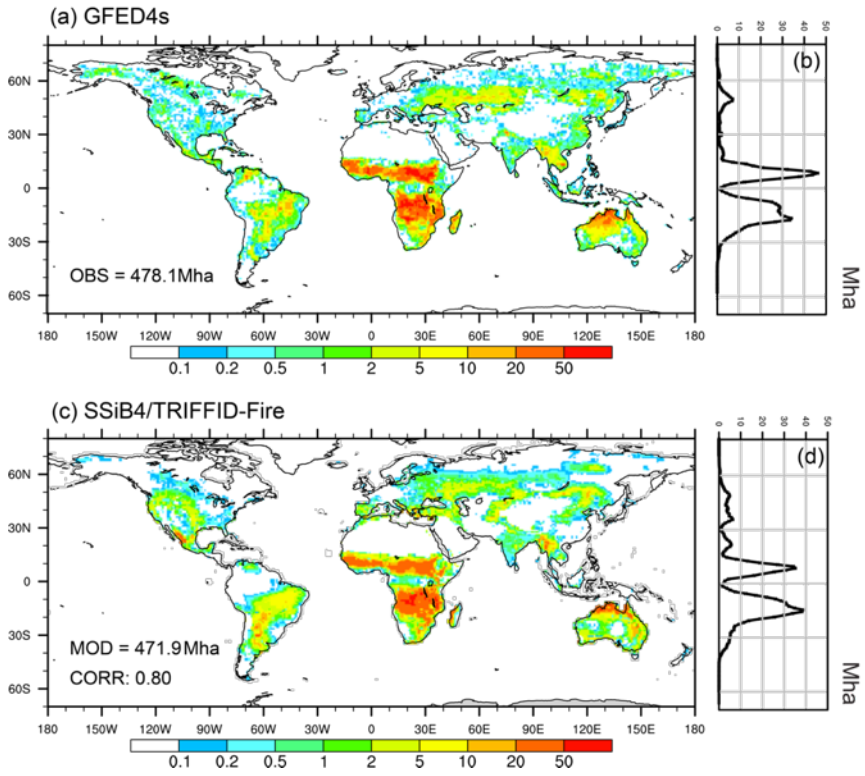

Figure 4.3 Spatial distribution of annual burned fraction (%) averaged over 2000–2014 for (a) GFED4s and (c) SSiB4/TRIFFID-Fire. The right panel shows the zonal mean burned area (Mha) for (b) GFED4s and (d) SSiB4/TRIFFID-Fire

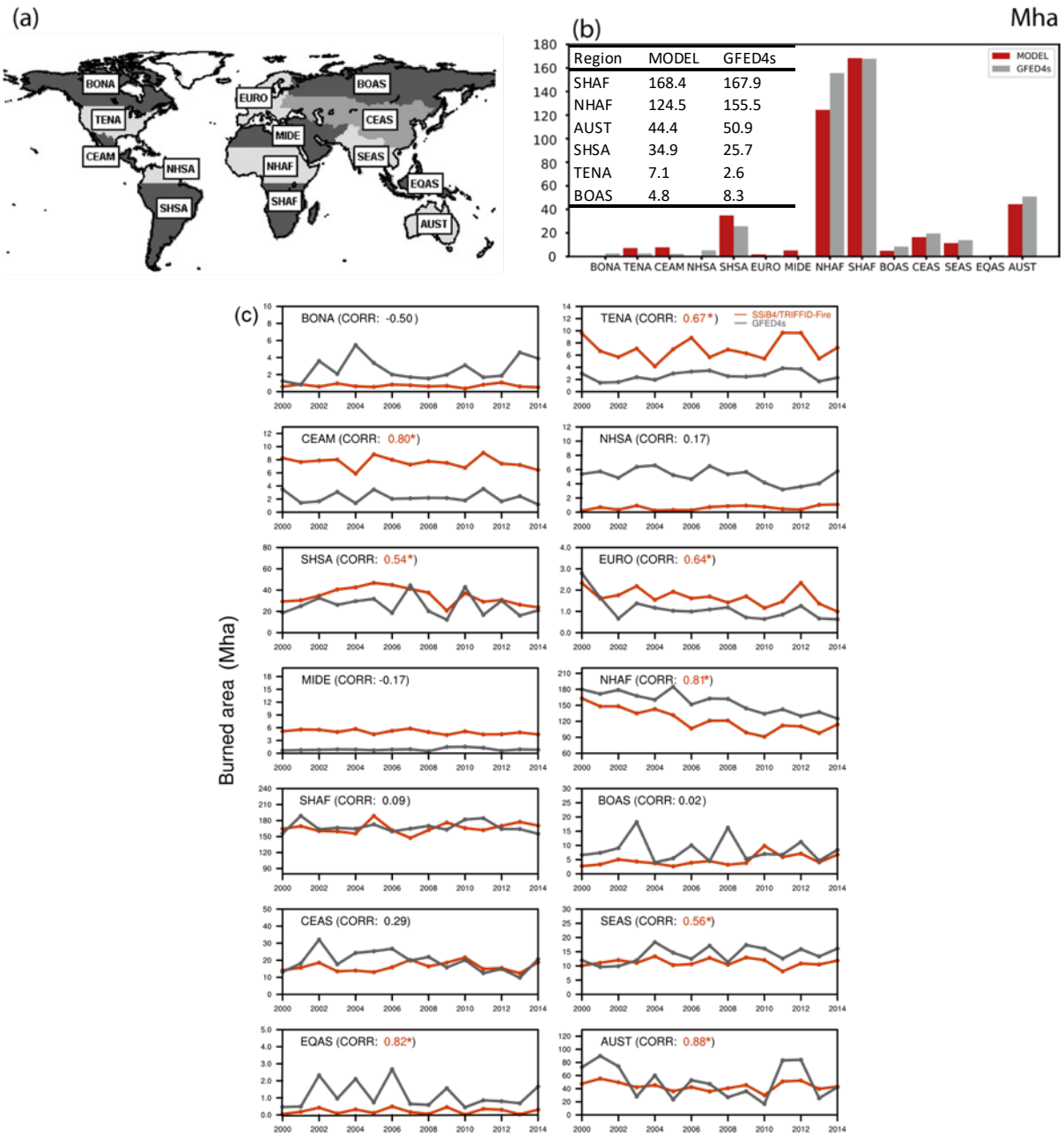

Figure 4.4 (a) Map of 14 regions used in this study, after Giglio et al. (2006, 2010) and van der Werf et al. (2006, 2010) (b) Annual burned area (Mha) averaged over 2000-2014 for GFED4s and SSiB4/TRIFFID-Fire in 14 regions (c) Annual burned area (Mha) for 2000–2014 for GFED4s and SSiB4/TRIFFID-Fire in 14 GFED regions. The "*" and the red color indicate the positive correlation is significant at $p < 0.05$.

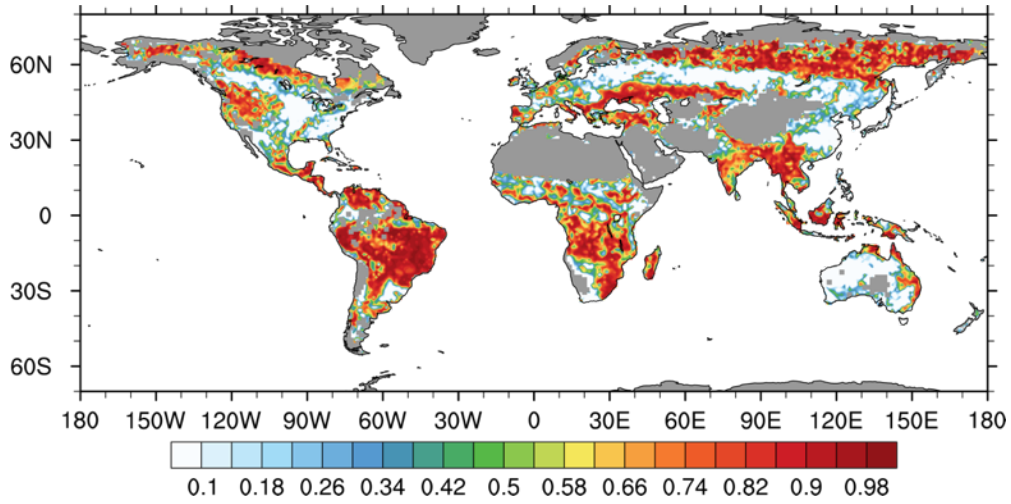

Figure 4.5 Temporal correlation of monthly burned area averaged over 2000-2014 between SSiB4/TRIFFID-Fire and GFED4s (grids with annual burned fraction < 0.001 % are masked)Figure 5. Temporal correlation of monthly burned area averaged over 2000-2014 between SSiB

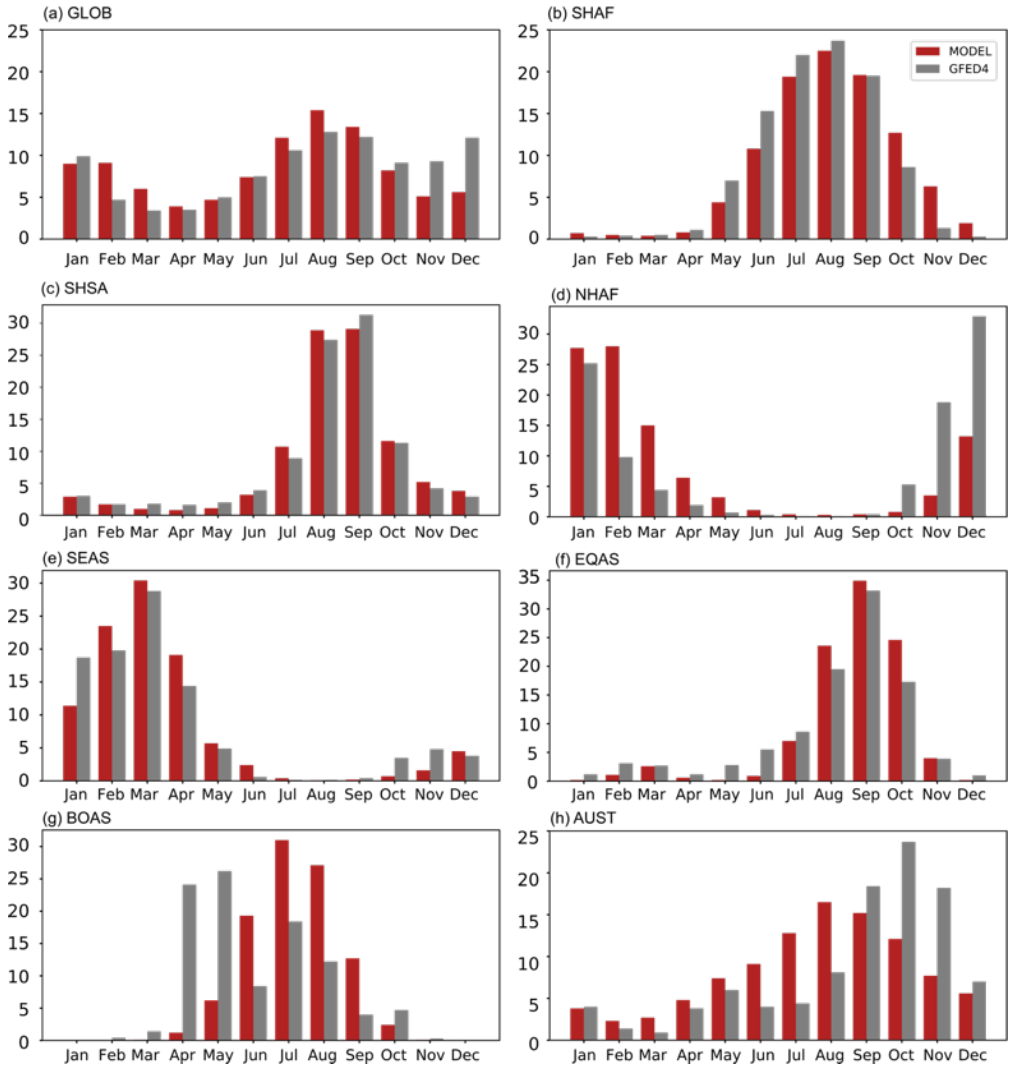

Figure 4.6 The contribution of monthly burned area to annual burned area (%) over the (a) GLOB, (b) SHAF, (c) SHSA, (d) NHSA, (e) SEAS, (f) EQAS, (g) BOAS, and (h) AUST averaged over 2000-2014 for SSiB4/TRIFFID-Fire and GFED4s

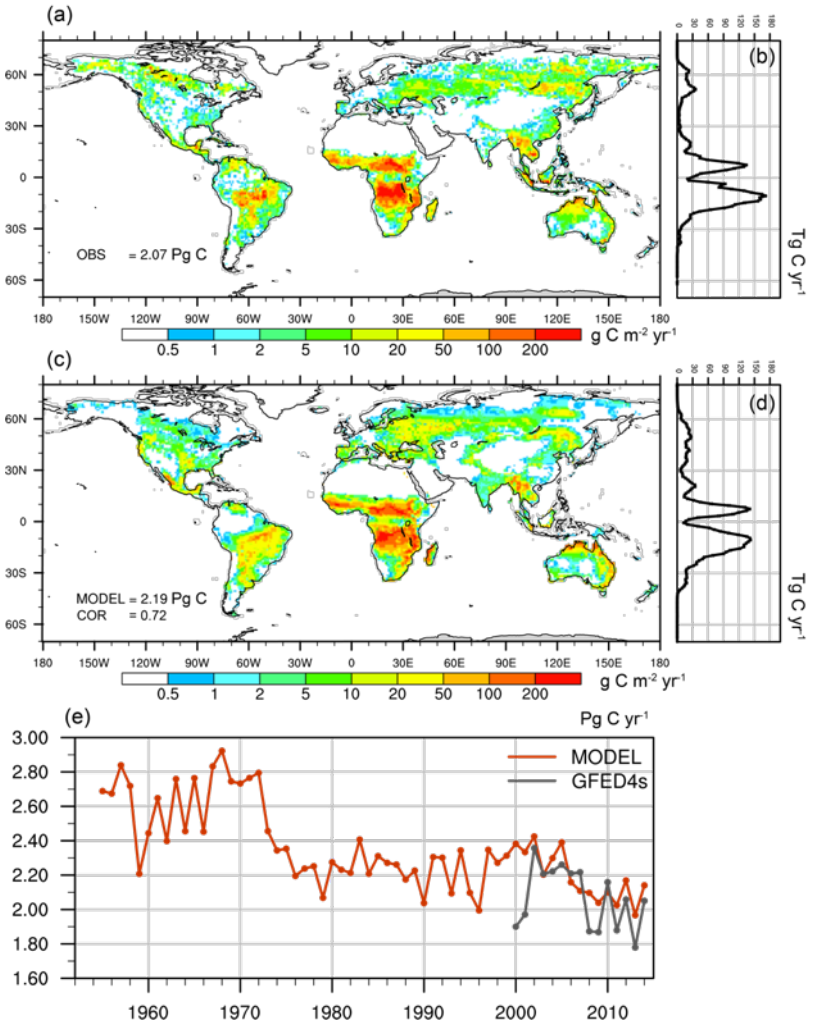

Figure 4.7 (a) Spatial distribution of annual carbon emission (g C yr^{-1}) averaged over 2000–2014 for GFED4s and (b) the latitudinal distribution of carbon emission (Tg C yr^{-1}); (c), (d) Same as (a), (b) but for SSiB4/TRIFFID-Fire (g C yr^{-1}); (e) Annual carbon emission (Pg C yr^{-1}) for GFED4s for 2000-2014 and for SSiB4/TRIFFID-Fire for 1948-2014

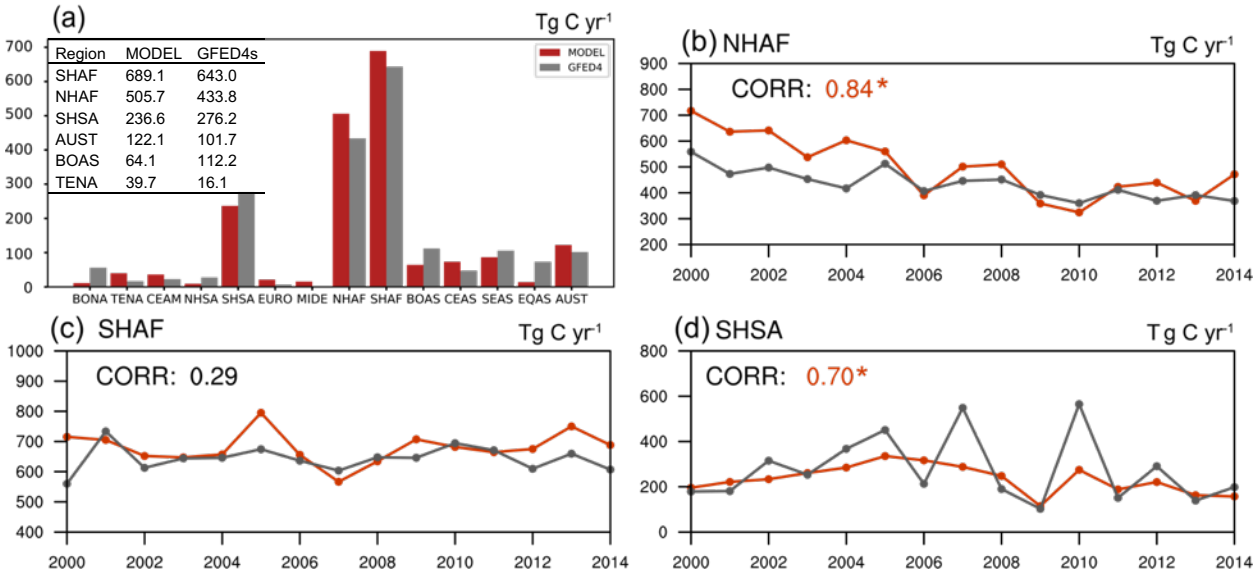

Figure 4.8 (a) Annual carbon emission averaged over 2000-2014 for GFED4s and SSiB4/TRIFFID-Fire in 14 GFED regions; (b)-(d) annual carbon emission in (b) SHAF, (c) NHAF, and (d) SHSA for 2000–2014 for GFED4s and SSiB4/TRIFFID-Fire. The "*" and red color indicate the correlation is significant at $p < 0.05$.

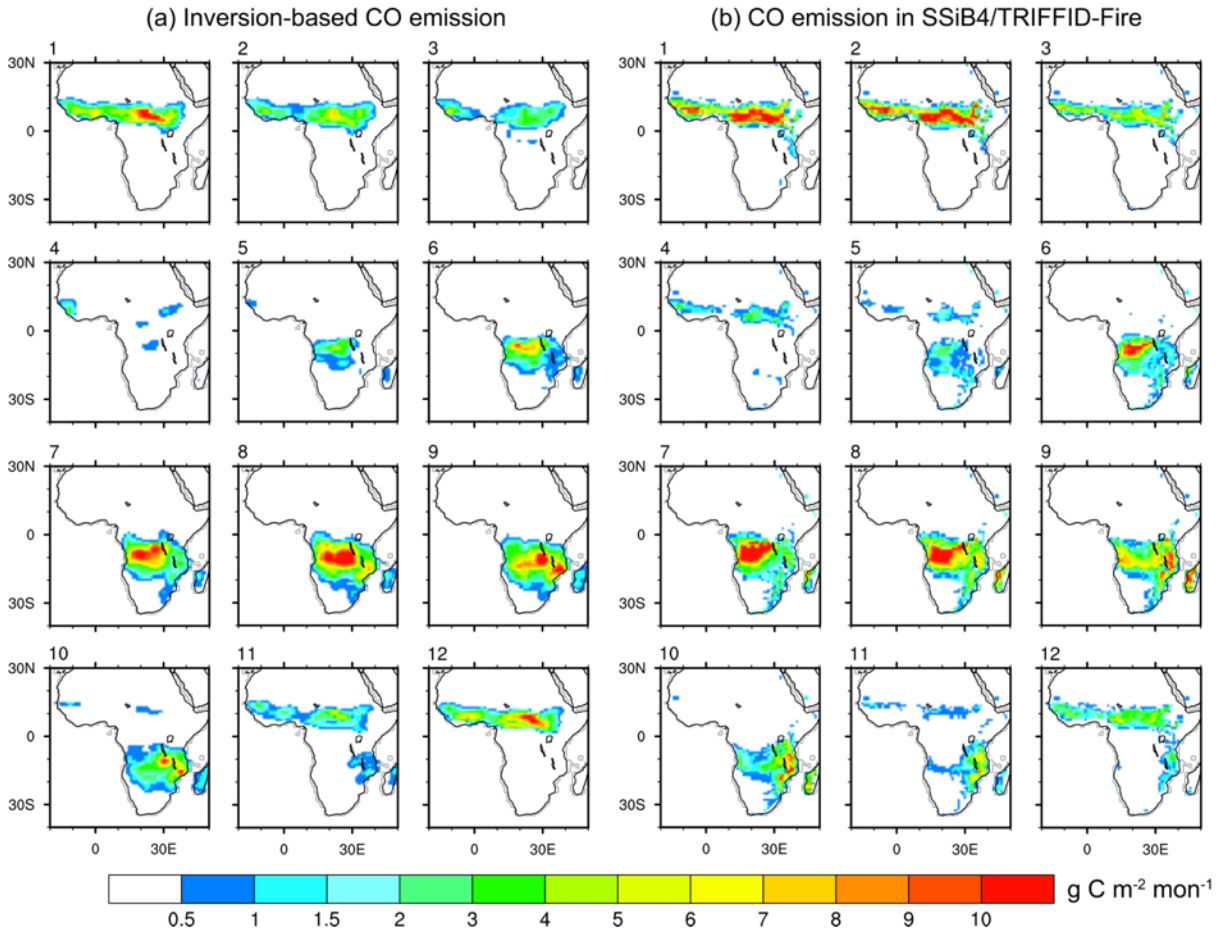

Figure 4.9 Monthly CO emission in Africa averaged in 2000-2014 from (a) Zheng et al. (2019) and (b) SSiB4/TRIFFID-Fire

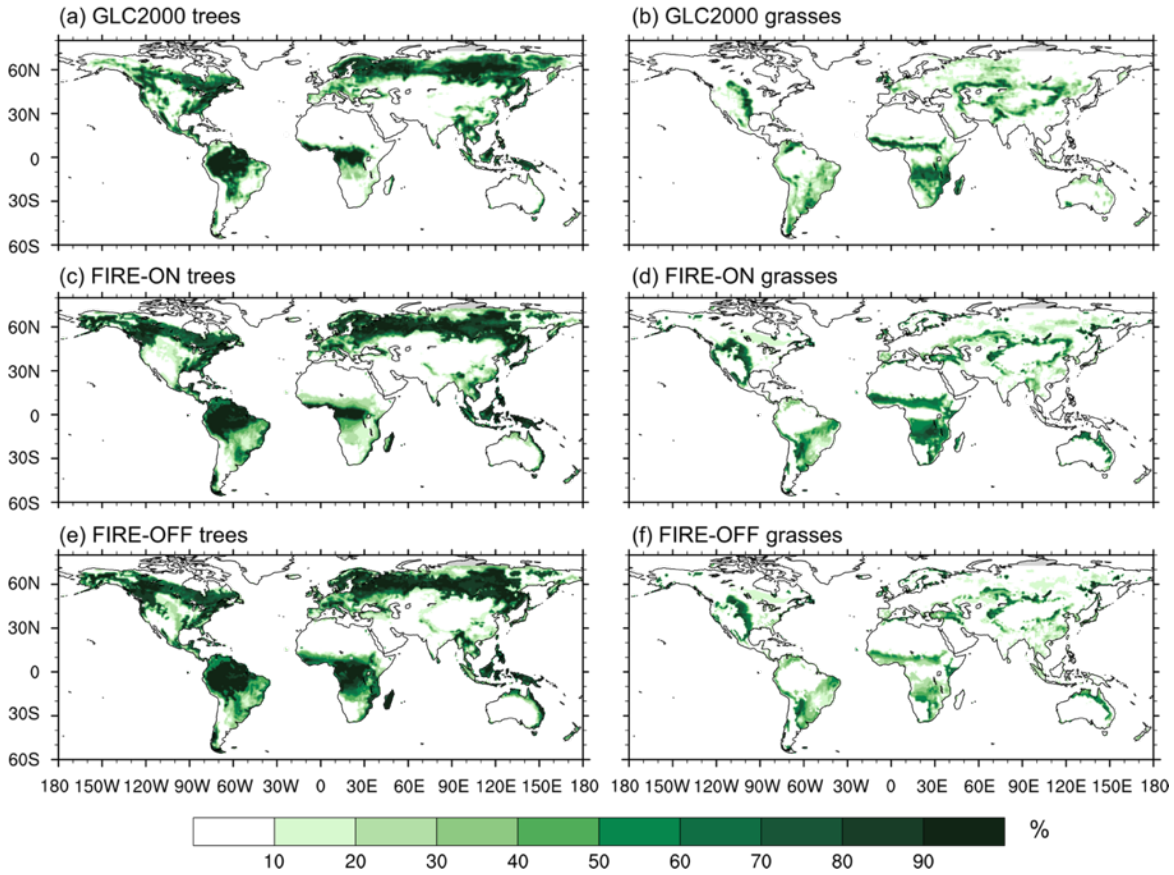

Figure 4.10 The fractional coverage of trees in (a) GLC2000, (c) FIRE-ON, and (e) FIRE-OFF and the fractional coverage of grasses in (b) GLC2000, (d) FIRE-ON, and (f) FIRE-OFF in 2000

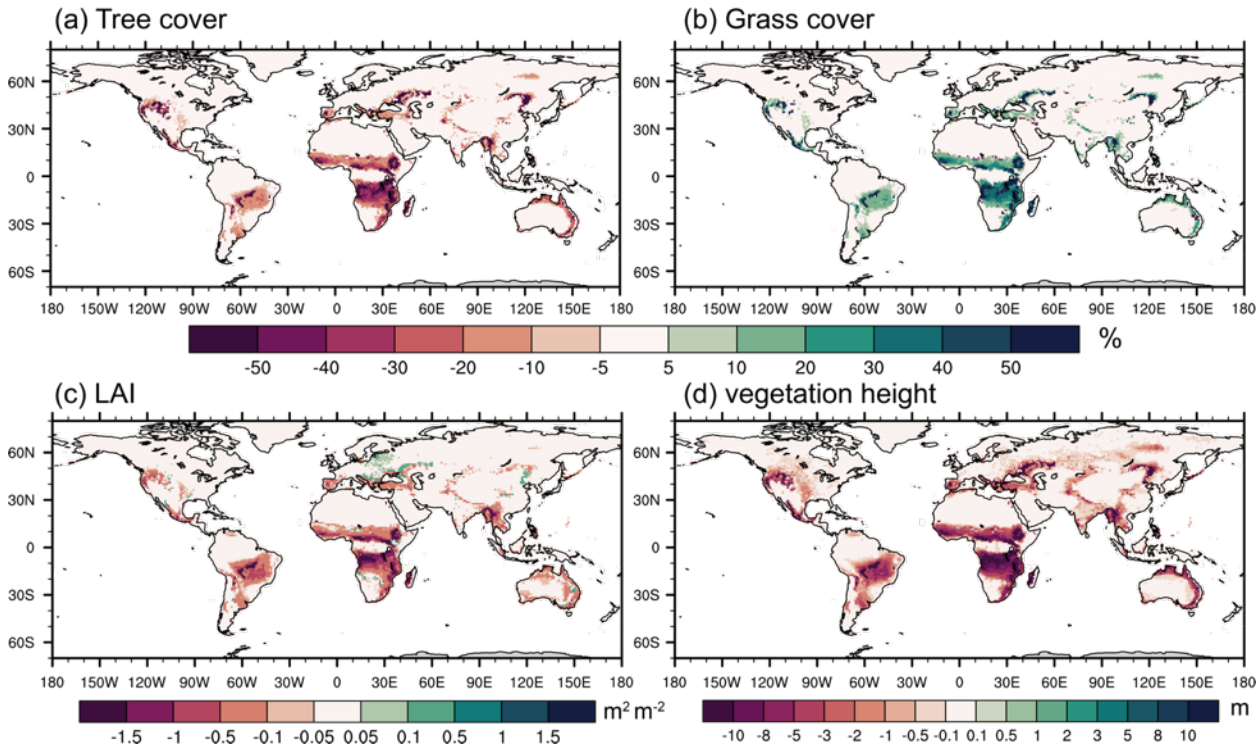

Figure 4.11 Differences in (a) tree cover (BET, NET, and BDT; %) (b) grass cover (C3 and C4; %), (c) LAI (m^2 m^{-2}), and (d) Vegetation height (m) in SSiB4/TRIFFID-Fire averaged over 2000-2014 between FIRE-ON and FIRE-OFF

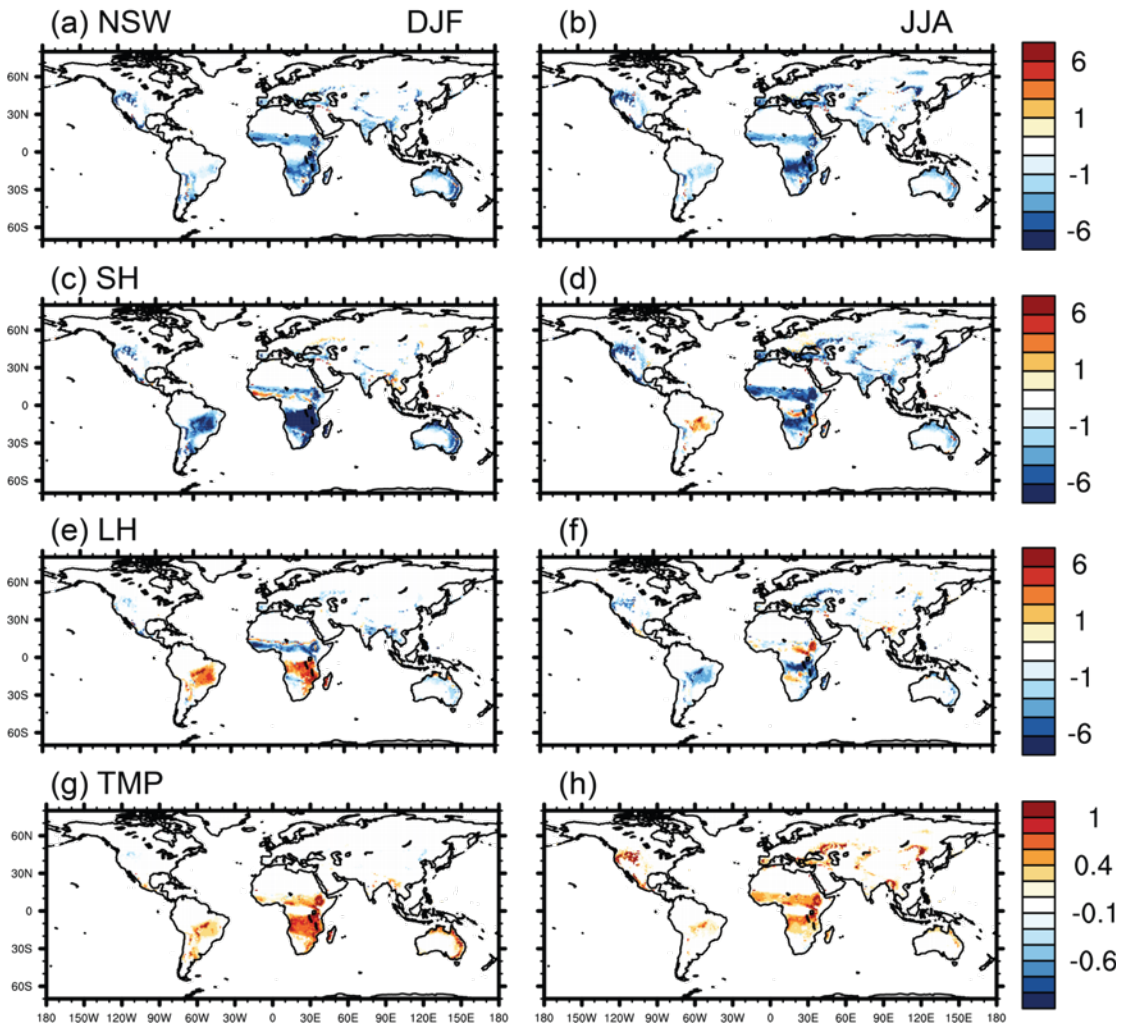

Figure 4.12 Differences in net shortwave (a, b; W m^{-2}), sensible heat (c, d; W m^{-2}), latent heat (e,f; W m^{-2}), and surface temperature (g, h; K) in DJF (a, c, e, and g), and JJA (b, d, f, and h) averaged over 2000-2014 between FIRE-ON and FIRE-OFF.

Reference

Amiro, B. D., Barr, A. G., Black, T. A., Iwashita, H., Kljun, N., McCaughey, J. H., Morgenstern, K., Murayama, S., Nesic, Z., Orchansky, A. L., and Saigusa, N.: Carbon, energy and water fluxes at mature and disturbed forest sites, Saskatchewan, Canada, Agr Forest Meteorol, 136, 237-251, 2006a.

Amiro, B. D., Orchansky, A. L., Barr, A. G., Black, T. A., Chambers, S. D., Chapin, F. S., Gouldenf, M. L., Litvakg, M., Liu, H. P., McCaughey, J. H., McMillan, A., and Randerson, J. T.: The effect of post-fire stand age on the boreal forest energy balance, Agr Forest Meteorol, 140, 41-50, 10.1016/j.agrformet.2006.02.014, 2006b.

Andela, N., Morton, D. C., Giglio, L., Chen, Y., van der Werf, G. R., Kasibhatla, P. S., DeFries, R. S., Collatz, G. J., Hantson, S., Kloster, S., Bachelet, D., Forrest, M., Lasslop, G., Li, F., Mangeon, S., Melton, J. R., Yue, C., and Randerson, J. T.: A human-driven decline in global burned area, Science, 356, 1356-1361, 10.1126/science.aal4108, 2017.

Andreae, M. O.: Emission of trace gases and aerosols from biomass burning – an updated assessment, Atmos. Chem. Phys., 19, 8523-8546, 10.5194/acp-19-8523-2019, 2019.

Archibald, S., Nickless, A., Govender, N., Scholes, R. J., and Lehsten, V.: Climate and the inter-annual variability of fire in southern Africa: a meta-analysis using long-term field data and satellite-derived burnt area data, Global Ecol Biogeogr, 19, 794-809, 10.1111/j.1466-8238.2010.00568.x, 2010.

Arora, V. K., and Boer, G. J.: Fire as an interactive component of dynamic vegetation models, J Geophys Res-Biogeo, 110, 10.1029/2005jg000042, 2005.

Bachelet, D., Ferschweiler, K., Sheehan, T. J., Sleeter, B. M., and Zhu, Z. L.: Projected carbon stocks in the conterminous USA with land use and variable fire regimes, Global Change Biol, 21, 4548-4560, 10.1111/gcb.13048, 2015.

Bartholome, E., and Belward, A. S.: GLC2000: a new approach to global land cover mapping from Earth observation data, Int J Remote Sens, 26, 1959-1977, 2005.

Bistinas, I., Harrison, S. P., Prentice, I. C., and Pereira, J. M. C.: Causal relationships versus emergent patterns in the global controls of fire frequency, Biogeosciences, 11, 5087-5101, 10.5194/bg-11-5087-2014, 2014.

Bond, W. J., Woodward, F. I., and Midgley, G. F.: The global distribution of ecosystems in a world without fire, New Phytol, 165, 525-537, 10.1111/j.1469-8137.2004.01252.x, 2005.

Bond-Lamberty, B., Peckham, S. D., Gower, S. T., and Ewers, B. E.: Effects of fire on regional evapotranspiration in the central Canadian boreal forest, Global Change Biol, 15, 1242-1254, 10.1111/j.1365-2486.2008.01776.x, 2009.

Bowman, D. M., Balch, J. K., Artaxo, P., Bond, W. J., Carlson, J. M., Cochrane, M. A., D'Antonio, C. M., Defries, R. S., Doyle, J. C., Harrison, S. P., Johnston, F. H., Keeley, J. E., Krawchuk, M. A., Kull, C. A., Marston, J. B., Moritz, M. A., Prentice, I. C., Roos, C. I., Scott, A. C., Swetnam, T. W., van der Werf, G. R., and Pyne, S. J.: Fire in the Earth system, Science, 324, 481-484, 10.1126/science.1163886, 2009.

Burton, C., Betts, R., Cardoso, M., Feldpausch, T. R., Harper, A., Jones, C. D., Kelley, D. I., Robertson, E., and Wiltshire, A.: Representation of fire, land-use change and vegetation dynamics in the Joint UK Land Environment Simulator vn4.9 (JULES), Geosci Model Dev, 12, 179-193, 10.5194/gmd-12-179-2019, 2019.

Chambers, S. D., and Chapin, F. S.: Fire effects on surface-atmosphere energy exchange in Alaskan black spruce ecosystems: Implications for feedbacks to regional climate, J Geophys Res-Atmos, 108, 10.1029/2001jd000530, 2002.

Chuvieco, E., Yue, C., Heil, A., Mouillot, F., Alonso-Canas, I., Padilla, M., Pereira, J. M., Oom, D., and Tansey, K.: A new global burned area product for climate assessment of fire impacts, Global Ecol Biogeogr, 25, 619-629, 10.1111/geb.12440, 2016.

Ciesin, F.: CIAT (Center for International Earth Science Information Network—CIESIN—Columbia University, United Nations Food and Agriculture Programme—FAO, and Centro Internacional de Agricultura Tropical—CIAT)(2005) Gridded Population of the World, Version 3 (GPWv3):

Population Count Grid. Palisades, NY: NASA Socioeconomic Data and Applications Center (SEDAC), Palisades, NY: NASA Socioeconomic Data and Applications Center (SEDAC), 2014.

Cox, P. M.: Description of the TRIFFID dynamic global vegetation model, 2001.

de Oliveira, C. P., Francelino, M. R., Daher, M., de Araujo, E. J. G., Sanches, L. D., de Andrade, K. D. C., and de Campos, J. S. N.: Estimation of the aboveground biomass and carbon stocks in open Brazilian Savannah developed on sandy soils, Carbon Balance and Management, 14, 2019.

De Sales, F., Xue, Y. K., and Okin, G. S.: Impact of burned areas on the northern African seasonal climate from the perspective of regional modeling, Climate Dynamics, 47, 3393-3413, 10.1007/s00382-015-2522-4, 2016.

Devine, A. P., Stott, I., McDonald, R. A., and Maclean, I. M. D.: Woody cover in wet and dry African savannas after six decades of experimental fires, J Ecol, 103, 473-478, 2015.

Dunin, F.: Run-off and drainage from grassland catchments, 1987.

Forkel, M., Andela, N., Harrison, S. P., Lasslop, G., van Marle, M., Chuvieco, E., Dorigo, W., Forrest, M., Hantson, S., Heil, A., Li, F., Melton, J., Sitch, S., Yue, C., and Arneth, A.: Emergent relationships with respect to burned area in global satellite observations and fire-enabled vegetation models, Biogeosciences, 16, 57-76, 10.5194/bg-16-57-2019, 2019.

Furley, P. A., Rees, R. M., Ryan, C. M., and Saiz, G.: Savanna burning and the assessment of long-term fire experiments with particular reference to Zimbabwe, Prog Phys Geog, 32, 611-634, 2008.

Gholz, H. L., and Clark, K. L.: Energy exchange across a chronosequence of slash pine forests in Florida, Agr Forest Meteorol, 112, 87-102, 2002.

Giglio, L., Csiszar, I., and Justice, C. O.: Global distribution and seasonality of active fires as observed with the Terra and Aqua Moderate Resolution Imaging Spectroradiometer (MODIS) sensors, J Geophys Res-Biogeo, 111, 10.1029/2005jg000142, 2006.

Giglio, L., Randerson, J. T., and van der Werf, G. R.: Analysis of daily, monthly, and annual burned area using the fourth-generation global fire emissions database (GFED4), J Geophys Res-Biogeo, 118, 317-328, 10.1002/jgrg.20042, 2013.

Giglio, L., Boschetti, L., Roy, D. P., Humber, M. L., and Justice, C. O.: The Collection 6 MODIS burned area mapping algorithm and product, Remote Sens Environ, 217, 72-85, 10.1016/j.rse.2018.08.005, 2018.

Goldewijk, K. K., Beusen, A., and Janssen, P.: Long-term dynamic modeling of global population and built-up area in a spatially explicit way: HYDE 3.1, Holocene, 20, 565-573, 2010.

Hamilton, D. S., Hantson, S., Scott, C. E., Kaplan, J. O., Pringle, K. J., Nieradzik, L. P., Rap, A., Folberth, G. A., Spracklen, D. V., and Carslaw, K. S.: Reassessment of pre-industrial fire emissions strongly affects anthropogenic aerosol forcing, Nat Commun, 9, 10.1038/s41467-018-05592-9, 2018.

Hantson, S., Kelley, D. I., Arneth, A., Harrison, S. P., Archibald, S., Bachelet, D., Forrest, M., Hickler, T., Lasslop, G., Li, F., Mangeon, S., Melton, J. R., Nieradzik, L., Rabin, S. S., Prentice, I. C., Sheehan, T., Sitch, S., Teckentrup, L., Voulgarakis, A., and Yue, C.: Quantitative assessment of fire and vegetation properties in simulations with fire-enabled vegetation models from the Fire Model Intercomparison Project, Geosci Model Dev, 13, 3299-3318, 10.5194/gmd-13-3299-2020, 2020.

Harper, A. B., Cox, P. M., Friedlingstein, P., Wiltshire, A. J., Jones, C. D., Sitch, S., Mercado, L. M., Groenendijk, M., Robertson, E., Kattge, J., Bonisch, G., Atkin, O. K., Bahn, M., Cornelissen, J., Niinemets, U., Onipchenko, V., Penuelas, J., Poorter, L., Reich, P. B., Soudzilovskaia, N. A., and van Bodegom, P.: Improved representation of plant functional types and physiology in the Joint UK Land Environment Simulator (JULES v4.2) using plant trait information, Geosci Model Dev, 9, 2415-2440, 10.5194/gmd-9-2415-2016, 2016.

Higgins, S. I., Bond, W. J., February, E. C., Bronn, A., Euston-Brown, D. I. W., Enslin, B., Govender, N., Rademan, L., O'Regan, S., Potgieter, A. L. F., Scheiter, S., Sowry, R., Trollope, L., and Trollope, W. S. W.: Effects of four decades of fire manipulation on woody vegetation structure in savanna, Ecology, 88, 1119-1125, 2007.

Huang, H., Xue, Y., Chilukoti, N., Liu, Y., Chen, G., and Diallo, I.: Assessing Global and Regional Effects of Reconstructed Land-Use and Land-Cover Change on Climate since 1950 Using a Coupled Land–Atmosphere–Ocean Model, J Climate, 33, 8997-9013, 2020.

Jiang, Y. Q., Lu, Z., Liu, X. H., Qian, Y., Zhang, K., Wang, Y. H., and Yang, X. Q.: Impacts of global open-fire aerosols on direct radiative, cloud and surface-albedo effects simulated with CAM5, Atmos Chem Phys, 16, 14805-14824, 10.5194/acp-16-14805-2016, 2016.

Johnston, F. H., Henderson, S. B., Chen, Y., Randerson, J. T., Marlier, M., DeFries, R. S., Kinney, P., Bowman, D. M. J. S., and Brauer, M.: Estimated Global Mortality Attributable to Smoke from Landscape Fires, Environ Health Persp, 120, 695-701, 10.1289/ehp.1104422, 2012.

Jung, M., Reichstein, M., Margolis, H. A., Cescatti, A., Richardson, A. D., Arain, M. A., Arneth, A., Bernhofer, C., Bonal, D., Chen, J. Q., Gianelle, D., Gobron, N., Kiely, G., Kutsch, W., Lasslop, G., Law, B. E., Lindroth, A., Merbold, L., Montagnani, L., Moors, E. J., Papale, D., Sottocornola, M., Vaccari, F., and Williams, C.: Global patterns of land-atmosphere fluxes of carbon dioxide, latent heat, and sensible heat derived from eddy covariance, satellite, and meteorological observations, J Geophys Res-Biogeo, 116, 2011.

Kloster, S., Mahowald, N. M., Randerson, J. T., and Lawrence, P. J.: The impacts of climate, land use, and demography on fires during the 21st century simulated by CLM-CN, Biogeosciences, 9, 509-525, 2012.

Langford, K. J.: Change in Yield of Water Following a Bushfire in a Forest of Eucalyptus Regnans, J Hydrol, 29, 87-114, 1976.

Lasslop, G., Thonicke, K., and Kloster, S.: SPITFIRE within the MPI Earth system model: Model development and evaluation, Journal of Advances in Modeling Earth Systems, 6, 740-755, 10.1002/2013ms000284, 2014.

Lasslop, G., Hantson, S., Harrison, S. P., Bachelet, D., Burton, C., Forkel, M., Forrest, M., Li, F., Melton, J. R., Yue, C., Archibald, S., Scheiter, S., Arneth, A., Hickler, T., and Sitch, S.: Global ecosystems and fire: Multi-model assessment of fire-induced tree-cover and carbon storage reduction, Global Change Biol, n/a, 10.1111/gcb.15160, 2020.

Lawrence, D. M., Fisher, R. A., Koven, C. D., Oleson, K. W., Swenson, S. C., Bonan, G., Collier, N., Ghimire, B., van Kampenhout, L., Kennedy, D., Kluzek, E., Lawrence, P. J., Li, F., Li, H. Y.,

Lombardozzi, D., Riley, W. J., Sacks, W. J., Shi, M. J., Vertenstein, M., Wieder, W. R., Xu, C. G., Ali, A. A., Badger, A. M., Bisht, G., van den Broeke, M., Brunke, M. A., Burns, S. P., Buzan, J., Clark, M., Craig, A., Dahlin, K., Drewniak, B., Fisher, J. B., Flanner, M., Fox, A. M., Gentine, P., Hoffman, F., Keppel-Aleks, G., Knox, R., Kumar, S., Lenaerts, J., Leung, L. R., Lipscomb, W. H., Lu, Y. Q., Pandey, A., Pelletier, J. D., Perket, J., Randerson, J. T., Ricciuto, D. M., Sanderson, B. M., Slater, A., Subin, Z. M., Tang, J. Y., Thomas, R. Q., Martin, M. V., and Zeng, X. B.: The Community Land Model Version 5: Description of New Features, Benchmarking, and Impact of Forcing Uncertainty, Journal of Advances in Modeling Earth Systems, 11, 4245-4287, 10.1029/2018ms001583, 2019.

Li, F., Zeng, X. D., and Levis, S.: A process-based fire parameterization of intermediate complexity in a Dynamic Global Vegetation Model, Biogeosciences, 9, 2761-2780, 10.5194/bg-9-2761-2012, 2012.

Li, F., Bond-Lamberty, B., and Levis, S.: Quantifying the role of fire in the Earth system - Part 2: Impact on the net carbon balance of global terrestrial ecosystems for the 20th century, Biogeosciences, 11, 1345-1360, 10.5194/bg-11-1345-2014, 2014.

Li, F., and Lawrence, D. M.: Role of Fire in the Global Land Water Budget during the Twentieth Century due to Changing Ecosystems, J Climate, 30, 1893-1908, 10.1175/Jcli-D-16-0460.1, 2017.

Li, F., Lawrence, D. M., and Bond-Lamberty, B.: Impact of fire on global land surface air temperature and energy budget for the 20th century due to changes within ecosystems (vol 12, 044014, 2017), Environ Res Lett, 12, 10.1088/1748-9326/aa727f, 2017.

Li, F., Martin, M. V., Andreae, M. O., Arneth, A., Hantson, S., Kaiser, J. W., Lasslop, G., Yue, C., Bachelet, D., Forrest, M., Kluzek, E., Liu, X. H., Mangeon, S., Melton, J. R., Ward, D. S., Darmenov, A., Hickler, T., Ichoku, C., Magi, B. I., Sitch, S., van der Werf, G. R., Wiedinmyer, C., and Rabin, S. S.: Historical (1700-2012) global multi-model estimates of the fire emissions from the Fire Modeling Intercomparison Project (FireMIP), Atmos Chem Phys, 19, 12545-12567, 10.5194/acp-19-12545-2019, 2019.

Liu, H. P., Randerson, J. T., Lindfors, J., and Chapin, F. S.: Changes in the surface energy budget after fire in boreal ecosystems of interior Alaska: An annual perspective, J Geophys Res-Atmos, 110, 10.1029/2004jd005158, 2005.

Liu, Y., Guo, W. D., and Song, Y. M.: Estimation of key surface parameters in semi-arid region and their impacts on improvement of surface fluxes simulation, Sci China Earth Sci, 59, 307-319, 10.1007/s11430-015-5140-4, 2016.

Liu, Y., Xue, Y. K., MacDonald, G., Cox, P., and Zhang, Z. Q.: Global vegetation variability and its response to elevated CO2, global warming, and climate variability - a study using the offline SSiB4/TRIFFID model and satellite data, Earth Syst Dynam, 10, 9-29, 2019.

Melton, J. R., and Arora, V. K.: Competition between plant functional types in the Canadian Terrestrial Ecosystem Model (CTEM) v.2.0, Geosci Model Dev, 9, 323-361, 2016.

Moreira, A. G.: Effects of fire protection on savanna structure in Central Brazil, Journal of Biogeography, 27, 1021-1029, 2000.

Oleson, K., Lawrence, D., Bonan, G., Drewniak, B., Huang, M., Koven, C., Levis, S., Li, F., Riley, W., and Subin, Z.: Technical Description of version 4.5 of the Community Land Model (CLM)(NCAR Technical Note No. NCAR/TN-503+ STR). Citeseer, National Center for Atmospheric Research, PO Box, 3000, 2013.

Pan, Y., Birdsey, R. A., Fang, J., Houghton, R., Kauppi, P. E., Kurz, W. A., Phillips, O. L., Shvidenko, A., Lewis, S. L., and Canadell, J. G.: A large and persistent carbon sink in the world's forests, Science, 333, 988-993, 2011.

Pfeiffer, M., Spessa, A., and Kaplan, J. O.: A model for global biomass burning in preindustrial time: LPJ-LMfire (v1.0), Geosci Model Dev, 6, 643-685, 10.5194/gmd-6-643-2013, 2013.

Piao, S. L., Sitch, S., Ciais, P., Friedlingstein, P., Peylin, P., Wang, X. H., Ahlstrom, A., Anav, A., Canadell, J. G., Cong, N., Huntingford, C., Jung, M., Levis, S., Levy, P. E., Li, J. S., Lin, X., Lomas, M. R., Lu, M., Luo, Y. Q., Ma, Y. C., Myneni, R. B., Poulter, B., Sun, Z. Z., Wang, T., Viovy, N., Zaehle,

S., and Zeng, N.: Evaluation of terrestrial carbon cycle models for their response to climate variability and to CO2 trends, Global Change Biol, 19, 2117-2132, 10.1111/gcb.12187, 2013.

Poulter, B., Cadule, P., Cheiney, A., Ciais, P., Hodson, E., Peylin, P., Plummer, S., Spessa, A., Saatchi, S., Yue, C., and Zimmermann, N. E.: Sensitivity of global terrestrial carbon cycle dynamics to variability in satellite-observed burned area, Global Biogeochem Cy, 29, 207-222, 2015.

Prentice, S., and Mackerras, D.: The ratio of cloud to cloud-ground lightning flashes in thunderstorms, J Appl Meteorol, 16, 545-550, 1977.

Rabin, S. S., Ward, D. S., Malyshev, S. L., Magi, B. I., Shevliakova, E., and Pacala, S. W.: A fire model with distinct crop, pasture, and non-agricultural burning: use of new data and a model-fitting algorithm for FINAL.1, Geosci Model Dev, 11, 815-842, 10.5194/gmd-11-815-2018, 2018.

Randerson, J. T., Chen, Y., van der Werf, G. R., Rogers, B. M., and Morton, D. C.: Global burned area and biomass burning emissions from small fires, J Geophys Res-Biogeo, 117, 10.1029/2012jg002128, 2012.

Ricciuto, D., Sargsyan, K., and Thornton, P.: The Impact of Parametric Uncertainties on Biogeochemistry in the E3SM Land Model, Journal of Advances in Modeling Earth Systems, 10, 297-319, 10.1002/2017ms000962, 2018.

Rogers, B. M., Randerson, J. T., and Bonan, G. B.: High-latitude cooling associated with landscape changes from North American boreal forest fires, Biogeosciences, 10, 699-718, 10.5194/bg-10-699-2013, 2013.

Saha, M. V., Scanlon, T. M., and D'Odorico, P.: Suppression of rainfall by fires in African drylands, Geophys Res Lett, 43, 8527-8533, 10.1002/2016gl069855, 2016.

Sankaran, M., Hanan, N. P., Scholes, R. J., Ratnam, J., Augustine, D. J., Cade, B. S., Gignoux, J., Higgins, S. I., Le Roux, X., Ludwig, F., Ardo, J., Banyikwa, F., Bronn, A., Bucini, G., Caylor, K. K., Coughenour, M. B., Diouf, A., Ekaya, W., Feral, C. J., February, E. C., Frost, P. G. H., Hiernaux, P., Hrabar, H., Metzger, K. L., Prins, H. H. T., Ringrose, S., Sea, W., Tews, J., Worden, J., and Zambatis, N.: Determinants of woody cover in African savannas, Nature, 438, 846-849, 2005.

Santos, A. J. B., Silva, G. T. D. A., Miranda, H. S., Miranda, A. C., and Lloyd, J.: Effects of fire on surface carbon, energy and water vapour fluxes over campo sujo savanna in central Brazil, Funct Ecol, 17, 711-719, 2003.

Scholes, R. J., Ward, D. E., and Justice, C. O.: Emissions of trace gases and aerosol particles due to vegetation burning in southern hemisphere Africa, J Geophys Res-Atmos, 101, 23677-23682, Doi 10.1029/95jd02049, 1996.

Schulze, E. D., Kelliher, F. M., Korner, C., Lloyd, J., and Leuning, R.: Relationships among Maximum Stomatal Conductance, Ecosystem Surface Conductance, Carbon Assimilation Rate, and Plant Nitrogen Nutrition - a Global Ecology Scaling Exercise, Annu Rev Ecol Syst, 25, 629-+, DOI 10.1146/annurev.es.25.110194.003213, 1994.

Seo, H., and Kim, Y.: Interactive impacts of fire and vegetation dynamics on global carbon and water budget using Community Land Model version 4.5, Geosci Model Dev, 12, 457-472, 10.5194/gmd-12-457-2019, 2019.

Shackleton, C., and Scholes, R. J.: Impact of fire frequency on woody community structure and soil nutrients in the Kruger National Park, Koedoe, 43, 75-81, 2000.

Sheffield, J., Goteti, G., and Wood, E. F.: Development of a 50-year high-resolution global dataset of meteorological forcings for land surface modeling, J Climate, 19, 3088-3111, Doi 10.1175/Jcli3790.1, 2006.

Shinoda, M., and Yamaguchi, Y.: Influence of soil moisture anomaly on temperature in the Sahel: A comparison between wet and dry decades, J Hydrometeorol, 4, 437-447, Doi 10.1175/1525-7541(2003)4<437:Iosmao>2.0.Co;2, 2003.

Smit, I. P. J., Asner, G. P., Govender, N., Kennedy-Bowdoin, T., Knapp, D. E., and Jacobson, J.: Effects of fire on woody vegetation structure in African savanna, Ecol Appl, 20, 1865-1875, 2010.

Sousa, W. P.: The Role of Disturbance in Natural Communities, Annu Rev Ecol Syst, 15, 353-391, DOI 10.1146/annurev.es.15.110184.002033, 1984.

Sun, G., Noormets, A., Gavazzi, M. J., McNulty, S. G., Chen, J., Domec, J. C., King, J. S., Amatya, D. M., and Skaggs, R. W.: Energy and water balance of two contrasting loblolly pine plantations on the lower coastal plain of North Carolina, USA, Forest Ecol Manag, 259, 1299-1310, 2010.

Teckentrup, L., Harrison, S. P., Hantson, S., Heil, A., Melton, J. R., Forrest, M., Li, F., Yue, C., Arneth, A., Hickler, T., Sitch, S., and Lasslop, G.: Response of simulated burned area to historical changes in environmental and anthropogenic factors: a comparison of seven fire models, Biogeosciences, 16, 3883-3910, 2019.

Thonicke, K., Venevsky, S., Sitch, S., and Cramer, W.: The role of fire disturbance for global vegetation dynamics: coupling fire into a Dynamic Global Vegetation Model, Global Ecol Biogeogr, 10, 661-677, DOI 10.1046/j.1466-822x.2001.00175.x, 2001.

Thonicke, K., Spessa, A., Prentice, I. C., Harrison, S. P., Dong, L., and Carmona-Moreno, C.: The influence of vegetation, fire spread and fire behaviour on biomass burning and trace gas emissions: results from a process-based model (vol 7, pg 1991, 2010), Biogeosciences, 7, 2191-2191, 10.5194/bg-7-2191-2010, 2010.

van der Werf, G. R., Randerson, J. T., Giglio, L., Collatz, G. J., Kasibhatla, P. S., and Arellano Jr, A. F.: Interannual variability in global biomass burning emissions from 1997 to 2004, Atmos Chem Phys, 6, 3423-3441, 2006.

van der Werf, G. R., Randerson, J. T., Giglio, L., Collatz, G. J., Mu, M., Kasibhatla, P. S., Morton, D. C., DeFries, R. S., Jin, Y., and van Leeuwen, T. T.: Global fire emissions and the contribution of deforestation, savanna, forest, agricultural, and peat fires (1997-2009), Atmos Chem Phys, 10, 11707-11735, 2010.

van der Werf, G. R., Randerson, J. T., Giglio, L., van Leeuwen, T. T., Chen, Y., Rogers, B. M., Mu, M. Q., van Marle, M. J. E., Morton, D. C., Collatz, G. J., Yokelson, R. J., and Kasibhatla, P. S.: Global fire emissions estimates during 1997-2016, Earth Syst Sci Data, 9, 697-720, 2017.

van Marle, M. J. E., Kloster, S., Magi, B. I., Marlon, J. R., Daniau, A. L., Field, R. D., Arneth, A., Forrest, M., Hantson, S., Kehrwald, N. M., Knorr, W., Lasslop, G., Li, F., Mangeon, S., Yue, C., Kaiser, J.

W., and van der Werf, G. R.: Historic global biomass burning emissions for CMIP6 (BB4CMIP) based on merging satellite observations with proxies and fire models (1750-2015), Geosci Model Dev, 10, 3329-3357, 10.5194/gmd-10-3329-2017, 2017.

van Vuuren, D. P., Lucas, P. L., and Hilderink, H.: Downscaling drivers of global environmental change: Enabling use of global SRES scenarios at the national and grid levels, Global Environ Chang, 17, 114-130, 2007.

van Wilgen, B. W., Govender, N., and Biggs, H. C.: The contribution of fire research to fire management: a critical review of a long-term experiment in the Kruger National Park, South Africa, Int J Wildland Fire, 16, 519-530, 2007.

Venevsky, S., Thonicke, K., Sitch, S., and Cramer, W.: Simulating fire regimes in human-dominated ecosystems: Iberian Peninsula case study, Global Change Biol, 8, 984-998, DOI 10.1046/j.1365-2486.2002.00528.x, 2002.

Venevsky, S., Le Page, Y., Pereira, J. M. C., and Wu, C.: Analysis fire patterns and drivers with a global SEVER-FIRE v1.0 model incorporated into dynamic global vegetation model and satellite and on-ground observations, Geosci. Model Dev., 12, 89-110, 10.5194/gmd-12-89-2019, 2019.

Ward, D. S., Kloster, S., Mahowald, N. M., Rogers, B. M., Randerson, J. T., and Hess, P. G.: The changing radiative forcing of fires: global model estimates for past, present and future, Atmos Chem Phys, 12, 10857-10886, 10.5194/acp-12-10857-2012, 2012.

Ward, D. S., Shevliakova, E., Malyshev, S., and Rabin, S.: Trends and Variability of Global Fire Emissions Due To Historical Anthropogenic Activities, Global Biogeochem Cy, 32, 122-142, 10.1002/2017gb005787, 2018.

Xia, X. G., Zong, X. M., and Sun, L.: Exceptionally active agricultural fire season in mid-eastern China in June 2012 and its impact on the atmospheric environment, J Geophys Res-Atmos, 118, 9889-9900, 10.1002/jgrd.50770, 2013.

Xue, Y., Sellers, P. J., Kinter, J. L., and Shukla, J.: A Simplified Biosphere Model for Global Climate Studies, J Climate, 4, 345-364, 10.1175/1520-0442(1991)004<0345:asbmfg>2.0.co;2, 1991.

Yang, J., Tian, H. Q., Tao, B., Ren, W., Kush, J., Liu, Y. Q., and Wang, Y. H.: Spatial and temporal patterns of global burned area in response to anthropogenic and environmental factors: Reconstructing global fire history for the 20th and early 21st centuries, J Geophys Res-Biogeo, 119, 249-263, 10.1002/2013jg002532, 2014.

Yang, J., Tian, H. Q., Tao, B., Ren, W., Pan, S. F., Liu, Y. Q., and Wang, Y. H.: A growing importance of large fires in conterminous United States during 1984-2012, J Geophys Res-Biogeo, 120, 2625-2640, 10.1002/2015jg002965, 2015.

Yue, C., Ciais, P., Cadule, P., Thonicke, K., Archibald, S., Poulter, B., Hao, W. M., Hantson, S., Mouillot, F., Friedlingstein, P., Maignan, F., and Viovy, N.: Modelling the role of fires in the terrestrial carbon balance by incorporating SPITFIRE into the global vegetation model ORCHIDEE - Part 1: simulating historical global burned area and fire regimes, Geosci Model Dev, 7, 2747-2767, 10.5194/gmd-7-2747-2014, 2014.

Yue, C., Ciais, P., Cadule, P., Thonicke, K., and van Leeuwen, T. T.: Modelling the role of fires in the terrestrial carbon balance by incorporating SPITFIRE into the global vegetation model ORCHIDEE - Part 2: Carbon emissions and the role of fires in the global carbon balance, Geosci Model Dev, 8, 1321-1338, 10.5194/gmd-8-1321-2015, 2015.

Zeng, F.-W., Koster, R. D., Lee, E., Follette-Cook, M. B., Weir, B., Colarco, P. R., Ott, L., and Poulter, B.: Use of CLM Carbon Dynamics in the Land Component of the NASA GMAO Earth System Model, 2019.

Zeng, X. D., Li, F., and Song, X.: Development of the IAP Dynamic Global Vegetation Model, Advances in Atmospheric Sciences, 31, 505-514, 10.1007/s00376-013-3155-3, 2014.

Zhan, X. W., Xue, Y. K., and Collatz, G. J.: An analytical approach for estimating CO2 and heat fluxes over the Amazonian region, Ecol Model, 162, 97-117, 2003.

Zhang, Z., Xue, Y., MacDonald, G., Cox, P. M., and Collatz, G. J.: Investigation of North American vegetation variability under recent climate: A study using the SSiB4/TRIFFID

biophysical/dynamic vegetation model, Journal of Geophysical Research: Atmospheres, 120, 1300-1321, 2015.

Zheng, B., Chevallier, F., Yin, Y., Ciais, P., Fortems-Cheiney, A., Deeter, M. N., Parker, R. J., Wang, Y. L., Worden, H. M., and Zhao, Y. H.: Global atmospheric carbon monoxide budget 2000-2017 inferred from multi-species atmospheric inversions, Earth Syst Sci Data, 11, 1411-1436, 10.5194/essd-11-1411-2019, 2019.

Zou, Y. F., Wang, Y. H., Qian, Y., Tian, H. Q., Yang, J., and Alvarado, E.: Using CESM-RESFire to understand climate-fire-ecosystem interactions and the implications for decadal climate variability, Atmos Chem Phys, 20, 995-1020, 10.5194/acp-20-995-2020, 2020.

Chapter 5 Improving SSiB4/TRIFFID-Fire and modeling the short-term fire effects on vegetation dynamics and surface energy in Southern Hemisphere Africa

This chapter will be submitted to the special issue "*The role of fire in the Earth system: understanding interactions with the land, atmosphere, and society*" on *Geoscientific Model Development* as

Huang, H., Y., Xue, Y., Liu, F., Li, G., Okin, 2021: Improving SSiB4/TRIFFID-Fire vegetation-fire model and modeling the short-term fire effects on vegetation dynamics and surface energy in Southern Hemisphere Africa, (*in prep*)

Abstract

Fire is an essential determinant to the structure and functioning of the savanna ecosystem. The abrupt changes after fire modify vegetation properties and energy fluxes exchanges between land and atmosphere. Yet these short-term fire effects on vegetation dynamic and surface energy balance have not been comprehensively investigated in fire-coupled vegetation models. This study applied the SSiB4/TRIFFID-Fire to study the monthly to annual fire impact in Southern Hemisphere Africa (SHAF), where the model was shown to reproduce the monthly fire regimes, vegetation productivity, and surface fluxes as compared to observation-derived datasets. An annual reduction in C3 and C4 grasses cover by 4 – 8 % is caused by fire for most areas between 5 °S - 20 °S while the tree cover reduction is mostly concentrated at the periphery of tropical rainforest.

The largest grass reduction is found at the beginning of the rainy season in November, which quickly recovers to unburned conditions before the next fire season. The removal of leaf area has caused an annual reduction in gross primary productivity (GPP) by 5-7% in SHAF, with the largest monthly reduction by 11% found in November. The albedo is increased due to exposure of bare soil, thus decreasing the surface net radiation. The sensible heat has dropped by 1.4 W m^{-2} due to an increase in aerodynamic resistance. The decrease in canopy transpiration is compensated by the increase in soil evaporation and finally causes a small annual change (0.1 W m^{-2}) in LH. While the inclusion of surface darkening effects has enhanced the shortwave absorption by surface, our findings on the decrease of SH and canopy transpiration by fire are generally consistent in both experiments.

5.1 Introduction

Fire is an integral component of the earth's ecosystem (Bond et al., 2005; Bowman et al., 2009). Through prevalent disturbance on surface biophysical properties (i.e., albedo and vegetation characteristics), fire alters radiative forcing on Earth surface and modifies the energy partitioning between latent heat and sensible heat fluxes (Chambers and Chapin, 2002; Bond-Lamberty et al., 2009). The change in boundary layer may cause feedback on monsoon and change the precipitation through biosphere-atmosphere interactions (Wendt et al., 2007; De Sales et al., 2016; Saha et al., 2016). Meanwhile, fires also alter atmospheric biogeochemical processes through release and absorption of carbon during the biomass combustion and post-fire vegetation regrowth, as well as the emissions of greenhouse gases (GHGs), aerosols, and volatile organic compounds (VOCs) (Scholes et al., 1996). The fire emitted GHGs and aerosols can exert radiative forcing in the atmosphere through greenhouse gases effects, aerosol-radiation interactions, and aerosol-cloud interactions (Ward et al., 2012; Jiang et al., 2016; Hamilton et al., 2018; Jiang et al., 2020; Zou et al., 2020). Both the biogeophysical and biogeochemical effects of fire influence the energy fluxes exchanges, hydrology cycle, and climate at local and regional scales

Fire models have been developed within the Dynamic Global Vegetation Models (DGVMs) to explicitly describe fire regimes in the past few decades (Thonicke et al., 2001; Venevsky et al., 2002; Arora and Boer, 2005; Thonicke et al., 2010; Li et al., 2012; Pfeiffer et al., 2013; Lasslop et al., 2014; Yue et al., 2014; Rabin et al., 2018; Burton et al., 2019; Venevsky et al., 2019). The fire-coupled DGVM has been widely used to study the role of fire on terrestrial carbon budget, surface energy balance, and water cycle (Bond and Midgley, 2012; Li et al., 2014; Yue et al., 2015; Li and Lawrence, 2017; Li et al., 2017; Seo and Kim, 2019; Huang et al., 2020b; Lasslop et al., 2020). These studies are referred to as the "long-term fire effect" where the simulations with fire are

compared with reference simulations representing "a world without fire". While much attention has been devoted to the long-term fire effects, there lacks an understanding of the short-term (monthly to annual scales) biogeophysical fire effects through the removal of vegetation and modification of albedo, roughness, and evapotranspiration. These impacts are nonnegligible at a regional scale due to the abrupt changes in surface properties, which modify the land-atmosphere interactions and are found to induce large-scale circulation changes (Saha et al., 2016; De Sales et al., 2018; Huang et al., 2020a). The short-term biogeophysical effects should be explicitly considered in assessments of fire impacts on weather and climate in a changing environment.

Observational studies have shown fire short-term biogeophysical effects on albedo change and surface radiation (Beringer et al., 2003; Veraverbeke et al., 2012; Gatebe et al., 2014; Saha et al., 2016; Dintwe et al., 2017; Saha et al., 2017; Liu et al., 2019b; Saha et al., 2019). While most studies found an instantaneous surface darkening associated with ash and charcoal deposition (Govaerts et al., 2002; Myhre et al., 2005), some observations reported that the darkening lasted for 10-60 days, followed by a gradual brightening when the charcoal was removed by wind erosion or surface runoff and bare soil was exposed (Lyons et al., 2008; Samain et al., 2008; Gatebe et al., 2014; Saha et al., 2017; Saha et al., 2019). However, other investigations found that the darkening can be maintained for more than 6 months, and the brightening effects were not evident for a majority of pixels in satellite-derived products (Jin and Roy, 2005; Dintwe et al., 2017). The variations come from various aspects, including the climate and soil properties of study regions, burning seasons, and criteria used to define the "control" pixel (Dintwe et al., 2017; Saha et al., 2019). The uncertainties in albedo change can cause an opposite effect in surface radiative forcing induced by fire (Lopez-Saldana et al., 2015; Liu et al., 2019b).

Fire is also found to influence precipitation in the subsequent rainy seasons and even in the next year through the feedbacks between fire, vegetation, and climate. The modeling studies by De Sales et al. (2016) and De Sales et al. (2018) examined fire effects on rainy in Northern Hemisphere Africa (NHAF) and Southern Hemisphere Africa (SHAF) by converting the MODIS burned area to LAI and vegetation cover changes. The authors found that fire has induced a weakening of West African monsoon progression due to the atmospheric cooling and subsidence, which finally resulted in a significant reduction of annual rainfall by 3.8% in NHAF savanna (De Sales et al., 2016). In SHAF, fire also resulted in a significant decrease in precipitation in September and October by 10% and 6%, associated with the evapotranspiration suppression caused by fire (De Sales et al., 2018). Using 15 years of MODIS burned area and TRMM rainfall retrievals, Saha et al. (2016) proposed negative feedback between fire, fuel load, and rainfall in which high-rainfall year is more likely to be followed by high fuel load and an extensively burned landscape in the dry season, and a low rainfall in the following wet season; the lower rainfall subsequently reduces fuel loads and the fire occurrence, and increases rainfall in the next year, completing the feedback loop.

Southern Hemisphere Africa (SHAF) has the largest continuous stretch of savanna covering an area of ~1.4×10^3 Mha of the land surface (Dintwe et al., 2017). The SHAF savanna has an annual burned area of 153.7 Mha yr^{-1} (Giglio et al., 2018) and carbon emission of 669 Tg C yr^{-1} (van der Werf et al., 2017), contributing to about 36 % and 31 % of the global total burned area and fire carbon emissions, respectively. The ecosystem has evolved over millions of years with fire as an essential contributor to its structure and function. It is therefore selected as the key region to quantify the fire effects on vegetation, surface radiative forcing, and energy/water exchanges between land and atmosphere.

In the modeling study of fire effects on SHAF (De Sales et al. 2018), the authors applied WRF/SSiB2, which assumes one vegetation type for each grid whose LAI is prescribed with climatological monthly variations. The post-fire vegetation recovery is implemented by simply taking a 140-day regrowth to unburned conditions. This study applies a process-based vegetation-fire model, SSiB4/TRIFFID-Fire, which explicitly simulates the burned area, fire disturbance on in vegetation properties, and the subsequent impact on surface energy. The model has been comprehensively evaluated with the observed global burned area and fire emissions in Huang et al. (2020b) and is also applied to study the long-term fire effects. This study further improves SSiB4/TRIFFID-Fire to better capture the temporal variations of fire regimes and vegetation productivity in SHAF at monthly scales. After comprehensive validate the simulated fire regimes, vegetation productivity, and surface fluxes with observations, we apply the model to investigate fire effects on vegetation cover, ecosystem properties, and surface energy in fire season and post-fire recovery season in SHAF.

5.2 Method

5.2.1 The SSiB4/TRIFFID-Fire vegetation-fire model

The Simplified Simple Biosphere Model (SSiB; Xue et al., 1991; Zhan et al., 2003) is a biophysical model which simulates surface radiation components, momentum fluxes, sensible heat (SH) and latent heat (LH) fluxes, soil moisture, surface temperature, and vegetation gross/net primary productivity (GPP/NPP) based on energy and water balance. The SSiB was coupled with a dynamic vegetation model, the Top-down Representation of Interactive Foliage and Flora Including Dynamics Model (TRIFFID), which describes the vegetation dynamics based on species competition for common resources and provides an interactive component in the feedback loop of

ecosystem and climate (Cox, 2001; Zhang et al., 2015; Harper et al., 2016; Liu et al., 2019a). The modeled PFTs in SSiB4/TRIFFID-Fire include broadleaf evergreen trees (BET), needleleaf evergreen trees (NET), broadleaf deciduous trees (BDT), C3 grasses, C4 plants, shrubs, and tundra. The PFT competition in TRIFFID is based on the Lotka-Volterra (LV) equation, which has been updated in Zhang et al. (2015) to represent the coexistence of grasses and shrubs. Liu et al. (2019a) further adjusted the large-scale disturbance (LSD) parameter, including the disturbance due to fires, pests, windthrow, and other processes, to allows for the coexistence between trees, C3 grasses, and C4 grasses. The simulated vegetation distribution has been assessed over Northern America (Zhang et al., 2015) and over the globe (Liu et al., 2019a). Their results show that SSiB4/TRIFFID captures key processes of vegetation-climate interactions.

The SSiB4/TRIFFID is further improved by incorporating a fire scheme (Li et al., 2012) to describe fire disturbance on vegetation dynamics and carbon budget (hereafter SSiB4/TRIFFID-Fire; Huang et al., 2020b). SSiB4/TRIFFID-Fire has been shown to reproduce the burned area and fire emissions across the spatial and temporal scales. Specifically, it produces realistic fire peak months and fire season duration in major fire regions, including Southern Hemisphere Africa (SHAF), South America, Southeast Asia, and Equatorial Asia. With an explicit description of the burned area, carbon emission, and fire disturbance on vegetation, SSiB4/TRIFFID-Fire captures fire-vegetation interactions under current climate and can be used to study fire effects on ecosystem characteristics and surface energy

5.2.2 Model Improvement

SSiB4/TRIFFID-Fire has been updated to improve the simulation of fire regimes, vegetation productivity, and surface fluxes on a monthly scale. The constant crop fraction from GLC2000 (Bartholome and Belward, 2005) in the previous version has been changed to an

annually-updated crop fraction from LUH2 (Hurtt et al., 2006; Hurtt et al., 2011) in the description of fire suppression on agricultural land. Previous studies have pointed out that agriculture expansion has influenced the spatial and temporal variations of the burned area beyond GDP and population effects and should be explicitly considered in the fire modeling (Andela et al., 2017; Lasslop and Kloster, 2017). LUH2 has a smaller crop fraction and a different spatial distribution in tropical regions than those in GLC2000. We therefore adjusted the fire spread, fuel combustibility, and carbon combustion parameters to reproduce the observed magnitude and temporal variations of burned area and carbon emission in satellite data.

Wet season accumulated productivity proves to be one of the determinants for the burned area and carbon emission in the following fire season (Forkel et al., 2019). In turn, vegetation productivity is influenced by phenology and fire. Therefore, we optimize parameters using an observation-based GPP dataset to ensure that the model captures the fire-vegetation-climate feedback. Our previous study showed that SSiB4/TRIFFID-Fire overestimated the annual mean GPP but captured its spatial distribution and interannual variations (Huang et al., 2020b). Within a year, the model simulates the GPP magnitude in the wet season but overestimates it in the dry season for savanna and grassland. By compiling 32 years of satellite data, Li et al. (2019) report that moisture condition (precipitation) is the first vital driver that positively affected monthly vegetation productivity in non-forest areas. In SSiB4, the vegetation productivity is closely associated with the soil moisture through the root-zone soil moisture potential factor $f(\theta)$:

$$f(\theta) = 1 - e^{-c_2[c1_1 - \ln(-ph_0 * \theta^{-b})]}, \quad (5.1)$$

where c_1, c_2, ph_0, and b are PFT-dependent parameters. $f(\theta)$ represents the soil moisture (θ) effects on stomatal resistance, which influences the CO_2 and water exchange and can also impact on leave fall. $f(\theta)$ does not play a role when it is closed to 1 and can largely suppress the

transpiration and vegetation productivity when it is close to 0. For C3 grasses and C4 grasses, the original $f(\theta)$ decreases sharply when soil moisture (θ) is between 0.3 – 0.4, yet does not play a role when soil moisture is higher than 0.4 (Figure 5.1). In SSiB4/TRIFFID-Fire, the simulated root-zone soil moisture is generally higher than 0.4 in the SHAF dry season. Therefore, we adjusted the coefficients c_1 and c_2 for C4 grasses to reflect the effects of soil water deficit on transpiration in a wider range of soil moisture between 0.4 – 0.6 (Figure 5.1a). The f(θ) for C3 grasses is also adjusted but is designed to be less sensitive to low moisture conditions (compared to C4 grasses) to make it more adaptive in the dry area (Figure 5.1b).

5.2.3 Experiment design

A series of offline experiments have been conducted using SSiB4/TRIFFID-Fire, including a spin-up simulation to reach quasi-equilibrium vegetation distribution and a transient run with varying climate forcings and CO_2 in 1948-2014 (Figure 5.2). The spin-up of SSiB4/TRIFFID-Fire is forced by 1948-1972 climatology forcing from Sheffield et al. (2006) and 1948 atmospheric CO_2 concentration with fire model turned on. The DGVM reaches a quasi-equilibrium status after 200 years of simulation (Figure 5.2). Based on the quasi-equilibrium status, a FIREON transient run is carried out with 3-hourly meteorological forcings, yearly updated atmospheric CO_2, and annual agriculture, population density, and GDP information from 1948 to 2014. The spin-up and transient runs are similar to those conducted in Huang et al. (2020b) except for the transient agriculture fraction. We focus on the period of 2000-2014 when the satellite observations are available for fire model validation.

To assess the fire effect at the seasonal scale, we conduct FIREOFF simulations branching from the control simulations on January 1st of each year between 2000 and 2013. The model is run for two years with the fire model switched off and all remaining parameters and input data the

same as those in FIREON. In all simulations, the vegetation distribution is allowed to respond to climate variations while it is only influenced by fire disturbance in FIREON. Each 2-year simulation in FIREOFF is regarded as an ensemble member, and the corresponding periods of FIREON are regarded as 14 ensemble members in the same way. The fire impact on vegetation properties and surface energy balance in fire season and post-fire recovery season would be quantified using the difference between the FIREON and FIREOFF (FIREON minus FIREOFF).

5.2.4 Validation data

Table 5.1 lists the data used for model input and evaluation. The input datasets for the fire model and land surface model are the same as our earlier study (Huang et al., 2020b) except for the annually-updated agriculture fraction from Hurtt et al. (2006; 2011). All datasets are interpolated to 1.0° × 1.0° spatial and 3-hourly temporal resolution to be used as model input.

The simulated burned area, carbon emission, vegetation productivity, and surface fluxes are evaluated against observations. The Global Fire Emission Database (GFED) is a fire dataset derived primarily from MODIS satellite (van der Werf et al., 2006; van der Werf et al., 2010; Giglio et al., 2013). The latest version, GFED4s, has been updated to include the contribution from small fires below the MODIS detection limit (van der Werf et al., 2017). The burned area and carbon emission obtained from https://www.globalfiredata.org/data.html are used to evaluate fire simulation in SHAF with a focus on monthly variations. FLUXNET Model Tree Ensemble (FLUXNET-MTE) GPP is upscaled from FLUXNET observations to the global scale using the machine learning technique MTE (Jung et al., 2011). The FLUXNET-MTE GPP in 1982–2011 downloaded from https://www.bgc-jena.mpg.de/geodb/projects/Data.php has been resampled to 1.0°×1.0° to be compared with SSiB4/TRIFFID-Fire.

The FLUXCOM provides monthly gridded LH and SH estimates at 0.5° spatial resolution and monthly steps (http://www.fluxcom.org/EF-Products/). The data is derived by merging energy flux measurements from FLUXNET eddy covariance tower with remote sensing and meteorological data using machine learning techniques (Jung et al., 2019). FLUXCOM database comprises of two complementary products for surface fluxes: FLUXCOM-RS integrates the FLUXNET measurement and 2001-2015 MODIS data in machine learning techniques, while FLUXCOM-METEO estimates surface fluxes from daily meteorological data and mean seasonal cycles of satellite data. The dataset is specially designed to quantify global land-atmosphere interactions and provide a benchmark for land surface model simulations.

5.3 Modeling fire effects in SHAF

5.3.1 Model validation

The study was conducted in SHAF. The Equatorial Africa (0° - 5°S), East Coast of SHAF, and East Coast of Madagascar Island are hot and humid throughout the year, with an annual mean temperature of 25 °C and rainfall exceeding 1200 mm year^{-1} (**Figure 5.3**a-b). From the equator to SH high latitude, the annual mean precipitation and temperature decrease while the seasonality is enhanced (**Figure 5.3**c-d). The SHAF savanna has a divergent climate during the wet season (November-April) and dry season (May-October). During the rainy season, the daily precipitation can reach 15 mm day^{-1}, resulting in significant floods in Zimbabwe, Zambia, Malawi, and Mozambique (https://reliefweb.int/report/malawi/south-east-africa-deadly-storms-and-floods-malawi-zambia-and-mozambique). The dry season for savanna includes May-October, which is characterized by little precipitation especially for June-July-August when monthly rainfall is less than 10 mm. SHAF has diverse ecosystems influenced by climate and fire. Equatorial Africa is

dominated by tropical rainforests, known as the Congolese rainforest. From tropical SHAF to southern hemisphere high latitude, the climatology land cover ranges from the densely forested area, savanna, grassland, shrubland, and desert correspondingly (Broxton et al., 2014). Figure 5.3e shows the dominant PFTs simulated in SSiB4/TRIFFID-Fire. The BET and BDT are concentrated in the tropical rainforest and eastern part of Madagascar Island. Most areas between 5-20 °S are dominated by C4 grasses with tree fraction varying between 10%-20% with moisture conditions. These regions are referred to as the savanna biome in the SHAF continent. C3 grass is mostly distributed in the eastern part of the SHAF along the Great Rift Valley and the eastern portion of the Great Escarpment. The shrub dominates the Southern African plateau. The fractional coverage of each PFT has been thoroughly validated with observations in Huang et al. (2020b).

The model description of fire regimes is compared against GFED4s which has been resampled to 1.0°×1.0°. According to GFED4s, an average of 175.6 Mha land surface area is burned each year in SHAF, emitting 678.9 Tg carbon into the atmosphere (Figure 5.4a). SSiB4/TRIFFID-Fire has captured the magnitude of annual burned area (180.7 Mha) and carbon emission (723.1 Tg C) with spatial correlation coefficients (SCC) of 0.74 and 0.70, respectively (Figure 5.4b,c). Fires are mostly found in Central Africa (5 °S to 20 °S), extending from the Atlantic Coast to Lake Tanganyika. The most extensive fire regions are located in savanna with intermediate productivity, where the aboveground biomass and dried soil conditions facilitate fire occurrence and spread in the dry season. Fires in tropical Congolese rainforest and drylands in Namibia and South Africa are constrained by climatic conditions and fuel load, respectively. The spatial distribution of burned area is more homogenous in the model, while the observations show some "hot spots" in Angola, Zambia, and the southern part of Congo. The heterogeneity in GFED4s may come from landscape fragmentation associated with intensive agriculture, which

limits the burned area by reducing fuel connectivity (Bistinas et al., 2014). Although SSiB4/TRIFFID-Fire excludes fire occurrence in agricultural fraction, it does not consider the full impact of landscape fragmentation on fire spread and therefore underestimates the strength of negative influence of cropland on the burned area. Besides, the simulation is conducted at 1.0° × 1.0° spatial resolution. The relatively coarse model resolution makes it harder to capture the spatial heterogeneity in fire simulation.

Fire in SHAF is concentrated in the dry season (Figure 5.4d). Following Venevsky et al. (2019), we define June-October as the fire season during which the monthly burned area contributes to more than $\frac{1}{12}$ of the annual burned area. The aboveground dried fuel is easily get ignited and can cause extreme fires in the dry season. The monthly burned area drops dramatically at the beginning of the rainy season and remains a low value until May in the next year. SHAF savanna fire has a clear distinction between June-October and November-May, reflecting the contrasting climate during the rainy (non-fire) season and dry (fire) season (Figure 5.3d).

We also evaluate the modeled GPP by comparing it with the FLUXNET-MET GPP product. The annual average GPP in 2000-2013 is 1283.4 g C m^{-2} $year^{-1}$, ranging from more than 2500 g C m^{-2} $year^{-1}$ in the tropical rainforest to less than 400 g C m^{-2} $year^{-1}$ in the shrubland (Figure 5.5a). The GPP magnitude and spatial distribution in SHAF are captured in SSiB4/TRIFFID-Fire (1326.3 C m^{-2} $year^{-1}$), with a SCC of 0.89 (Figure 5.5b). The model has captured the monthly variations of GPP with a correlation of higher than 0.7 for most grid cells ($p<0.05$; Figure 5.5c), although it slightly underestimates GPP in the dry season (Figure 5.5d). Observational studies have shown that GPP in 3-6 months preceding the fire season is a vital predictor for savanna fire (Forkel et al., 2019). SSiB4/TRIFFID-Fire uses aboveground biomass, which is related to vegetation productivity accumulation in the preceding months, to describe the constraint of fuel availability

on fire ignition. On the other hand, fire also influences the vegetation productivity in SHAF (Dintwe et al., 2017). The effect can last two to six months, depending on the land cover types. The simulated vegetation productivity is in a good consistency to that in observations at the monthly scale (Figure 5.5d), indicating that SSiB4/TRIFFID-Fire captures some key processes in fire–vegetation-climate interactions, which is important to study fire effects on the ecosystem.

The simulated energy fluxes are compared with FLUXCOM datasets to evaluate the surface flux partitioning between LH and SH. The spatial distribution of LH shows a predominant horizontal zonality in both FLUXCOM-METEO and model, decreasing from 100 W m^{-2} in tropical Congolese forest to less than 30 W m^{-2} in Kalahari Desert (Figure 5.6a,b). Regions surrounding Lake Tanganyika have a much smaller annual precipitation (600 mm $year^{-1}$ in Figure 5.3b) and, therefore, have a smaller LH than the west part of SHAF. In contrast, SH in SHAF peaks in the desert and gradually decreases towards the tropical forest (Figure 5.6c). SSiB4/TRIFFID-Fire captures the latitudinal distribution of SH yet underestimates its magnitude in the Kalahari Desert (Figure 5.6d).

We further compare the monthly variations of LH and SH in SSiB4/TRIFFID-Fire against the observations from FLUXCOM-METEO and FLUXCOM-RS. There is a high agreement in the regional average and range of LH/SH between the model and two observation-derived datasets (Figure 5.6e-f). The LH peaks in the rainy season (December-January-February; DJF) and gradually declines and reaches the minimum at the end of the dry season (June-July-August; JJA). SSiB4/TRIFFID-Fire tends to underestimate LH in the wet season but accurately simulates its magnitude in the dry season. It captures the peak of SH in September/October while slightly overestimates it in January-February-March. Jung et al. (2019) pointed out that the FLUXCOM LH estimates in Africa are larger than other observation-based datasets. In this consideration, the

model simulated LH may compensate for the wet bias in FLUXCOM datasets. Overall, the model is shown to reproduce the annual surface fluxes distribution and their seasonality in SHAF.

The comparison with observations shows that SSiB4/TRIFFID-Fire is capable of reproducing the annual mean burned area and the intra-annual variations over SHAF. The seasonal cycle of vegetation productivity and surface energy fluxes are captured, indicating the fire-coupled vegetation model has captured some key processes in the feedback between fire, vegetation, and surface energy. We then investigated the short-term (monthly to annual scales) fire effects on vegetation and surface energy using FIREON minus FIREOFF. The annual fire effects are referred to as differences between FIREON and FIREOFF from June to May in the next year, including a complete fire season and post-fire recovery season. We also look at how fire effects on PFT coverage, vegetation productivity, and surface energy evolve month by month and the subsequent recovery during the recovery period.

5.3.2 Fire effects on vegetation

The reoccurrence of fire changes the fractional coverage of trees and short PFTs in the South Hemisphere Africa. Figure 5.7a and Figure 5.7b show the spatial distribution of trees (BET and BDT) and C3/C4 grasses in FIREOFF, respectively. As shown in Figure 5.7a, forests are located in the equatorial Africa and the east coast of Africa. C3 and C4 PFTs dominate most areas between 5S and 20S and the eastern portion of the Great Escarpment. Tree cover is reduced by 0.2% to 0.6% per year in Africa savanna and can exceed by 1% in the transition zone between savanna and Congolese forest (Figure 5.7c; FIREON minus FIREOFF), indicating fire is an important contributor to tropical deforestation (Hansen et al., 2013). For regions with a burned fraction greater than 10%, we find an annual decrease in C3/C4 grasses fraction by 4-8%, whose magnitude generally proportional to the grid burned fraction (Figure 5.7d). We further calculate

the grass cover change per burned area to investigate if other conditions have played a role in the fire impact on vegetation cover . A larger reduction in C3 and C4 fraction is found in drier regions (annual rainfall < 600 mm $year^{-1}$) with GPP generally smaller than 800 g C m^{-2} $year^{-1}$ (not shown). The larger fire effects could be explained by the slower recovery after fire corresponding to the lower vegetation productivity.

The monthly fire effects on vegetation cover and the subsequent recovery in the following rainy season are shown in Figure 5.7e. The dark green and light green bars denote changes in tree cover and C3/C4 grass cover between FIREON and FIREOFF, which are linked to the monthly burned fraction denoted by the red line. There is little fire during the precedent wet season in SHAF, and vegetation removal by fire is negligible from January through May. While the burned area peaks in August and gradually decreases after that, fire disturbance on C3 and C4 grasses accumulates during the entire fire season until October. The vegetation recovery is limited during June-October when the arid conditions produce very small vegetation productivity. In the dry season, the monthly precipitation is generally smaller than 20 mm $month^{-1}$ and the GPP is 50 g C m^{-2} $year^{-1}$, only $\frac{1}{3}$ of that in the wet months (Figure 5.5d). Fire effects reach the maximum in November when a decrease of 11% is found in the grass coverage. In the rainy season, vegetation recovery is accelerated and fractional change of C3 and C4 grasses by fire is diminished from December to April in the following year. At the end of the rainy season, little difference is found in the grasses cover between FIREON and FIREOFF.

A maximum decrease of tree cover (primarily BET and BDT) by 0.6 % is found in SHAF in the fire season, especially in the wet areas and the boundary of tropical forests. Different from the fast recovery of grass PFTs, the tree cover reduction generally does not return to the unburned conditions within one growing season. Our finding is supported by observational studies that fire

plays a key role in tropical forest loss (Cochrane et al., 1999; Hansen et al., 2013). Meanwhile, fire-induced forest clearance facilitates the growth and spread of grass PFTs, allowing for the coexistence between trees and grasses in the savanna ecosystem which could otherwise be encroached by trees (Higgins et al., 2007; Furley et al., 2008).

The removal of vegetation canopy has caused a reduction in canopy area and vegetation productivity, reflected by the changes of LAI and GPP (Figure 5.8a-b). For most parts of SHAF savanna, fire has caused a relative change of LAI by -3% to -5%, whose magnitude is proportional to the burned area. Over all grids with a burned fraction higher than 10%, a decrease of LAI by 0.11 m^2 m^{-2} is simulated on average, accompanied by a decrease of vegetation height by 0.15 m. The fire impact on LAI accumulates in the dry season, during which the LAI consumption by fire outcompetes the recovery (Figure 5.8c). The fire impact on LAI peaks in November when a reduction by 11% is found in LAI. A grater magnitude of relative change (-5% to -7%) is found in fire effects on vegetation productivity (GPP and NPP). Overall, we find a reduction in GPP and NPP by 62 g C $year^{-1}$ and 35 g C $year^{-1}$. The changes in vegetation cover and properties (GPP, NPP, LAI, and vegetation height) influence the radiation absorbed by the surface and the energy partitioning between LH and SH.

5.3.3 Fire effects on surface energy

Over SHAF, a decrease of surface net shortwave radiation (NSW) is found by an average of 0.60 W m^{-2} (Figure 5.9a). The magnitude of change ranges between -2.9 W m^{-2} and 0.8 W m^{-2} (Figure 5.9d) in different grids, generally increasing with the burned area. During the fire season (June-October), the fire consumption of vegetation canopy has resulted in an exposure of bare soil which generally has a higher reflectance than vegetation canopy. Therefore, the surface NSW is reduced (Figure 5.10a), especially in October (-1.5 W m^{-2}) when the arid soil has distinct contrast

in the surface albedo compared to the surrounding vegetation area. The fire effect on albedo quickly diminishes when soil is moist by rain and becomes invisible in the middle of the rainy season.

The vegetation removal after fires has reduced the grid-average vegetation height, which leads to a decrease in surface roughness length and an increase in aerodynamic resistance. The changes of aerodynamic features influence near-surface drag force, affecting the sensible heat flux exchange between land and atmosphere (Liu et al., 2016). In this experiment, a widespread reduction in SH is simulated by 0.3 – 4.0 W m^{-2} in different grids. The magnitude is generally proportional to the annual burned fraction in that grid (Figure 5.9b). The monthly fire effect on SH peaks in November, producing a decrease by 2.9 W m^{-2} in regions with an annual burned fraction greater than 10 %. The suppression in surface heating is expected to cause an atmospheric cooling and subsidence near the surface. There is a small LH change (-0.1 W m^{-2}) at the annual scale (Figure 5.9c) due to contrasting LH changes in the fire season and the following rainy season (discussed later). Overall, we find a slight increase in surface temperature by 0.14 K ranging from 0.0 - 0.3 K (Figure 5.9d), which is dominated by the changes in SH and LH fluxes.

In fire season (June-October), a maximum LH reduction by 0.7 W m^{-2} is found, while in the following rainy season, LH can be enhanced by 0.7 W m^{-2} in February (Figure 5.10c). The change of LH is related to the competing effects between transpiration decrease and soil evaporation increase. When fire occurs, the removal of vegetation leaf area (Figure 5.8a) has caused a decline in vegetation transpiration (Figure 5.10e) accompanied by an increase in soil moisture at root-zone and deeper layer (Figure 5.11b-c) when less soil water is transported to the atmosphere. Meanwhile, soil evaporation can be enhanced as surface resistance is reduced when dense plant canopy is removed (Schulze et al., 1994), especially when the soil is nearly saturated

(Dunin, 1987; Gholz and Clark, 2002). Indeed, the simulated evaporation increase is weak during the dry season and is greatly enhanced in November when the soil is refilled after rain (Figure 5.10f). The elevated soil evaporation has caused a decrease in the surface layer soil moisture (Figure 5.11a), which is confined in wet months when soil is moist by rains.

5.4 Discussion and conclusion

5.4.1 Surface darkening effects due to fire

Our previous experiment design primarily examines the biophysical impacts of fire on surface energy balance due to vegetation clearance. To assess how surface darkening effects can influence our previous conclusion, we conducted a sensitivity test ($FIREON_{dark}$) following the methodology in De Sales et al. (2018). In $FIREON_{dark}$, surface albedo is reduced to 0.1 for 60 days, after which albedo is returned to the unburned condition to mimic the removal of ash and charcoal by wind and precipitation. The value of the darkening period is taken from Saha et al. (2019) which showed that brightening occurs after 60 days on average in SHAF.

The inclusion of soil darkening effects after fire does not affect the simulation of the annual burned fraction, carbon emission, and GPP, as we find relative differences less than 0.002% and SCC higher than 0.99 in $FIREON_{dark}$ and FIREON in SHAF. The regional averaged fire effects calculated from $FIREON_{dark}$ minus FIREOFF are 0.11 m^2 m^{-2}, 0.09 m, 64.4 g C yr^{-1}, and 36.7 g C yr^{-1} for LAI, vegetation height, GPP, and NPP, which are highly consistent with the values we calculated from FIREON minus FIREOFF). The simulated changes in vegetation structure and productivity ($FIREON_{dark}$ minus FIREOFF) are consistent with our previous conclusion at the monthly scale with the maximum change occurring in November. When soil darkening is considered, we find a regional increase of NSW by 0.07 W m^{-2} on the annual scale, which is

opposite to our previous findings that fire has caused NSW to decrease by 0.60 W m^{-2}. Despite the opposite change in NSW associated with the darkening surface, SH and transpiration are reduced by 1.0 W m^{-2} and 1.4 W m^{-2} between $FIREON_{dark}$ and FIREOFF, which are generally consistent with the previous conclusion that fire decreases SH and transpiration by 1.4 W m^{-2} and 1.5 W m^{-2} respectively (FIREON minus FIREOFF). An increase in surface temperature by 0.17 K is simulated when the soil darkening effect is included, slightly higher than the temperature change between FIREON and FIREOFF (0.14 K). Although NSW changes are divergent with/without soil darkening effects, the similar changes in SH and transpiration indicate that surface flux changes are dominated by aerodynamic/canopy resistance rather than surface radiation in the tropics, in accordance with our previous finding in a land degradation experiment (Huang et al., 2020a).

We acknowledge that uncertainties may be induced as we assigned a 60-day recovery period and an albedo of 0.1 to mimic soil darkening effects for all pixels regardless of the background climate, vegetation type, soil properties, and the season fire occurs. All these factors may play a role in the albedo anomalies after ash deposition, the amount of brightening, and the evolution of radiative forcing after fire (Dintwe et al., 2017; Saha et al., 2017). Due to the limited number of observations and variety in the post-fire albedo anomalies, we are currently unable to constrain the uncertainty in the description of the surface darkening effect. Therefore, the purpose of sensitivity tests is to investigate how surface darkening effects affect our conclusions in Section 3, rather than to provide a quantitative estimate on uncertainties range induced by surface darkening.

5.4.2 Uncertainty and limitation

Besides the darkening effect associated with charcoal deposition, our quantification of fire effects is subjected to uncertainties induced by the exclusion of atmospheric feedback in the offline

model and the parametrization of vegetation recovery after disturbance in the fire-vegetation model. Although our experiments demonstrate that resistance plays a dominant role in surface fluxes change, atmospheric feedback may influence temperature/moisture gradient between land and atmosphere and alter the magnitude of SH and LH change (Huang et al., 2020a), which could not be quantified as we use fixed atmospheric conditions from the forcing. Besides, De Sales et al. (2018) have shown that fire may cause a decrease in atmospheric convective instability, which subsequently suppresses precipitation in the following rainy season. The precipitation changes may exert negative feedback on evapotranspiration and vegetation recovery, which could not be described in the offline fire-vegetation model.

Besides, the parameterizations of fire impact on vegetation and post-fire recovery could be model dependent. In SSiB4/TRFFID-Fire, the fire impact is decided by combustion completeness and mortality factors, and the vegetation recovery is determined by the net carbon availability, inter-PFT competition, and disturbance strength. While the extensive validation of fire regimes and vegetation productivity proves that our model has captured the key processes in fire-vegetation interactions, the parametrization of fire disturbance and post-fire recovery may influence the evolution of fire effects on the monthly scale. Observational studies support our conclusion that the savanna biome in SHAF is highly adaptive to fire and can mostly recover to unburned conditions within a year (Gatebe et al., 2014; Dintwe et al., 2017) yet these studies are rare. We emphasize that this study provides the first attempt to explore the short-term fire effects on the vegetation dynamics and surface energy budget using fire-coupled DGVM. More simulations should be conducted using different land surface models, DGVM, and fire models to evaluate the robustness of model results and estimate the uncertainties in the simulated fire effects.

5.4.3 Conclusions

Fire modifies vegetation dynamics and surface properties. These biogeophysical effects influence the energy fluxes exchanges, hydrology cycle, and regional and global climate. A property quantification of the short-term fire effects is critical to understand the role of fire in earth's climate system and predicting future fire–vegetation-climate interactions. This study applied SSiB4/TRIFFID-Fire to investigate the monthly to annual scale fire impact in SHAF, where fire acts as an essential determination to the structure and functioning of the local ecosystem. The model is shown to reproduce the fire regimes, vegetation productivity, and surface fluxes compared to observation-derived datasets. The fire effects are investigated using FIREON minus FIREOFF. A sensitivity test is also conducted to examine the soil darkening effects on the simulated fire impact on vegetation dynamics and surface energy.

Fire has caused an annual reduction in grass cover by 4 - 8% for most fire grids. The largest reduction is found at the end of fire season or the beginning of the rainy season (October to November), which quickly diminishes before the next fire season. The reduction of tree cover is concentrated at the transition zone between tropical forest and savanna. While the tree cover decrease is much smaller, it is irreversible in one recovery season. The low fire adaptivity in tree PFTs makes it highly vulnerable to fire and can cause large-scale deforestation in extreme years. The canopy removal has caused an annual reduction in LAI and GPP by 3-5% by 5-7% respectively. The largest productivity change is found in November when the LAI and GPP are reduced by 11 %. The albedo is increased due to bare soil exposure, thus decreasing the shortwave radiation absorbed by the surface. SH is decreased by 1.4 W m^{-2} due to an increase in aerodynamic resistance. Canopy transpiration has dropped as well, which is compensated by the increase in soil evaporation and finally causes a small annual effect on LH (0.1 W m^{-2}). Although the incorporation

of surface darkening effect has enhanced surface shortwave absorption, the fire impact on vegetation characteristics, surface fluxes, and soil moisture are highly consistent with the simulated effects without descriptions of charcoal deposition.

Tables and Figures

Table 5.1 Datasets used to drive SSiB4/TRIFFID-Fire and evaluate simulations

Variables	Sources	Resolution
Surface air temperature		
Surface pressure		
Specific humidity		
Wind speed	Sheffield et al. (2006)	1°, 3-hourly
Downward shortwave radiation		
Downward longwave radiation		
Precipitation		
Lightning frequency	NASA LIS/OTD v2.2	2.5°, 2-hourly
Population density	GPWv3 (CIESIN, 2005);	0.5°, 5 yearly
	HYDE v3.1 (Klein Goldewijk et al., 2010)	5', 10 yearly
GDP	van Vuuren et al. (2006)	0.5°, in 2000
Agriculture fraction	LUH2 (Hurtt et al., 2006; 2011)	0.25°, yearly
Burned area Carbon emission	GFED4s (Randerson et al., 2012; van der Werf et al. 2017)	0.25°, monthly
GPP	FLUXNET-MTE (Jung et al. 2009)	0.5°, monthly
Latent heat Sensible heat	FLUXCOM (Jung et al., 2019)	0.0833° and 0.5°, monthly

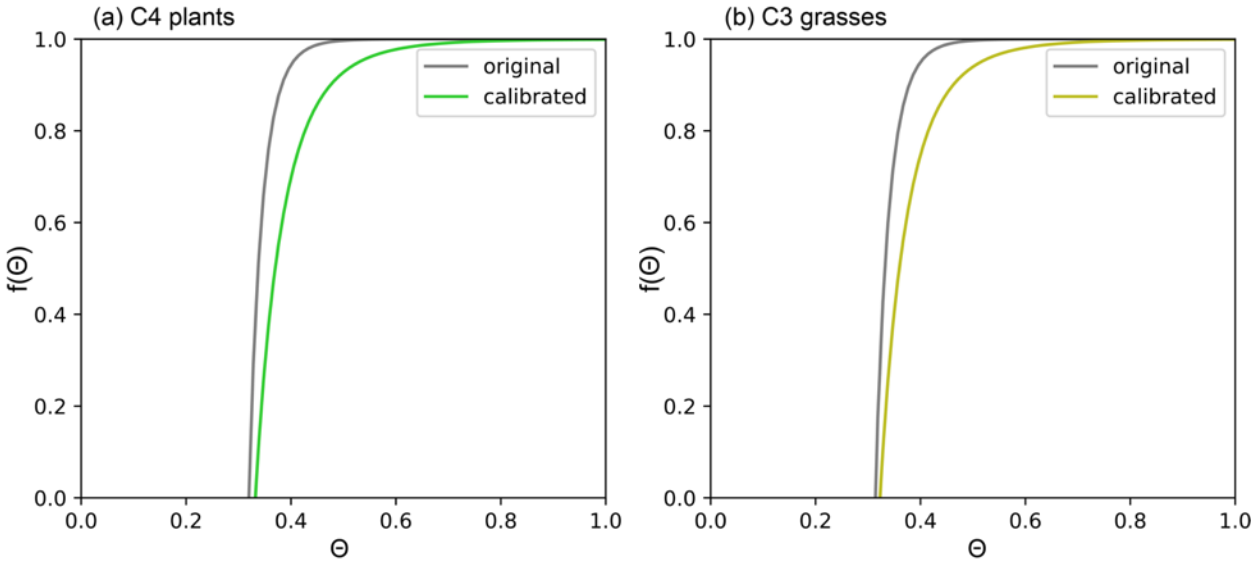

Figure 5.1 $f(\theta)$ calibration for (a) C4 grasses and (b) C3 grasses

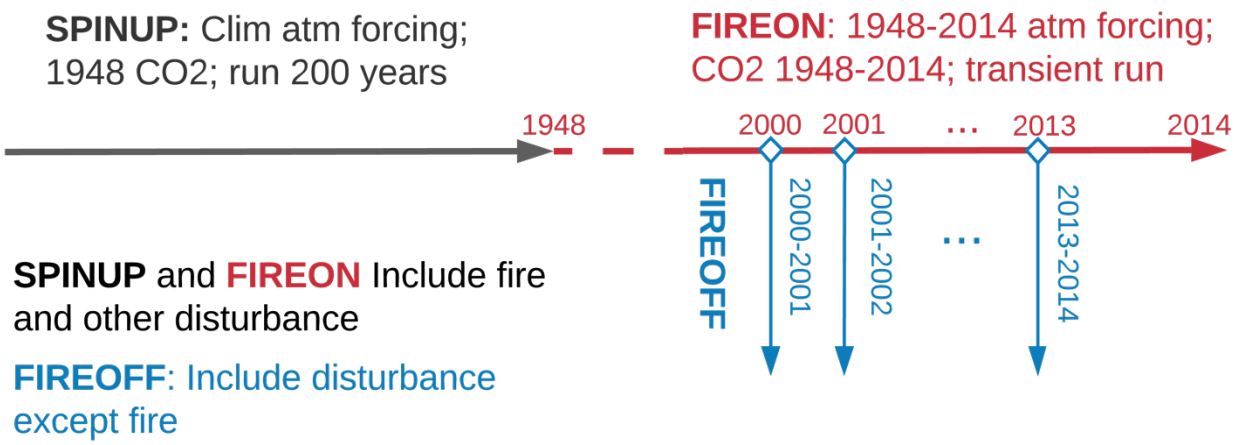

Figure 5.2 Experiment Design for fire effects in SHAF (0ºN-37ºN; 0ºW-50ºW)

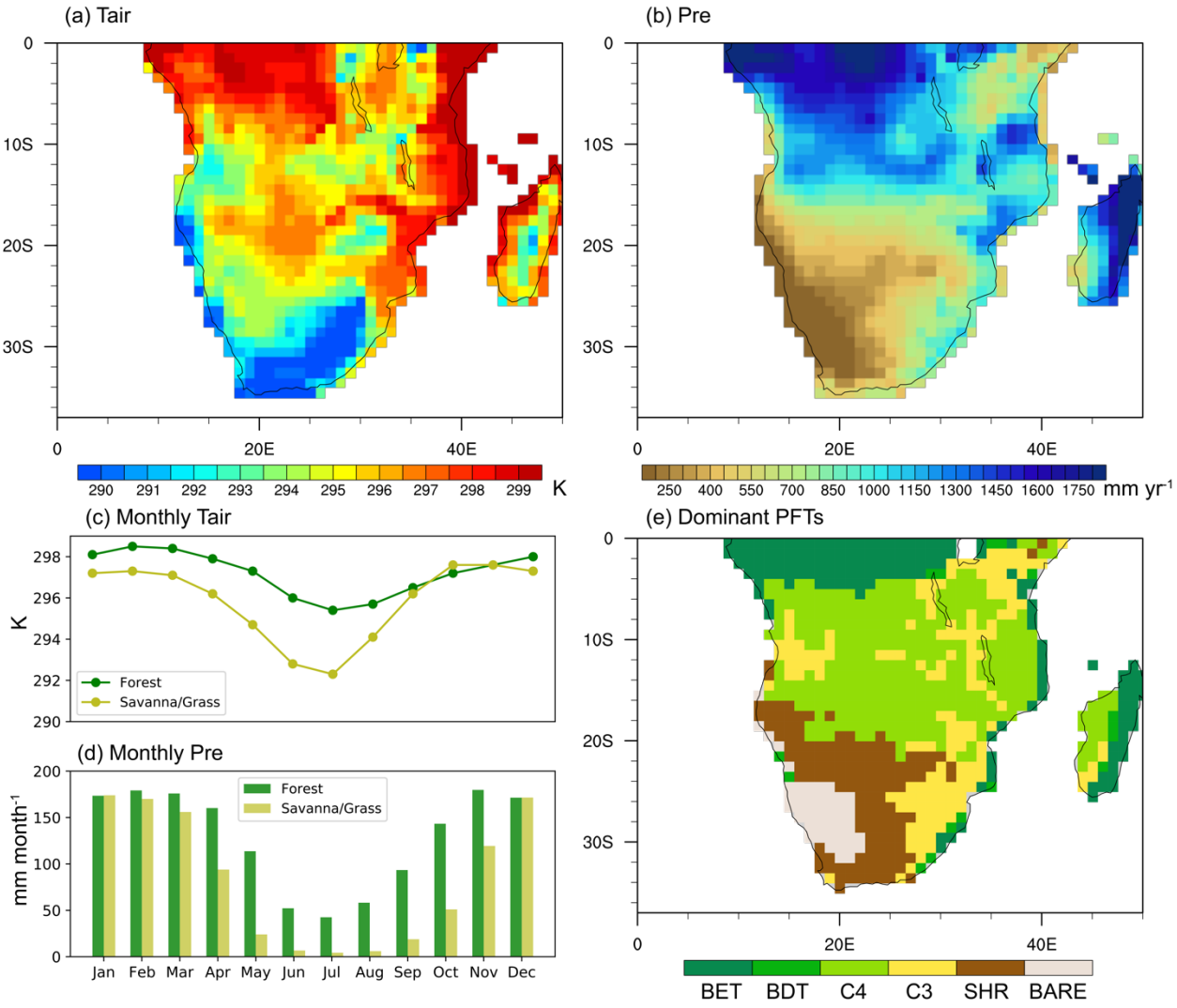

Figure 5.3 (a)-(d) Climate of SHAF from Sheffield et al. (2006) averaged in 2000-2014 (a) annual mean air temperature (Tair), (b) annual total precipitation (PRE), (c) monthly Tair (d) Monthly Pre, and (e) dominant PFTs for each grid simulated in SSiB4/TRIFFID-Fire

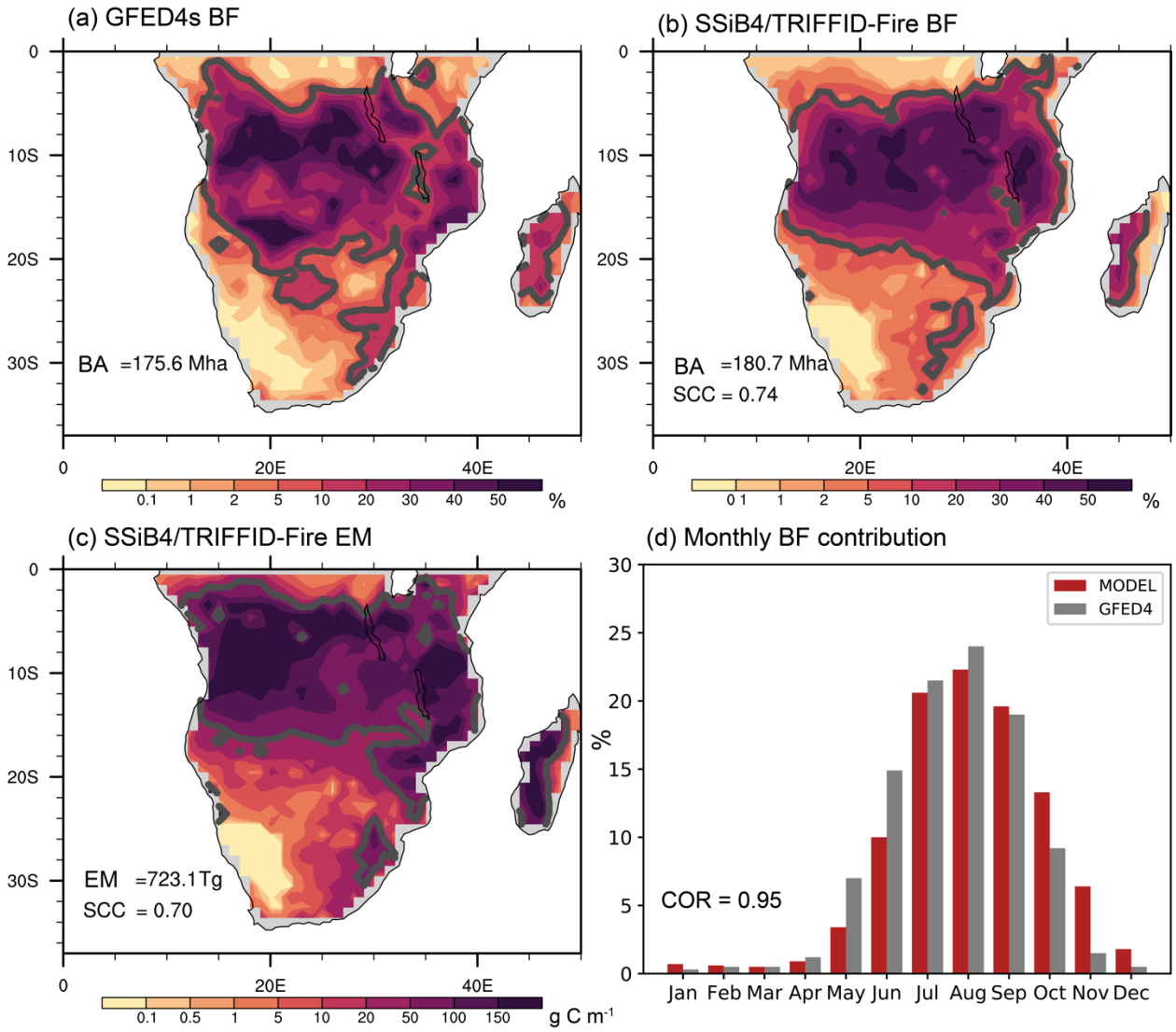

Figure 5.4 (a) Annual burned fraction (BF) averaged over 2000–2014 in GFED4s, (b) same as (a) but in SSiB4/TRIFFID-Fire, (c) Annual carbon emission (EM) averaged over 2000–2014 in SSiB4/TRIFFID-Fire, and (d) Contribution of monthly burned fraction to annual burned fraction in model and observation (BA: total burned area in SHAF; SCC: spatial correlation coefficient; COR: temporal correlation coefficient).

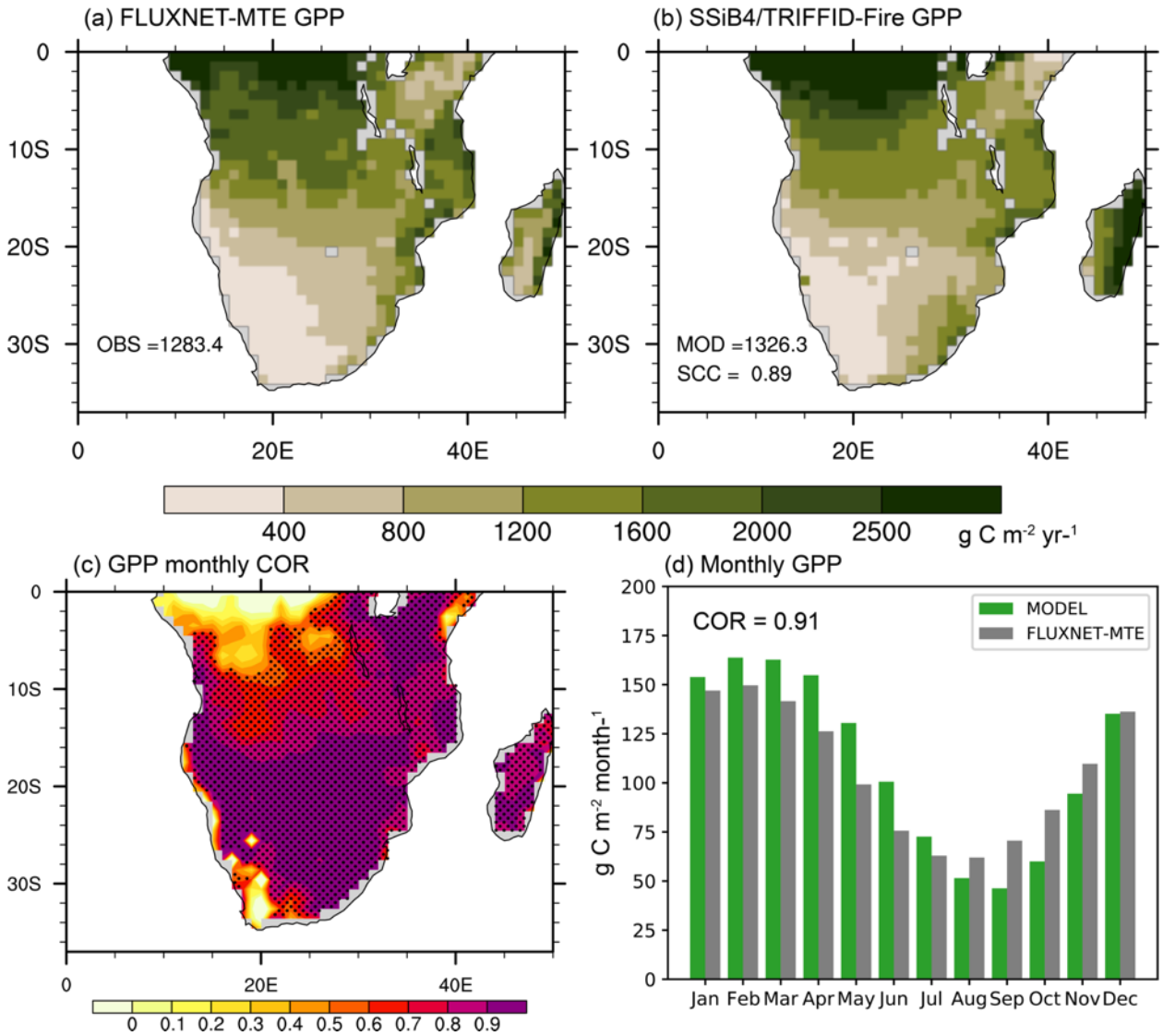

Figure 5.5 Annual GPP averaged over 2000–2011 in (a) FLUXNET-MTE, (b) SSiB4/TRIFFID-Fire, (c) Point-by-point climatology monthly correlation between FLUXNET-MTE and SSiB4/TRIFFID-Fire , and (d) Monthly GPP in model and observation

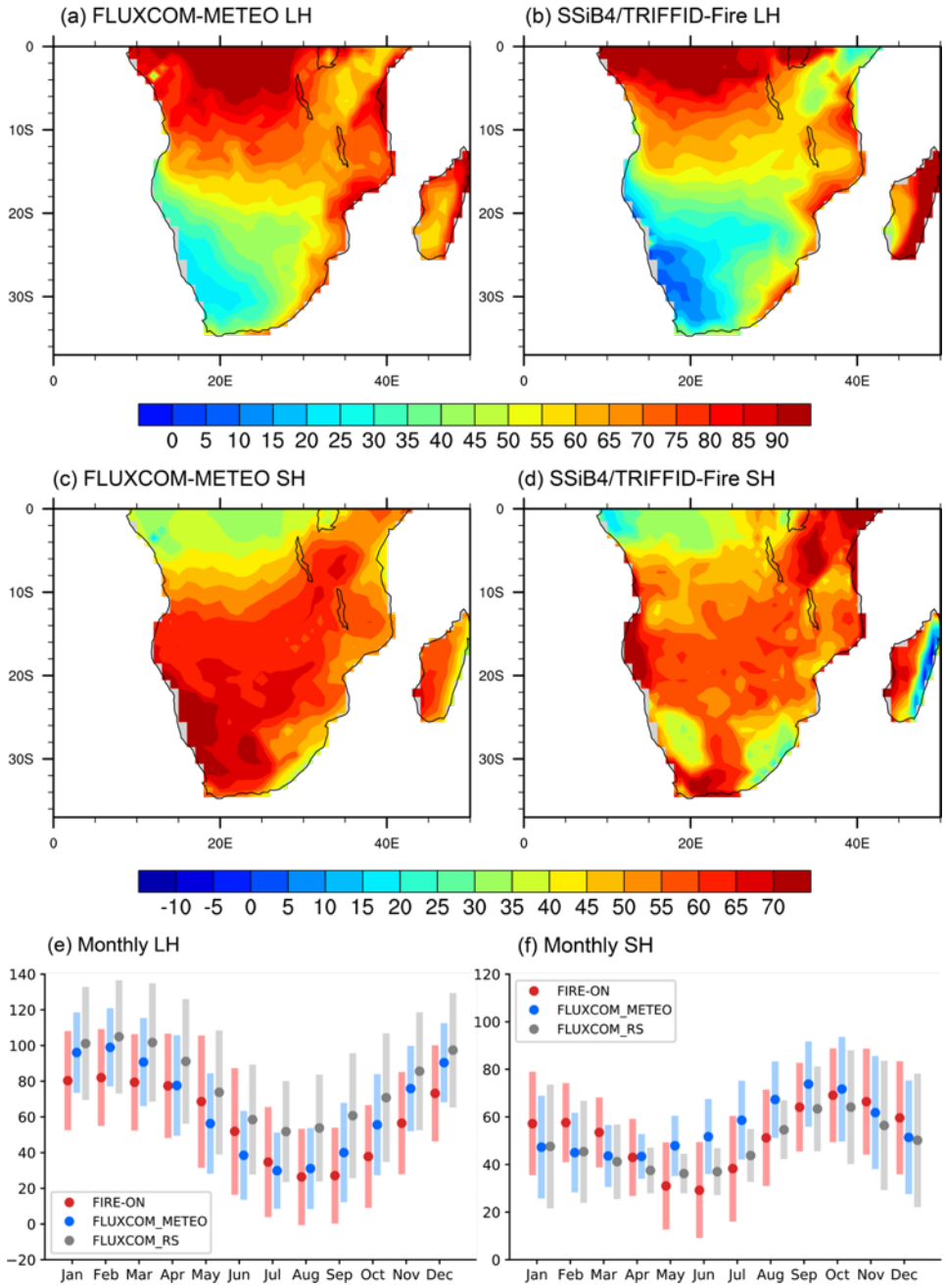

Figure 5.6 Annual LH averaged over 2000–2014 in (a) FLUXCOM-METEO, (b) s SSiB4/TRIFFID-Fire, Annual SH averaged over 2000–2014 in (c) FLUXCOM-METEO, (d) SSiB4/TRIFFID-Fire, Monthly (e) LH and (f) SH in model, FLUXCOM-METEO, and FLUXCOM-RS. The dots in (e) and (f) denote the regional mean values while the bars denote the LH/SH values within one standard deviation of the mean of all grid points

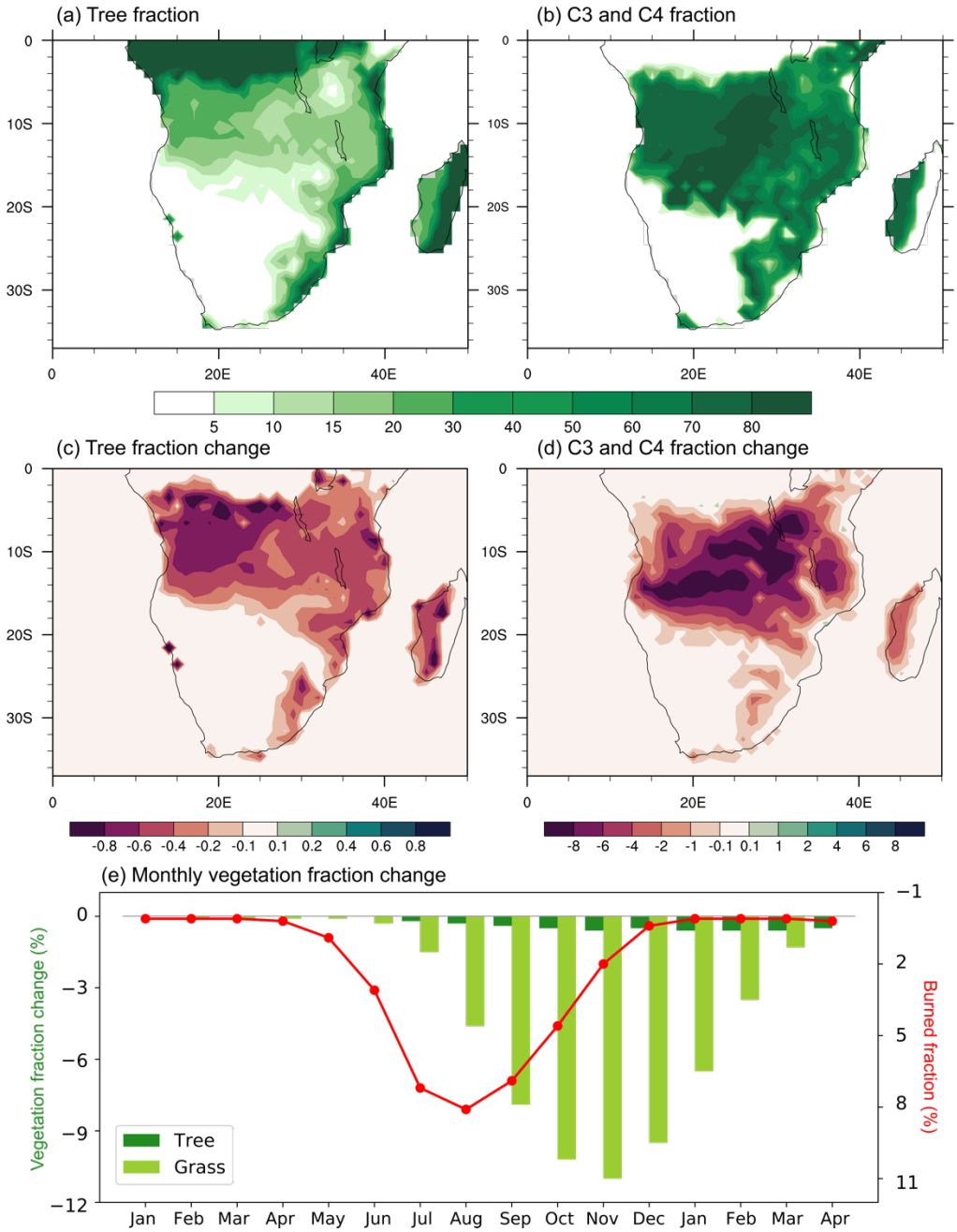

Figure 5.7 (a)-(b) 2000–2014 annual (a) tree fraction and (b) C4/C3 grass fraction in FIREOFF, (c)-(d) 2000–2014 annual fire effects on (c) tree fraction and (b) grass fraction (e) Monthly fire effects on the fractional coverage of trees and C4/C3 grasses with burned area overlaid (The areal-average is calculated using grids with an annual burned fraction of more than 10%). The y-axis of burned fraction in (e) is reversed.

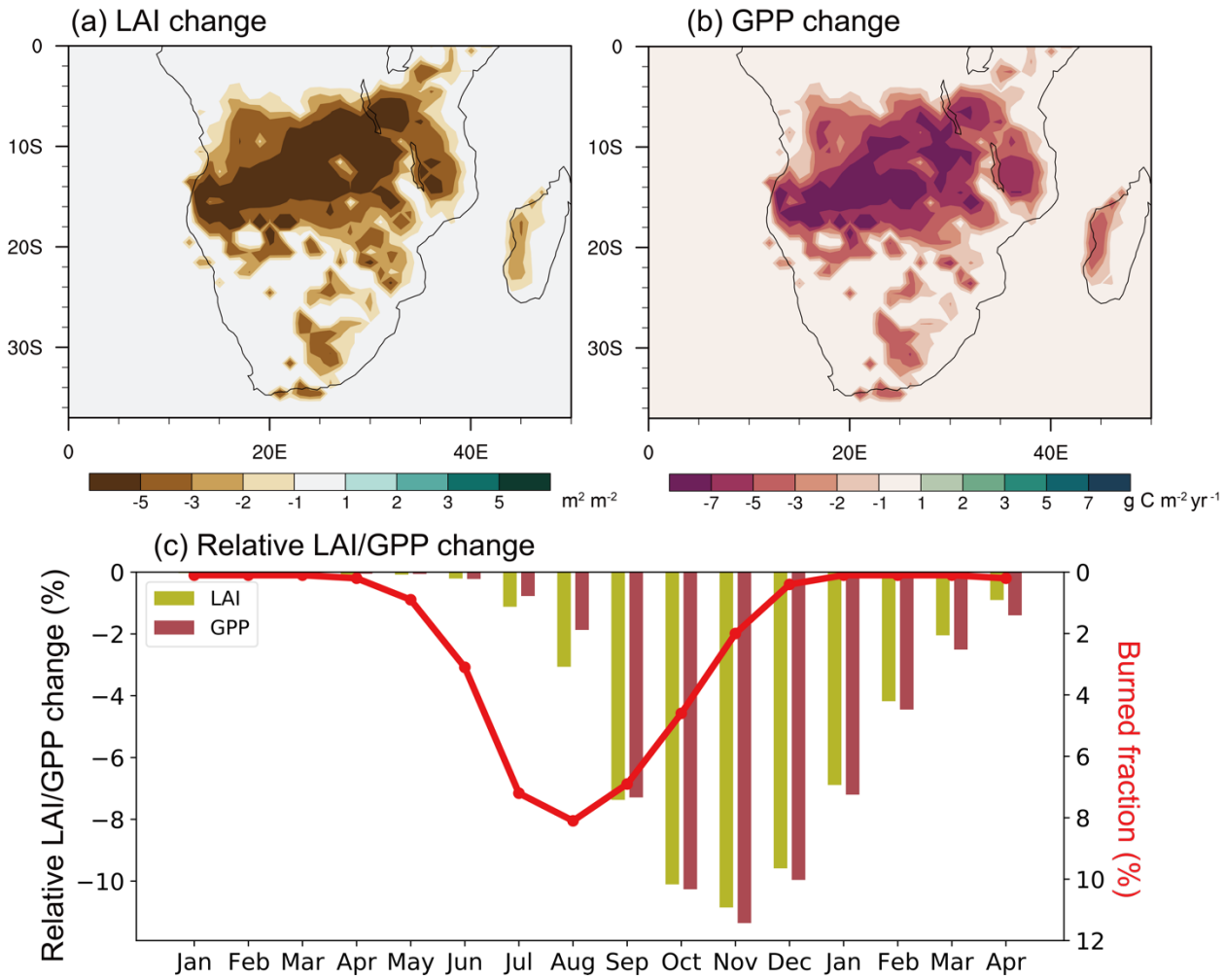

Figure 5.8 2000–2014 annual fire effects on (a) LAI and (b) GPP, and (c) Monthly fire effects on the LAI/GPP with burned area overlaid (The areal-average is calculated using grids with an annual burned fraction of more than 10%). The y-axis of burned fraction in (c) is reversed.

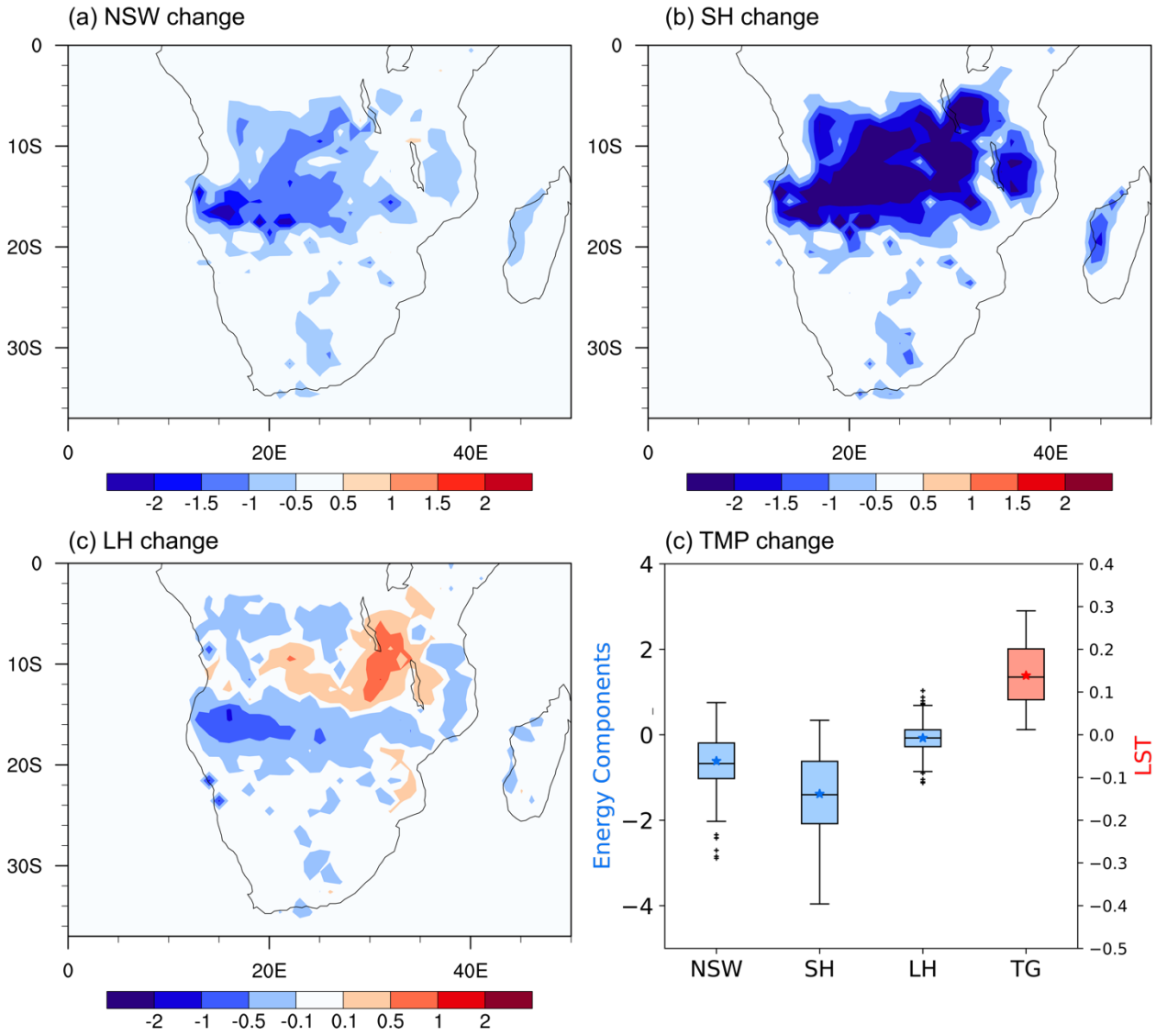

Figure 5.9 2000–2014 annual fire effects on (a) NSW, (b) SH, (c) LH, and (d) annual fire effects on NSW, SH, LH, and TMP for each grid with an annual burned fraction greater than 10%. The dots denote the areal-average fire effects in SHAF

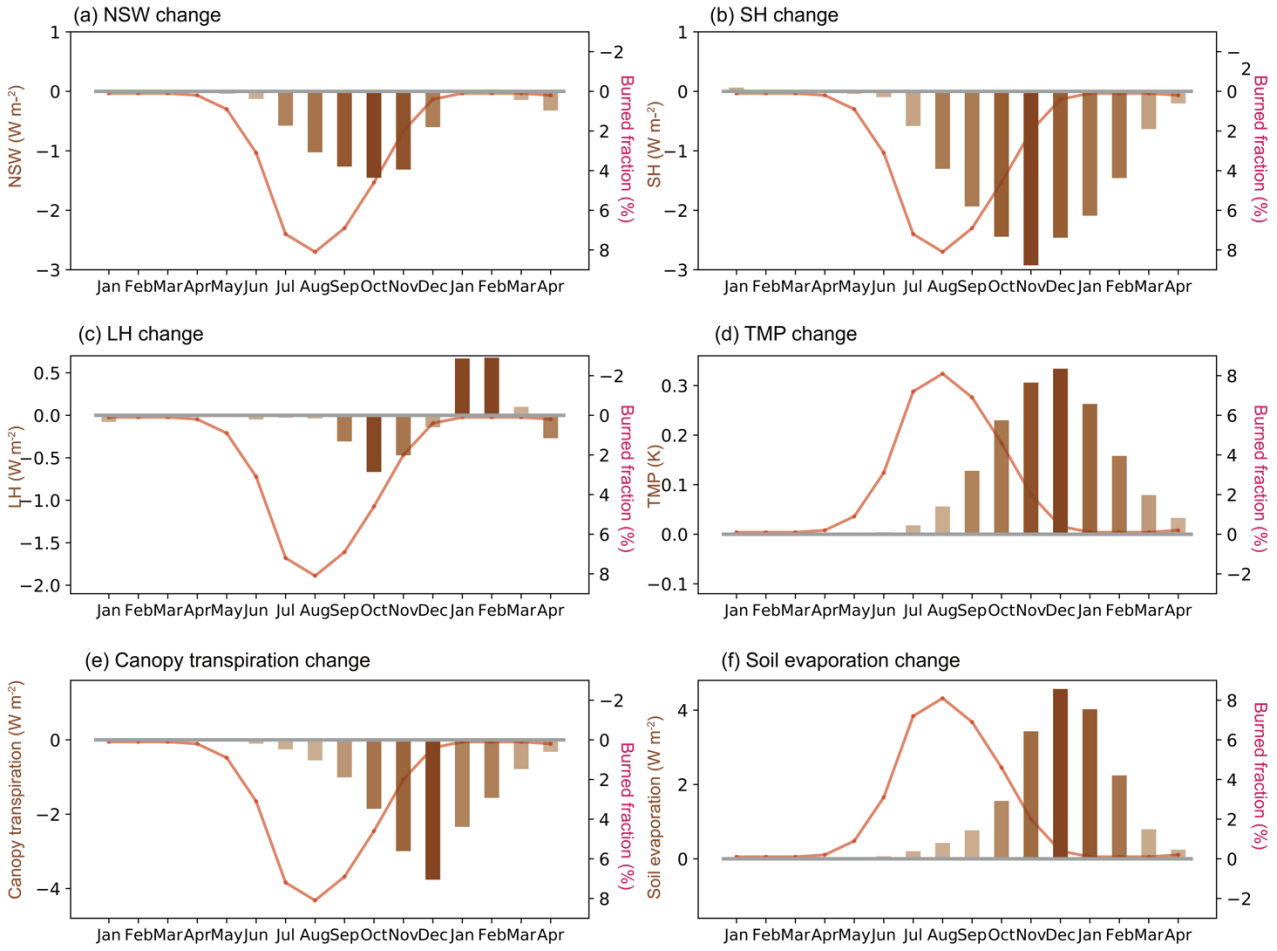

Figure 5.10 2000–2014 monthly fire effects on (a) NSW, (b) SH, (c) LH, (d) TMP, (e) canopy transpiration, and (f) soil evaporation with burned fraction overlaid. The y-axis of burned fraction in (a-c) and (e) are reversed.

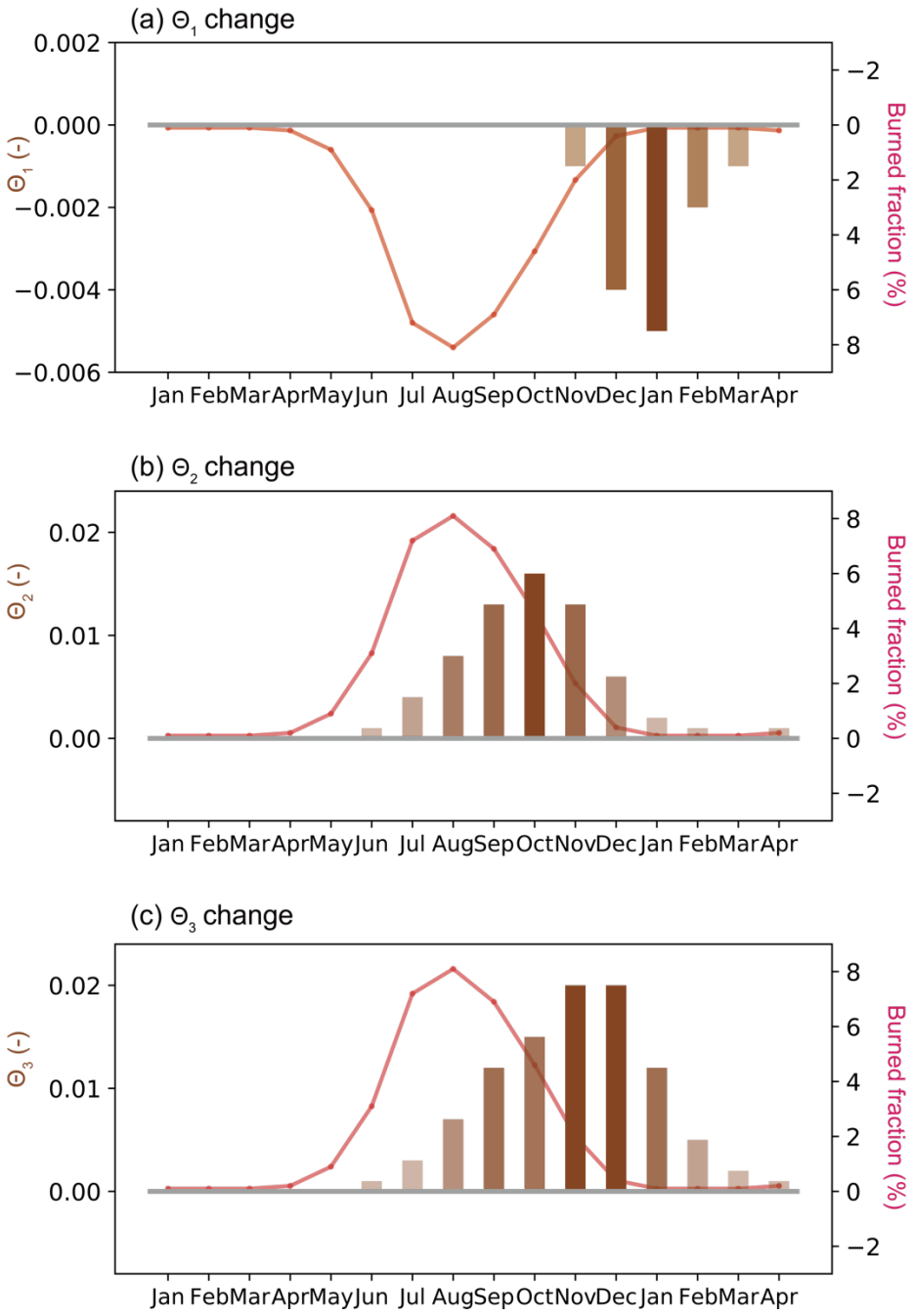

Figure 5.11 2000-2014 monthly fire effects on (a) θ_1, (b) θ_2, and (c) θ_3 with burned fraction overlaid. The y-axis of burned fraction in (a) is reversed.

Reference

Andela, N., Morton, D. C., Giglio, L., Chen, Y., van der Werf, G. R., Kasibhatla, P. S., DeFries, R. S., Collatz, G. J., Hantson, S., Kloster, S., Bachelet, D., Forrest, M., Lasslop, G., Li, F., Mangeon, S., Melton, J. R., Yue, C., and Randerson, J. T.: A human-driven decline in global burned area, Science, 356, 1356-1361, 10.1126/science.aal4108, 2017.

Arora, V. K., and Boer, G. J.: Fire as an interactive component of dynamic vegetation models, J Geophys Res-Biogeo, 110, 10.1029/2005jg000042, 2005.

Bartholome, E., and Belward, A. S.: GLC2000: a new approach to global land cover mapping from Earth observation data, Int J Remote Sens, 26, 1959-1977, 2005.

Beringer, J., Hutley, L. B., Tapper, N. J., Coutts, A., Kerley, A., and O'Grady, A. P.: Fire impacts on surface heat, moisture and carbon fluxes from a tropical savanna in northern Australia, Int J Wildland Fire, 12, 333-340, 10.1071/Wf03023, 2003.

Bistinas, I., Harrison, S. P., Prentice, I. C., and Pereira, J. M. C.: Causal relationships versus emergent patterns in the global controls of fire frequency, Biogeosciences, 11, 5087-5101, 10.5194/bg-11-5087-2014, 2014.

Bond, W. J., Woodward, F. I., and Midgley, G. F.: The global distribution of ecosystems in a world without fire, New Phytol, 165, 525-537, 10.1111/j.1469-8137.2004.01252.x, 2005.

Bond, W. J., and Midgley, G. F.: Carbon dioxide and the uneasy interactions of trees and savannah grasses, Philos T R Soc B, 367, 601-612, 10.1098/rstb.2011.0182, 2012.

Bond-Lamberty, B., Peckham, S. D., Gower, S. T., and Ewers, B. E.: Effects of fire on regional evapotranspiration in the central Canadian boreal forest, Global Change Biol, 15, 1242-1254, 10.1111/j.1365-2486.2008.01776.x, 2009.

Bowman, D. M., Balch, J. K., Artaxo, P., Bond, W. J., Carlson, J. M., Cochrane, M. A., D'Antonio, C. M., Defries, R. S., Doyle, J. C., Harrison, S. P., Johnston, F. H., Keeley, J. E., Krawchuk, M. A., Kull, C. A., Marston, J. B., Moritz, M. A., Prentice, I. C., Roos, C. I., Scott, A. C., Swetnam, T. W., van

der Werf, G. R., and Pyne, S. J.: Fire in the Earth system, Science, 324, 481-484, 10.1126/science.1163886, 2009.

Broxton, P. D., Zeng, X., Sulla-Menashe, D., and Troch, P. A.: A global land cover climatology using MODIS data, J Appl Meteorol Clim, 53, 1593-1605, 2014.

Burton, C., Betts, R., Cardoso, M., Feldpausch, T. R., Harper, A., Jones, C. D., Kelley, D. I., Robertson, E., and Wiltshire, A.: Representation of fire, land-use change and vegetation dynamics in the Joint UK Land Environment Simulator vn4.9 (JULES), Geosci Model Dev, 12, 179-193, 10.5194/gmd-12-179-2019, 2019.

Chambers, S. D., and Chapin, F. S.: Fire effects on surface-atmosphere energy exchange in Alaskan black spruce ecosystems: Implications for feedbacks to regional climate, J Geophys Res-Atmos, 108, 10.1029/2001jd000530, 2002.

Cochrane, M. A., Alencar, A., Schulze, M. D., Souza, C. M., Nepstad, D. C., Lefebvre, P., and Davidson, E. A.: Positive feedbacks in the fire dynamic of closed canopy tropical forests, Science, 284, 1832-1835, 1999.

Cox, P. M.: Description of the TRIFFID dynamic global vegetation model, 2001.

De Sales, F., Xue, Y. K., and Okin, G. S.: Impact of burned areas on the northern African seasonal climate from the perspective of regional modeling, Climate Dynamics, 47, 3393-3413, 10.1007/s00382-015-2522-4, 2016.

De Sales, F., Okin, G. S., Xue, Y., and Dintwe, K.: On the effects of wildfires on precipitation in Southern Africa, Climate Dynamics, 1-17, 2018.

Dintwe, K., Okin, G. S., and Xue, Y. K.: Fire-induced albedo change and surface radiative forcing in sub-Saharan Africa savanna ecosystems: Implications for the energy balance, J Geophys Res-Atmos, 122, 6186-6201, 10.1002/2016jd026318, 2017.

Dunin, F.: Run-off and drainage from grassland catchments, 1987.

Forkel, M., Andela, N., Harrison, S. P., Lasslop, G., van Marle, M., Chuvieco, E., Dorigo, W., Forrest, M., Hantson, S., Heil, A., Li, F., Melton, J., Sitch, S., Yue, C., and Arneth, A.: Emergent relationships

with respect to burned area in global satellite observations and fire-enabled vegetation models, Biogeosciences, 16, 57-76, 10.5194/bg-16-57-2019, 2019.

Furley, P. A., Rees, R. M., Ryan, C. M., and Saiz, G.: Savanna burning and the assessment of long-term fire experiments with particular reference to Zimbabwe, Prog Phys Geog, 32, 611-634, 2008.

Gatebe, C. K., Ichoku, C. M., Poudyal, R., Roman, M. O., and Wilcox, E.: Surface albedo darkening from wildfires in northern sub-Saharan Africa, Environ Res Lett, 9, 2014.

Gholz, H. L., and Clark, K. L.: Energy exchange across a chronosequence of slash pine forests in Florida, Agr Forest Meteorol, 112, 87-102, 2002.

Giglio, L., Randerson, J. T., and van der Werf, G. R.: Analysis of daily, monthly, and annual burned area using the fourth-generation global fire emissions database (GFED4), J Geophys Res-Biogeo, 118, 317-328, 10.1002/jgrg.20042, 2013.

Giglio, L., Boschetti, L., Roy, D. P., Humber, M. L., and Justice, C. O.: The Collection 6 MODIS burned area mapping algorithm and product, Remote Sens Environ, 217, 72-85, 10.1016/j.rse.2018.08.005, 2018.

Govaerts, Y. M., Pereira, J. M., Pinty, B., and Mota, B.: Impact of fires on surface albedo dynamics over the African continent, Journal of Geophysical Research: Atmospheres, 107, ACL 8-1-ACL 8-12, https://doi.org/10.1029/2002JD002388, 2002.

Hamilton, D. S., Hantson, S., Scott, C. E., Kaplan, J. O., Pringle, K. J., Nieradzik, L. P., Rap, A., Folberth, G. A., Spracklen, D. V., and Carslaw, K. S.: Reassessment of pre-industrial fire emissions strongly affects anthropogenic aerosol forcing, Nat Commun, 9, 10.1038/s41467-018-05592-9, 2018.

Hansen, M. C., Potapov, P. V., Moore, R., Hancher, M., Turubanova, S. A., Tyukavina, A., Thau, D., Stehman, S., Goetz, S. J., and Loveland, T. R.: High-resolution global maps of 21st-century forest cover change, Science, 342, 850-853, 2013.

Harper, A. B., Cox, P. M., Friedlingstein, P., Wiltshire, A. J., Jones, C. D., Sitch, S., Mercado, L. M., Groenendijk, M., Robertson, E., and Kattge, J.: Improved representation of plant functional types

and physiology in the Joint UK Land Environment Simulator (JULES v4. 2) using plant trait information, Geosci Model Dev, 9, 2415-2440, 2016.

Higgins, S. I., Bond, W. J., February, E. C., Bronn, A., Euston-Brown, D. I. W., Enslin, B., Govender, N., Rademan, L., O'Regan, S., Potgieter, A. L. F., Scheiter, S., Sowry, R., Trollope, L., and Trollope, W. S. W.: Effects of four decades of fire manipulation on woody vegetation structure in savanna, Ecology, 88, 1119-1125, 2007.

Huang, H., Xue, Y., Chilukoti, N., Liu, Y., Chen, G., and Diallo, I.: Assessing Global and Regional Effects of Reconstructed Land-Use and Land-Cover Change on Climate since 1950 Using a Coupled Land–Atmosphere–Ocean Model, J Climate, 33, 8997-9013, 2020a.

Huang, H., Xue, Y., Li, F., and Liu, Y.: Modeling long-term fire impact on ecosystem characteristics and surface energy using a process-based vegetation–fire model SSiB4/TRIFFID-Fire v1.0, Geosci. Model Dev., 13, 6029-6050, 10.5194/gmd-13-6029-2020, 2020b.

Hurtt, G. C., Frolking, S., Fearon, M. G., Moore, B., Shevliakova, E., Malyshev, S., Pacala, S. W., and Houghton, R. A.: The underpinnings of land-use history: three centuries of global gridded land-use transitions, wood-harvest activity, and resulting secondary lands, Global Change Biol, 12, 1208-1229, 10.1111/j.1365-2486.2006.01150.x, 2006.

Hurtt, G. C., Chini, L. P., Frolking, S., Betts, R. A., Feddema, J., Fischer, G., Fisk, J. P., Hibbard, K., Houghton, R. A., Janetos, A., Jones, C. D., Kindermann, G., Kinoshita, T., Goldewijk, K. K., Riahi, K., Shevliakova, E., Smith, S., Stehfest, E., Thomson, A., Thornton, P., van Vuuren, D. P., and Wang, Y. P.: Harmonization of land-use scenarios for the period 1500-2100: 600 years of global gridded annual land-use transitions, wood harvest, and resulting secondary lands, Climatic Change, 109, 117-161, 10.1007/s10584-011-0153-2, 2011.

Jiang, Y., Yang, X.-Q., Liu, X., Qian, Y., Zhang, K., Wang, M., Li, F., Wang, Y., and Lu, Z.: Impacts of wildfire aerosols on global energy budget and climate: The role of climate feedbacks, J Climate, 33, 3351-3366, 2020.

Jiang, Y. Q., Lu, Z., Liu, X. H., Qian, Y., Zhang, K., Wang, Y. H., and Yang, X. Q.: Impacts of global open-fire aerosols on direct radiative, cloud and surface-albedo effects simulated with CAM5, Atmos Chem Phys, 16, 14805-14824, 10.5194/acp-16-14805-2016, 2016.

Jin, Y., and Roy, D. P.: Fire-induced albedo change and its radiative forcing at the surface in northern Australia, Geophys Res Lett, 32, 2005.

Jung, M., Koirala, S., Weber, U., Ichii, K., Gans, F., Camps-Valls, G., Papale, D., Schwalm, C., Tramontana, G., and Reichstein, M.: The FLUXCOM ensemble of global land-atmosphere energy fluxes, Scientific Data, 6, 74, 10.1038/s41597-019-0076-8, 2019.

Lasslop, G., Thonicke, K., and Kloster, S.: SPITFIRE within the MPI Earth system model: Model development and evaluation, Journal of Advances in Modeling Earth Systems, 6, 740-755, 10.1002/2013ms000284, 2014.

Lasslop, G., and Kloster, S.: Human impact on wildfires varies between regions and with vegetation productivity, Environ Res Lett, 12, 115011, 2017.

Lasslop, G., Hantson, S., Harrison, S. P., Bachelet, D., Burton, C., Forkel, M., Forrest, M., Li, F., Melton, J. R., Yue, C., Archibald, S., Scheiter, S., Arneth, A., Hickler, T., and Sitch, S.: Global ecosystems and fire: Multi-model assessment of fire-induced tree-cover and carbon storage reduction, Global Change Biol, n/a, 10.1111/gcb.15160, 2020.

Li, F., Zeng, X. D., and Levis, S.: A process-based fire parameterization of intermediate complexity in a Dynamic Global Vegetation Model, Biogeosciences, 9, 2761-2780, 10.5194/bg-9-2761-2012, 2012.

Li, F., Bond-Lamberty, B., and Levis, S.: Quantifying the role of fire in the Earth system - Part 2: Impact on the net carbon balance of global terrestrial ecosystems for the 20th century, Biogeosciences, 11, 1345-1360, 10.5194/bg-11-1345-2014, 2014.

Li, F., and Lawrence, D. M.: Role of Fire in the Global Land Water Budget during the Twentieth Century due to Changing Ecosystems, J Climate, 30, 1893-1908, 10.1175/Jcli-D-16-0460.1, 2017.

Li, F., Lawrence, D. M., and Bond-Lamberty, B.: Impact of fire on global land surface air temperature and energy budget for the 20th century due to changes within ecosystems (vol 12, 044014, 2017), Environ Res Lett, 12, 10.1088/1748-9326/aa727f, 2017.

Li, W., Du, J., Li, S., Zhou, X., Duan, Z., Li, R., Wu, S., Wang, S., and Li, M.: The variation of vegetation productivity and its relationship to temperature and precipitation based on the GLASS-LAI of different African ecosystems from 1982 to 2013, International journal of biometeorology, 63, 847-860, 2019.

Liu, Y., Guo, W. D., and Song, Y. M.: Estimation of key surface parameters in semi-arid region and their impacts on improvement of surface fluxes simulation, Sci China Earth Sci, 59, 307-319, 10.1007/s11430-015-5140-4, 2016.

Liu, Y., Xue, Y. K., MacDonald, G., Cox, P., and Zhang, Z. Q.: Global vegetation variability and its response to elevated CO2, global warming, and climate variability - a study using the offline SSiB4/TRIFFID model and satellite data, Earth Syst Dynam, 10, 9-29, 2019a.

Liu, Z. H., Ballantyne, A. P., and Cooper, L. A.: Biophysical feedback of global forest fires on surface temperature, Nat Commun, 10, 2019b.

Lopez-Saldana, G., Bistinas, I., and Pereira, J. M. C.: Global analysis of radiative forcing from fire-induced shortwave albedo change, Biogeosciences, 12, 557-565, 10.5194/bg-12-557-2015, 2015.

Lyons, E. A., Jin, Y. F., and Randerson, J. T.: Changes in surface albedo after fire in boreal forest ecosystems of interior Alaska assessed using MODIS satellite observations, J Geophys Res-Biogeo, 113, G02012, 10.1029/2007jg000606, 2008.

Myhre, G., Govaerts, Y., Haywood, J. M., Berntsen, T. K., and Lattanzio, A.: Radiative effect of surface albedo change from biomass burning, Geophys Res Lett, 32, L20812, 10.1029/2005gl022897, 2005.

Pfeiffer, M., Spessa, A., and Kaplan, J. O.: A model for global biomass burning in preindustrial time: LPJ-LMfire (v1.0), Geosci Model Dev, 6, 643-685, 10.5194/gmd-6-643-2013, 2013.

Rabin, S. S., Ward, D. S., Malyshev, S. L., Magi, B. I., Shevliakova, E., and Pacala, S. W.: A fire model with distinct crop, pasture, and non-agricultural burning: use of new data and a model-fitting algorithm for FINAL.1, Geosci Model Dev, 11, 815-842, 10.5194/gmd-11-815-2018, 2018.

Saha, M. V., Scanlon, T. M., and D'Odorico, P.: Suppression of rainfall by fires in African drylands, Geophys Res Lett, 43, 8527-8533, 10.1002/2016gl069855, 2016.

Saha, M. V., D'Odorico, P., and Scanlon, T. M.: Albedo changes after fire as an explanation of fire-induced rainfall suppression, Geophys Res Lett, 44, 3916-3923, 10.1002/2017gl073623, 2017.

Saha, M. V., D'Odorico, P., and Scanlon, T. M.: Kalahari Wildfires Drive Continental Post-Fire Brightening in Sub-Saharan Africa, Remote Sensing, 11, 10.3390/rs11091090, 2019.

Samain, O., Kergoat, L., Hiernaux, P., Guichard, F., Mougin, E., Timouk, F., and Lavenu, F.: Analysis of the in situ and MODIS albedo variability at multiple timescales in the Sahel, Journal of Geophysical Research: Atmospheres, 113, 10.1029/2007JD009174, 2008.

Scholes, R. J., Ward, D. E., and Justice, C. O.: Emissions of trace gases and aerosol particles due to vegetation burning in southern hemisphere Africa, J Geophys Res-Atmos, 101, 23677-23682, Doi 10.1029/95jd02049, 1996.

Schulze, E. D., Kelliher, F. M., Korner, C., Lloyd, J., and Leuning, R.: Relationships among Maximum Stomatal Conductance, Ecosystem Surface Conductance, Carbon Assimilation Rate, and Plant Nitrogen Nutrition - a Global Ecology Scaling Exercise, Annu Rev Ecol Syst, 25, 629-+, DOI 10.1146/annurev.es.25.110194.003213, 1994.

Seo, H., and Kim, Y.: Interactive impacts of fire and vegetation dynamics on global carbon and water budget using Community Land Model version 4.5, Geosci Model Dev, 12, 457-472, 10.5194/gmd-12-457-2019, 2019.

Sheffield, J., Goteti, G., and Wood, E. F.: Development of a 50-year high-resolution global dataset of meteorological forcings for land surface modeling, J Climate, 19, 3088-3111, Doi 10.1175/Jcli3790.1, 2006.

Thonicke, K., Venevsky, S., Sitch, S., and Cramer, W.: The role of fire disturbance for global vegetation dynamics: coupling fire into a Dynamic Global Vegetation Model, Global Ecol Biogeogr, 10, 661-677, DOI 10.1046/j.1466-822x.2001.00175.x, 2001.

Thonicke, K., Spessa, A., Prentice, I. C., Harrison, S. P., Dong, L., and Carmona-Moreno, C.: The influence of vegetation, fire spread and fire behaviour on biomass burning and trace gas emissions: results from a process-based model (vol 7, pg 1991, 2010), Biogeosciences, 7, 2191-2191, 10.5194/bg-7-2191-2010, 2010.

van der Werf, G. R., Randerson, J. T., Giglio, L., Collatz, G. J., Kasibhatla, P. S., and Arellano Jr, A. F.: Interannual variability in global biomass burning emissions from 1997 to 2004, Atmos Chem Phys, 6, 3423-3441, 2006.

van der Werf, G. R., Randerson, J. T., Giglio, L., Collatz, G. J., Mu, M., Kasibhatla, P. S., Morton, D. C., DeFries, R. S., Jin, Y., and van Leeuwen, T. T.: Global fire emissions and the contribution of deforestation, savanna, forest, agricultural, and peat fires (1997-2009), Atmos Chem Phys, 10, 11707-11735, 2010.

van der Werf, G. R., Randerson, J. T., Giglio, L., van Leeuwen, T. T., Chen, Y., Rogers, B. M., Mu, M. Q., van Marle, M. J. E., Morton, D. C., Collatz, G. J., Yokelson, R. J., and Kasibhatla, P. S.: Global fire emissions estimates during 1997-2016, Earth Syst Sci Data, 9, 697-720, 2017.

Venevsky, S., Thonicke, K., Sitch, S., and Cramer, W.: Simulating fire regimes in human-dominated ecosystems: Iberian Peninsula case study, Global Change Biol, 8, 984-998, DOI 10.1046/j.1365-2486.2002.00528.x, 2002.

Venevsky, S., Le Page, Y., Pereira, J. M. C., and Wu, C.: Analysis fire patterns and drivers with a global SEVER-FIRE v1.0 model incorporated into dynamic global vegetation model and satellite and on-ground observations, Geosci. Model Dev., 12, 89-110, 10.5194/gmd-12-89-2019, 2019.

Veraverbeke, S., Verstraeten, W. W., Lhermitte, S., Van de Kerchove, R., and Goossens, R.: Assessment of post-fire changes in land surface temperature and surface albedo, and their relation with fire-burn severity using multitemporal MODIS imagery, Int J Wildland Fire, 21, 243-256, 2012.

Ward, D. S., Kloster, S., Mahowald, N. M., Rogers, B. M., Randerson, J. T., and Hess, P. G.: The changing radiative forcing of fires: global model estimates for past, present and future, Atmos Chem Phys, 12, 10857-10886, 10.5194/acp-12-10857-2012, 2012.

Wendt, C. K., Beringer, J., Tapper, N. J., and Hutley, L. B.: Local boundary-layer development over burnt and unburnt tropical savanna: an observational study, Bound-Lay Meteorol, 124, 291-304, 2007.

Xue, Y., Sellers, P. J., Kinter, J. L., and Shukla, J.: A Simplified Biosphere Model for Global Climate Studies, J Climate, 4, 345-364, 10.1175/1520-0442(1991)004<0345:asbmfg>2.0.co;2, 1991.

Yue, C., Ciais, P., Cadule, P., Thonicke, K., Archibald, S., Poulter, B., Hao, W. M., Hantson, S., Mouillot, F., Friedlingstein, P., Maignan, F., and Viovy, N.: Modelling the role of fires in the terrestrial carbon balance by incorporating SPITFIRE into the global vegetation model ORCHIDEE - Part 1: simulating historical global burned area and fire regimes, Geosci Model Dev, 7, 2747-2767, 10.5194/gmd-7-2747-2014, 2014.

Yue, C., Ciais, P., Cadule, P., Thonicke, K., and van Leeuwen, T. T.: Modelling the role of fires in the terrestrial carbon balance by incorporating SPITFIRE into the global vegetation model ORCHIDEE - Part 2: Carbon emissions and the role of fires in the global carbon balance, Geosci Model Dev, 8, 1321-1338, 10.5194/gmd-8-1321-2015, 2015.

Zhan, X. W., Xue, Y. K., and Collatz, G. J.: An analytical approach for estimating CO2 and heat fluxes over the Amazonian region, Ecol Model, 162, 97-117, 2003.

Zhang, Z., Xue, Y., MacDonald, G., Cox, P. M., and Collatz, G. J.: Investigation of North American vegetation variability under recent climate: A study using the SSiB4/TRIFFID biophysical/dynamic vegetation model, Journal of Geophysical Research: Atmospheres, 120, 1300-1321, 2015.

Zou, Y. F., Wang, Y. H., Qian, Y., Tian, H. Q., Yang, J., and Alvarado, E.: Using CESM-RESFire to understand climate-fire-ecosystem interactions and the implications for decadal climate variability, Atmos Chem Phys, 20, 995-1020, 10.5194/acp-20-995-2020, 2020.

Appendix A

Assessing global and regional effects of reconstructed land use and land cover change since 1950 on climate using a coupled land-atmosphere-ocean model – Supplementary Material

Appendix A provides supporting information for Chapter 3, which has been published in its current form in the Journal of Climate. © American Meteorological Society. Used with permission.

[**Huang, H.**, Y. Xue, N. Chilukoti, Y. Liu, G. Chen, and I. Diallo: Assessing Global and Regional Effects of Reconstructed Land-Use and Land-Cover Change on Climate since 1950 Using a Coupled Land–Atmosphere–Ocean Model. J. Climate, 33, 8997–9013, https://doi.org/10.1175/JCLI-D-20-0108.1, 2020.]

Section 1. Energy balance and energy transport of the atmosphere

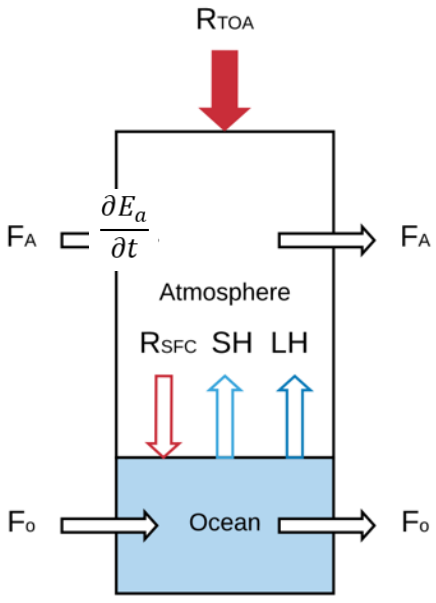

The methodology to compute the energy flux in the atmosphere system and the northward energy transport is based on Hartmann (1994). The energy balance for the atmosphere can be written as:

$$\frac{\partial E_a}{\partial t} = R_{ATM} \cdot s - \Delta F_a \qquad (S1)$$

where E_a (J) is the total energy in the atmosphere, $s = 2\pi R^2 cos\theta$ (m^2) is the area of latitudinal band at latitude θ (R is the earth radius), F_a (W) is the zonally averaged energy flux being transported northward by the atmosphere at a given latitude θ, and ΔF_a is the divergence of the horizontal energy flux in the atmosphere. R_{ATM} (W m^{-2}) is the net thermal heating within the atmosphere, including top-of-atmosphere (TOA) radiation (R_{TOA}; W m^{-2}), surface radiation (R_{SFC}; W m^{-2}), latent heat (LH; W m^{-2}), and sensible heat (SH; W m^{-2}):

$$R_{ATM} = R_{TOA} - R_{SFC} + LH + SH \quad (S2)$$

For long-term averaging, the time rate of energy change ($\frac{\partial E_a}{\partial t}$) can be neglected, and the energy surplus/deficit in the atmosphere must be balanced by meridional energy divergence/convergence. As such, an approximate balance between heating within the atmosphere and horizontal energy transport can be written as:

$$R_{ATM} \cdot s = \Delta F_a \quad (S3)$$

The zonal mean of R_{ATM} based on CTL is shown in Fig. 11a, which is consistent with the R_{ATM} calculated from the observations in Zhang and Rossow (1997). In the CTL, the R_{ATM} shows a thermal heating in the atmosphere between about 35° North and 35° South, with a bimodal distribution around the equator. The atmosphere poleward of 35° in both hemispheres experiences thermal cooling.

Since there is no horizontal flux at the south pole, following Hartman et al. (1994), the latitudinal mean of horizontal flux at latitude θ can be expressed as:

$$F_a(\theta) = \int_{-\frac{\pi}{2}}^{\theta} 2\pi a^2 cos\theta R_{ATM}\, d\theta \quad (S4)$$

As indicated by Eq. (S4), a positive/negative F_a indicates an energy surplus/deficit accumulated from the South Pole to the given latitude, which necessitates a northward/southward energy transport across that latitude. The atmosphere meridional energy flux in the CTL is shown in Fig. 11b, in which a positive value indicates northward energy flux and a negative value indicates southward energy flux, which is also similar to Zhang and Rossow (1997). The accumulated atmospheric cooling from the South Pole to a latitude corresponds to a negative F_a (southward energy flux) in the Southern Hemisphere. F_a becomes positive (northward energy flux) when more latitudes with energy surplus are involved and reaches its maximum at about 35°N. The cross-equatorial energy flux shows southward transport ($F_a(0°) < 0$) in the CTL.

Section 2. Equatorial energy transport, Hadley circulation, and ITCZ

The key to understanding Hadley cell and ITCZ response to thermal forcings is the relation between atmospheric energy transport and Hadley cell. The atmospheric meridional energy transport is dominated by the Hadley circulation in the tropics and transient eddy flux at mid-latitudes (Peixoto and Oort 1984). The cross-equatorial energy transport is in the direction of the mass transport by the upper branch of the Hadley cell, as the Hadley cell has more moist static energy (the sum of SH, LH, and geopotential energy) in the upper troposphere than in the lower troposphere (while the SH and LH are larger in the lower troposphere, the potential energy is smaller there). Moreover, the quantity of the meridional atmospheric energy transport in the tropics is proportional to the mass transport of the Hadley circulation (Frierson 2007):

$$\Delta m = \frac{\int_0^{Ps} \bar{v}\,\bar{m}\,dp}{\int_{Pm}^{Ps} \bar{v}\,dp} \quad (S5)$$

where m is the moist static energy per unit mass (J kg^{-1}), Δm (J kg^{-1}) is the total atmospheric energy transport per unit mass transport, and v is the meridional mass flux (kg s^{-1}). $\int_0^{Ps} \bar{v}\,\bar{m}\,dp$ is the atmospheric column energy transport from the surface (p_s) to the top of the atmosphere; $\int_{Pm}^{Ps} \bar{v}\,dp$ is the mass transport of the Hadley circulation from the surface (p_s) to the mid-troposphere (p_m). As Δm does not change apparently (Kang et al. 2009), tropical atmospheric energy transport is proportional to the mass transport, indicating the energy transport is realized through the mass transport of the Hadley cell. When a forcing occurs in one hemisphere, the change in energy transport in the tropical region imposes an anomalous mass transport, which would require a modification of the Hadley circulation, leading to a potential meridional shift of Hadley cell and ITCZ position.

Section 3. The definition of ITCZ width in Byrne and Schneider (2016)

We follow the definition and calculation of the ITCZ width in Byrne and Schneider (2016). In Byrne and Schneider (2016), the boundaries of ITCZ are defined as the latitude where the absolute value of the stream function (700 to 300 hPa with mass weighting) has a local maximum $\frac{\partial \psi}{\partial \phi}$ [see Fig. 2 in Byrne and Schneider (2016)]. The ITCZ width is defined as the meridional distance between the northern and southern boundaries of the ITCZ. The ITCZ width calculated using the ERA-Interim reanalysis in 1998-2014 periods is 27º in Byrne and Schneider (2016).

Below we show the vertically averaged annual and zonal mean meridional stream function (700 to 300 hPa with mass weighting) in 1950-2015 in our CTL simulation. The northern boundary (ϕ_N), southern boundary (ϕ_S) of the ITCZ and ITCZ width are denoted in the figure below.

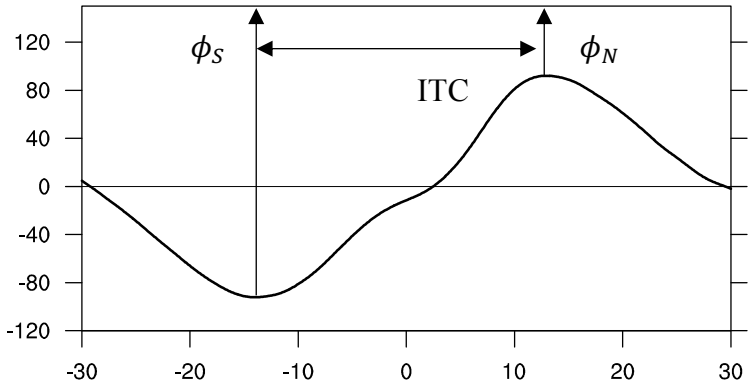

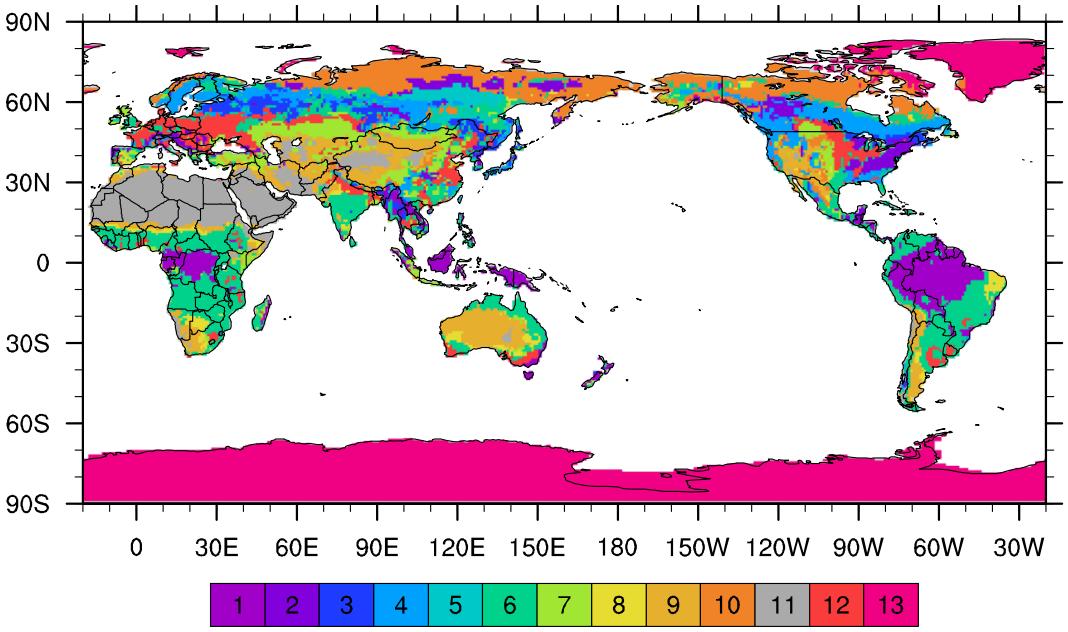

Figure S1 Potential vegetation map in SSiB2

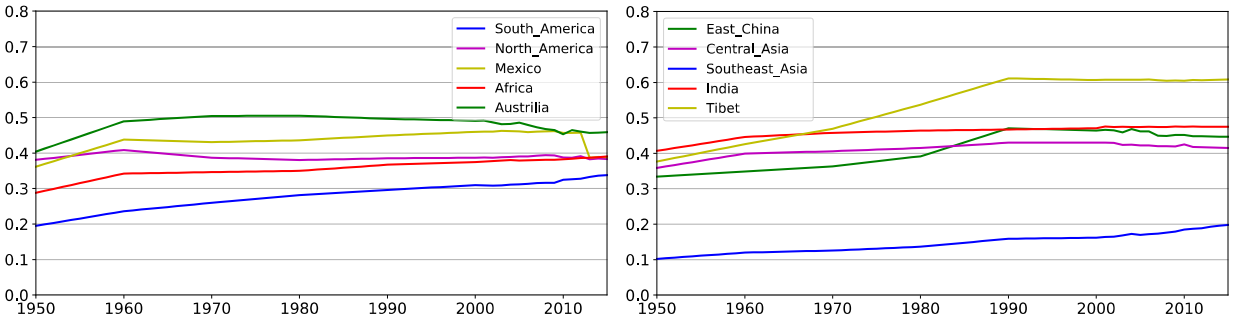

Figure S2 Time series of LULCC fraction in LUH2 for various sub-domains from 1950 to 2015.

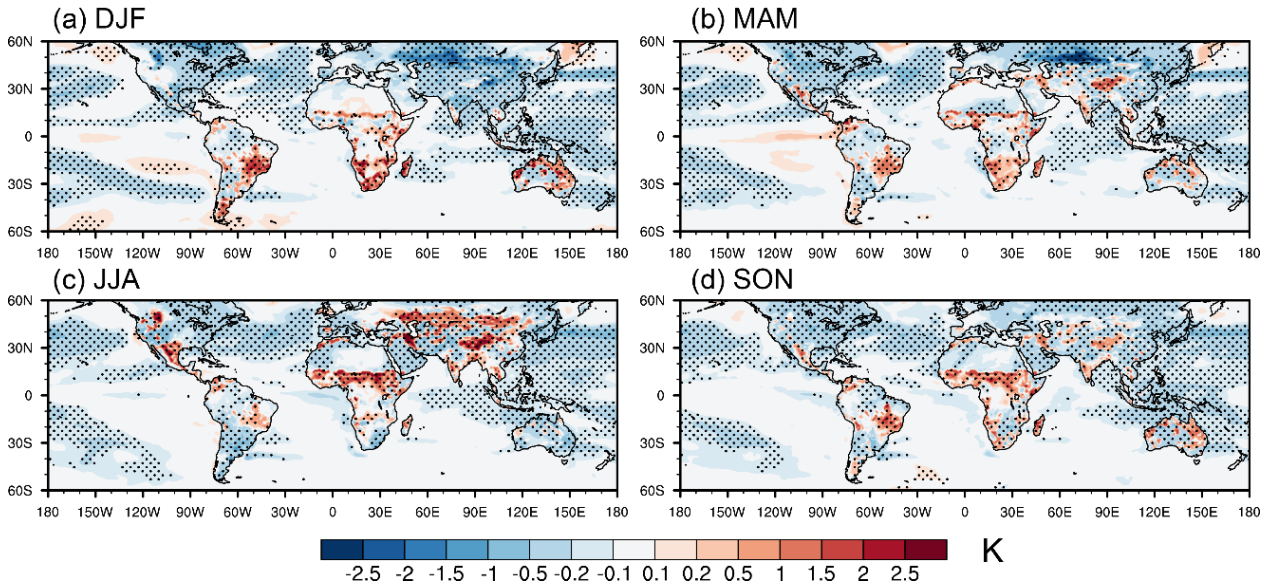

Figure. S3 Seasonal surface temperature difference (K) due to LULCC during 1950-2015 (LULCC – CTL) in (a) DJF, (b) MAM, (c) JJA, and (d) SON. Stippling indicates that the response is statistically significant at the 95% confidence level.

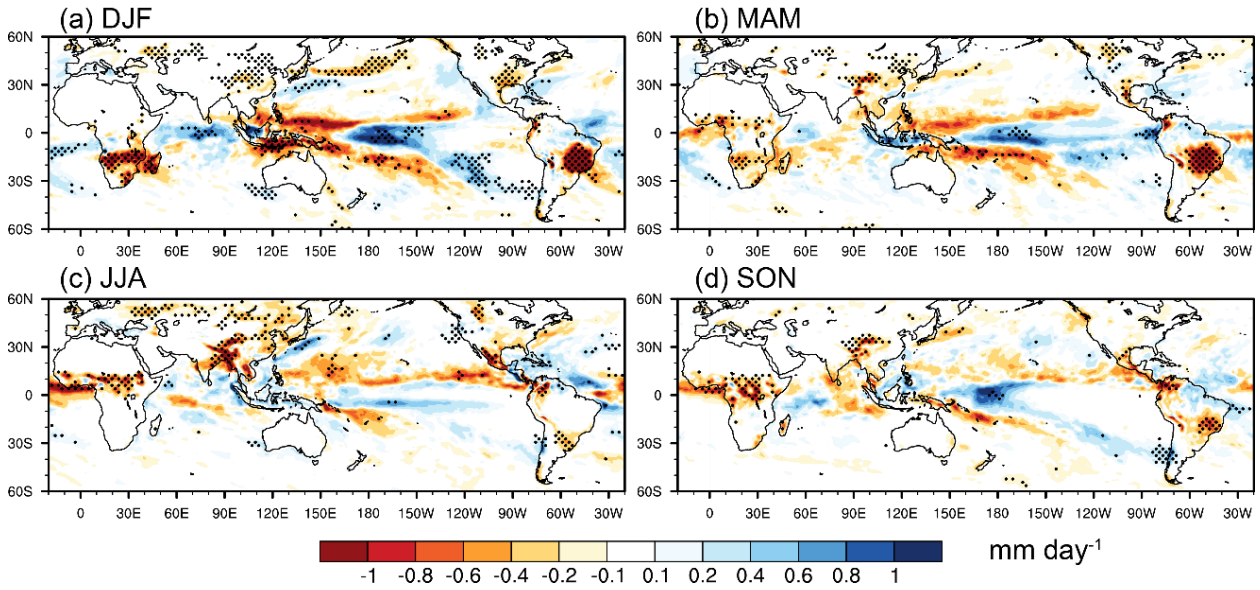

Figure. S4 Seasonal difference of precipitation (in mm day^{-1}) due to LULCC effects during 1950-2015 (LULCC – CTL) in (a) DJF, (b) MAM, (c) JJA, and (d) SON. Stippling indicates statistical significance at the 90% confidence level.

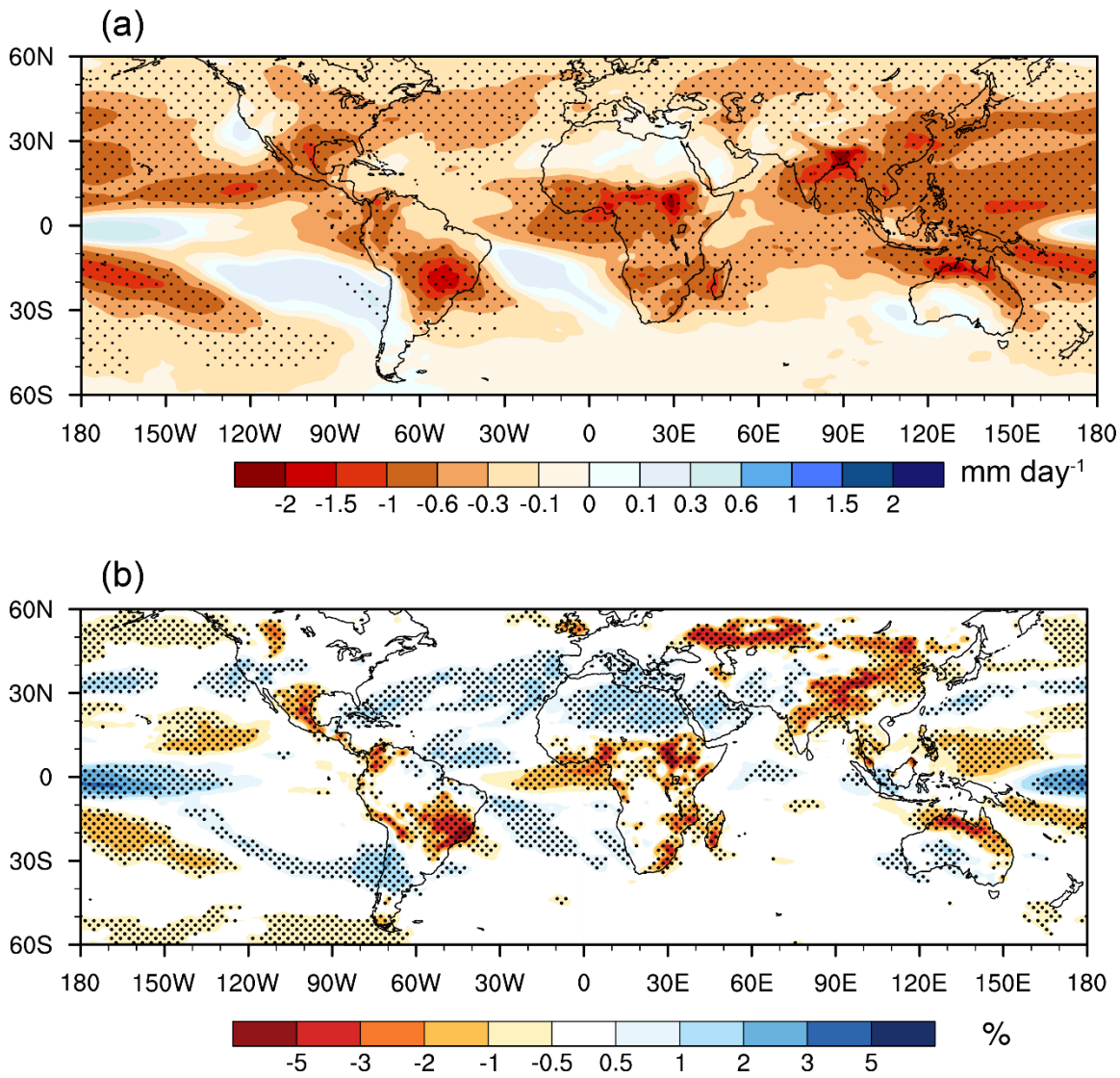

Figure S5. Annual difference of (a) precipitable water (mm day^{-1}) and (b) total cloud cover (%) due to LULCC effects in 1950-2015 (LULCC-CTL). Stippling indicates that the response is statistically significant at the 95% confidence level.

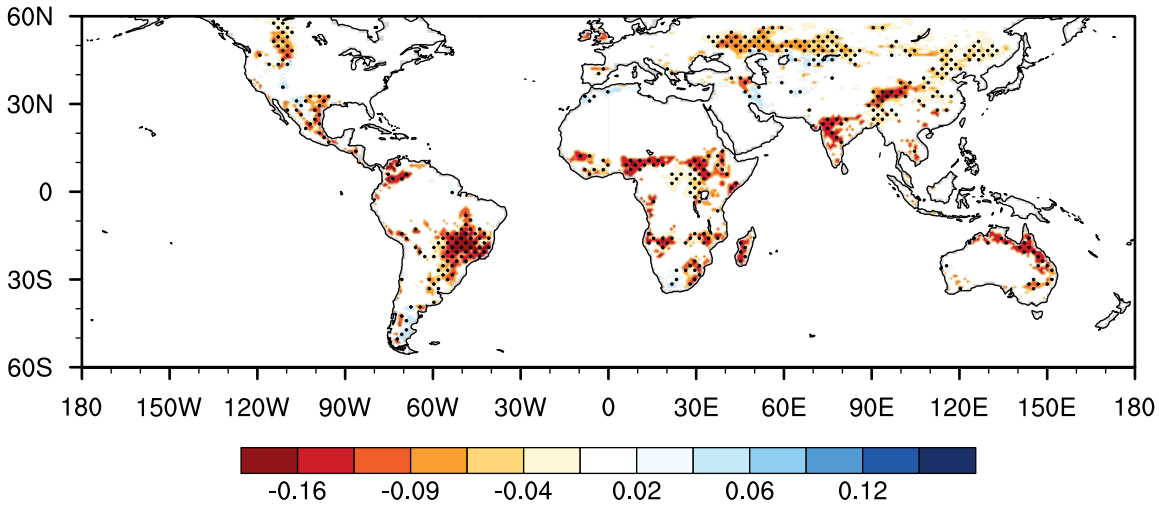

Figure S6. Annual difference of top-layer soil moisture due to LULCC effects (LULCC-CTL) in 1950-2015. Stippling indicates that the response is statistically significant at 95% confidence level.

References:

Byrne, M. P., and T. Schneider, 2016: Energetic Constraints on the Width of the Intertropical Convergence Zone. *J Climate*, **29,** 4709-4721.

Frierson, D. M. W., 2007: The dynamics of idealized convection schemes and their effect on the zonally averaged tropical circulation. *J. Atmos. Sci.*, 64, 1959-1976. https://doi.org/10.1175/JAS3935.1.

Hartmann, D. L., 1994: *Global Physical Climatology*. Academic Press, 425 pp

Kang, S. M., D. M. W. Frierson, and I. M. Held, 2009: The Tropical Response to Extratropical Thermal Forcing in an Idealized GCM: The Importance of Radiative Feedbacks and Convective Parameterization. *J. Atmos. Sci.*, **66,** 2812-2827, https://doi.org/10.1175/2009JAS2924.1.

Peixoto, J. P., and A. H. Oort, 1984: Physics of Climate. *Rev. Mod. Phys.*, 56, 365-429.

Zhang, Y. C., and W. B. Rossow, 1997: Estimating meridional energy transports by the atmospheric and oceanic general circulations using boundary fluxes. J Climate, 10, 2358-2373.

Appendix B

Modeling long-term fire impact on ecosystem characteristics and surface energy using a process-based vegetation-fire model SSiB4/TRIFFID-Fire v1.0 – Supplementary Material

Appendix B provides supporting information for Chapter 4, which has been published in its current form in the Geoscientific Model Development

[**Huang, H.**, Xue, Y., Li, F., and Liu, Y.: Modeling long-term fire impact on ecosystem characteristics and surface energy using a process-based vegetation-fire model SSiB4/TRIFFID-Fire v1. 0, Geoscientific Model Development, 1-41, 2020.]

Table S1. The maximum fire spread rate u_{max} (m s^{-1}) for PFTs in SSiB4/TRIFFID-Fire

Vegetation Types	u_{max}
BET	0.13
NET	0.15
BDT	0.13
C3 grasses	0.25
C4 grasses	0.25
Shrubs	0.18
Tundra	0.25

Table S2. PFT-dependent combustion completeness factors for leaves (CC_{leaf}), stems (CC_{wood}), roots (CC_{root}), and litter (CC_{litter}), and mortality factors for leaves (M_{leaf}), stems (M_{wood}), roots (M_{root}).

PFT	CC_{leaf}	CC_{wood}	CC_{root}	CC_{litter}	M_{leaf}	M_{wood}	M_{root}
BET	0.70	0.08	0.00	0.30	0.70	0.10	0.10
NET	0.70	0.13	0.00	0.55	0.70	0.15	0.15
BDT	0.70	0.08	0.00	0.30	0.70	0.10	0.10
C3 grasses	0.80	0.50	0.00	0.80	0.80	0.50	0.30
C4 grasses	0.80	0.50	0.00	0.80	0.80	0.50	0.30
Shrubs	0.70	0.18	0.00	0.80	0.70	0.20	0.15
Tundra	0.70	0.18	0.00	0.80	0.70	0.20	0.15

Table S3. Emission factors, EMx (g species (kg dm)$^{-1}$), for PFTs in SSiB4/TRIFFID-Fire

EM	BET	NET	BDT	C3 grasses	C4 grasses	Shrubs	Tundra
EM_{CO2}	1613	1549	1566	1647	1647	1647	1647
EM_{CO}	108	124	108	70	70	70	70
EM_{CH4}	6.3	5.1	5.8	2.5	2.5	2.5	2.5
EM_{NMHC}	7.1	5.3	14.6	5.7	5.7	5.7	5.7
EM_{H2}	3.11	1.66	2.09	0.97	0.97	0.97	0.97
EM_{NOx}	2.55	1.69	2.90	2.58	2.58	2.58	2.58
EM_{N2O}	0.2	0.25	0.25	0.18	0.18	0.18	0.18
EM_{PM25}	8.3	20.2	18.1	7.5	7.5	7.5	7.5
EM_{TPM}	10.9	15.3	18.1	8.5	8.5	8.5	8.5
EM_{TPC}	6.0	10.6	8.4	3.4	3.4	3.4	3.4
EM_{OC}	4.5	10.1	8.9	3.1	3.1	3.1	3.1
EM_{BC}	0.49	0.50	0.66	0.51	0.51	0.51	0.51

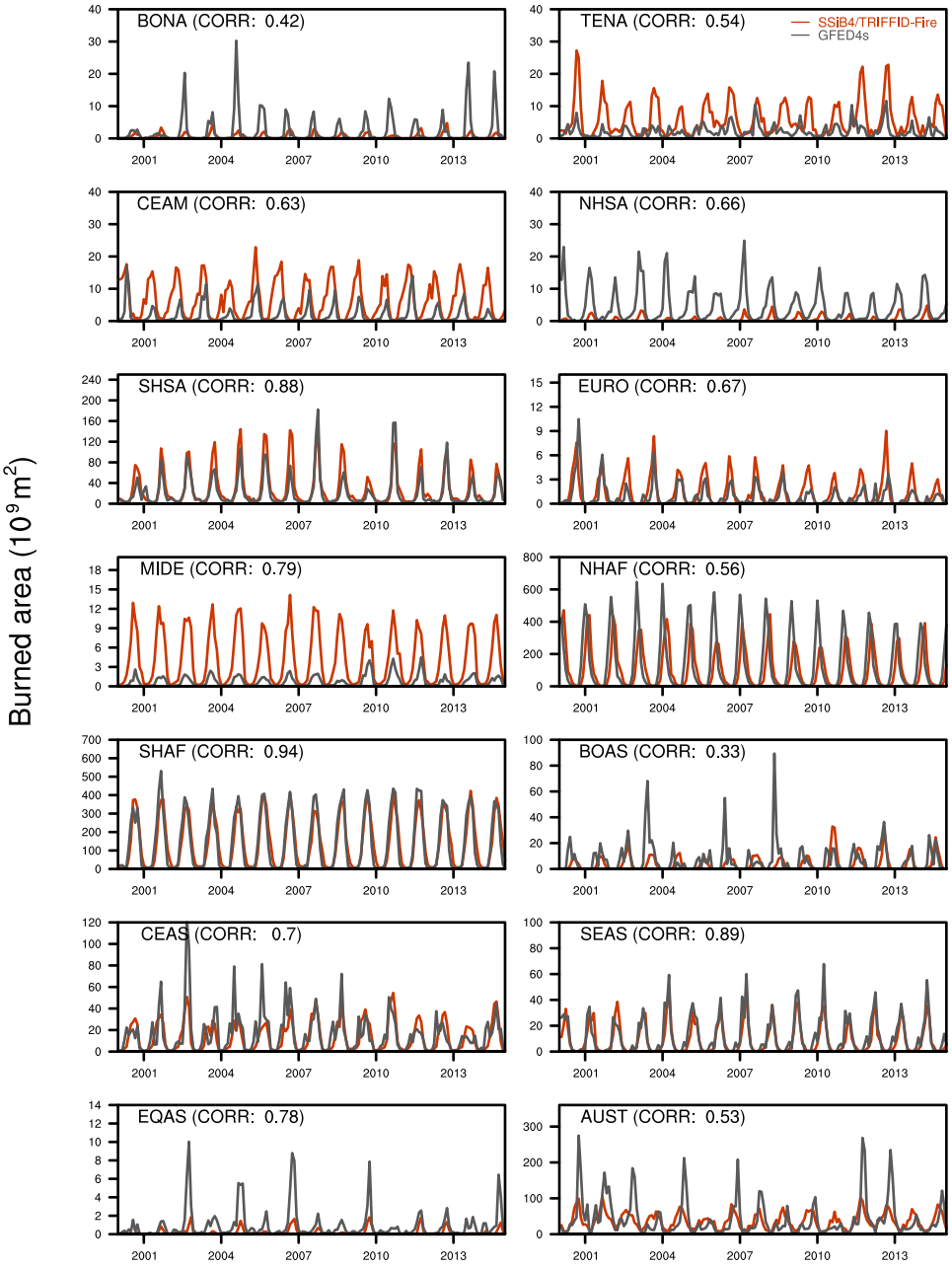

Figure S1. Monthly burned area (0.1 Mha) for 2000–2014 for GFED4s and SSiB4/TRIFFID-Fire in 14 GFED regions

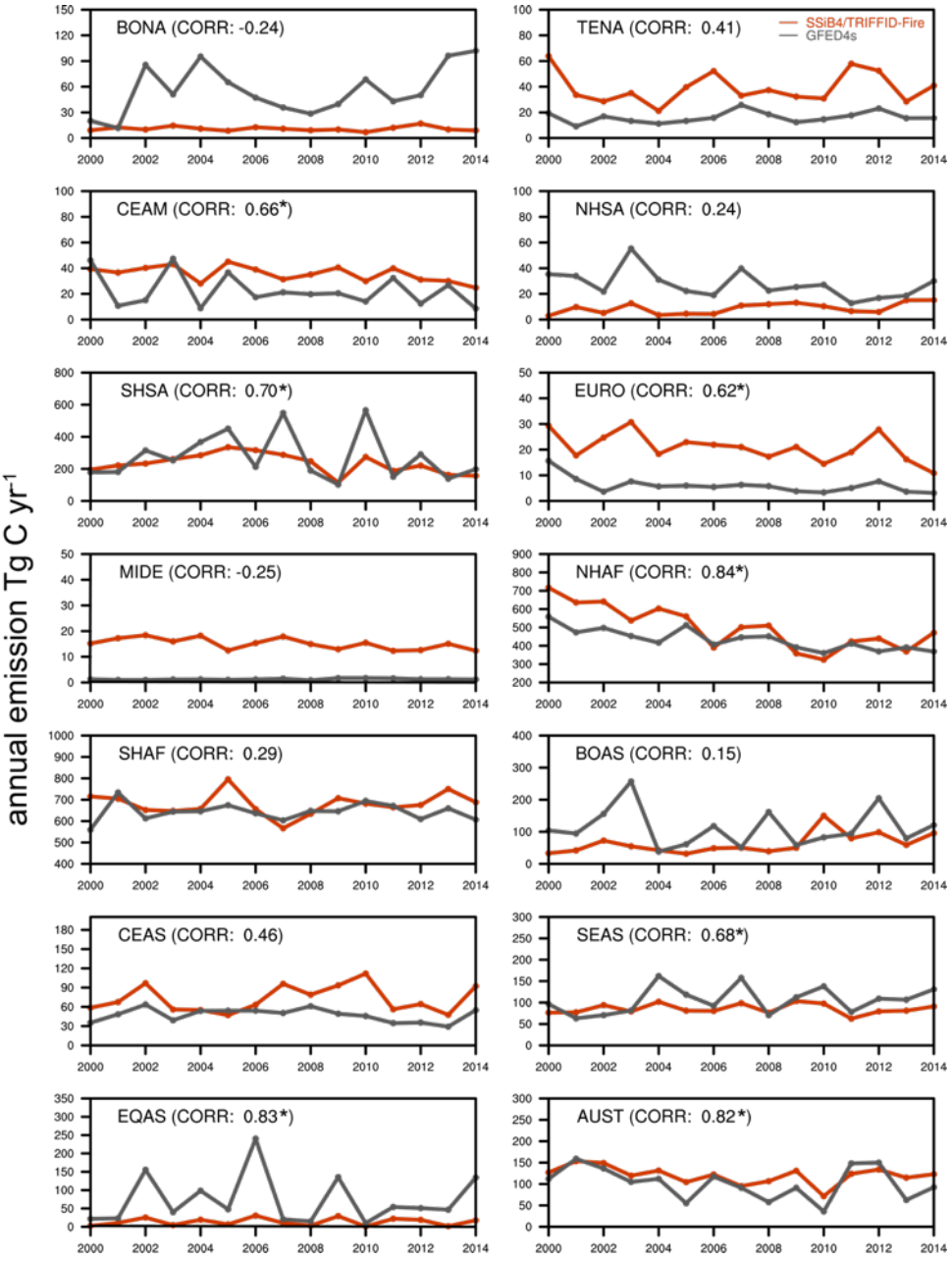

Figure S2. Annual carbon emission (Tg C yr^{-1}) for 2000-2014 for GFED4s and SSiB4/TRIFFID-Fire in 14 GFED regions. The "*" indicates the correlation is significant at $p < 0.05$.

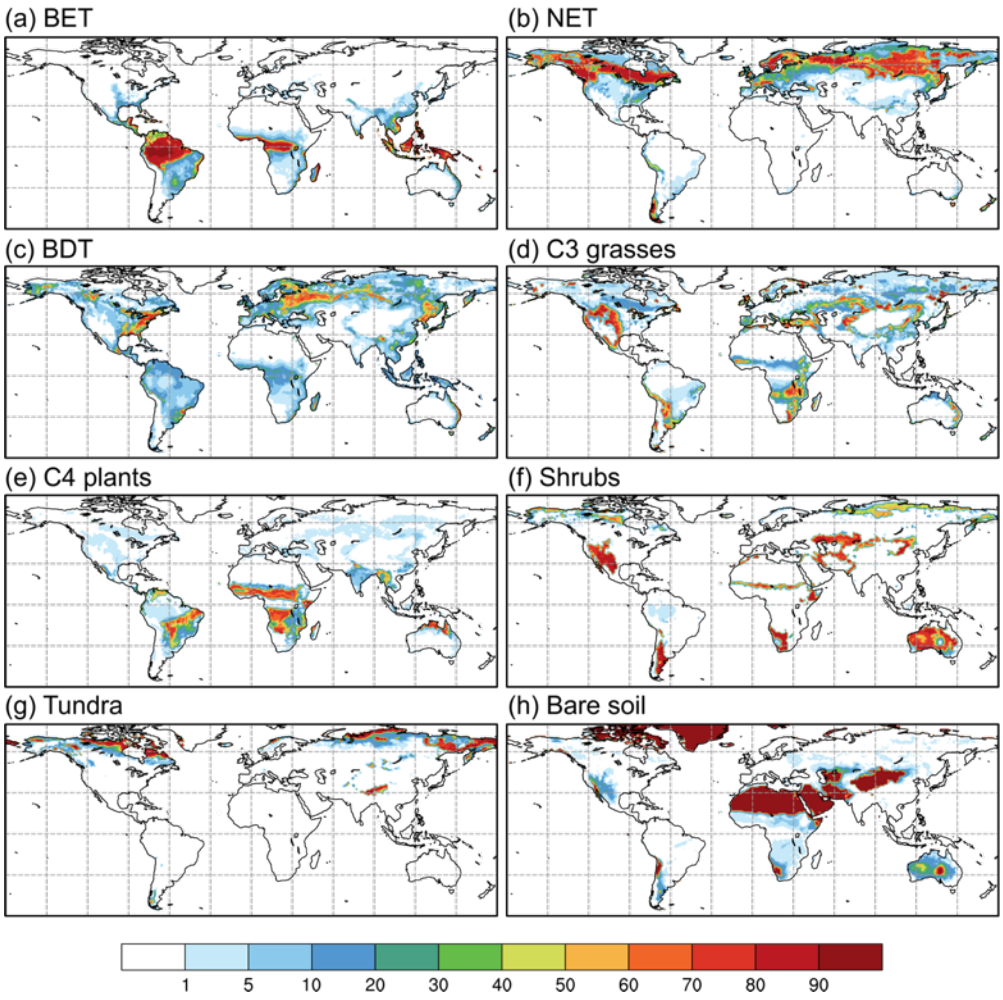

Figure S3. Fractional coverage (%) of (a) broadleaf evergreen trees (BET), (b) needleleaf evergreen trees (NET), (c) broadleaf deciduous trees (BDT), (d) C3 grasses, (e) C4 plants, (f) shrubs, (g) tundra, and (h) bare land in 2000 in SSiB4/TRIFFID-Fire.

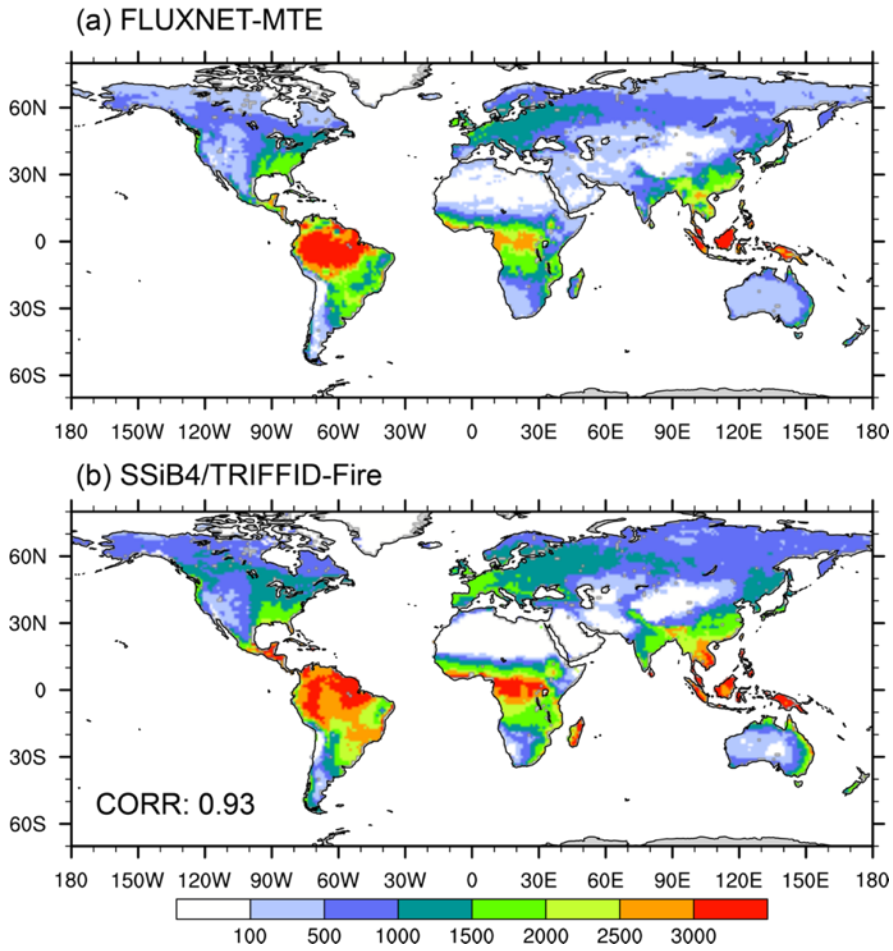

Figure S4. Spatial distribution of annual GPP (g C m^{-2} $year^{-1}$) averaged over 1982–2011 for (a) FLUXNET-MTE and (b) SSiB4/TRIFFID-Fire

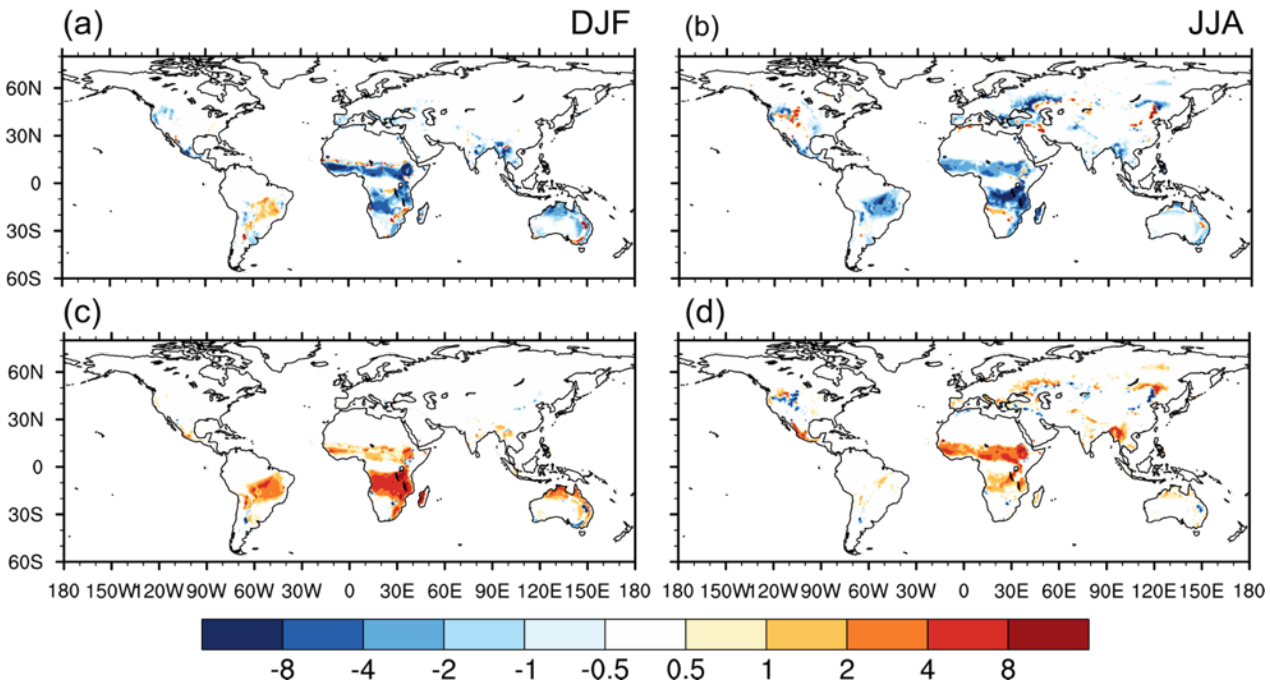

Figure S5. Difference in canopy transpiration (a, b; W m^{-2}) and ground evaporation (c, d; W m^{-2}) in DJF (a,c) and JJA (b,d) averaged over 2000-2014 between FIRE-ON and FIRE-OFF